

University of Louisville

ThinkIR: The University of Louisville's Institutional Repository

Electronic Theses and Dissertations

8-2022

Development and applications of a sensor for measurement of different modes of heat transfer on foods in a residential oven.

Kervins Petit-Bois
University of Louisville

Follow this and additional works at: <https://ir.library.louisville.edu/etd>



Part of the [Heat Transfer, Combustion Commons](#)

Recommended Citation

Petit-Bois, Kervins, "Development and applications of a sensor for measurement of different modes of heat transfer on foods in a residential oven." (2022). *Electronic Theses and Dissertations*. Paper 3965. <https://doi.org/10.18297/etd/3965>

This Master's Thesis is brought to you for free and open access by ThinkIR: The University of Louisville's Institutional Repository. It has been accepted for inclusion in Electronic Theses and Dissertations by an authorized administrator of ThinkIR: The University of Louisville's Institutional Repository. This title appears here courtesy of the author, who has retained all other copyrights. For more information, please contact thinkir@louisville.edu.

DEVELOPMENT AND APPLICATION OF A SENSOR FOR
MEASUREMENT OF DIFFERENT MODES OF HEAT TRANSFER ON FOODS
IN A RESIDENTIAL OVEN

By

Kervins Petit-Bois

B.S, Florida International University, 2019

A Thesis Submitted to the Faculty of the University of Louisville

J.B. Speed School of Engineering

In Partial Fulfillment of the requirements

For the degree of

Master of Science

In Mechanical Engineering

Department of Mechanical Engineering

University of Louisville

Louisville, Ky

August 2022

DEVELOPMENT AND APPLICATION OF A SENSOR FOR
MEASUREMENT OF DIFFERENT MODES OF HEAT TRANSFER ON FOODS
IN A RESIDENTIAL OVEN

By

Kervins Petit-Bois

B.S, Florida International University, 2019

A Thesis Approved On

August 4th, 2022

by the following Thesis Committee:

Dr. Ellen Brehob, Thesis Co-Advisor

Dr. Andrea Kelecy, Thesis Co-Advisor

Dr. Thomas Roussel, Committee Member

DEDICATION

I dedicate this thesis to my family and friends who have taught me the spirit of continuously challenging myself to become a better person each day. Throughout this study they tenaciously provided support and encouragement to ensure that I remained motivated.

ACKNOWLEDGMENT

I would like to thank my advisors, Dr. Kelecy and Dr. Brehob for their commitment, support, and encouragement throughout this study. I am thankful for advisors that take a genuine interest in my learning and demonstrate such a strong passion for physics that is demonstrated in their teaching. Additionally, I am thankful for my GE Appliances technical team for supporting me throughout the life of this study, including James Armstrong, Eric Schott Johnson, Christopher O'Malley, Sabrina Hannah, and Amelia Hensley. Lastly, I am thankful for my GE appliances management team, including Michael Ekbundit and Tim O'Connell who have created the opportunities for this project to be sponsored and funded.

ABSTRACT

DEVELOPMENT AND APPLICATION OF A SENSOR FOR MEASUREMENT
OF DIFFERENT MODES OF HEAT TRANSFER ON FOODS IN A
RESIDENTIAL OVEN

Kervins Petit-Bois

August 4th, 2022

Thermal characterization of an oven is an important part of designing an oven. Understanding how changes in cooking algorithm, oven construction, and oven materials affect cooking performance is critical in ensuring that an oven is properly designed. Often temperature data is used to characterize oven behavior, but this neglects the mode of heat transfer used to achieve these temperatures. Several studies have compared the different modes of heat transfer and cooking performance and have shown that cooking performance in radiation dominated modes are different than in convection dominated modes. The goal of this study is to develop a heat flux sensor that can be used in a residential oven operating at 375°F, mimicking the bake conditions of sugar cookies. The sensor designed must break heat transfer into conduction, convection, and radiation. The sensor designed must have nondestructive requirements for sensor use, be usable in an array of multiple sensors, and be lower cost than its predecessor the RC01 heat flux sensor.

A composite material heat flux sensor was designed that consists of a thin foil styled heat flux sensor mounted on to an aluminum mass embedded into an

insulation base. This thin foil styled heat flux sensor was used to measure convection or radiation and convection depending on its emissivity. A second aluminum mass was embedded into the bottom of the insulation to serve as a conduction path during experiments. The sensor designed provided a cost reduction of 90% when compared to the RC01 sensor

This heat flux sensor was deployed in a residential oven where three distinct cooking modes were tested: traditional bake, convection bake, and the air fry mode. These modes provided a radiation dominated mode, a convection dominated mode, and a mode that is a balance of both. In these oven tests the average of six high emissivity sensors and six low emissivity sensors was used to characterize the runs. The tests are run for ten minutes to mimic cooking test procedure and are run three times in each cooking mode to measure repeatability of each sensor. The maximum coefficient of variation measured for a sensor is 6.1%, all other sensors had a coefficient of variation of less than 5%.

The heat flux results from the oven tests reflected design intent for each mode in this study. A comparison of the average heat flux values for each mode can be seen below. Traditional bake is a mode reliant on the heating elements cycling and only natural convection. Convection bake multi and air fry deploy a combination of different heating elements and the convection fan to improve air flow. A pseudo energy efficiency is calculated that considers a ratio of energy stored by the sensors to energy consumed by the unit and shows that on average traditional bake, convection bake multi, and air fry had efficiency values of 12.16%, 22.37%, and 22.28% respectively. This demonstrates the

TABLE OF CONTENTS

List of Tables	x
List of Figures	xii
1 Introduction	1
2 Literature Review	4
2.1 Food Heat Transfer Studies	4
2.2 Oven Heat Transfer.....	9
2.3 Heat Flux Sensors.....	12
3 Heat Flux Sensor Development.....	17
3.1 Sensor Design Process.....	17
3.2 Sensor Design Criteria	20
3.3 Introduction to Heat Flux Sensor.....	20
3.4 Sensor Market Study.....	22
3.5 Sensor Supporting Theory	23
3.6 Initial Sensor Design	25
3.7 Sensor Design Optimization.....	30
4 Sensor Calibration	44
4.1 Supplier Calibration and Specifications.....	44
4.2 Radiation Calibration.....	45
4.2.1 Radiation Theory	45
4.2.2 Radiation Calibration Setup.....	49
4.2.3 Radiation Calibration Results	52
4.3 Convection Calibration	58
4.3.1 Convection Theory	58

	4.3.2 Convection Calibration Set Up	60
	4.3.3 Convection Calibration Results	62
5	Oven Test Results	70
	5.1 Oven Test Setup	70
	5.2 Oven Level Calibration.....	75
	5.3 Oven Test Results.....	82
	5.3.1 Traditional Bake Results.....	82
	5.3.2 Convection Bake Multi-Rack Results	91
	5.3.3 Air Fry Results.....	95
	5.4 Repeatability	101
	5.4.1 Traditional Bake Repeatability.....	101
	5.4.2 Convection Bake Multi Repeatability	104
	5.4.3 Air Fry Repeatability	107
	5.5 Oven mode comparison	110
6	Discussion	115
	6.1 Conclusions	115
	6.2 Future Work	117
	References	119
	Appendices.....	121
	A. Appendix I Radiation Calibration Graphs	121
	B. Appendix II Convection Calibration Graphs	132
	C. Appendix III Oven Test Graphs	149
	D. Appendix IV Sensor Material Specifications.....	164
	Curriculum Vitae	168

LIST OF TABLES

Table 1. Correlation between heat transfer coefficients and quality of the radiant wall oven baked potato strips.....	8
Table 2 Market Sensor Summary	22
Table 3 Insulation Material Summary	29
Table 4 Revision history of the insulation base designed	31
Table 5 Calibration summary from Supplier using ASTM Standard C1130	44
Table 6 Summary of the average heat flux readings between 30 and 60 minutes for each run.....	55
Table 7 Velocity measurements	67
Table 8 Overview of oven modes used in testing	74
Table 9 Overview of heating elements used in study and duty cycles/ Although the modes are controlled to a similar center oven temperature it is achieved in different ways.....	74
Table 10 Test run order matrix for assembly calibration testing	77
Table 11 Heat flux average results for oven calibration testing. A heat map is applied to each individual column to show the variation in magnitude of each sensor at a position. The averages have their own heat map to show which positions and sensors measure high or low.	78
Table 12 Correction coefficient matrix for assembly calibration testing. The initial heat flux matrices are multiplied by the correction coefficients to obtain these corrected heat flux values	80
Table 13 Unit power and temperature averages during assembly calibration testing	81
Table 14 Traditional bake unit summary.....	103
Table 15 Traditional Bake 3-run heat flux summary for heat flux sensor and bottom mass	103
Table 16 Average heat flux for all gold or black sensors and for all three Traditional Bake runs	104
Table 17 Convection bake multi three run unit summary.....	105

Table 18 Convection bake multi black and gold Sensor 3-run Average summary	106
Table 19 Convection bake multi 3-run heat flux summary for heat flux sensor and bottom mass	106
Table 20 Air fry three run unit summary	108
Table 21 Air fry black and gold sensor 3-run average summary	108
Table 22 Air fry 3-run heat flux summary for heat flux sensor and bottom mass	109
Table 23 Traditional bake, convection bake multi, and air fry 3 run average summary	111
Table 24 Range of 6 black and 6 gold heat flux sensors across each run in the three different oven modes	112
Table 25 Comparison of run efficiency for the three cooking modes	114
Table 26 Top mass, bottom mass, and insulation base measurements for each heat flux sensor assembly	164

LIST OF FIGURES

Figure 1-1 Residential Wall Oven	3
Figure 2-1 Profile of sponge cakes baked at different are temperatures and velocities. (Sato et al.,1987).....	6
Figure 2-2 Cookie Color vs Heating Time.....	9
Figure 2-3 Oven Scheme used in energy balance study in a residential oven (Ramirez, 2015)	10
Figure 2-4 Energy Breakdown of residential oven with a porous brick load (Ramirez,2015)	11
Figure 2-5 H-Monitor deployed for CFD modeling of heat transfer in pilot oven .	12
Figure 2-6 Separation of convective and radiative heat fluxes (Khaled et al. (2010))	13
Figure 2-7 Schematic of plate thermometer (Liu, 2010).....	14
Figure 2-8 Surface temperature measured and ideal surface temperature correlation (Liu, 2021)	15
Figure 3-1 Sensor Design Process.....	17
Figure 3-2 Hukseflux RC01 water cooled heat flux sensor with water line connected. The RC01 heat flux sensor is equipped with a low emissivity and high emissivity surface that can collect a combined radiation and convection reading and convection reading.....	18
Figure 3-3 Heat Flux results for 30-minute testing using the RC01 heat flux sensor. This test is run in a 350°F gas range and is started with an ambient oven start. The total heat flux is derived from a high emissivity surface and radiative heat flux is a product of total heat flux minus convective heat flux measured by the low emissivity surface.	19
Figure 3-4 Fluxteq Illustration of heat flow through sensor	21
Figure 3-5 Diagram of composite sensor.....	24
Figure 3-6 Energy balance of thermal masses (bottom mass is left and top mass is right)	24
Figure 3-7 Biot number evaluated at various heat transfer coefficients for various radii thermal masses (note convection coefficient in W/m^2-K)	26

Figure 3-8 Aluminum Discs used for temperature limit testing	27
Figure 3-9 Time to 300°F using twp different sizes of aluminum masses	27
Figure 3-10 Results of 375°F oven tests with aluminum masses of different sizes. The test time to design to is 10 minutes with a temperature limit of 300°F.	28
Figure 3-11 Composite Heat Flux Sensor Concept 1 Prototype	30
Figure 3-12 Revision 2 simulation at steady state temperatures for thermal mass with reduced area contact with the bottom mass at constant surface temperature	34
Figure 3-13 Revision 3 simulation at steady state temperatures for thermal mass with point contacts with the bottom mass at constant surface temperature	35
Figure 3-14 Test setup for isothermal conduction tests	36
Figure 3-15 Diagram of infill density used for insulation base	37
Figure 3-16 Isothermal conduction test results using closed loop cooking pan set at 300°F. Solid lines represent temperature and use the primary y-axis. The dashed lines uses secondary y-axis and represent heat transfer rate.	38
Figure 3-17 Reflective tape on insulation base	39
Figure 3-18 Reflective vs non-reflective insulation base surface results	40
Figure 3-19 Cross sectional view showing insulation height and spacing between the aluminum masses	41
Figure 3-20 “Short” and “Tall” sensor test set up	41
Figure 3-21 Temperatures for sensors built with different insulation heights	42
Figure 3-22 Temperatures measured for sensors built with high infill (100%) and low infill (20%).....	43
Figure 4-1 Radiation enclosure designed for radiation calibration testing	46
Figure 4-2 Thermal resistance and resulting heat flux equation for a three-surface enclosure with one surface reradiating (Theodore et al., 2011)	46
Figure 4-3 Thermal resistance and resulting heat flux equation of two nonblack surfaces of known geometry (Theodore et al., 2011).....	47

Figure 4-4 View factor case of finite circular disc parallel to rectangle separated by distance (Abishek et al., 1995)	48
Figure 4-5 Theoretical heat flux calculated for various sensor temperatures in radiation calibration configuration	49
Figure 4-6 Diagram of radiation chamber used for heat flux sensor calibration..	50
Figure 4-7 Experimental Setup for radiation calibration chamber	51
Figure 4-8 Thermal plot showing surface, sensor, and heater temperatures measured for sensor 1 300°F(top) and 400°F test(bottom) test.....	53
Figure 4-9 Heat flux versus time for 300°F(top) and 400°F(bottom) heater tests for all 12 sensors.	54
Figure 4-10 Comparison of heat flux averages during last 30 minutes of each test for both temperature configurations	55
Figure 4-11 Heat flux vs sensor temperature for 300°F (top) and 400°F(bottom)	57
Figure 4-12 Convection calibration chamber diagram	59
Figure 4-13 Theoretical heat flux as a function of sensor temperature for low and high air velocity	60
Figure 4-14 Experimental setup used in convection calibration of heat flux sensors	61
Figure 4-15 Front view of convection calibration chamber with heat flux sensor in position of test with air flowing out of the page	62
Figure 4-16 Temperature data over time Low Velocity (top) High Velocity (bottom)	63
Figure 4-17 Heat flux versus time for low and high air velocity.....	64
Figure 4-18 Heat flux versus sensor temperature for sensor 1 at low and high air velocities (labels are getting small here).....	65
Figure 4-19 Low and high velocity plots for each sensor in convection calibration study(top) and normalized subset of sensors (bottom)	66
Figure 4-20 Three heat flux as a function of temperature without disassembling between runs for sensor 6 (top) and sensor 4 (bottom)	68

Figure 4-21 Three run test with disassembling sensors for sensor 6 (top) and sensor 4(bottom).....	69
Figure 5-1 Twelve heat flux sensor array CAD assembly (left) and assembly layout and numbering (right)	70
Figure 5-2 Instrumented PTS9000 electric wall oven unit used in study	72
Figure 5-3 Heat flux sensor array in oven.....	72
Figure 5-4 Overview of oven operation in traditional bake. Test period is where heat flux sensors are collecting data.....	73
Figure 5-5 The air flow in the oven is controlled by a by the convection fan. Clockwise rotation leads to horizontal air flow configuration(left) and counterclockwise rotation leads to perpendicular air flow configuration (right).	75
Figure 5-6 Schematic of final heat flux assembly used in oven level testing	76
Figure 5-7 Electric wall oven heating elements used in traditional bake.....	82
Figure 5-8 Heat flux measure for Traditional Bake, run 1 heat flux over time	83
Figure 5-9 Interior oven temperatures measured for Traditional Bake, run 1	83
Figure 5-10 Average heat flux measured for a 10 minute test in Traditional Bake, run 1.....	85
Figure 5-11 Temperature over time for the top mass for top mass in Traditional Bake, run 1	86
Figure 5-12 Temperature over time for bottom mass in Traditional Bake, run 1.	86
Figure 5-13 Diagram of sensor zone configuration.....	87
Figure 5-14 Zonal heat flux vs time for TB run 1.....	89
Figure 5-15 Fraction of each mode of heat transfer by zone for Traditional Bake, run 1.....	90
Figure 5-16 Heat flux sensor measurement versus top mass flux calculated using aluminum mass temperature	90
Figure 5-17 Heating elements and fans used in Convection Bake Multi.....	91
Figure 5-18 Heat flux measured for Convection Bake Multi, run 1	91
Figure 5-19 Interior oven temperatures measured for Convection Bake Multi, run 1.....	92

Figure 5-20 CBM Zonal heat flux over time	93
Figure 5-21 Average heat flux sensor reading Convection Bake Multi, run 1	94
Figure 5-22 Heat flux for each mode of heat transfer for Convection Bake Multi, run 1.....	94
Figure 5-23 Fraction of each mode of heat transfer by zone for Convection Bake Multi, run 1	95
Figure 5-24 Air fry elements used.....	96
Figure 5-25AF run 1 heat flux vs time.....	96
Figure 5-26 Air fry run 1 unit temperature and power over time	97
Figure 5-27 AF run 1 Zonal Approach	98
Figure 5-28 Air fry run 1 heat flux averages over 10-minute test.....	99
Figure 5-29 Air fry run 1 zonal heat flux breakdown	99
Figure 5-30 Air fry run 1 energy ratios	100
Figure 5-31 Comparison of average heat flux measured for three runs of Traditional Bake.....	102
Figure 5-32 Convection bake multi 3 run averages	105
Figure 5-33 Average heat flux measured three runs of the Air Fry cooking mode	107
Figure 5-34 Radiation, convection, and conduction average for each cooking mode using the average of all sensors for each run across all three runs for each mode.....	111
Figure 5-35 Ten second moving averages of heat flux profile for one run of the three oven modes using sensor 6 and 7.....	113
Figure 0-1 Sensor 2 radiation calibration thermal plots. Temperature data and heat flux data for 300°F test can be seen in top and 400°F test can be seen in bottom graph.	121
Figure 0-2 Sensor 3 radiation calibration thermal plots. Temperature data and heat flux data for 300°F test can be seen in top and 400°F test can be seen in bottom graph.	122

Figure 0-3 Sensor 4 radiation calibration thermal plots. Temperature data and heat flux data for 300°F test can be seen in top and 400°F test can be seen in bottom graph.	123
Figure 0-4 Sensor 5 radiation calibration thermal plots. Temperature data and heat flux data for 300°F test can be seen in top and 400°F test can be seen in bottom graph.	124
Figure 0-5 Sensor 6 radiation calibration thermal plots. Temperature data and heat flux data for 300°F test can be seen in top and 400°F test can be seen in bottom graph.	125
Figure 0-6 Sensor 7 radiation calibration thermal plots. Temperature data and heat flux data for 300°F test can be seen in top and 400°F test can be seen in bottom graph.	126
Figure 0-7 Sensor 8 radiation calibration thermal plots. Temperature data and heat flux data for 300°F test can be seen in top and 400°F test can be seen in bottom graph.	127
Figure 0-8 Sensor 9 radiation calibration thermal plots. Temperature data and heat flux data for 300°F test can be seen in top and 400°F test can be seen in bottom graph.	128
Figure 0-9 Sensor 10 radiation calibration thermal plots. Temperature data and heat flux data for 300°F test can be seen in top and 400°F test can be seen in bottom graph.	129
Figure 0-10 Sensor 11 radiation calibration thermal plots. Temperature data and heat flux data for 300°F test can be seen in top and 400°F test can be seen in bottom graph.	130
Figure 0-11 Sensor 12 radiation calibration thermal plots. Temperature data and heat flux data for 300°F test can be seen in top and 400°F test can be seen in bottom graph.	131
Figure 0-12 Sensor 2 convection calibration results. The first two graphs are temperature plots for the sensor, aluminum mass, and the air inlet and outlet temperature. The sensor temperature and aluminum temperature are measured to be the same. Inlet and outlet display no measurable	

changes in temperature. The bottom graph represents heat flux over time for low and high velocity tests. 133

Figure 0-13 Sensor 3 convection calibration results. The first two graphs are temperature plots for the sensor, aluminum mass, and the air inlet and outlet temperature. The sensor temperature and aluminum temperature are measured to be the same. Inlet and outlet display no measurable changes in temperature. The bottom graph represents heat flux over time for low and high velocity tests. 135

Figure 0-14 Sensor 4 convection calibration results. The first two graphs are temperature plots for the sensor, aluminum mass, and the air inlet and outlet temperature. The sensor temperature and aluminum temperature are measured to be the same. Inlet and outlet display no measurable changes in temperature. The bottom graph represents heat flux over time for low and high velocity tests. 136

Figure 0-15 Sensor 5 convection calibration results. The first two graphs are temperature plots for the sensor, aluminum mass, and the air inlet and outlet temperature. The sensor temperature and aluminum temperature are measured to be the same. Inlet and outlet display no measurable changes in temperature. The bottom graph represents heat flux over time for low and high velocity tests. 138

Figure 0-16 Sensor 6 convection calibration results. The first two graphs are temperature plots for the sensor, aluminum mass, and the air inlet and outlet temperature. The sensor temperature and aluminum temperature are measured to be the same. Inlet and outlet display no measurable changes in temperature. The bottom graph represents heat flux over time for low and high velocity tests. 139

Figure 0-17 Sensor 7 convection calibration results. The first two graphs are temperature plots for the sensor, aluminum mass, and the air inlet and outlet temperature. The sensor temperature and aluminum temperature are measured to be the same. Inlet and outlet display no measurable

changes in temperature. The bottom graph represents heat flux over time for low and high velocity tests	141
Figure 0-18 Sensor 8 convection calibration results. The first two graphs are temperature plots for the sensor, aluminum mass, and the air inlet and outlet temperature. The sensor temperature and aluminum temperature are measured to be the same. Inlet and outlet display no measurable changes in temperature. The bottom graph represents heat flux over time for low and high velocity tests.	142
Figure 0-19 Sensor 9 convection calibration results. The first two graphs are temperature plots for the sensor, aluminum mass, and the air inlet and outlet temperature. The sensor temperature and aluminum temperature are measured to be the same. Inlet and outlet display no measurable changes in temperature. The bottom graph represents heat flux over time for low and high velocity tests.	144
Figure 0-20 Sensor 10 convection calibration results. The first two graphs are temperature plots for the sensor, aluminum mass, and the air inlet and outlet temperature. The sensor temperature and aluminum temperature are measured to be the same. Inlet and outlet display no measurable changes in temperature. The bottom graph represents heat flux over time for low and high velocity tests.	145
Figure 0-21 Sensor 11 convection calibration results. The first two graphs are temperature plots for the sensor, aluminum mass, and the air inlet and outlet temperature. The sensor temperature and aluminum temperature are measured to be the same. Inlet and outlet display no measurable changes in temperature. The bottom graph represents heat flux over time for low and high velocity tests.	147
Figure 0-22 Sensor 12 convection calibration results. The first two graphs are temperature plots for the sensor, aluminum mass, and the air inlet and outlet temperature. The sensor temperature and aluminum temperature are measured to be the same. Inlet and outlet display no measurable	

changes in temperature. The bottom graph represents heat flux over time for low and high velocity tests.	148
Figure 0-23 Heat flux measure for Traditional Bake, run 2 heat flux over time .	149
Figure 0-24 Zonal heat flux measure for Traditional Bake, run 2 heat flux over time	149
Figure 0-25 Heat flux measure for Traditional Bake, run 2 heat flux over time .	150
Figure 0-26 Temperature over time for the top mass for top mass in Traditional Bake, run 2	150
Figure 0-27 Temperature over time for the bottom mass for top mass in Traditional Bake, run 2.....	151
Figure 0-28 Heat flux measure for Traditional Bake, run 3 heat flux over time .	151
Figure 0-29 Zonal heat flux measure for Traditional Bake, run 3 heat flux over time	152
Figure 0-30 Interior oven temperatures measured for Traditional Bake, run 3 .	152
Figure 0-31 Temperature over time for the top mass for top mass in Traditional Bake, run 3	153
Figure 0-32 Temperature over time for the bottom mass for top mass in Traditional Bake, run 3.....	153
Figure 0-33 Heat flux measure for Convection Bake Multi, run 2 heat flux over time	154
Figure 0-34 Heat flux measure for Convection Bake Multi, run 2 heat flux over time	154
Figure 0-35 Heat flux measure for Convection Bake Multi, run 2 heat flux over time	155
Figure 0-36 Temperature over time for the top mass for top mass in Convection Bake Multi, run 2	155
Figure 0-37 Temperature over time for the top mass for bottom mass in Convection Bake Multi, run 2	156
Figure 0-38 Heat flux measure for Convection Bake Multi, run 3 heat flux over time	156

Figure 0-39 Zonal heat flux measure for Convection Bake Multi, run 3 heat flux over time	157
Figure 0-40 Heat flux measure for Convection Bake Multi, run 3 heat flux over time	157
Figure 0-41 Temperature over time for the top mass for top mass in Convection Bake Multi, run 3	158
Figure 0-42 Temperature over time for the top mass for bottom mass in Convection Bake Multi, run 3	158
Figure 0-43 Heat flux measure for Air Fry, run 2 heat flux over time	159
Figure 0-44 Zonal heat flux measure for Air Fry, run 2 heat flux over time	159
Figure 0-45 Heat flux measure for Air Fry, run 2 heat flux over time	160
Figure 0-46 Temperature over time for the top mass for top mass in Air Fry, run 2	160
Figure 0-47 Temperature over time for the bottom mass for top mass in Air Fry, run 2	161
Figure 0-48 Heat flux measure for Air Fry, run 3 heat flux over time	161
Figure 0-49 Zonal heat flux measure for Air Fry, run 3 heat flux over time	162
Figure 0-50 Heat flux measure for Air Fry, run 3 heat flux over time	162
Figure 0-51 Temperature over time for the top mass for top mass in Air Fry, run 3	163
Figure 0-52 Temperature over time for the bottom mass for top mass in Air Fry, run 3	163
Figure 0-53 HukseFlux heat flux sensor specifications	166
Figure 0-54 HukseFlux black and gold sticker specifications	167

1 INTRODUCTION

Maintaining a consistent thermal environment is usually desirable in residential and industrial ovens. Many tools are used to learn about thermal environments to improve the cooking performance of ovens. These tools typically involve measuring different temperatures, air velocities, and heat flux profiles for the oven. In combination with these physical measurements, computer simulations are often run for additional guidance to help draw conclusions. Industrial ovens vary from residential ovens in many ways but one key difference between residential ovens and industrial ovens is that the expectation for an industrial oven is to cook one type of food as consistently as possible while residential ovens are expected to cook a variety of foods

Both industrial and residential ovens have their own unique problems. Industrial ovens are usually many times larger than a residential oven. The industrial oven supplier Despatch Thermal Processing Technology sells industrial ovens upwards of 216 cubic feet for ovens that are big enough for the user to walk in and 12.5 cubic feet for conveyer belt ovens. They are one of many suppliers that sell industrial ovens that need to be fine-tuned for similar performance across different areas to produce uniform cooking results. Residential ovens are usually much smaller with dimensions of around 5 cubic feet. Residential ovens are mass produced, leading to a need for similar

performance from unit to unit. The goal in residential oven design is to make hundreds of thousands of units that behave similarly to ensure that recipes can be followed regardless of unit and have consistent output to the user.

To ensure that oven performance is desirable at different stages of development of a residential oven many different food metrics are evaluated. Metrics tend to vary from food to food but some of the metrics that are used in evaluating food performance include color, texture, shape, and rise height. Food is difficult to assess experimentally since ultimately one of the most important qualities of food is taste, which is a very subjective quality. When designing a residential oven there are many parameters to consider that can affect the outcome of the food being cooked. Figure 1-1 outlines the basic components that are traditionally in an oven. At minimum, there is a broil element (which is a heat source from the top of a unit, and a bake element (which is a heat source from the bottom). The broil element is the only element with that is exposed and not behind the ovens sheet metal. Modern residential ovens often include a convection element located in the back of the unit and a convection fan that can be cycled on and off. From a control standpoint there is a lot of opportunity to modify bake, broil, convection element wattage and length of time that the element is on. Adjusting these parameters affects the quality of cooking the food load will experience. Various studies have shown the effect of different conduction (between cookware and food) , convection, and radiation ratios and timing of these ratios on food cooking performance.

Different foods are cooked in different ways because specific thermal environments are more ideal to bring out different aspects of food. To increase the level of control that engineers have in oven design it is important to better understand what mode of heat transfer is significant when cooking foods in an oven design. With this goal in mind the emphasis of this research will be on designing a heat flux sensor able to determine the convective, radiative, and conduction component of heat transfer in a residential oven.

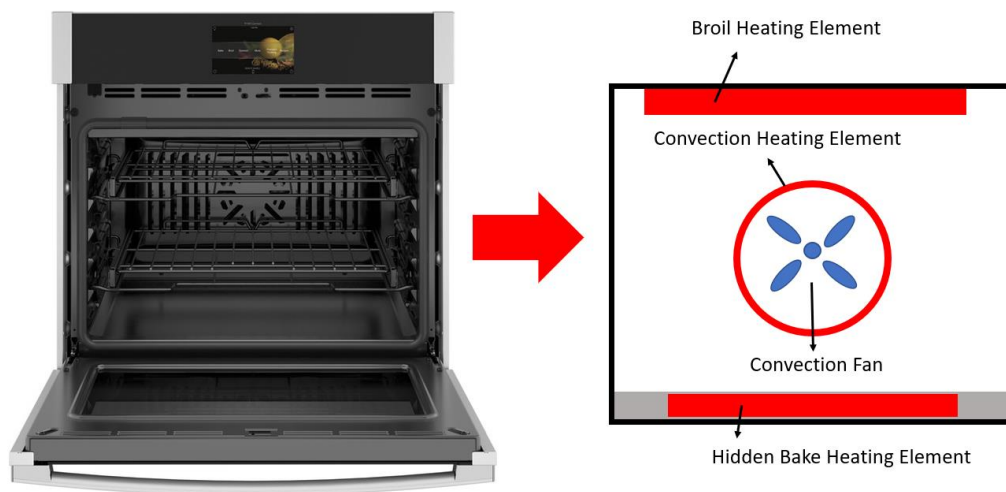


Figure 1-1 Residential Wall Oven

The purpose of this study was to design a heat flux sensor for use in a residential oven to compare cooking performance of sugar cookies to heat flux measurements. The heat flux sensor designed should measure the three modes of heat transfer to improve current thermal characterization methods of an oven.

2 LITERATURE REVIEW

The review of background research is broken into three main sections: food heat transfer studies, food oven heat transfer, and heat flux sensor applications.

2.1 Food Heat Transfer Studies

Standing (1974) published a report highlighting efforts in quantifying the effects of the different modes of heat transfer on the performance of biscuits during bake. In this literature five key categories of heat transfer are identified and explored; conduction from support medium, free convection, forced convection, radiation from surroundings, and radiation from flames. Isolated testing was done using a direct heat source to simulate a conduction only path. A controlled electric oven where convection and radiation can be assessed individually and in combination was also used. An effective thermal conductivity for biscuits was determined and a convection coefficient and emissivity value were determined experimentally to help continue their assessment since food properties are relatively undefined and non-constant. From this study on individual modes of heat transfer it was concluded that the key impacts of the different modes were “oven spring” by conduction, browning by radiation, and drying by convection. When attempting to use one single mode to bake biscuits there were obvious deficiencies in cooking performance. Some of these

deficiencies included lack of browning without the presence of radiation and change in moisture content in the convection case. It can be concluded that each mode of heat transfer is meaningful when baking and can contribute to different cooking performance metrics. Fahoul et al. (1993) also attempted to model heat and mass transfer of biscuits in a tunnel oven. In this study a tool was developed to predict resulting temperature profile, and end moisture content of biscuits during runs. The difficulties of collecting thermal data on biscuit food load was noted as a source of error as well as the lack of precise knowledge of properties that are essential for calculations.

A separate analysis of modes of heat transfer was run by Saxena (1994) in a Tandoor oven focusing on the impacts of the different modes of heat transfer in baking the Indian national product roti. In this analysis roti is baked under nontraditional conditions which attempt to remove the supporting conduction path of heat transfer. To explore a radiation dominated bake, conduction from the support surface is limited by using a cloth instead of a traditional baking tray. It is observed that the characteristics typically exhibited by roti change when using this method. These changes included a difference in the browning profile of roti and a difference of the texture of the bottom of the roti, as well as notable differences in characteristic flavor. From this study it was concluded that the different modes of heat transfer work together to contribute to different aspects of baking roti.

A similar analysis was done by Sato et al. (1987) highlighting the effects of apparent heat transfer coefficient which is the sum of convective and radiative

heat transfer coefficient. This apparent heat transfer coefficient is examined at various air temperatures and air velocities in this study. The apparent heat transfer coefficient is found by using an aluminum cylinder as a test apparatus. This apparent heat transfer coefficient is useful in determining the heat load experienced by a food load placed in the same environment. The report places a higher emphasis on convection by investigating variables such as air velocity and air temperature while monitoring food variables such as weight loss, browning, firmness, and change in height.

In Figure 2-1, a side view of a sponge cake baked with the exact same ingredients and prepared the same way but baked with differing air temperatures and air velocity is shown. The cake baked in lower temperature and high velocity has a more uniform and desirable profile when compared to the cake baked with higher air temperature but lower air velocity. This study further emphasizes the impact of varying the magnitude of the different modes of heat transfer.

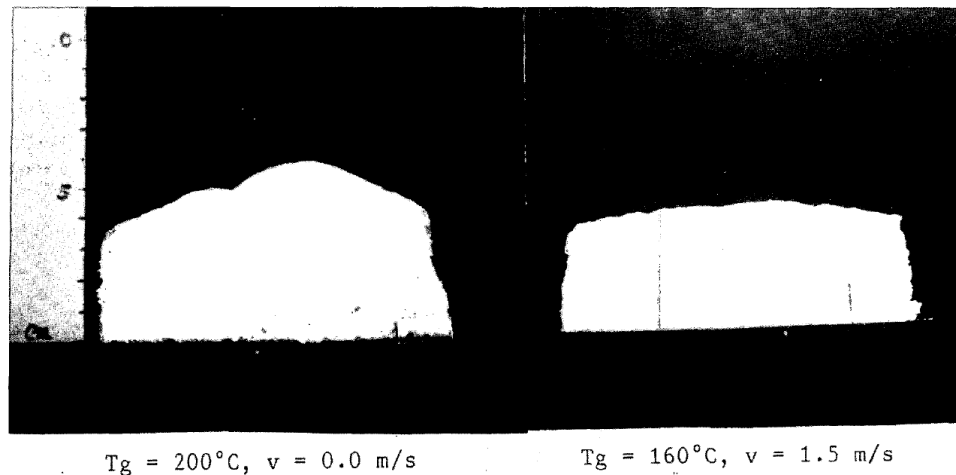


Figure 2-1 Profile of sponge cakes baked at different air temperatures and velocities. (Sato et al.,1987)

A heat transfer analysis of breaded vs non breaded chicken in a pilot scale residential wall oven was conducted by Ozen (2020). The purpose is to determine the impact of processing parameters such as oven set temperature, duration of test, and breading flour used. The deployment of a metallic heat flux sensor onto the surface of the chicken nuggets is used for this study. The chicken nuggets used were prepared in a similar fashion being controlled to a pre breaded weight of 17.7 grams. The experiments were run in a radiant wall oven set at temperatures of 347°C, 367°C, 387°C, and 407° C and at processing times of 4 minutes, 5.5 minutes, and 7 minutes. From the experiments they were able to determine the minimum time to safely bake chicken nuggets following USDA guidance regardless of breading type, the impact of different breading, and that no breading yields the highest heat flux measurement.

Another radiant wall oven study is run by Singh et al. (2021). This study involves the use of heat flux sensors to help determine the impact of heat flux on different cooking parameters such as potato cutting force, puncture force, lightness, chroma, hue, and moisture content. Potato wedges were baked in a radiant wall oven while embedded with a T-type thermocouple. A T- type thermocouple collected air temperature, and a heat flux sensor collected heat flux data during bake. Tests were run at 12 different time and temperature combinations and were repeated 3 different times for each configuration. Pearson correlation coefficients between heat transfer coefficients derived from heat flux measurement and the different cooking quality parameters from this study are

shared below. A positive value for correlation coefficient indicates a direct relationship while a negative value indicates an indirect relationship. In this study cutting force and cutting test demonstrated negative correlation values with significant P-values. In this study parameter “U” is used to represent the overall heat transfer coefficient and parameter “h_R” is used to represent the radiative heat transfer coefficient. The measured range of heat flux in this study was 10.2-20.0 kW/m². The results highlight the impact that the rate of heat transfer can have on different cooking parameters measured in this study.

Parameters	Cutting force	Cutting test–linear distance	Puncture force	Puncture test–linear distance	Lightness	Chroma	Hue	Moisture content
U	-0.43 (0.011)	-0.38 (0.025)	-0.27 (0.12)	-0.15 (0.39)	0.12 (0.51)	-0.12 (0.48)	0.19 (0.27)	0.13 (0.46)
h _R	-0.39 (0.024)	-0.34 (0.046)	-0.2 (0.25)	-0.14 (0.44)	0.08 (0.65)	-0.13 (0.46)	0.16 (0.38)	0.087 (0.62)

^aPearson correlation coefficients between two parameters are significant when *p*-value < 0.05. *P*-values are given in parenthesis.

Table 1. Correlation between heat transfer coefficients and quality of the radiant wall oven baked potato strips

Another example of the effect of different modes of heat transfer on food comes from Shinbukawa (1989) who ran a study on cookies. Tests were run in a radiation dominated mode and convection dominated mode is used and resulting cooking parameters compared. For both modes the oven was maintained at 200°C, and data collected for different cooking times.

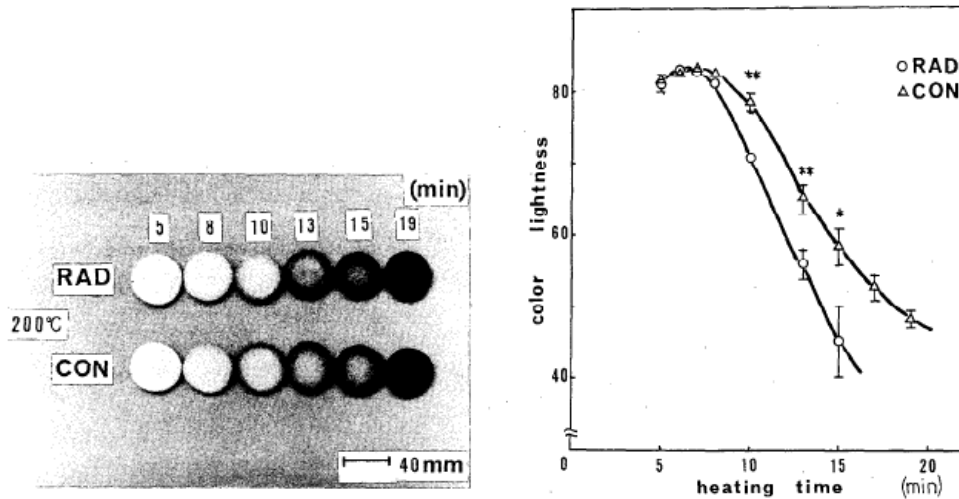


Figure 2-2 Cookie Color vs Heating Time

This study shows the impact of heat transfer mode on color score measured by a colorimeter and reported as an L-value. The radiation dominated mode had a lower score versus heating time (meaning darker cookies).

2.2 Oven Heat Transfer

In attempt to capture the thermal characteristics of an oven many tools are used such as computational simulations, and physical experiments with controlled test apparatuses. One study takes a unique approach in modeling the energy balance of a residential wall oven and was run by Ramirez (2016). In this study, a porous brick filled with a known and measurable amount of water was used to mimic a food load. The brick's porous nature and known geometry and absorption rate allowed for repeatable experiments which is extremely difficult with actual food loads. The porous brick load allowed more information to be collected during the baking process giving insight on the effects of evaporation in

addition to the sensible portion of the brick, but it doesn't provide information on the magnitudes of the different modes of heat transfer. Experiments were run using the porous brick load and temperature is used as a tool in comparing experiments to simulation. The simulations were used to determine the approximate energy balance for different periods of the baking process for both a convection configuration and radiation configuration. The radiation configuration used bake and broil elements to heat the oven shown in Figure 2-3. The convection configuration differs from the radiation configuration because it uses a fan and the ring heater to circulate hot air. The energy balance for steady state operation is shared below. The percentages below represent the approximate energy needed to keep elements, oven cavity, and external sheets at desired temperatures as well as the amount of energy used to heat the brick, evaporate water, and account for loss to the environment that are external to the oven.

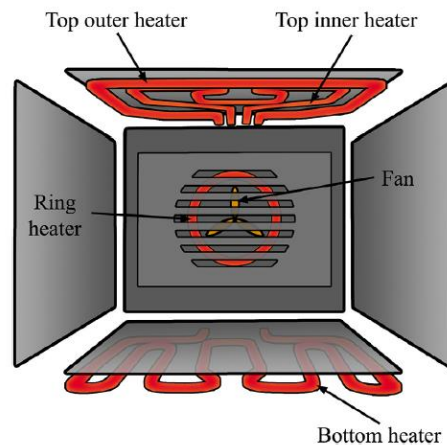


Figure 2-3 Oven Scheme used in energy balance study in a residential oven (Ramirez, 2015)

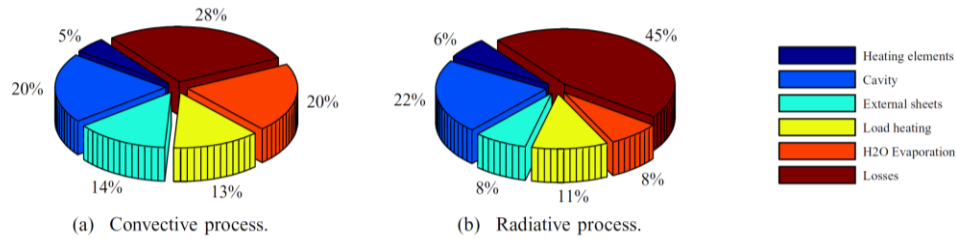


Figure 2-4 Energy Breakdown of residential oven with a porous brick load (Ramirez,2015)

This study emphasizes the role that different heat transfer ratios can have on a heating load as demonstrated in the percent of total energy received by the load and water evaporation. From this study convective dominant heating had a meaningful impact on water evaporation rate when compared to radiation dominant processes.

Another attempt to model heat transfer in an oven was done on a pilot oven scale by Boulet (2010). This modeling method combines the use of heat flux measuring devices in experiments and computational fluid dynamics for simulations to develop a description of heat transfer in a pilot wall oven with radiation dominated heat transfer that is mixed with convection. In this study the use of a heat flux sensor known as h monitor (shown below in Figure 2-5) is deployed for experiments. This h monitor is a composite material that consists of two aluminum plates separated by an insulative material. The premise behind this heat flux sensor is that the aluminum masses will have uniform temperature (considering a Biot number far less than 0.1) so the storage term for both masses can be used to measure heat flux in the oven.

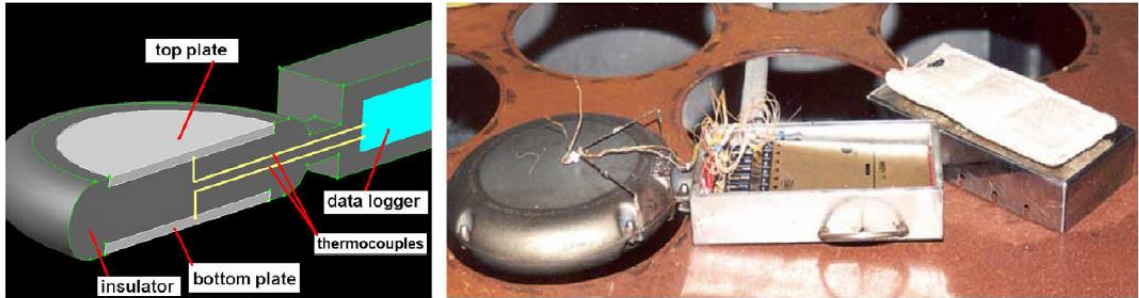


Figure 2-5 H-Monitor deployed for CFD modeling of heat transfer in pilot oven

In this study it was shown that the use of a heat flux meter like the h monitor can be critical in understanding the transient behavior when baking in an oven. Similar approaches are taken by Zareifard (2005) when attempting to characterize the uniformity of heat flux in a pilot oven.

2.3 Heat Flux Sensors

In many industries detailed descriptions of a thermal environment is needed so heat flux sensors are often deployed. In the automotive industry the deployment of plate styled heat flux sensors of varying emissivity is used to measure radiative and convective heat flux. Khaled et al. (2010) proposed the use of these heat flux sensors for under-the-hood applications. The custom heat flux sensor uses a material of known properties and geometry and thermocouples embedded across the thickness. This technique is known as a temperature gradient styled sensor and is often used due to its usefulness without complex calculations. The custom sensor developed also uses two coatings of different emissivity to help determine the convective and radiative components of heat transfer. An example of this sensor configuration is shown

below. The results of this custom heat flux sensor were compared to a reference flat plate sensor inserted at a section of the car hood and error between the two was found to be around 10%. An error analysis of the sources of error with heat flux sensors showed that the main sources of errors related to the attachment of the heat flux sensor to the surface and the emissivity measurements of the heat flux sensors.

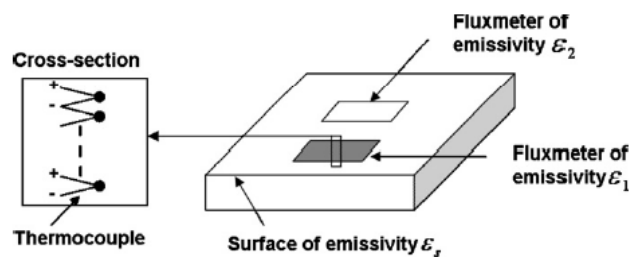


Figure 2-6 Separation of convective and radiative heat fluxes (Khaled et al. (2010))

The development of a new method to calculate radiant heat flux using a plate thermometer is outlined by Liu (2021). This plate thermometer is a heat flux sensor (shown below) that consists of a Inconel Alloy 600 which is mounted to two layers of insulation, both layers being made of ceramic fiber.

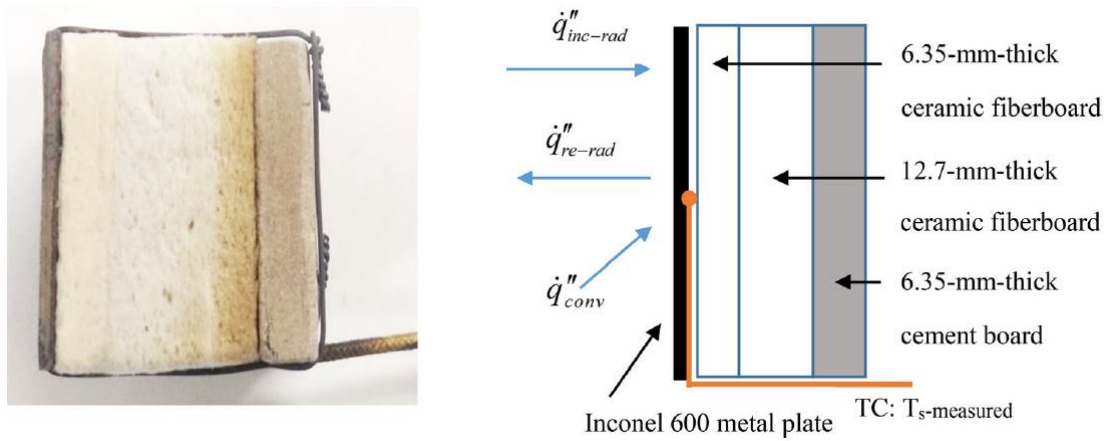


Figure 2-7 Schematic of plate thermometer (Liu, 2010)

A thermocouple is used, and the lumped heat capacitance analysis is applied when valid to approximate a heat flux measurement. This study observed that with the energy balance above there is typically some error between heat flux reported when compared to a standard water-cooled heat flux gauge. In this study a cone calorimeter is used to calibrate this plate style heat flux gauge and provide a relationship between T_s -ideal and T_s -measured. The correlation for the sensor used in this is shown below.

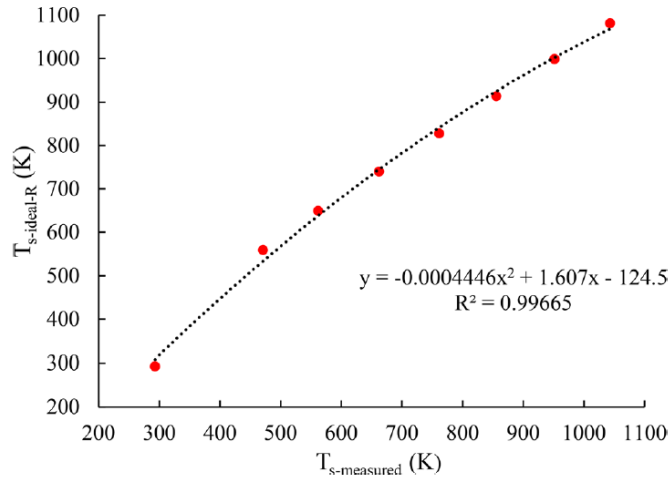


Figure 2-8 Surface temperature measured and ideal surface temperature correlation (Liu, 2021)

Experiments are run using a regular pan fire and fire swirl comparing the results of this plate style heat flux gauge and a water-cooled total heat flux gauge. The results from this study demonstrate the effectiveness of a composite material heat flux gauge at measuring heat flux in various thermal environments.

Another study by Pullins (2010) highlighted the impacts of different modes of heat transfer and the effects they have when calibrating a heat flux sensor. Different modes of heat transfer may yield different results. Radiation based calibration is often used and can be done either by characterizing heat transfer based on the Stefan-Boltzmann principle or by using a secondary heat flux sensor. One method established by the NIST provides a way to calibrate using radiation correlations at room temperature by the use of an electrical substitution radiometer as a reference heat flux sensor. In this study a high temperature heat flux sensor is tested and calibrated across a temperature range of 100°C to

900°C to determine the impacts that temperature may have on sensitivity. The results of this study show that heat flux sensor sensitivity is dependent on the thermal conductivity of the sensor which varies with temperature introducing a need for temperature versus sensitivity study for heat flux sensors. These temperature impacts on heat flux sensors are also observed by Van der Ham (2018).

In summary, the background research provides examples of technologies and methods deployed to characterize different ovens, different food performance metrics, and describes the working principle behind some of these technologies and methods. The different technologies deployed across the various studies serve as a guide in the design of a sensor that measures conduction, convection, and radiation in attempt to analyze cookie baking in a residential electric oven. Currently there aren't any sensors that measure the conduction component of heat transfer.

3 HEAT FLUX SENSOR DEVELOPMENT

3.1 Sensor Design Process

An overview of the design process followed for the sensor can be seen in Figure 3-1.

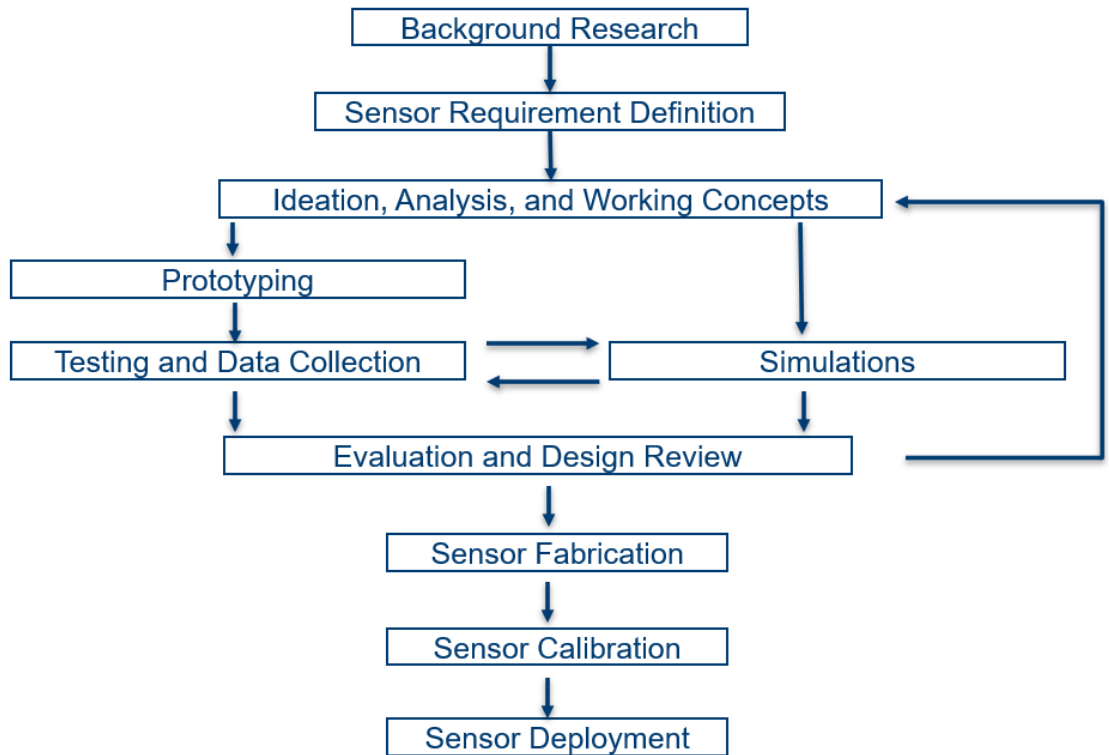


Figure 3-1 Sensor Design Process

The design process started with a background search on heat flux sensors available and learning about the capabilities of heat flux sensors. Considerations are placed on expected application of these heat flux sensors as well as some technical specifications that decide if each heat flux sensor is usable in an oven environment. Historically GE Appliances (GEA) deployed a Hukseflux RC01 water cooled sensor which has been discontinued. This sensor is used as the reference that other sensors are compared to in initial market research. Results from tests using this sensor can be seen in Figure 3-3.

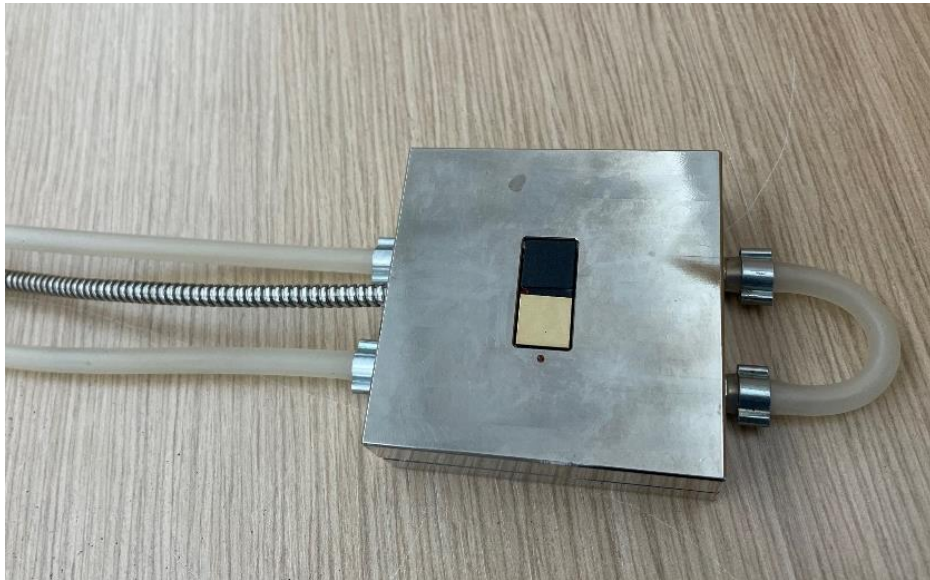


Figure 3-2 Hukseflux RC01 water cooled heat flux sensor with water line connected. The RC01 heat flux sensor is equipped with a low emissivity and high emissivity surface that can collect a combined radiation and convection reading and convection reading.

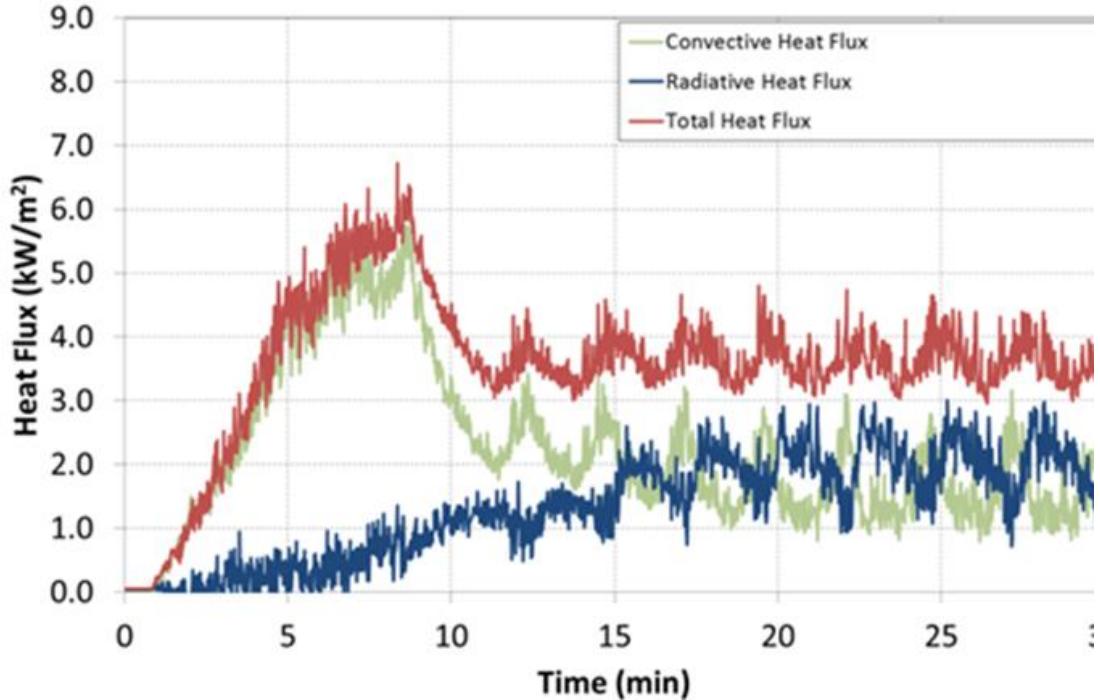


Figure 3-3 Heat Flux results for 30-minute testing using the RC01 heat flux sensor. This test is run in a 350°F gas range and is started with an ambient oven start. The total heat flux is derived from a high emissivity surface and radiative heat flux is a product of total heat flux minus convective heat flux measured by the low emissivity surface.

From initial market research there are a few heat flux sensors capable of being used in a residential oven application but are limited in different ways such as temperature limit, response time, or heat flux range. There are also third-party suppliers, such as Thistle Voyager, who develop “modular” heat flux sensing systems intended for use in calibration of industrial ovens. The design criteria needed for the next generation of heat flux sensing at GEA is based on performance of the RC01 heat flux sensor and the limitations from the thermal environment GEA plans to test in. The RC01 heat flux sensor was discontinued

during market research but at the time of GEA's purchase it was sold for \$10,982.00.

3.2 Sensor Design Criteria

The first design criteria for the heat flux sensor is that the sensor can be used in a high temperature environment of temperatures upwards to 375°F (oven set temperature that will be used to simulate baking conditions for sugar cookies). The second criteria is the capability to be multi-purpose in sensor configuration to allow for tests of different oven modes and in different positions. Desirable features to increase the versatility of sensor application include minimum sensor overall size, minimal additional equipment for sensor use, and non-stringent requirements for sensor mounting. The third criteria for the heat flux sensor revolve around cost and making sure it is feasible to have an array of multiple sensors for different tests. The sensor used for cost comparison is the RC01 heat flux sensor. The final criteria for this heat flux sensor is the capability to break down heat flux readings into convection, radiation, and conduction. The ability to measure all three modes of heat transfer is where most heat flux sensors on the market fail. To measure conduction some modifications are needed.

3.3 Introduction to Heat Flux Sensor

A schematic of a heat flux gage is shown in Figure 3-4. Information on sensor geometry and material properties at sensor conditions and relative temperature difference between two surfaces on the same body is used to

determine a local heat flux measurement. This can be seen by most heat flux sensors on the market whether they are thin foil heat flux sensors, water cooled heat flux sensors, or plate heat flux sensors. Some key differences between different heat flux sensors come from the materials used which vastly impacts the sensors performance at different temperature ranges. Many heat flux sensors available in the market today use Fourier's law of heat conduction as a guiding principle. Figure 3-4 shows an example of the application of Fourier's law (1) for heat flux sensors.

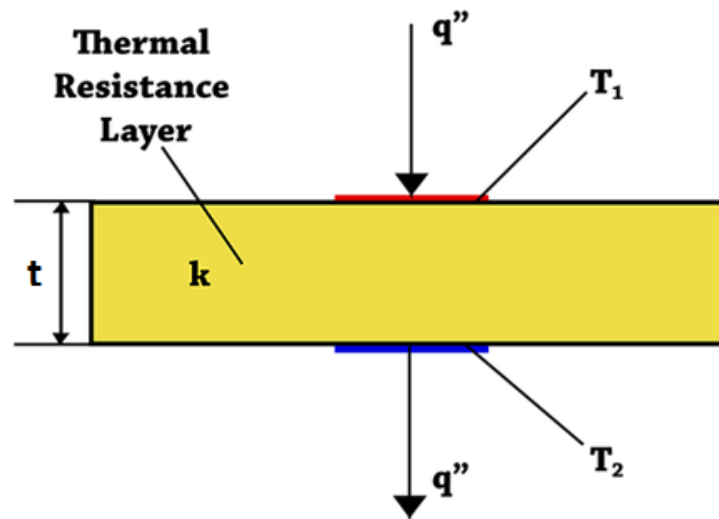


Figure 3-4 Fluxteq Illustration of heat flow through sensor

$$q'' = - \frac{k * (T_2 - T_1)}{t} \quad (1)$$

Conduction is driven by a temperature difference. In this instance T_1 represents the hotter side and T_2 represents the cooler side so heat flows from

top to bottom. The term k represents the thermal conductivity of the material that heat is flowing through and is typically a property that varies with temperature.

The term A represents cross sectional area of the material, which is perpendicular to the thickness, t. This equation assumes steady state 1-D conduction through a material.

3.4 Sensor Market Study

For the initial market study, emphasis was placed on passive, plate and thin foil styled heat flux sensors. There are active sensors which include features such as water cooling, but to minimize need for modifications on the unit during testing and potential impacts of water lines, these styles of sensors were not considered in this study. A summary of sensors available during the time of this project can be seen in table 2. For max heat flux range needed the RC01 heat flux sensors range is used as a reference.

Table 2 Market Sensor Summary

Sensor	Supplier	Response Time [S]	Temp Limit [F]	Max Heat Flux Range $[\frac{W}{m^2}]$	Nominal Sensitivity $[V*(\frac{W}{m^2})^{-1}]$	Cost per sensor
IHF01	HukseFlux	60	1652	1.00E+06	9.00E-09	\$1,248
IHF02	HukseFlux	210	1652	1.00E+05	2.50E-07	\$2,080
HTHFS-01	FluxTeq	N/A	1832	N/A	3.00E-08	Quote
Ultra-09	FluxTeq	5	392	N/A	1.00E-05	\$565
FCR	Wuntronic	N/A	1020.2	1.58E+04	1.79E-06	Quote
FGS01	HukseFlux	N/A	1202	8.00E+05	9.00E-09	Quote
FHF04	HukseFlux	3	302	1.00E+04	1.10E-05	\$460
RC01	Hukseflux	0.5	482	1.00E+04	3.00E-06	\$10,982

From the sensors currently available on the market, two sensors fit the requirements due to response time: the Fluxteq Ultra-09 and the HukseFlux FHF04. The sensors that had the best temperature limits were plate styled heat flux sensors which also had longer response times due to increased sensor thermal mass. Thermal mass is the product of the mass of a material and the specific heat. The Ultra-09 had a slightly higher temperature limit and slightly slower response time than the FHF04, but the FHF04 has stickers available for evaluating radiative and convective modes of heat transfer. Due to this the FHF04 sensor was selected with the assumption that the 300°F temperature limit can be circumvented by mounting the sensor on a heat sink with the appropriate properties.

3.5 Sensor Supporting Theory

The initial design concept for the composite heat flux sensor is shown in Figure 3-5. This assembly consists of a FHF04 HukseFlux heat flux sensor, two thermal masses, two J-type thermocouples, and an insulation material. The bottom thermal mass that contacts the cookie sheet measures conduction. The energy balance for the top and bottom thermal mass can be seen in Figure 3-6. The conduction for the bottom mass is calculated using the energy storage term which can be calculated using the change in temperature measured by a J-type thermocouple embedded in the center of the mass. The equation for the top and bottom thermal mass is shown in equation 2. There is some energy transfer

between the bottom thermal mass and the insulation that is assumed to be losses from mass onto insulation.

The top thermal mass in this assembly is indicative of the radiation and convection from the oven. All sides of the top mass are insulated except for the top surface. The heat flux sensor is mounted to the top of this mass and will provide a voltage reading that can be converted into heat flux using its sensitivity. The energy calculation from the thermal mass will be different from the sensor reading and that difference will be energy transfer between the mass and the insulation. The energy balance of the top thermal mass-heat flux sensor assembly is shown in Figure 3-6.

$$\dot{E}_{st} = \dot{m} * C_p \frac{dT}{dt} \quad (2)$$

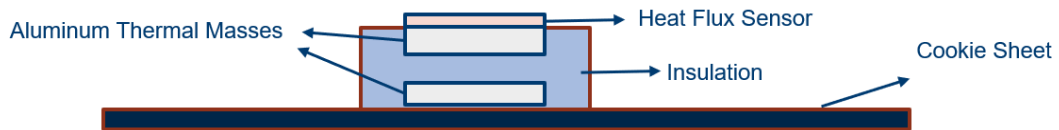


Figure 3-5 Diagram of composite sensor

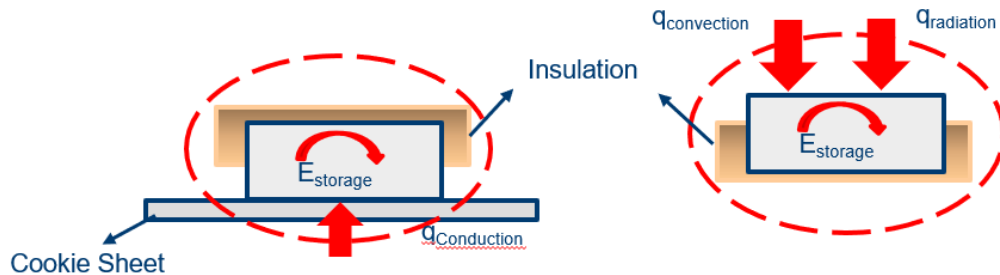


Figure 3-6 Energy balance of thermal masses (bottom mass is left and top mass is right)

3.6 Initial Sensor Design

A key requirement for the thermal mass selected is that it must stay below 300°F to stay in the safe operation zone for the heat flux sensor selected. Other important features for the material chosen for the thermal mass is to have a high thermal conductivity (to limit temperature gradient in the mass), easy manufacturability, and relatively high specific heat. The material that met these requirements at a reasonable cost per pound was Aluminum 6061.

To determine if the thermal gradient of the thermal mass is negligible the first step was to evaluate the Biot number and ensure that it is less than 0.1. The Biot number describes the ratio of conductive thermal resistance versus convective and radiative thermal resistance and is shown in Equation 3. In this equation “h” represents the heat transfer coefficient, L_c represents the characteristic length, and “k” is the thermal conductivity of the material. The characteristic length varies based on geometry of the material but can be found using the ratio of volume to surface area.

$$Bi = \frac{hL_c}{k} < 0.1 \quad (3)$$

$$L_c = \frac{Volume}{Surface Area} \quad (4)$$

Aluminum masses of variable volumetric footprints and masses are placed in the oven in different configurations. For initial calculations heat transfer coefficient based on ranges for natural convection and forced convection found in a study run by Cernela et al. (2014). Although dependent on location in oven, the

study highlighted that a heat transfer coefficient of 20 W/m²-K can be observed in an oven using forced convection. Figure 3-7 demonstrates that even at heat transfer coefficients higher than found in the study that the Biot number for aluminum masses were less than 0.1.

Aluminum discs of two- and three-inch diameters were tested since they are readily available and the minimum diameter to mount the heat flux sensor selected is 2 inches. Half inch and one inch thickness discs are tested with J-type thermocouples attached to the top surface using aluminum tape as shown in Figure 3-8.

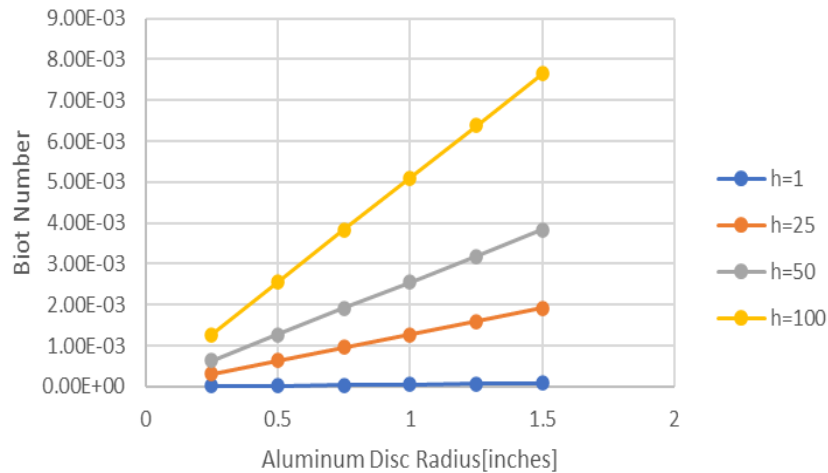


Figure 3-7 Biot number evaluated at various heat transfer coefficients for various radii thermal masses (note convection coefficient in W/m²-K)

The conservation of energy at any instant of time “t” is shown in Equation 5. This energy balance can be expressed as Equation 8 with the assumption that the surface area of radiation is the same as the surface area of convection. With

the assumption that temperature will behave linearly as a function of time an expression for time can be seen in Equation 9.

$$E_{rad} + E_{conv} = E_{st} \tag{5}$$

$$E_{rad} = \sigma * \epsilon * A * (T_{surr}^4 - T^4) \tag{6}$$

$$E_{conv} = h * A * (T_{\infty} - T) \tag{7}$$

$$\sigma * \epsilon * A * (T_{surr}^4 - T^4) + h * A * (T_{\infty} - T) = m * C_p \frac{dT}{dt} \tag{8}$$

$$\Delta t = \frac{m * C_p * (T - T_i)}{\sigma * \epsilon * A * (T_{surr}^4 - T^4) + h * A * (T_{\infty} - T)} \tag{9}$$



Figure 3-8 Aluminum Discs used for temperature limit testing

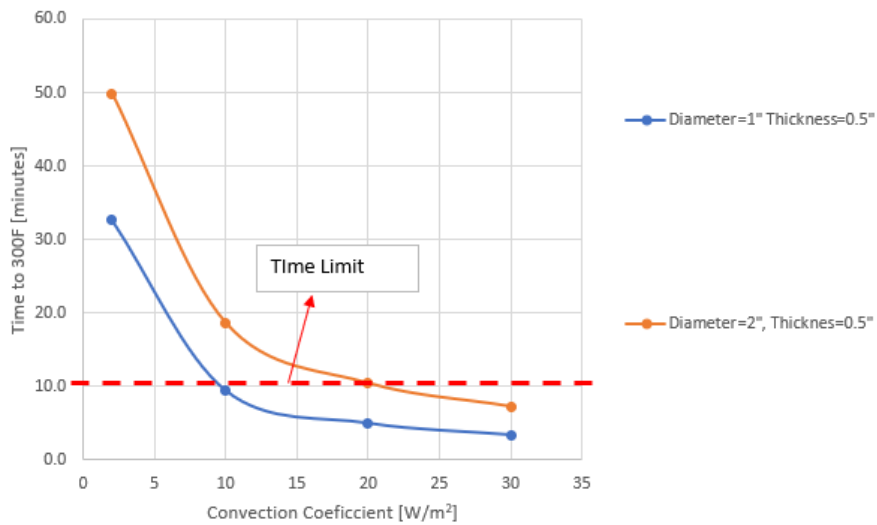


Figure 3-9 Time to 300°F using twp different sizes of aluminum masses

Initial heat transfer calculations placed the 2-inch diameter disc right at the temperature limit for 20 W/m²-K. This case represents a very aggressive case with all sides uninsulated leading to higher rates of heat transfer for initial analysis.

Following the analysis of Biot number, experiments are run to find actual time to heat different masses to 300°F. The tests were run with completely exposed aluminum masses representing a worst operating condition then when in assembly where surfaces will be insulated. The results of these tests can be seen in Figure 3-10.

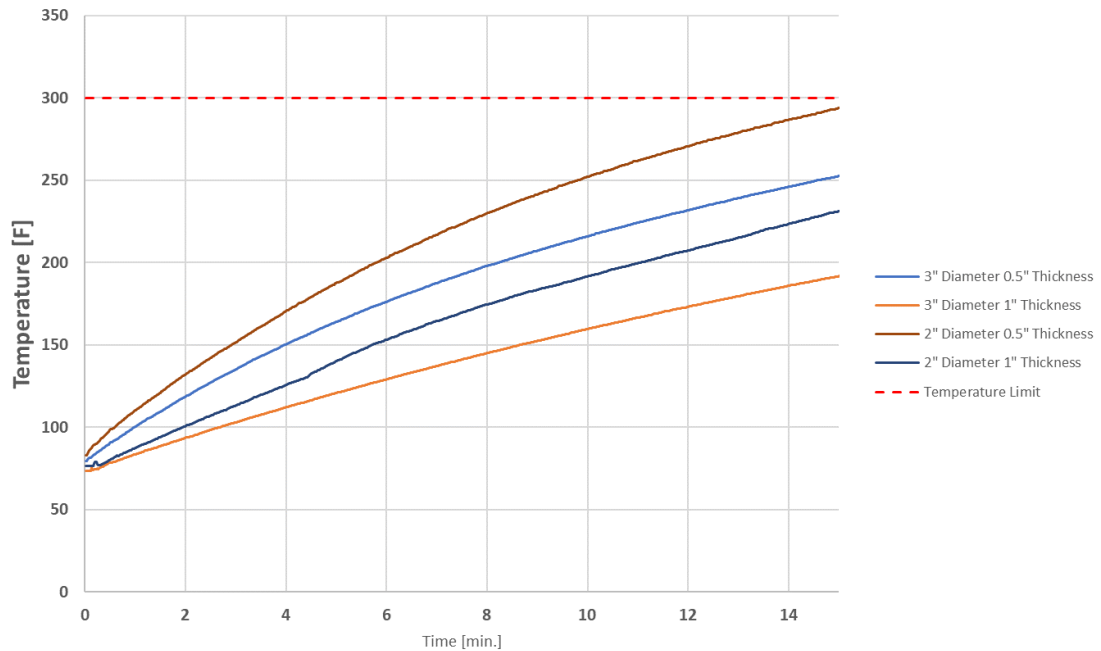


Figure 3-10 Results of 375°F oven tests with aluminum masses of different sizes. The test time to design to is 10 minutes with a temperature limit of 300°F.

After verifying that the sensor can be placed in high temperature environments and be kept at safe sensor temperatures with the use of aluminum masses, the next step was to determine how to implement two separate masses in one sensor assembly and minimize the heat transfer between the masses. With this goal in mind various insulation materials are considered with the goal of finding a rigid, and nontoxic material that can withstand a 375°F environment without melting or destructive deformation. The materials shown in Table 3 are considered. Of all the materials surveyed the material that provided the properties needed as well as offered the highest manufacturability and the best availability was Polyetherimide(PEI). PEI is available as a printable resin from Strasys allowing for 3D printing.

Table 3 Insulation Material Summary

Material	Temp Limit [F]	Thermal Conductivity [W/m-K]	Density [kg/m³]	Specific Heat [J/kg-C]
PPS (Polyphenylene Sulfide)	500	0.2-0.5	1350-1800	1000-1500
PEEK (Polyetherketoneketone)	572	0.25	1270	1000
PTFE (Polytetrafluoroethylene)	621	0.3	2170	1110
Polyetherimide (PEI)	400	0.22	1290	1470-1530
Polyamide 12 (Nylon 12)	350	.09-.23	1001	2100

3.7 Sensor Design Optimization

The first concept for this composite heat flux sensor assembly was designed and prototyped for feasibility testing and named revision 0. Revision 0 can be seen in Figure 3-11 and consists of two 2 inch by 2 inch aluminum masses that are half an inch thick, and a Nylon 12 plastic base. These masses are used instead of two-inch diameter discs because they allow for exact mounting of the 2 inch by 2 inch heat flux sensors. The aluminum masses are embedded and are held in place using a press fit. The first prototype is used as a fit and function check with available materials while the final insulation material (PEI) was acquired.

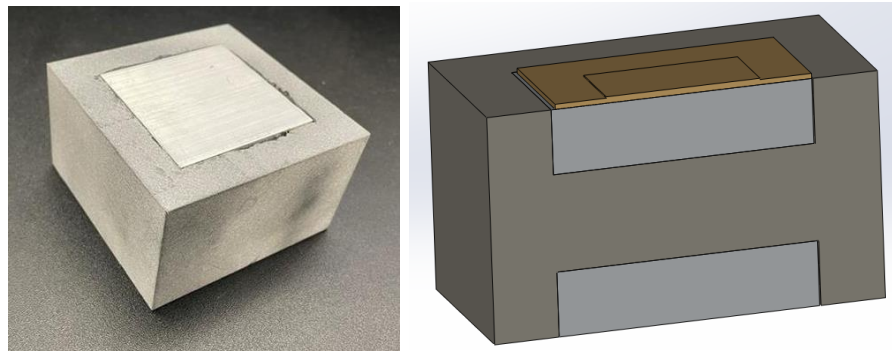
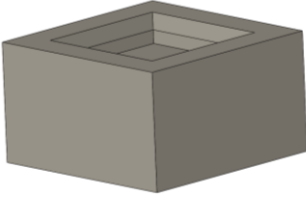
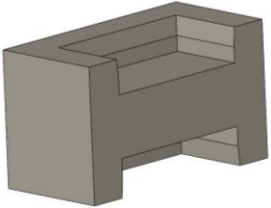
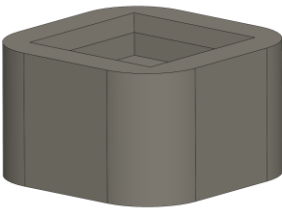
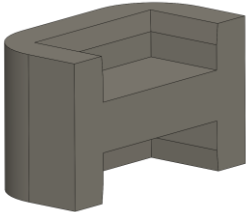


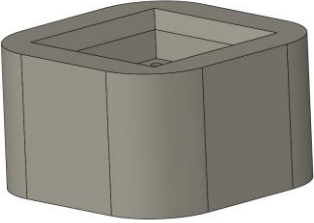
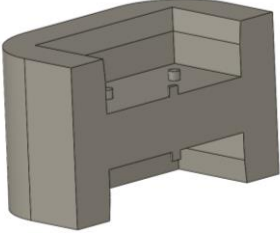
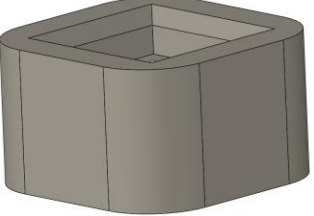
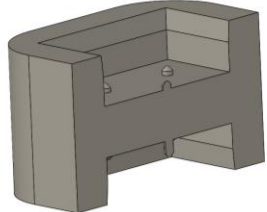
Figure 3-11 Composite Heat Flux Sensor Concept 1 Prototype

With the current press fit for the aluminum masses and the plastic base it is difficult to disassemble the sensor nondestructively. With the FHF04 heat flux sensor mounted, sensor damage can occur which may have an effect on performance.

The current press fit design also ensures an intimate contact between masses and insulation material. This contact condition leads to increased heat transfer between the masses and insulation. To reduce the conduction between the masses and the plastic base, a reduced contact area is used by including draft angle on the mating surfaces. This draft angle also improves the ergonomics of assembly and disassembly. Another consideration from this prototype was to decrease the insulation height for the bottom mass opening. Decreasing this dimension allows for the bottom aluminum mass to be the only part of the assembly touching the cookware and removes the direct conduction path from cookware to insulation. The final change from revision 0 is to round the edges of the assembly to minimize sharp corners in high velocity airflow tests. The changes can be seen in Table 4.

Table 4 Revision history of the insulation base designed

Revision # Notes	Isometric View	Cross Section View
Revision 0: Initial concept of insulation base with slots for masses		
Revision 1: Improved concept with rounded edges and improved slots for masses		

Revision # Notes	Isometric View	Cross Section View
Revision 2: Improved concept with reduced contact area for support surfaces of mass		
Revision 3: Improved concept with spherical contact area for masses.		

After modifying revision 0 of the sensor assembly, further testing was done. The first stage is “isothermal conduction” testing where this sensor is placed on a constant temperature surface and the bottom mass is used as a direct conduction path for the sensor. The purpose of this testing is to determine how effective the insulator is at separating the top and bottom mass and to determine the approximate energy storage of the insulation. The first few iterations of this study were performed with Creo Parametric 4.0’s Thermal Analysis package.

The boundaries for the isothermal conduction test are that the heating surface that contacts the bottom mass is held at a constant temperature of 300°F. Sensor assembly is subject to natural convection with air at a temperature of 70°F. For the simulation, a convection coefficient is not defined but instead

resolved using surface temperature of the insulation and the ambient air temperature.

In the first iteration (see Figure 3-11) where there is a face-to-face contact between top and bottom masses and the insulations a direct conduction path from bottom to top mass is evident. The bottom mass reaches steady state throughout the material as shown by solid white color. Throughout the insulation there is a gradual decrease in temperature as shown in the plot. The simulations were run with a solid base material as opposed to the hexcomb insulation that will be manufactured. Asymmetry is observed in the temperature gradients in the simulation, this is attributed to the thermocouple channels seen on the right of each simulation. These thermocouple channels are filled with air, as opposed to solid material, which may influence the model's solution. Despite these differences, the simulations serve as a demonstration of the impacts of the intimate contacts between the masses and insulation.

For revision 2 of the insulation base, the contact area of the top mass is reduced by implementing standoffs significantly reducing the contact area of the bottom surface of the top mass by 99.8%. Revision 2 still includes the contact between the side surfaces that mate with the aluminum mass and doesn't incorporate minimal contact area for the bottom mass.

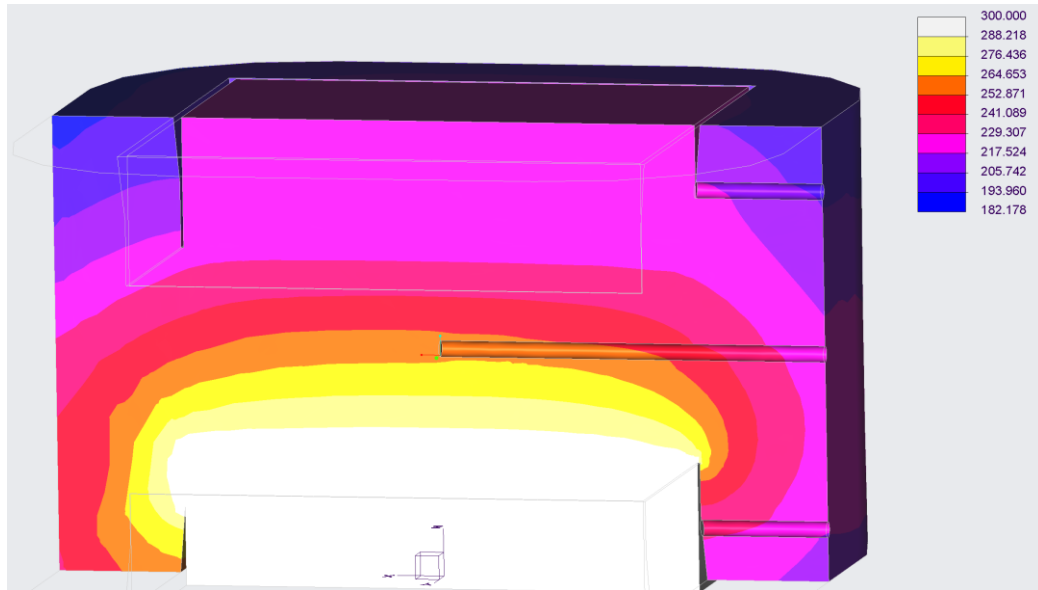


Figure 3-11 Revision 1 simulation at steady state temperatures for thermal mass with face-to-face contact with the bottom mass at constant surface temperature

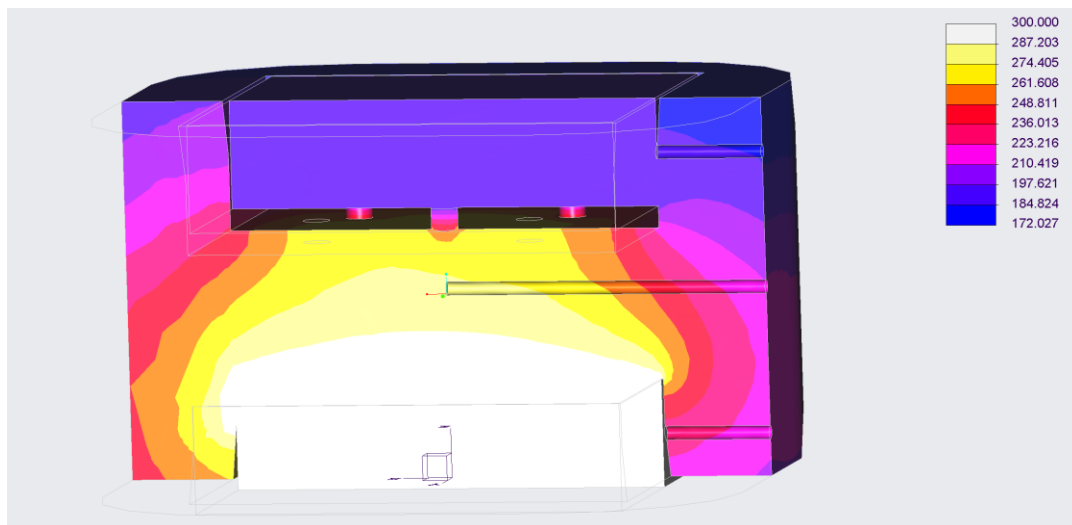


Figure 3-12 Revision 2 simulation at steady state temperatures for thermal mass with reduced area contact with the bottom mass at constant surface temperature

The third iteration of the insulation base includes spherical domes on top of the 5 contact areas to reduce contact area to a point to face contact. This mating condition significantly reduces the heat transfer between the top mass and the rest of the insulation base. The same mating geometry is used at the bottom opening of the insulation to reduce heat transfer between bottom mass and the rest of the insulation.

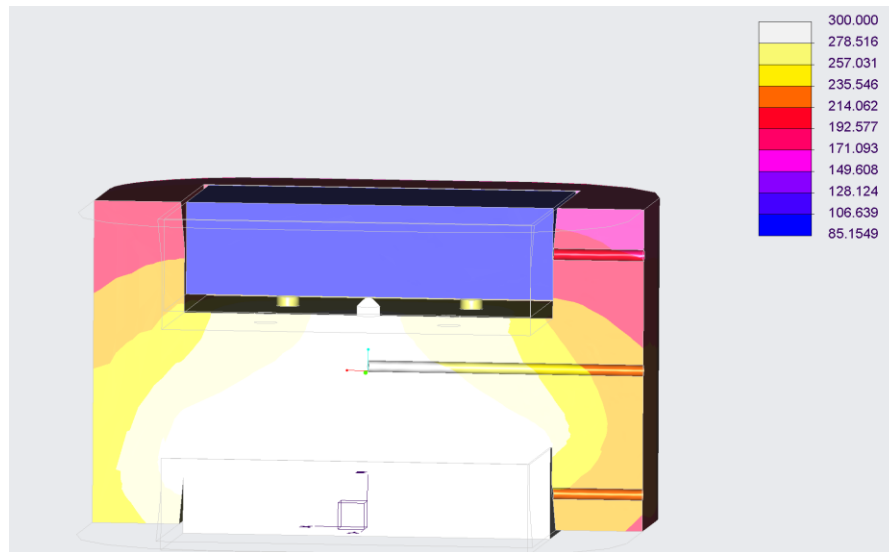


Figure 3-13 Revision 3 simulation at steady state temperatures for thermal mass with point contacts with the bottom mass at constant surface temperature

Following the simulations, isothermal conduction experiments were conducted to validate the simulation results. The insulation base was prototyped, and masses were installed and evaluated using similar conditions as the simulations. To maintain a constant surface temperature for the bottom mass a constant temperature heating pan was used. In this test the temperature of the room, the temperature of the heating pan, and the temperature of all three

components of the sensor assembly were recorded over time. The test set up described for the isothermal conduction testing can be seen in Figure 3-14. A prototype was made for revision 3 that was printed using Ultem1010 and includes two J-type thermocouples that are adhered to aluminum mass surfaces using aluminum tape, and a J-type thermocouple is also embedded into the plastic base.

The method of embedding the thermocouple into the insulation is limited by the capabilities of welding or fixing the thermocouple onto the material so temperature measurements of insulation is only taken for testing. The insulation is 3D printed using Ultem with infill densities of 20 percent for this study. Higher density infills for insulation promotes higher levels of heat transfer due to improved conduction with increased contact area (increasing effective thermal conductivity), so a low density is used. Figure 3-15 shows the geometry used for infill and demonstrates the impact of different infill percentages on internal geometry of insulation base.



Figure 3-14 Test setup for isothermal conduction tests

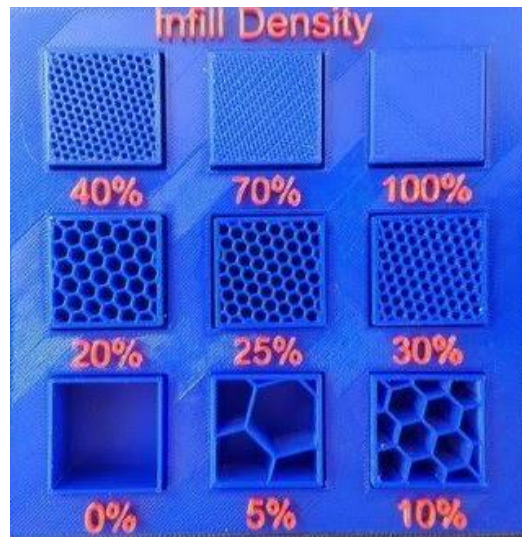


Figure 3-15 Diagram of infill density used for insulation base

In this analysis an instantaneous power term is calculated using the change in temperature over time of the top and bottom aluminum masses. This instantaneous power term is calculated using Equation 2 in 30 second intervals. Figure 3-16 shows a plot of temperature of the heating surface as well as the 3 subcomponents of the sensor assembly over time. This figure also shows the calculated rate of energy stored in the top and bottom masses.

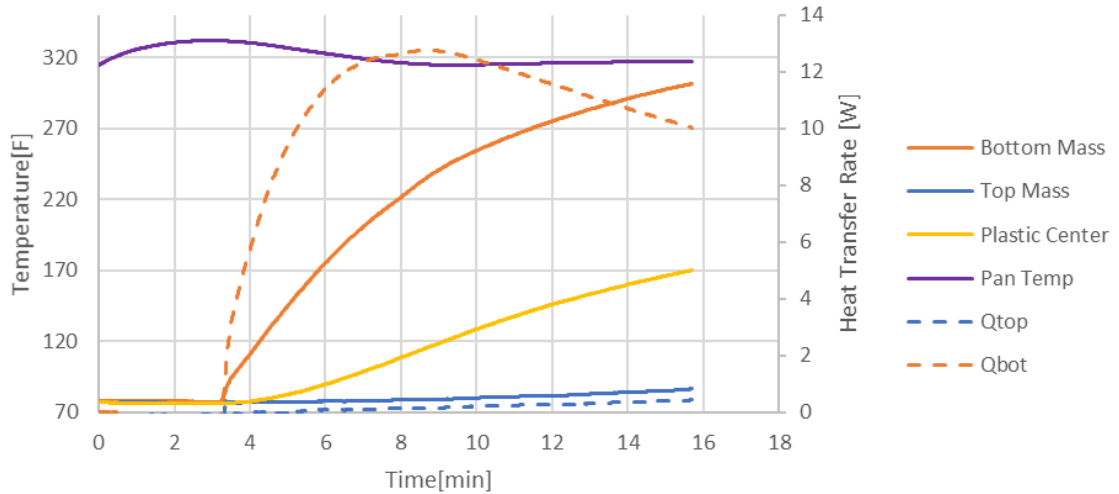


Figure 3-16 Isothermal conduction test results using closed loop cooking pan set at 300°F. Solid lines represent temperature and use the primary y-axis. The dashed lines uses secondary y-axis and represent heat transfer rate.

In this experiment the bottom mass, which serves as a direct conduction path is the mass with the highest power calculate and increases in temperature by 241 °F. The top mass which is insulated on all surfaces and only has the top surface exposed to ambient stays near ambient temperatures increasing by only 8°F. The plastic base which separates the two masses does see an increase in temperature of 100°F. This experiment is in agreement with the simulation for revision 3 of the insulation. The final revision of this sensor incorporates the spherical contact points into the bottom mass and decreases the contact area of the side surfaces of insulation and mass.

With the general concept for the sensor validated, there are a few other design parameters that can be optimized. These parameters include insulation emissivity, insulation height, and insulation infill density. Oven level tests are

used for these experiments where the sensor is subject to the same environment as intended use. These tests were run in a GE Appliances PTS9000 electric wall oven using the 375°F traditional bake setting.

To reduce the energy storage of the insulation base during testing a low emissivity coating was applied. Reducing the emissivity of the exposed surfaces of the insulation should lead to decreased radiation from environment to insulation which helps in minimizing the influence of the insulation onto the aluminum masses. For experimentation a layer of aluminum tape was used around the plastic base completely covering exposed areas as seen in Figure 3-17. This prototype includes J-type thermocouples embedded into the aluminum masses using a set screw and one J-type thermocouple in the plastic base.

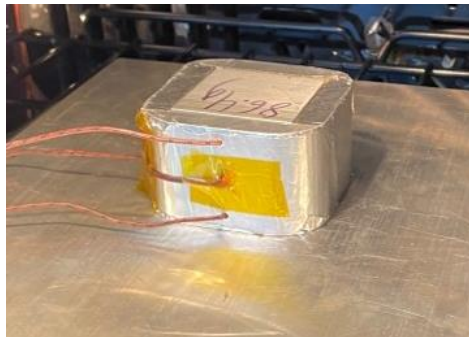


Figure 3-17 Reflective tape on insulation base

For the comparison of reflective insulation versus non-reflective surfaces initially the temperature of the reflective insulation rises much slower but reached the same final temperature. For lowering the emissivity, the adhesive on the

reflective tape degraded after a few runs and as the impact was not significant the low emissivity surface coating was not used.

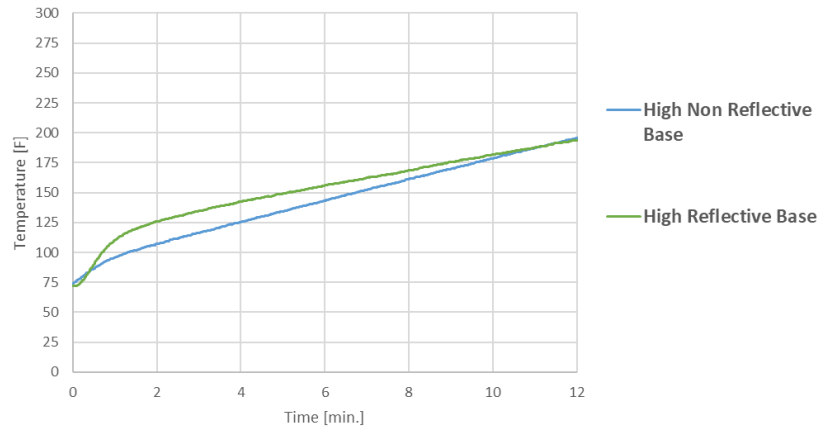


Figure 3-18 Reflective vs non-reflective insulation base surface results

Another parameter investigated is the height of the insulation base. Currently the height is defined by the thickness of the aluminum masses and the space between them. The height needed to insert the aluminum masses is fixed but there is an opportunity to reduce the space between them. Experiments were run using an insulation base with a total height of $H=1.75$ inches and another base with $H=1.50$ inches. The altered dimensions can be seen in the cross-section shown Figure 3-19, and the final assembled versions in Figure 3-20.

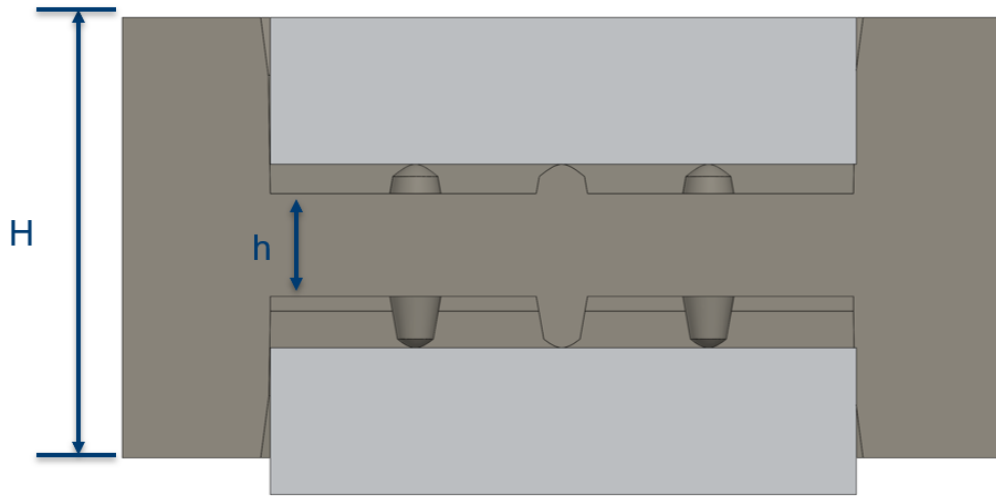


Figure 3-19 Cross sectional view showing insulation height and spacing between the aluminum masses

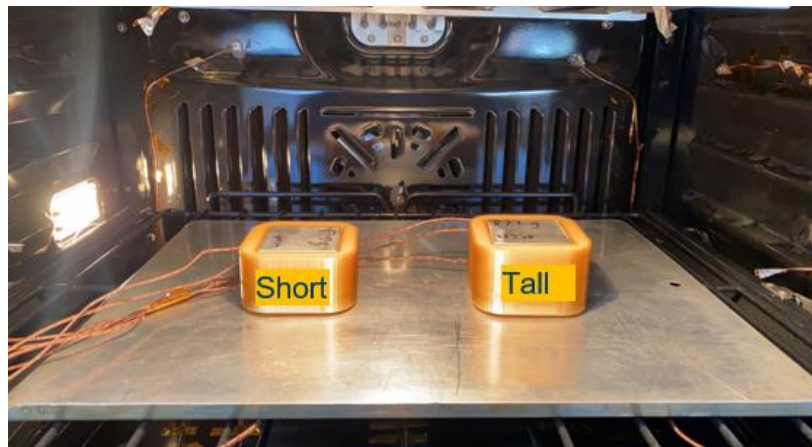


Figure 3-20 “Short” and “Tall” sensor test set up

This reduction in height led to a 21% decrease in total insulation base volume. This reduction in volume is accompanied by differences insulation temperature as well as bottom mass temperature as shown in Figure 3-21. For the reduced height insulation due to less mass being available for storage there

is an increase in core temperature. The top mass temperatures are similar for both configurations. The reduced height insulation base behaves similarly to the increased height but has added benefits of being less expensive and reducing the thermal load of the sensor, so it was selected.

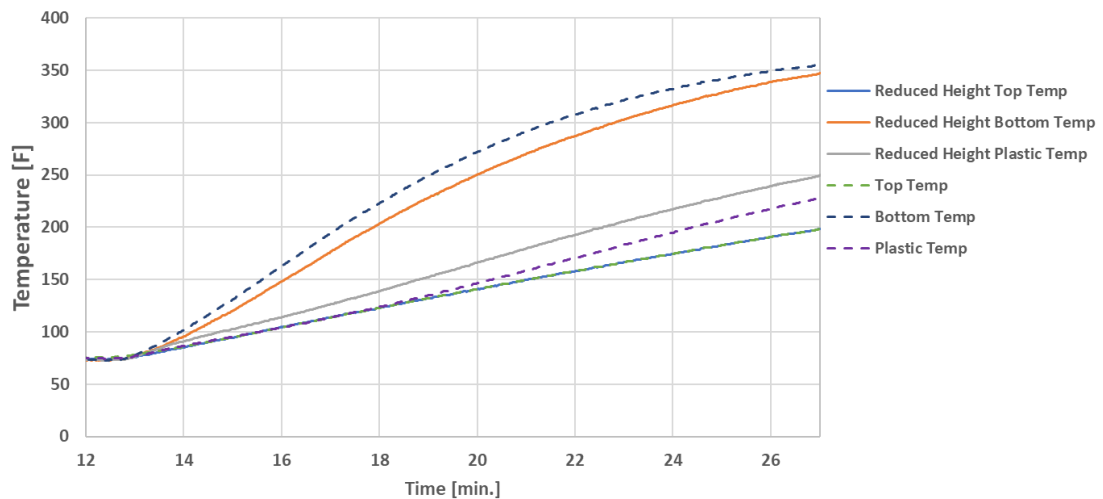


Figure 3-21 Temperatures for sensors built with different insulation heights

The final insulation base parameter evaluated is infill percentage. A reduced infill percentage reduces the conductive path across the insulation material so it should better decouple the top mass from the bottom mass. In addition, reducing infill percentages reduces cost of insulation and reduces the thermal mass since it reduces the total mass of the insulation. The results in Figure 3-22 demonstrate that high infill results in slightly lower temperature for the top mass and insulation, but slightly lower temperatures for the bottom mass.

The trends in temperature are comparable for both low and high infill, but low infill has a reduced thermal mass. With these results and the considerations mentioned low infill of 20% was chosen for this sensor design.

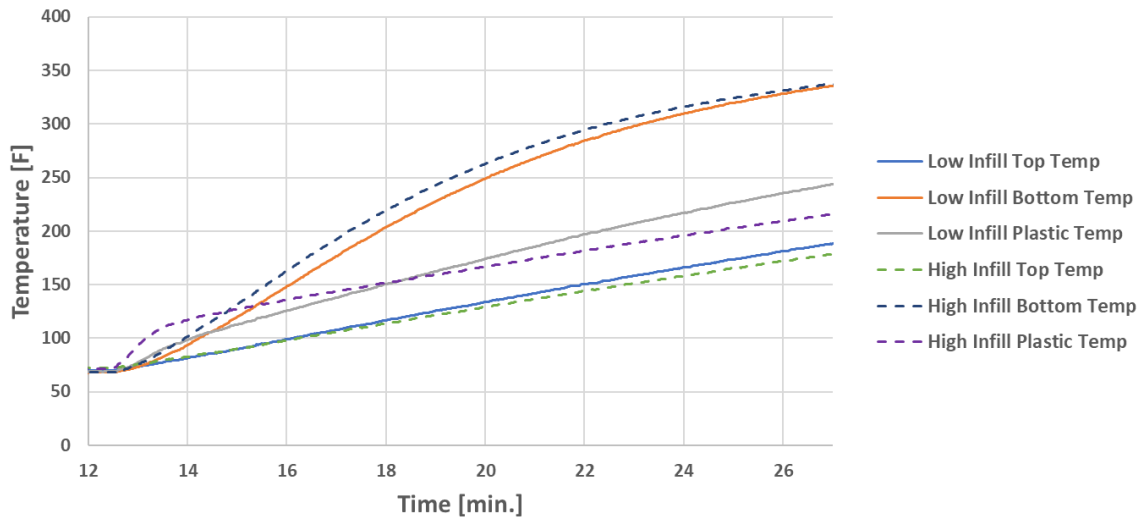


Figure 3-22 Temperatures measured for sensors built with high infill (100%) and low infill (20%)

4 SENSOR CALIBRATION

This section highlights the calibration of the heat flux sensors; first by supplier and then the method developed for internal use. The heat flux calibration method described for internal use is intended to capture behavior in convection and radiation dominated environments and serve as a way to calibrate sensors over time.

4.1 Supplier Calibration and Specifications

For the FHF04 sensors that were used in the heat flux sensor assembly there are three components provided by the supplier and held to their standard. The components are the FHF04 heat flux sensors, the black stickers, and the gold stickers. The FHF04 sensors were calibrated to ASTM standard C1130-17 which is a standard for calibrating thin-film heat flux transducers using a guarded hot plate, a heat flowmeter, and a thin heater apparatus. The heat flux apparatus used is described in ASTM standard C1114-06 and the operation mode is described in ASTM standard C1044-06. A summary of the calibration for each sensor can be seen in

Table 5. The emissivity of black and gold stickers for common situations and at temperatures less than 250°C is 0.9 and 0.01, respectively.

Table 5 Calibration summary from Supplier using ASTM Standard C1130

Sensor #	Serial #	Sensitivity [V/(W/m ²)]	Calibration Uncertainty [V/(W/m ²)]	Uncertainty Percentage
1	2643	1.109E-05	5.50E-07	4.96%

2	2635	1.194E-05	6.00E-07	5.03%
3	2645	1.152E-05	5.80E-07	5.03%
4	2636	1.076E-05	5.40E-07	5.02%
5	2637	1.108E-05	5.50E-07	4.96%
6	2641	1.081E-05	5.40E-07	5.00%
7	2640	1.118E-05	5.60E-07	5.01%
8	2644	1.053E-05	5.30E-07	5.03%
9	2642	1.130E-05	5.70E-07	5.04%
10	2639	1.147E-05	5.70E-07	4.97%
11	2638	1.185E-05	5.90E-07	4.98%
12	2597	1.108E-05	5.90E-07	5.32%

4.2 Radiation Calibration

4.2.1 Radiation Theory

The first principal equations that were used for comparison between heat flux sensor and theory was derived from radiation exchanged between two surfaces and a reradiating surface. The electrical analogy between circuits and heat transfer is used considering the surface resistance of the heater, sensor, reradiating surface, and the space resistance between the three. The geometry used for the radiation calibration enclosure can be seen in Figure 4-1. The thermal resistance network for this scenario and the resulting equation can be seen in Figure 4-2 and is highlighted by Bergman et al. (2011). In this resistance network the view factor between the sensor and the reradiating surface is 0 so the thermal resistance network simplifies to

Figure 4-3.

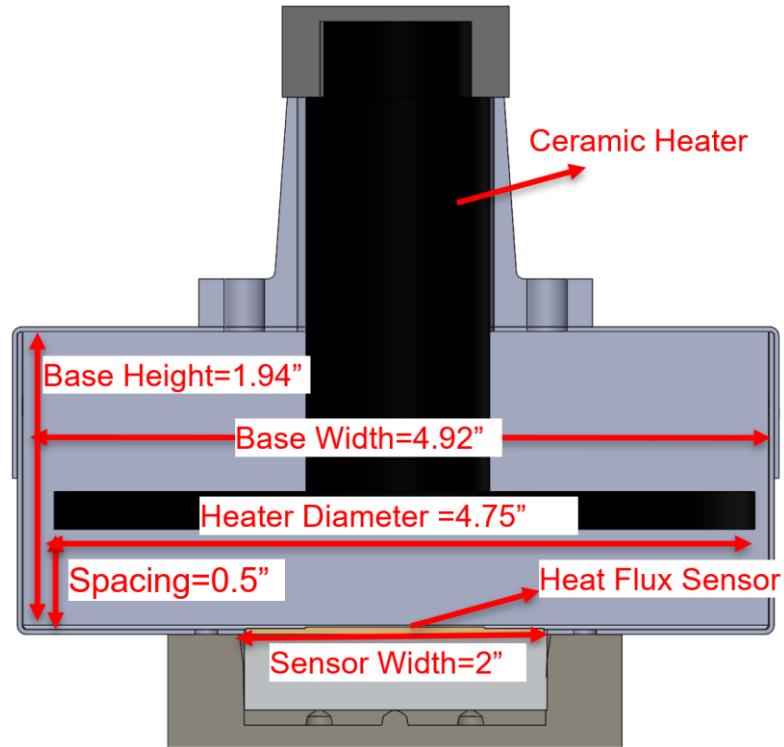
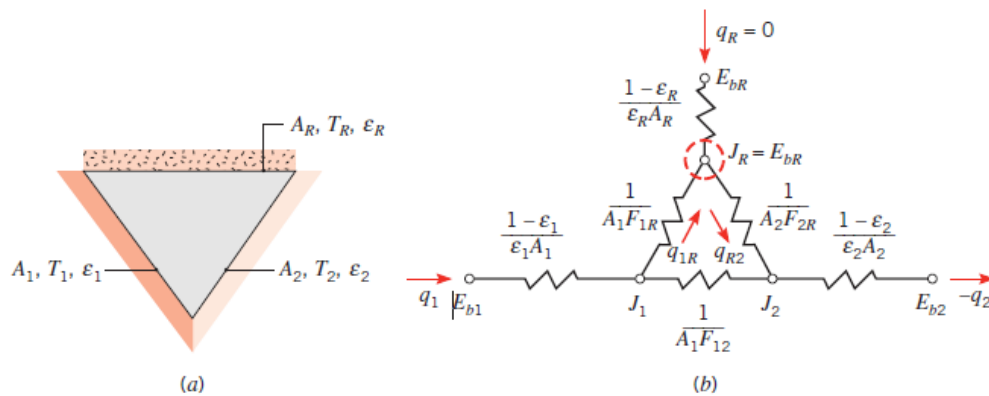


Figure 4-1 Radiation enclosure designed for radiation calibration testing



$$q_1 = -q_2 = \frac{E_{b1} - E_{b2}}{\frac{1 - \epsilon_1}{\epsilon_1 A_1} + \frac{1}{A_1 F_{12} + [(1/A_1 F_{1R}) + (1/A_2 F_{2R})]^{-1}} + \frac{1 - \epsilon_2}{\epsilon_2 A_2}}$$

Figure 4-2 Thermal resistance and resulting heat flux equation for a three-surface enclosure with one surface reradiating (Theodore et al., 2011)

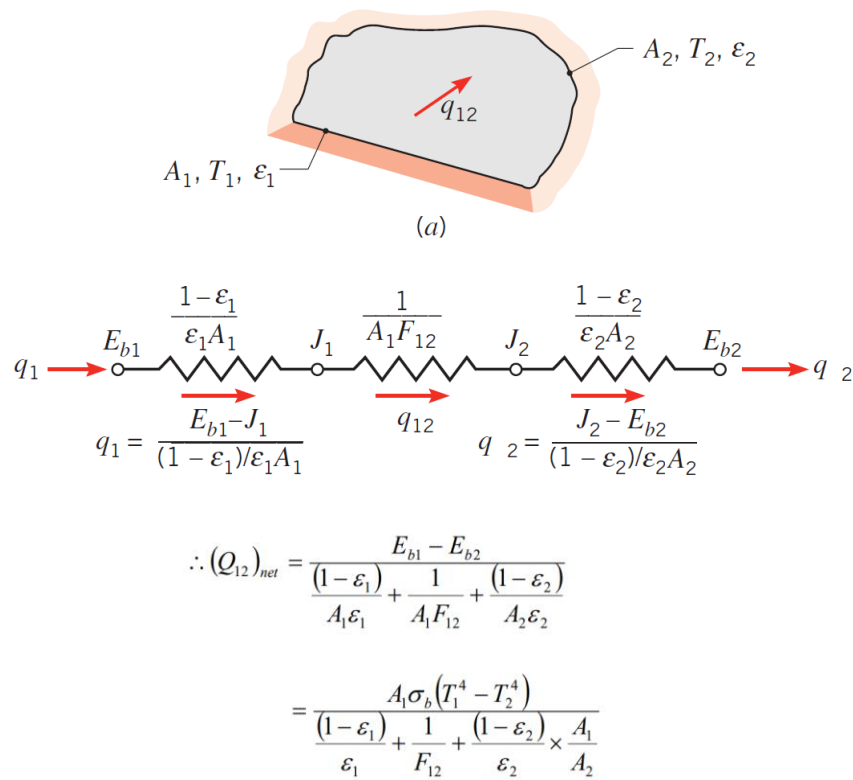
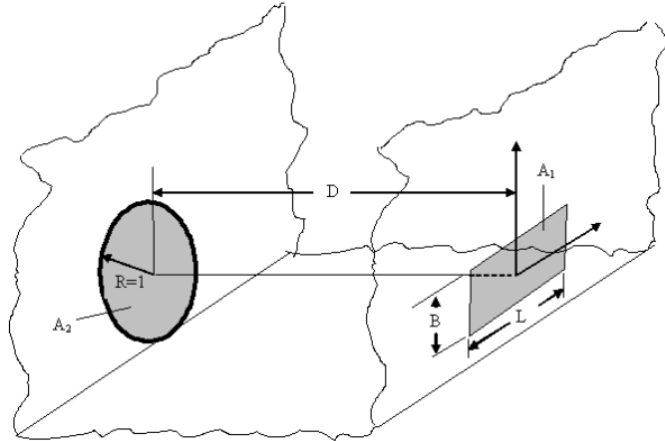


Figure 4-3 Thermal resistance and resulting heat flux equation of two nonblack surfaces of known geometry (Theodore et al., 2011)

In these equations E represents the emissive power of each surface, J represents the radiosity, and F represents the view factor for the geometry. For this study the subscript 1 denotes the heater, the subscript 2 denotes the sensor. and R represents the reradiating surface parallel to the sensor. The side walls view factor to the sensor were not considered due to the minimal area that is exposed to the sensor. The view factor case here used is that of a circular disc with a midline perpendicular to a rectangular surface separated by a known

distance. This view factor case can be seen below in Figure 4-4 and supporting equations are derived from Abishek et al (1995). Key assumptions in this study were that convection effects were negligible, reradiation from walls are negligible, and that the heat flux sensor and heater are gray and diffuse



For $0.1 \leq L \leq 2.0$; $0.1 \leq B \leq 2.0$; $0.1 \leq D \leq 10.0$ (max error $\pm 12.03\%$)

$$F_{1-2} = \frac{1.0152(1 + L^{1.0251})(1 + B^{3.4915})}{(1 + L^{1.195})(1 + B^{3.656})[D^{1.9767} + (1 + D)^{0.3047} - 0.0175]}$$

For $2.0 \leq L \leq 10.0$; $2.0 \leq B \leq 10.0$; $0.1 \leq D \leq 2.0$ (max error $\pm 12.59\%$)

$$F_{1-2} = \frac{3.2718(1 + D^{1.6491})^{0.2834}}{[D^{1.5138} + (BL)^{0.495}]^{2.0417}}$$

For $2.0 \leq L \leq 10.0$; $2.0 \leq B \leq 10.0$; $2.0 \leq D \leq 10.0$ (max error $\pm 11.42\%$)

$$F_{1-2} = \frac{1.1947(1 + L^{0.4609})(1 + B^{0.46})}{(1 + L^{0.5111})(1 + B^{0.5102})(D^{2.0405} + B^{1.195} + L^{1.1949} - 3.4734)}$$

For $0.1 \leq L \leq 2.0$; $2.0 \leq B \leq 10.0$; $0.1 \leq D \leq 10.0$ (max error $\pm 18.64\%$)

$$F_{1-2} = 3.0932D^{0.1128}[BL + (BL)^2 + D + D^2 + D^4]^{-0.0188}(D^{1.0657} + L^{0.0215}B^{0.4893})^{-2.2497}$$

Figure 4-4 View factor case of finite circular disc parallel to rectangle separated by distance (Abishek et al., 1995)

With the geometric configuration of the radiation calibration chamber a view factor of 0.2342 is calculated. For a constant temperature for the heater, the view factor and surface areas calculated, and the emissivity provided, a theoretical heat flux curve is developed. This heat flux curve can be seen in Figure 4-5 and represents the instantaneous heat flux experienced by the sensor for different sensor temperatures and the given heater temperature.

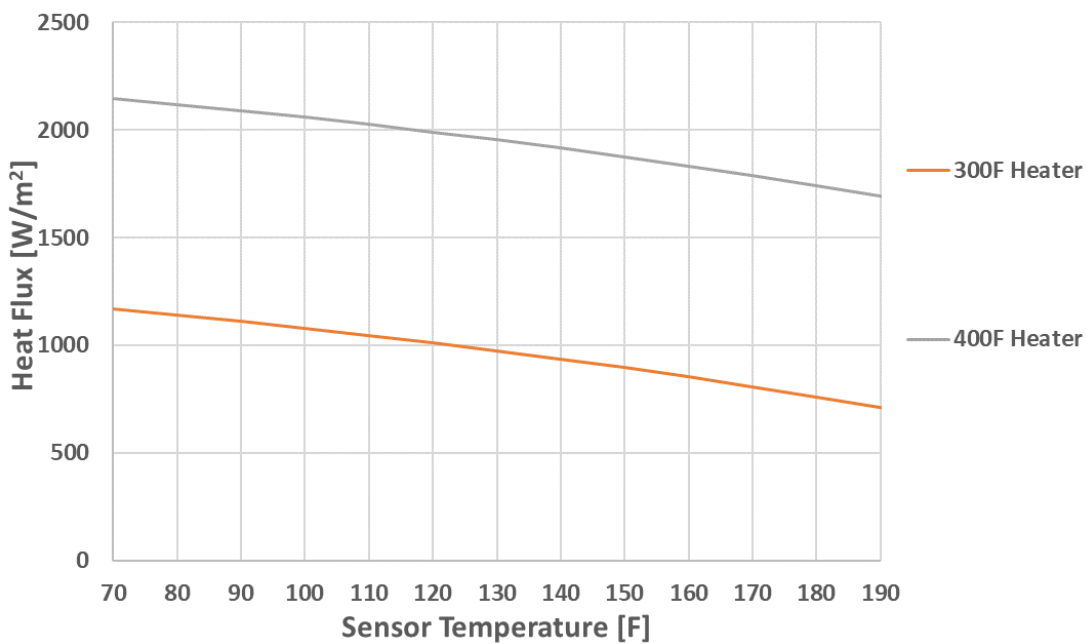


Figure 4-5 Theoretical heat flux calculated for various sensor temperatures in radiation calibration configuration

4.2.2 Radiation Calibration Setup

Traditional heat flux sensors typically make a 1-D approximation for calibration and follow standards where there is a known heater power, a highly thermal conductive heat spreader, and not heat loss to the environment. The

intention is that heat flux sensor measurement should correspond with heater rating. These heat flux sensors typically do not have the capability of breaking heat flux into convection and radiation but instead provide an overall indication of local heat flow perpendicular to sensor.

Methods have been used to calibrate radiation specifically using water cooled heat flux sensors (or other reference heat flux sensors) and variable temperature black bodies. Close cases for calibration combination cases come from open flame tests with water cooled sensor as an absolute reference. For internal use the traditional means of calibration for radiation-based meters aren't available and a custom calibration set-up was designed and can be seen in **Error! Reference source not found..** This method compares the supplier calibrated reading of the heat flux sensor to theoretical calculations.

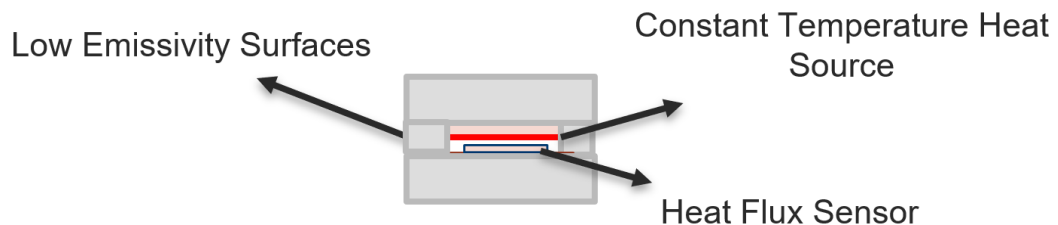


Figure 4-6 Diagram of radiation chamber used for heat flux sensor calibration

The constant temperature heat source used for this radiation calibration chamber is a ceramic heater. The emissivity of the ceramic heater is 0.88. and was found by measuring its temperature with an infrared thermometer and J-type

thermocouple. The emissivity setting of the infrared camera was adjusted until the temperature matched the J-type thermocouple reading, and that emissivity value was taken to be the true emissivity of the heater. The same procedure was used to determine the base emissivity of the sensor without a black or gold sticker. This emissivity is found to be 0.75. The heater is controlled by a PID controller to maintain a constant surface temperature at 300 °F and 400 °F. The radiation chamber enclosure is made of sheet metal and lined with aluminum foil to lower the emissivity of the walls. The heat flux sensor being tested is mounted onto an aluminum mass and that mass is placed onto an insulation base. A layer of thermal grease is used to improve contact between the sensor and the aluminum mass. The experimental set up can be seen in Figure 4-7.

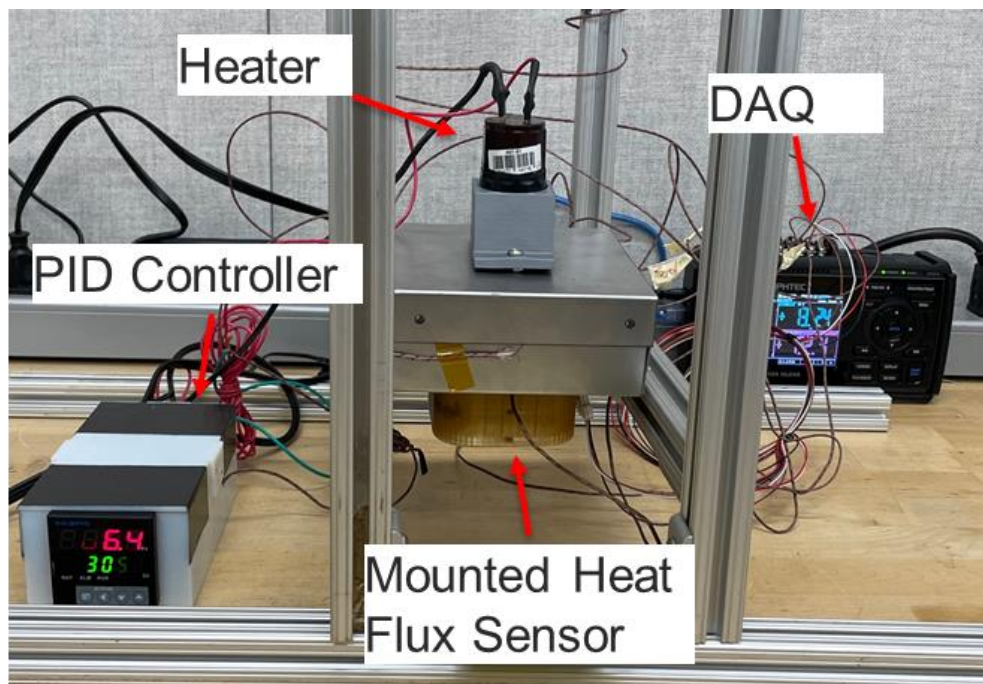


Figure 4-7 Experimental Setup for radiation calibration chamber

The surface temperatures of all the surfaces and the heater were collected using J-type thermocouples attached by welding to the walls and using high temperature ceramic epoxy for the heater. Each sensor was tested for an hour at each heater temperature setting, 300°F and 400°F.

4.2.3 Radiation Calibration Results

Each tests uses the nominal calibration sensitivity from supplier to convert each sensor voltage reading into a heat flux reading. The thermal plot for one run can be seen in Figure 4-8. The heater starts at room temperature and is heated to the set temperature in the first two minutes. This room temperature heater start is used for each test. Within the first 10 minutes of each test, the surface temperatures are stable. The term “ dT ” shown in this figure plots the difference between the sensor temperature and the heater temperature. The heat flux plot in Figure 4-9 shows the relationship between heat flux and the temperature difference between the heater and sensor. For both heater temperature configurations each heat flux sensor is stable at 30 minutes. The oscillations in heat flux (and the temperatures in Fig. 4-6) are directly related to the cycling of the ceramic heater.

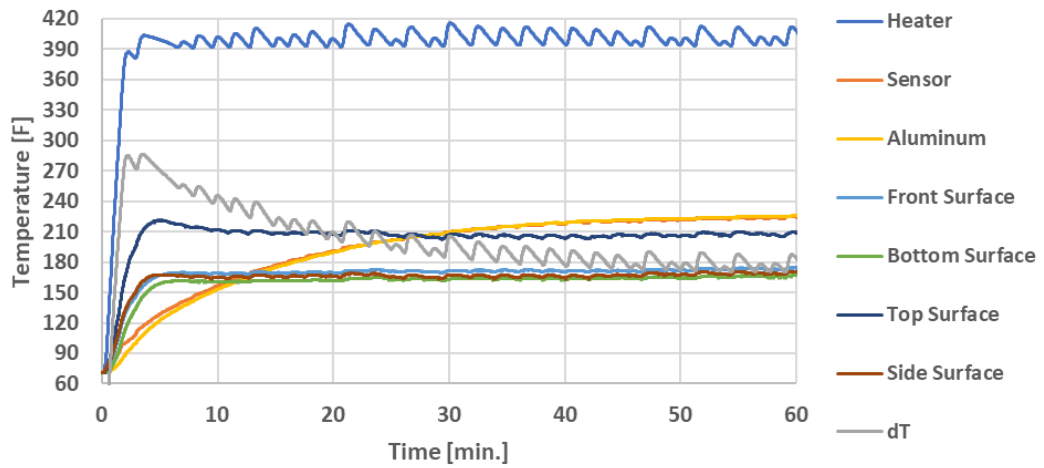
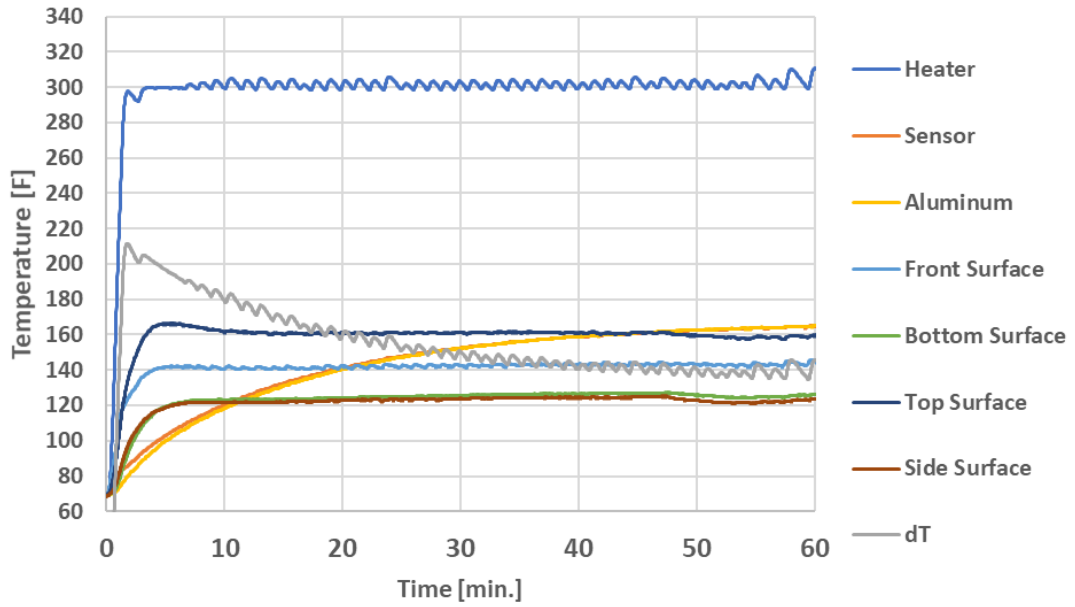


Figure 4-8 Thermal plot showing surface, sensor, and heater temperatures measured for sensor 1 300°F(top) and 400°F test(bottom) test

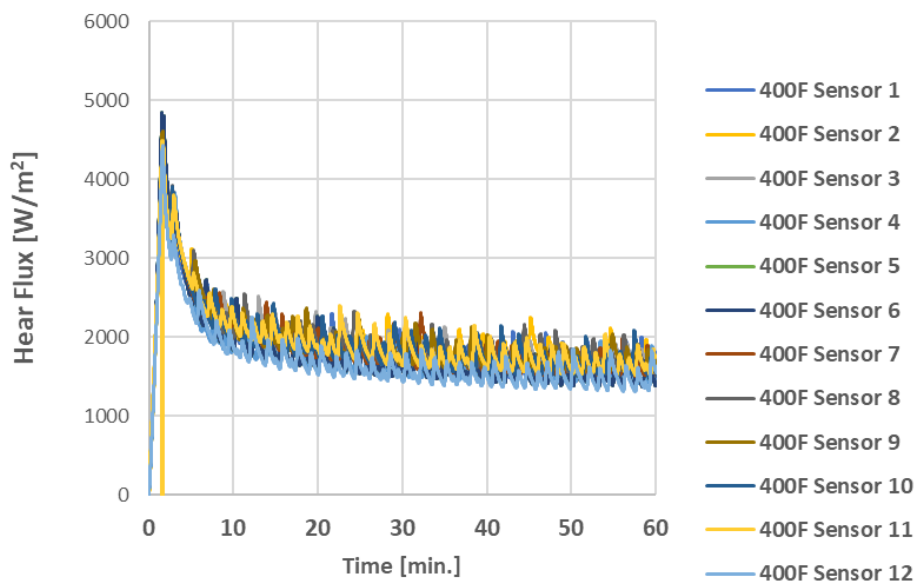
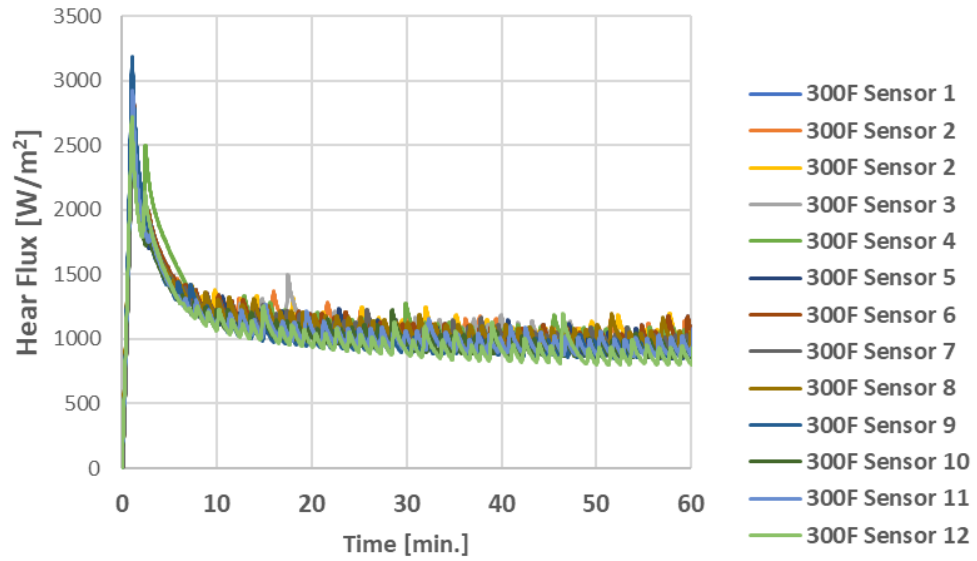


Figure 4-9 Heat flux versus time for 300°F(top) and 400°F(bottom) heater tests for all 12 sensors.

A comparison among the sensors was made during the stable heat flux period between 30 and 60 minutes during the test. The average reading for the

30 minutes was taken and used to compare the sensors during that period (see Figure 4-8). Each sensor is tested individually but the environments are identical for each test. The statistical summary table for all twelve sensors can be seen Table 6. Although there was low coefficient of variation between the 12 sensors there is a 10.03% and 10.50% difference amongst the sensors at 300°F and 400°F tests, respectively.

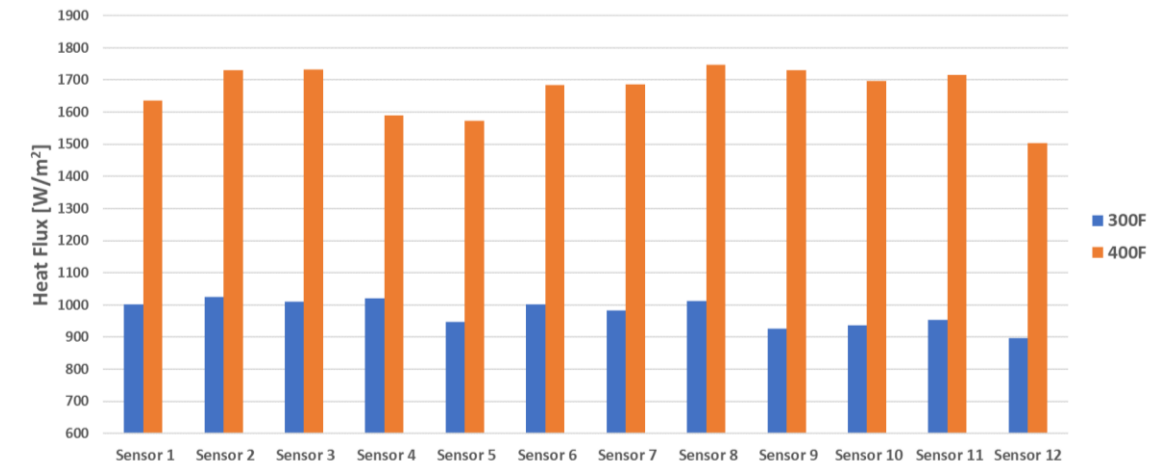


Figure 4-10 Comparison of heat flux averages during last 30 minutes of each test for both temperature configurations

Table 6 Summary of the average heat flux readings between 30 and 60 minutes for each run

	Heater Temperature	
	300°F	400°F
Average heat flux (W/m²)	976	1684
Range	98	174
Std. Dev.	34	57
COV	3.51%	3.36%

A comparison of the theoretical heat flux curve and the heat flux measured at various sensor temperatures was performed and plotted in Figure 4-11. This comparison takes the heat flux versus time results of each test and considers the heat flux versus sensor temperature to commonize each test since they weren't run at the same time and to compare to the theory case. For each test the heat flux sensor starts at 0 until the 3 second response time is reached, and the first reading is collected. For both heater temperatures, the heater ramps up to temperature for the first three minutes of the test. For the 300°F test the heater the sensor reaches ~91°F and for the 400°F the sensor reaches ~112°F. This can be seen in the initial ramp up period of each sensor before stabilizing and syncing with the heater cycles.

Overall, the sensors overpredicted heat flux in the radiation dominated experiment compared to the theoretical curves developed. Some of the assumptions made for this analysis included neglecting natural convection due to the enclosed nature of the chamber as well as neglecting reradiation from surrounding surfaces due to the low emissivity of the aluminum foil covered surroundings. These assumptions may contribute to the over prediction of measurements compared to the theory case.

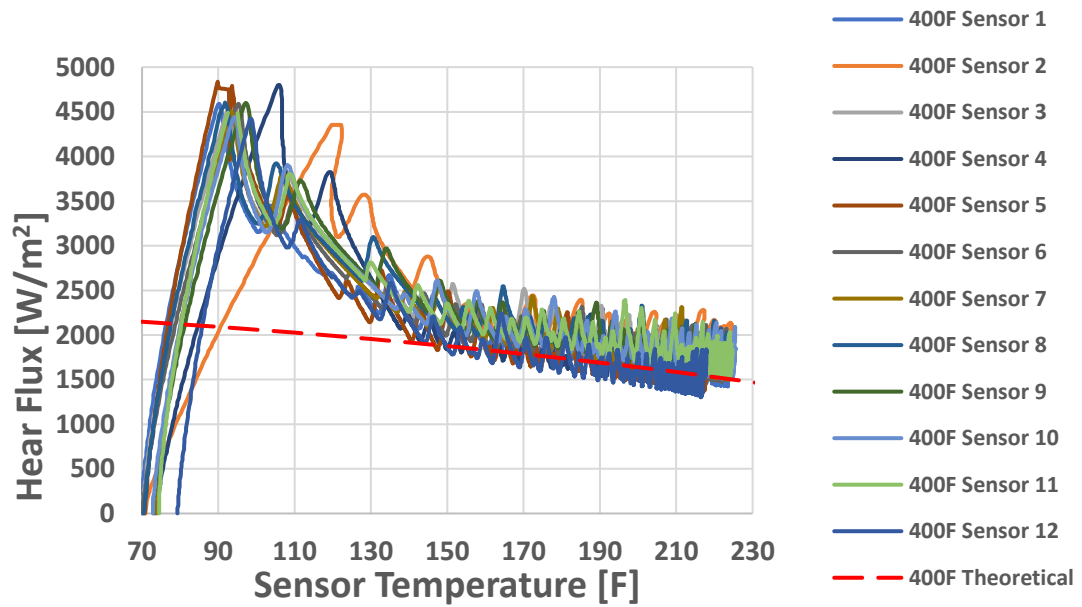
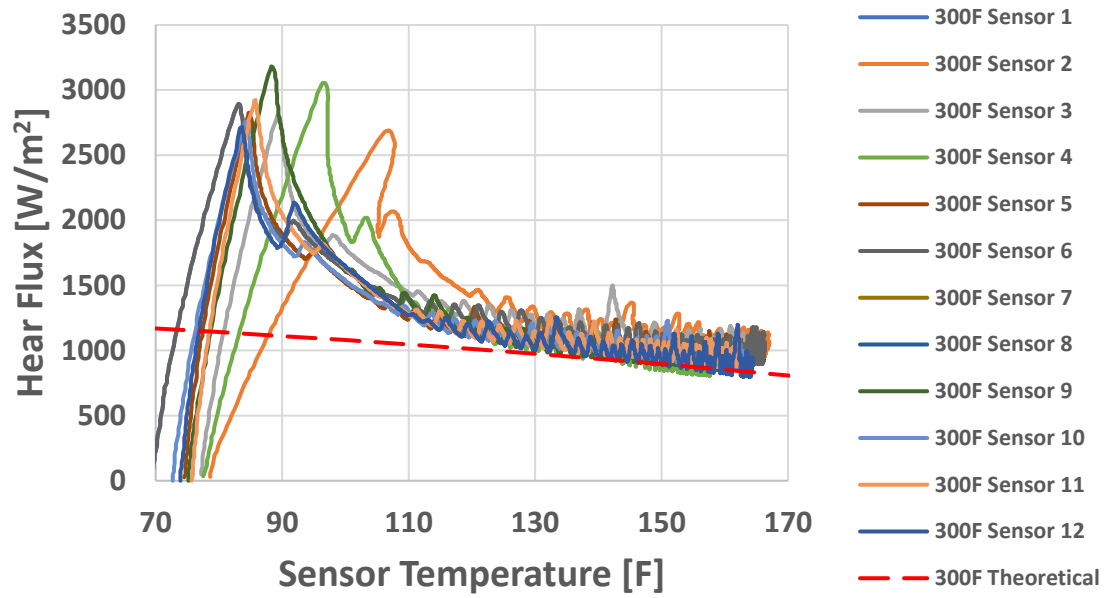


Figure 4-11 Heat flux vs sensor temperature for 300°F (top) and 400°F(bottom)

4.3 Convection Calibration

4.3.1 Convection Theory

A theoretical comparison was applied for convection. Newtons law of cooling was used to calculate convection heat transfer to the heat flux sensor. Newtons law of cooling can be seen in Equation 10.

$$q'' = h * (T(t) - T_{air}) \quad (10)$$

Using Newtons law of cooling a calculation of heat flux can be made that considers the temperature difference between the sensor and the air, and the convection coefficient, h . This convection coefficient is dependent on the Nusselt number, which is related to the Reynolds number, the type of flow being considered, and Prandtl number. For flow over a flat plate the Reynolds number was checked to determine whether the flow is laminar or turbulent since this contributes to the rate of heat transfer. Reynolds number was calculated using Equation 11. Based on previous experience with residential ovens, a low velocity of 2.5 m/s, and a high velocity of 10 m/s were chosen for lower and upper bounds for testing. The Reynolds number was calculated using the film properties of air, the length of the sensor, as well as the air velocity. For both velocities selected the Reynolds number was far less than the critical Reynolds number of 500,000 shows that flow over the heat flux gage surface is laminar.

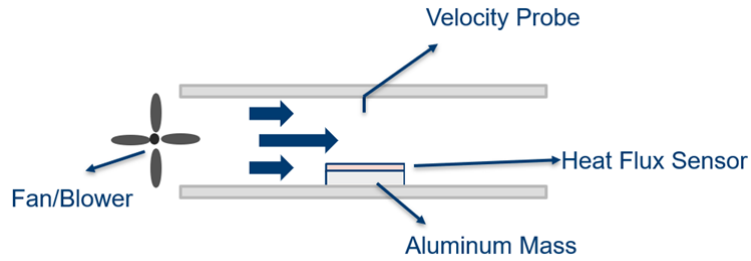


Figure 4-12 Convection calibration chamber diagram

$$Re = \frac{v * L * \rho}{\mu} \quad (11)$$

For parallel flow over a flat plate in the laminar regime the Nusselt correlation for an isothermal plate is shown in Equation 12. The Nusselt number in this instance represents the average Nusselt for the surface being considered.

$$Nu_L = \frac{hL}{k_f} = 0.664 * Re_x^{\frac{1}{2}} * Pr^{\frac{1}{3}} \quad (12)$$

Using this Nusselt correlation the equation for heat flux be seen in Equation 13.

$$q'' = \frac{k_f (.664 (\frac{v * L * \rho}{\mu})^{\frac{1}{2}} * Pr^{\frac{1}{3}})}{L} * (T(t) - T_{amb}) \quad (13)$$

This equation was used to determine the instantaneous heat flux using data collected from the experimental set up highlighted in the next section. A schematic of the convection calibration chamber can be seen in Figure 4-12. The theoretical heat flux versus sensor temperature line can be seen below in Figure 4-13. The calculated convection coefficient for the low and high velocity test case

was 27 and 54 W/m²-K respectively. The key assumptions made in this study include radiation being negligible due to the low emissivity aluminum coated surface in the enclosure, air supply being constant temperature axially and longitudinally, wall temperature is constant for all walls, air properties can be evaluated at film temperature, flow is steady and incompressible, and that there are constant fluid properties.

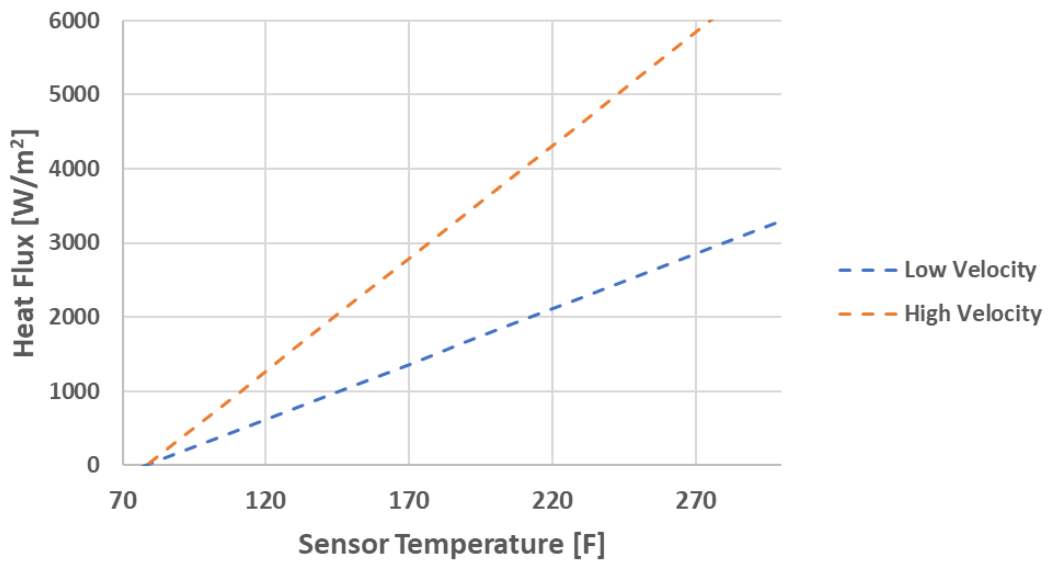


Figure 4-13 Theoretical heat flux as a function of sensor temperature for low and high air velocity

4.3.2 Convection Calibration Set Up

The experimental setup used for the convection calibration chamber consisted of an AMCA 210-99 air flow test chamber, the twelve heat flux sensors, an aluminum mass, and an oven used to preheat the aluminum mass and sensor. This experimental set up can be seen below in Figure 4-14. A front view

can be seen in Figure 4-15 that shows the flow straighteners used to reduce turbulence in the flow. A Kanomax 6501 series hot wire anemometer equipped with an omnidirectional needle probe is used to measure the air velocity an inch above the heat flux sensor surface.

To start the convection calibration tests the airflow chamber is first set to desired flow rate. After that an aluminum mass with the heat flux sensor mounted on top is placed into an oven to preheat until it reaches 250°F. Once the sensor is preheated it is placed into the convection chamber in the marked location. The test is run for 15 minutes or until the sensor cools to room temperature. Once the test is done the airflow chamber is reconfigured for the next flow rate.

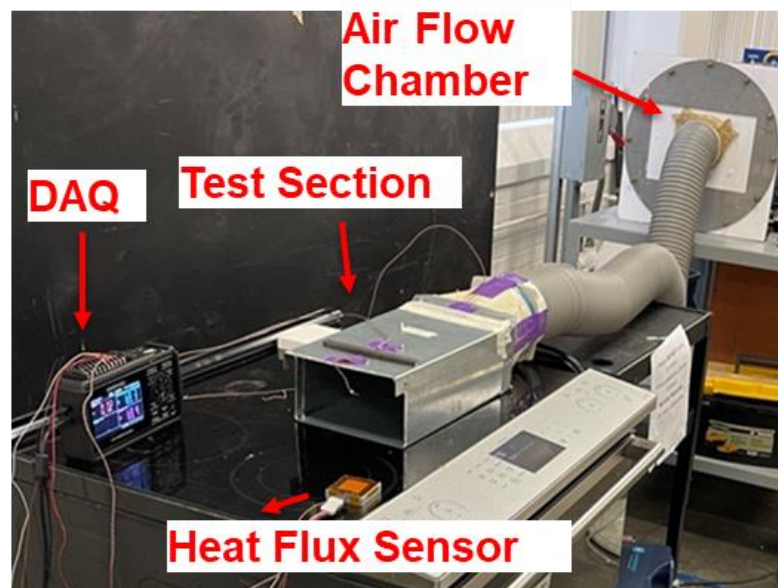


Figure 4-14 Experimental setup used in convection calibration of heat flux sensors

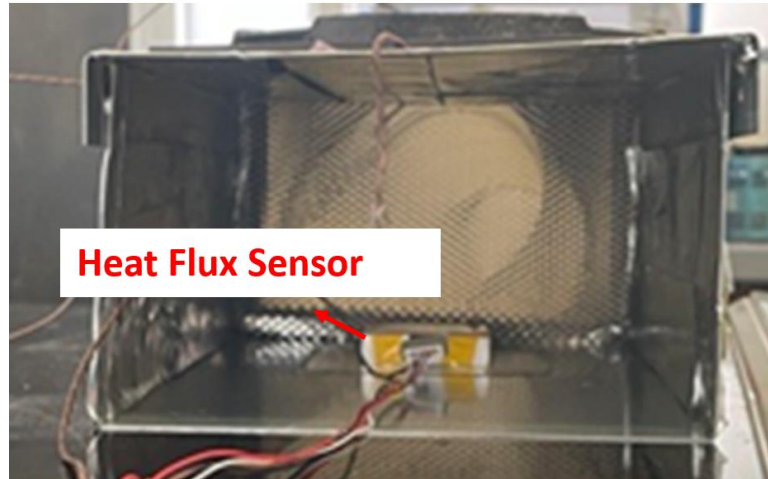


Figure 4-15 Front view of convection calibration chamber with heat flux sensor in position of test with air flowing out of the page

4.3.3 Convection Calibration Results

The nominal sensitivity of each sensor was used to convert the voltage readings measured during testing into temperature values and that data for low velocity and high velocity can be seen in Figure 4-16. The measurements for inlet and outlet air temperatures are the same as well as the measurements for sensor and aluminum temperatures.

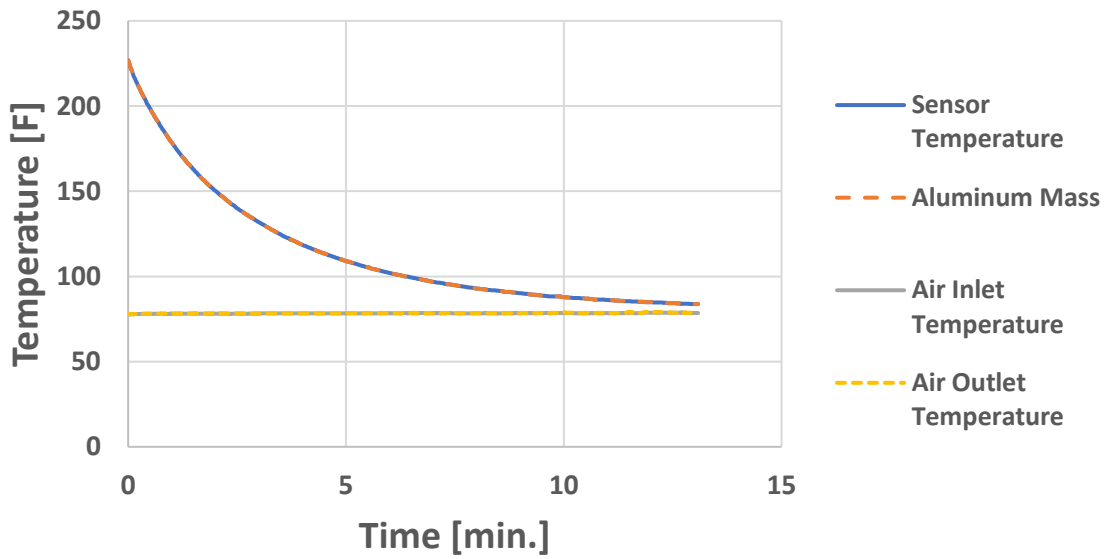
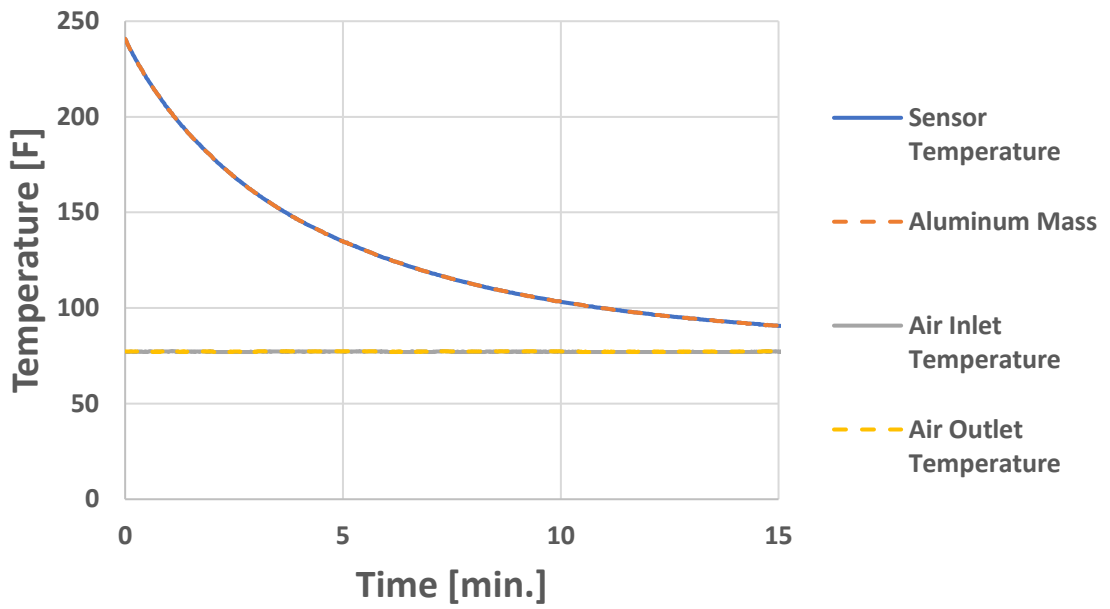


Figure 4-16 Temperature data over time Low Velocity (top) High Velocity (bottom)

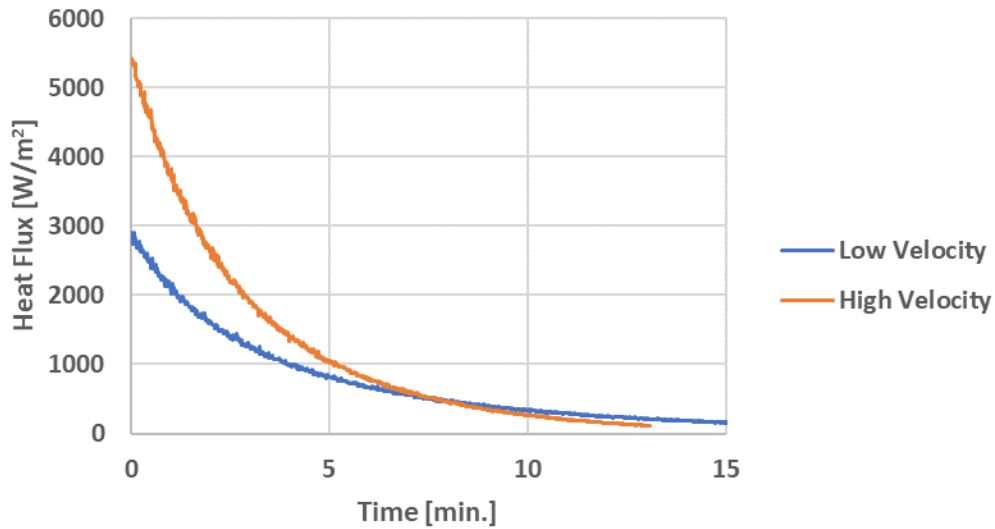


Figure 4-17 Heat flux versus time for low and high air velocity

Figure 4-17 shows the heat flux profile for the low and high velocity tests. For both tests the profile of heat flux curve is proportional to the temperature difference between the sensor and air. The results for the low and high velocity test for sensor one can be seen in Figure 4-18 as heat flux versus sensor temperature. For both the low and high velocity tests there is a linear heat flux profile. For both tests, following Equation 13, the slope of each line is directly related to the square root of the velocity. The square root of the low velocity is 1.58 and the square root of the high velocity is 3.16. Following Newtons law of cooling the difference between heat flux reading for low and high velocity should be different by a factor of 2 since the square roots of velocities are related by a factor of 2 and all the other parameters remain the same. Both the theoretical line and the experimental line reflect this relationship.

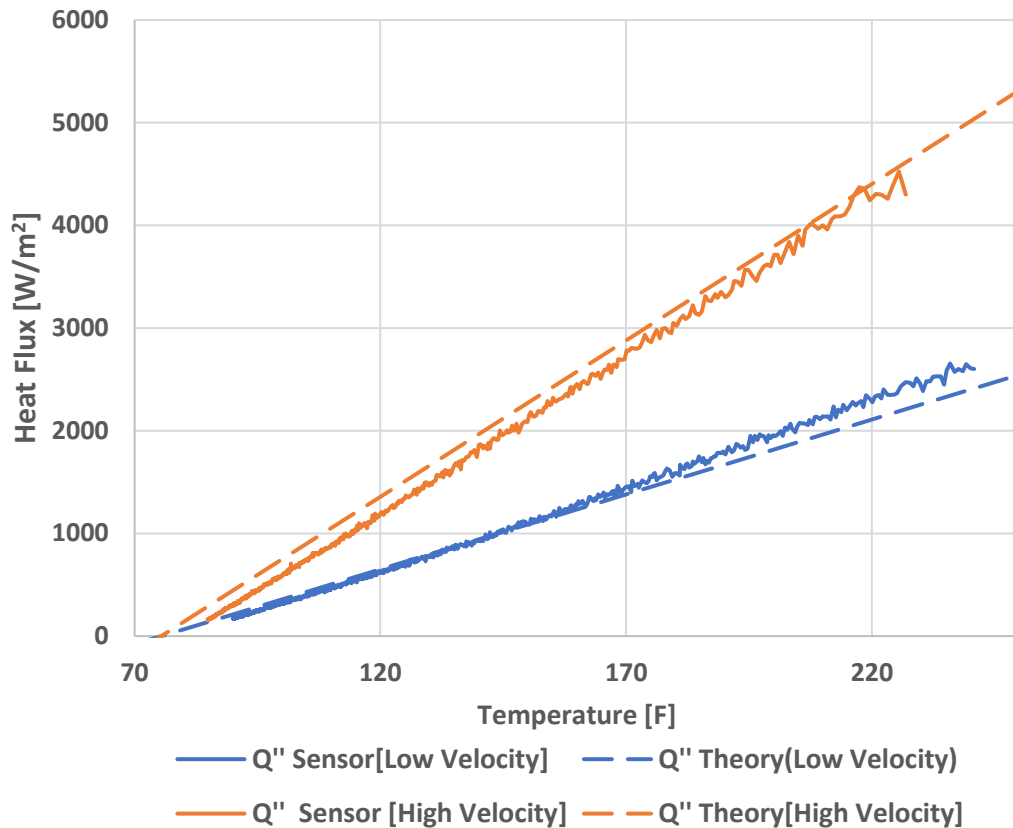


Figure 4-18 Heat flux versus sensor temperature for sensor 1 at low and high air velocities (labels are getting small here)

The heat flux lines for all 12 sensors can be seen in Figure 4-19. A subset of these sensors is normalized by dividing the heat flux reading by the square root of the measured velocity and this can also be seen in Figure 4-19. Each heat flux line behaved similarly but had a different effective slope. Part of this difference is due to each test having legitimately different air velocities. A summary of the air velocity of each test can be seen in Table 7. Relative to the theoretical low and high velocity heat flux line, each sensor followed the same behavior as sensor 1. Each sensor over predicted at higher temperatures and

gradually getting closer to theoretical line at lower temperatures. One possible cause of this can be the assumption that radiation is negligible. A non-negligible radiation term would describe the difference between theory and measured varied based on sensor surface temperature.

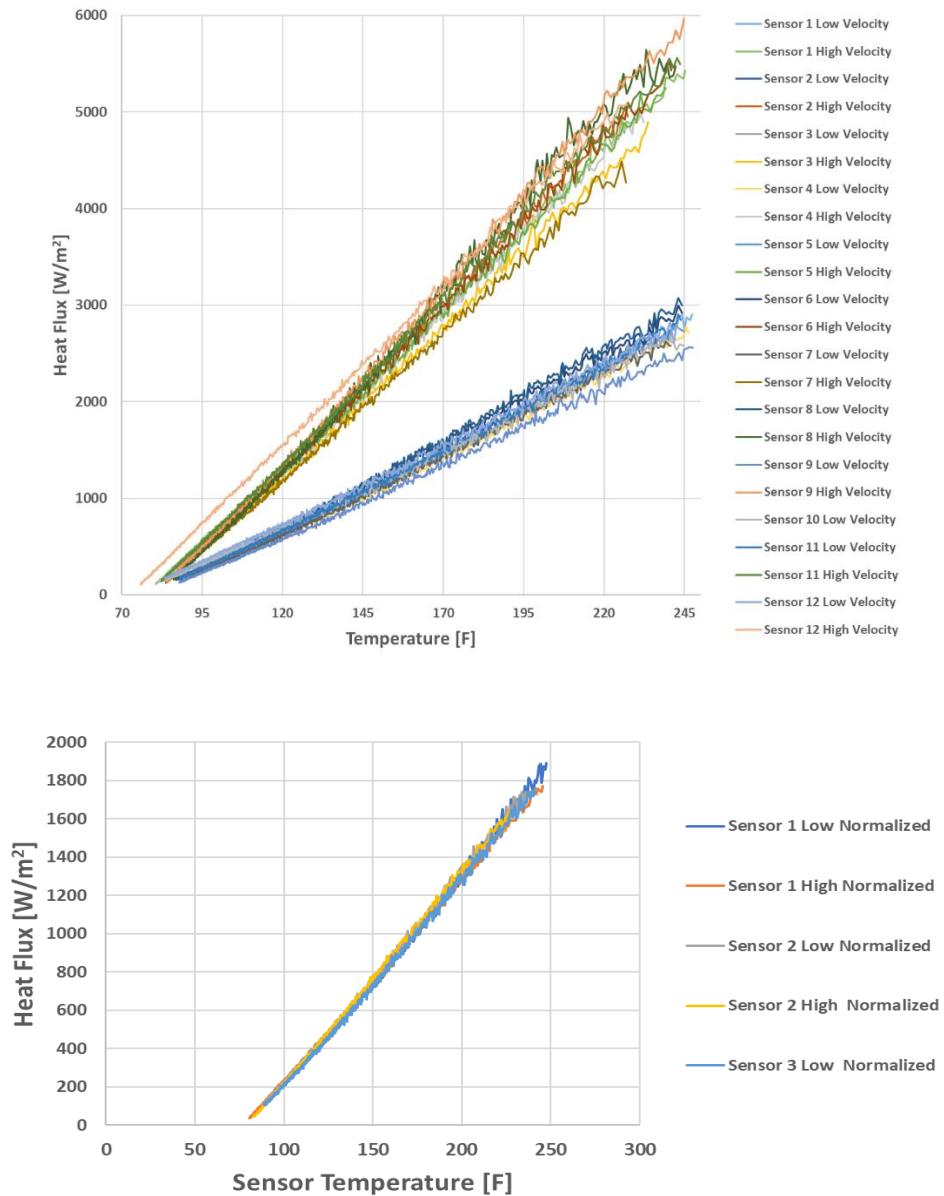


Figure 4-19 Low and high velocity plots for each sensor in convection calibration study(top) and normalized subset of sensors (bottom)

Table 7 Velocity measurements

Sensor #	Ambient Temp [F]	Low Velocity	High Velocity
		Anemometer Velocity [m/s]	Anemometer Velocity [m/s]
1	75.7	2.35	9.75
2	76.6	2.32	9.75
3	78.8	2.34	10.20
4	77.7	2.31	9.75
5	76.8	2.34	9.65
6	75.0	2.40	10.60
7	79.9	2.31	9.18
8	80.0	2.25	9.50
9	78.0	2.26	10.10
10	75.0	2.44	10.60
11	73.6	2.30	9.41
12	74	2.35	9.41

Following the single test runs for each sensor, repeat tests were run on a subset of sensors. Sensors 4 and 6 were tested two and three times in two configurations. The first test run was without disassembling the heat flux sensors from mass, the second run was while disassembling between each run. For the runs where the sensor is not disassembled the heat flux lines are identical for both low and high velocity across both sensors. For the runs where the sensor was disassembled between each run, there are differences in heat flux for both sensors. Identical procedures were followed between each test and comparable velocities were measured. The same aluminum mass was used for all tests. The likely source for variation was in thermal grease application when mounting sensor. Thermal grease was implemented at the sensor to aluminum mass interface to minimize contact resistance between the two surfaces, but this

introduced the opportunity for thermal grease variation. This subset of tests demonstrated the importance of accounting for differences in assemblies when using the heat flux sensor prompting the need for assembly level calibration as well as improved procedures for sensor assembly. Although variation is introduced in assembly, heat flux sensor still follows same behavior as theoretical case.

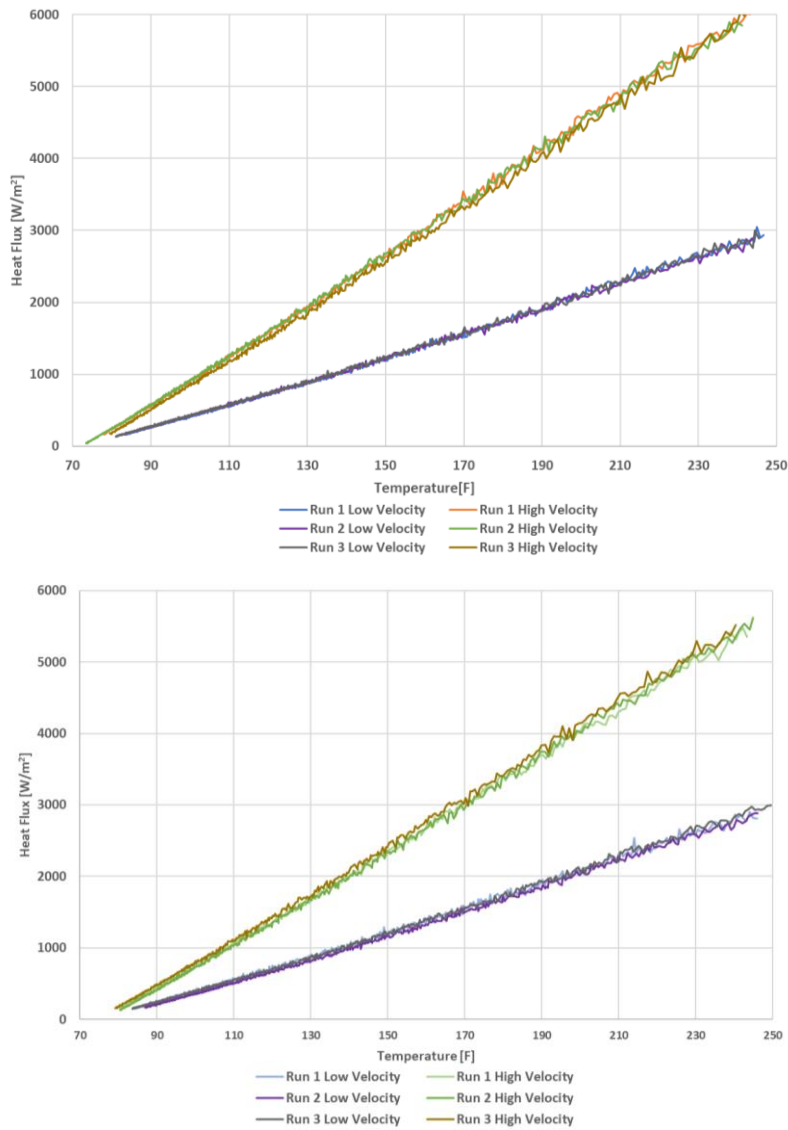


Figure 4-20 Three heat flux as a function of temperature without disassembling between runs for sensor 6 (top) and sensor 4 (bottom)

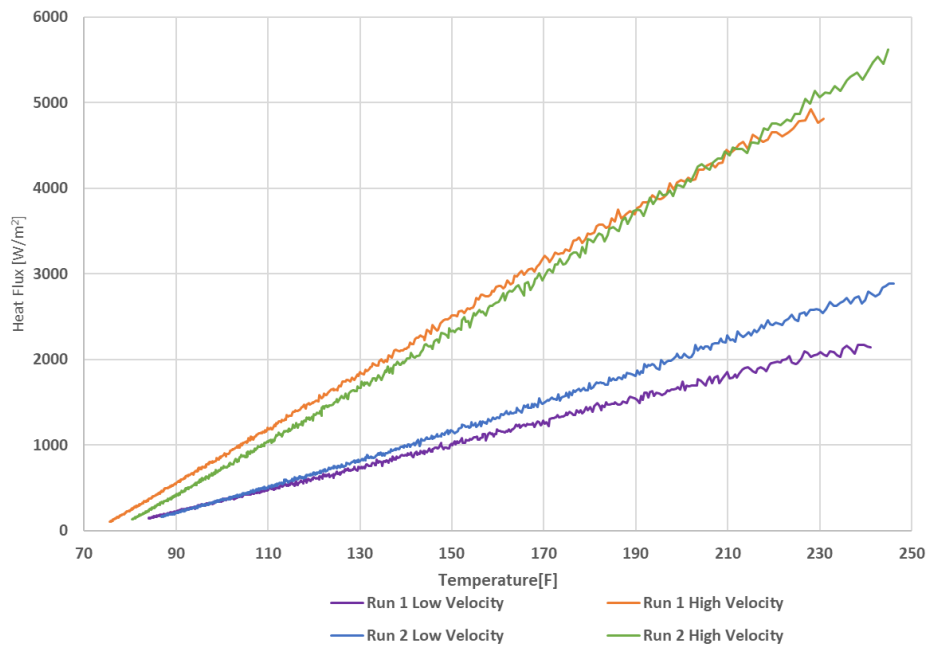
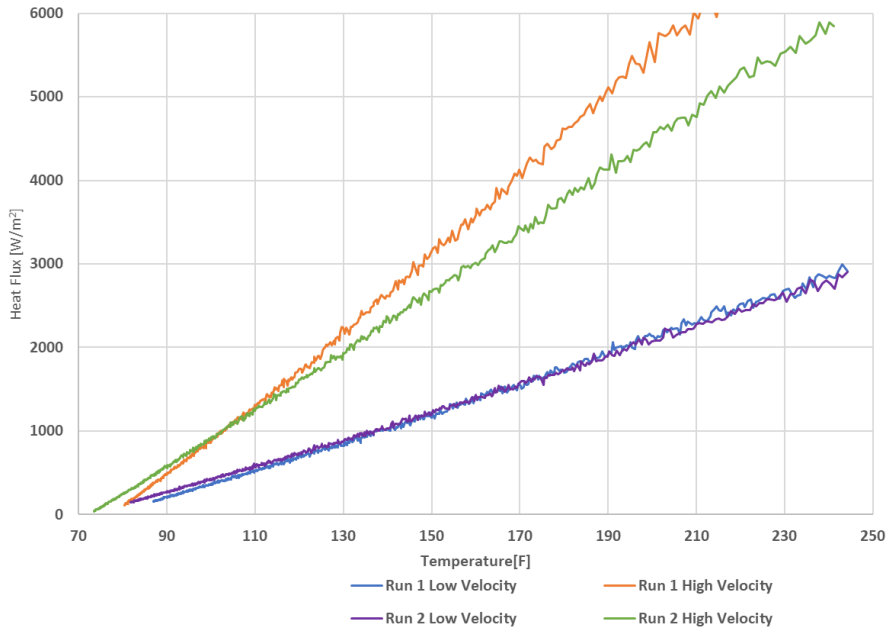


Figure 4-21 Three run test with disassembling sensors for sensor 6 (top) and sensor 4(bottom)

5 OVEN TEST RESULTS

5.1 Oven Test Setup

For oven level testing an array of 12 heat flux sensor assemblies are evenly distributed onto a cookie sheet. The 12 sensors array consists of six high emissivity black stickers which measure the radiation and convection component of heat transfer, and six low emissivity gold stickers which measure the convection component of heat transfer. The sensors are positioned in an alternating pattern as shown in Figure 5-1. The cookie sheet is modified to have locating features that are used to locate each sensor and prevent rotation and sensor misalignment during handling. The array of twelve sensors is used to measure the spatial variation in heat flux across the zone that the heat flux sensors are placed in.

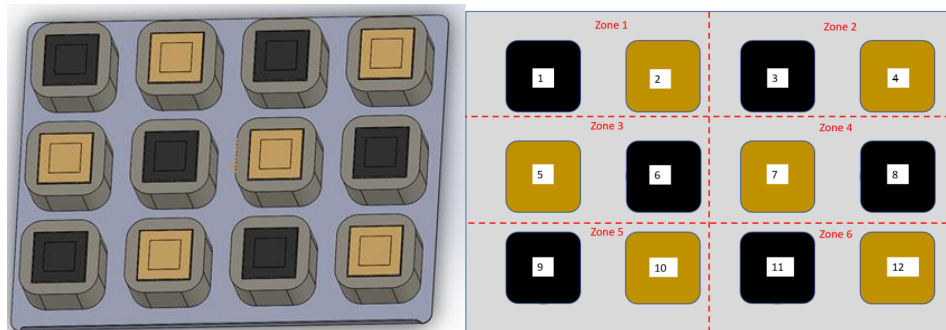


Figure 5-1 Twelve heat flux sensor array CAD assembly (left) and assembly layout and numbering (right)

For testing of the heat flux sensor assembly, the same PTS9000 GE Appliances oven from the sensor development tests is used. The heating element power ratings for the hidden bake, broil, broil assist, and convection element are 3850, 3300, 1000 and 2400 Watts, respectively. Surface temperatures and air temperatures of the unit are recorded during each run. Three distinct modes are used for evaluating the heat flux sensor assembly. Traditional bake (TB), Convection bake multi-rack (CBM), and Air Fry (AF). These three modes were run at an oven setpoint of 375°F. Traditional bake offers a set up that is radiation dominant with no convection fan used. CBM offers a test that is similar to traditional bake in heater element cycling but incorporates the convection fan and convection element to increase air flow. Air fry decreases use of the bake heating element and incorporates the convection element and fan more than the other modes. For each test the input power is monitored to determine when specific elements are cycling on or off. Surface and air temperatures of the unit is monitored to determine resulting thermal environment from unit operation.



Figure 5-2 Instrumented PTS9000 electric wall oven unit used in study

For all three cooking modes a single roller rack is used and placed in the third rack position from the bottom of the oven. The 12-sensor array is positioned in the center of this roller rack as shown in Figure 5-3.



Figure 5-3 Heat flux sensor array in oven

At the start of the test the oven was set to the desired mode and setpoint and allowed to reach a steady state center oven temperature by running 30 minutes (with preheat time included). At the 30-minute mark the oven door was opened and sensors placed in the center of oven. The door is held open for 20 seconds. Once door is closed data collection was started and run for 10 minutes. After 10 minutes the test is stopped, the sensor array is removed from the oven, and the oven is allowed to cool down. A summary for the cooking modes used can be seen in Table 8. An overview of the duty cycles and power ratings for each element can be seen below in Table 9. An overview of the test cycle can be seen in Figure 5-4.

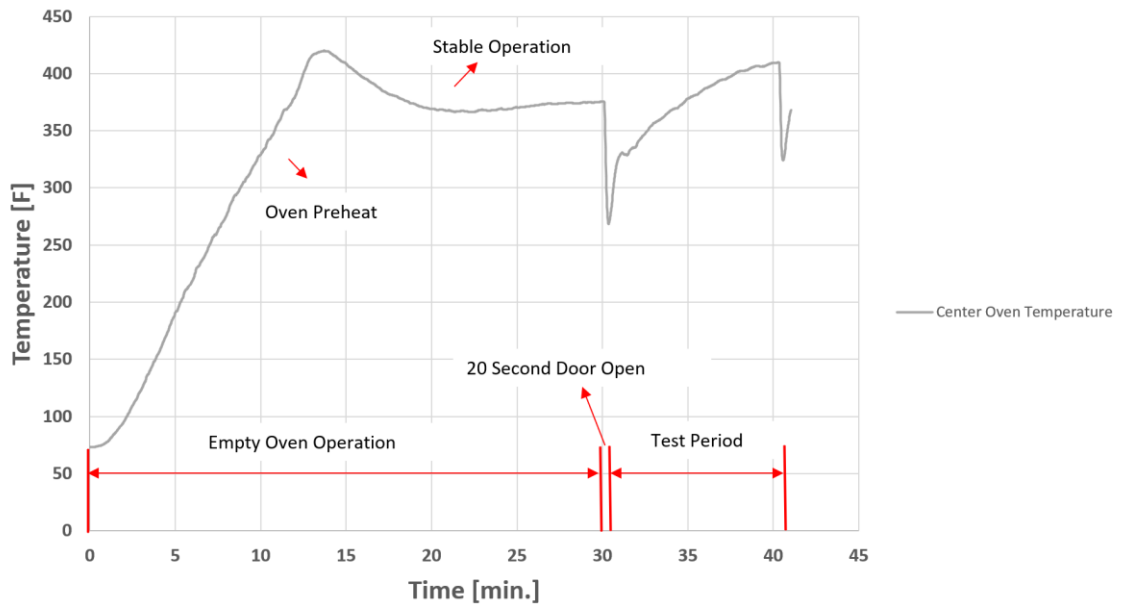


Figure 5-4 Overview of oven operation in traditional bake. Test period is where heat flux sensors are collecting data.

Table 8 Overview of oven modes used in testing

Cooking Mode	Heating Elements Used	Convection Fan Status
Traditional Bake	Hidden Bake, Broil, Broil Assist	Off
Convection Bake Multi-Rack	Hidden Bake, Convection	Horizontal Flow
Air Fry	Broil, Broil Assist Convection	Horizontal/ Perpendicular Flow

Table 9 Overview of heating elements used in study and duty cycles/ Although the modes are controlled to a similar center oven temperature it is achieved in different ways.

<u>Traditional Bake</u>	Wattage	Duty Cycle%
Hidden Bake	2850	20.71%
Broil	3300	4.89%
Broil Assist	1000	4.89%
Convection Element	2400	0.00%
<u>Convection Bake Multi-Rack</u>	Wattage	Duty Cycle%
Hidden Bake	2850	5.22%
Broil	3300	0.00%
Broil Assist	1000	0.00%
Convection Element	2400	26.89%
<u>Air Fry</u>	Wattage	Duty Cycle%
Hidden Bake	2850	0.00%
Broil	3300	11.44%
Broil Assist	1000	11.44%
Convection Element	2400	15.11%



Figure 5-5 The air flow in the oven is controlled by a by the convection fan. Clockwise rotation leads to horizontal air flow configuration(left) and counterclockwise rotation leads to perpendicular air flow configuration (right).

5.2 Oven Level Calibration

Sensor level calibration revealed that there are assembly factors that play a role in the heat flux reading such as thermal grease application, heat flux sensor installation, low and high emissivity sticker application, and inherit sensor bias. To account for the contributions of all the sources that can play a role in sensor assembly variation a test matrix was developed to calibrate each sensor assembly. The assembly level tests were run with an assembly that consist of the FHF04 heat flux sensors, the insulation base, the FHF04 sticker, and two aluminum masses embedded with J-type thermocouples. Once assembled sensors were not disassembled for the rest of the study. This sensor assembly can be seen again in Figure 5-6.

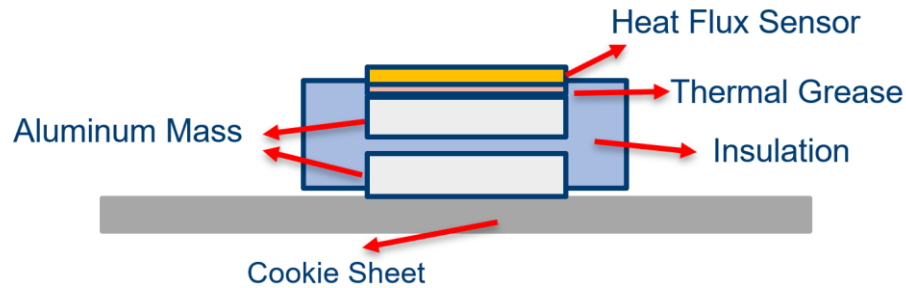


Figure 5-6 Schematic of final heat flux assembly used in oven level testing

In order to calibrate in environments representative of sensor use the same PTS9000 GE Appliances electric wall oven was used as in the other development tests. The traditional bake was used for the calibration tests. The approach for this calibration was to have all 12 sensors attached to a cooking sheet and use the 12 sensor cookie sheet assembly to run six different traditional bake tests. These tests are all for the exact same duration and follow the same procedure. The oven is allowed to run for 30 minutes to reach steady state, once the oven is in steady state operation the door is open for 20 seconds to allow the sensor assembly to be placed in the center of the oven. The test was run for 10 minutes to collect heat flux and corresponding oven temperature data.

Within these six different tests the sensor positions were shuffled to account for the spatial variation in heat flux within the wall oven. There are six different positions for black stickered sensors and six different positions for gold stickered sensors. Each sensor was rotated through each position and the average of all six sensors was used as a reference value for what the true

reading should be for that position. The test matrix for this series of tests can be seen in Table 10, where each value in the table corresponds to a run number.

Table 10 Test run order matrix for assembly calibration testing

Black Sticker Matrix						
	Position 1	Position 3	Position 6	Position 8	Position 9	Position 11
Sensor 1	1	2	3	4	5	6
Sensor 3	2	1	6	5	3	4
Sensor 6	3	6	1	2	4	5
Sensor 8	4	5	2	1	6	3
Sensor 9	5	3	4	6	1	2
Sensor 11	6	4	5	3	2	1
Gold Sticker Matrix						
	Position 2	Position 4	Position 5	Position 7	Position 10	Position 12
Sensor 2	1	2	3	4	5	6
Sensor 4	2	1	6	5	3	4
Sensor 5	3	6	1	2	4	5
Sensor 7	4	5	2	1	6	3
Sensor 10	5	3	4	6	1	2
Sensor 12	6	4	5	3	2	1

In the sensor sub-assembly calibration tests the average reading of each sensor was taken for the duration of the test. This average was used as the comparative value across positions and sensors and can be seen below in Table 11. A heat map is used to show areas of high heat flux and low heat flux within each column of the results matrix. Separate heat maps are applied to the sensor average as well as the position average to determine which positions in the oven experience higher levels of heat flux as well as to the sensors to determine which sensors are biased to read higher levels of heat flux. For the black sensors, sensor 8 had the lowest heat flux average compared to the other sensors and

position 9 had the lowest positional average. For the gold sensors, sensor 12 had the lowest sensor average and position 5 had the lowest positional average. For the black sensor averages there was a range of 182 W/m² and a positional range of 210 W/m². For the gold sensor averages there was a range of 42 W/m² and a positional range of 67 W/m². These ranges are for sensor averages for duration of the tests, and the range of individual data points would be greater. The positional range for this test series represents the measured spatial variation in heat flux in the oven since it is a function of the reading of each sensor. The sensors range represents the difference between the sensors across each run since it is a product of the sensor reading as a function of each position. The positional range demonstrates that there is spatial dependence to heat flux readings since the bias of each sensor is embedded into the average

Table 11 Heat flux average results for oven calibration testing. A heat map is applied to each individual column to show the variation in magnitude of each sensor at a position. The averages have their own heat map to show which positions and sensors measure high or low.

Black Sticker Matrix Heat Flux [W/m ²]							
	Position 1	Position 3	Position 6	Position 8	Position 9	Position 11	Sensor Average
Sensor 1	2672	2765	2789	2663	2577	2783	2708
Sensor 3	2571	2724	2818	2727	2634	2569	2674
Sensor 6	2549	2785	2805	2643	2496	2660	2656
Sensor 8	2656	2471	2676	2675	2501	2413	2565
Sensor 9	2741	2770	2769	2872	2675	2643	2745
Sensor 11	2654	2838	2843	2821	2557	2770	2747
Position Average	2640	2726	2783	2733	2573	2640	

Gold Sticker Matrix Heat Flux [W/m ²]							
	Position 2	Position 4	Position 5	Position 7	Position 10	Position 12	Sensor Average
Sensor 2	730	748	688	721	739	746	729
Sensor 4	731	747	726	756	779	752	749
Sensor 5	748	770	706	712	739	768	740
Sensor 7	718	777	662	753	720	717	724
Sensor 10	738	776	684	710	734	703	724
Sensor 12	675	733	683	764	678	707	706
Position Average	723	758	692	736	731	732	

In order to adjust each sensor to its known bias from the position average the ratio of each sensor is taken in respect to the position average. Ideally the average ratio for each sensor would be used as a correction factor. The correction matrix developed can be seen in Table 12. A ratio greater than one indicates that the sensor is biased to read higher than the positional average. A ratio less than one indicates that the sensor reads lower. The correction factors developed in this section were not used for the remainder of the study due to the variation in unit from run to run. This variation in oven unit operations lead to thermal environments that are slightly different across each run influencing the effective correction coefficient. The average temperature for each surface in the oven as well as the average input power into the unit can be seen in Table 13. Due to this variation in thermal environment during the assembly level calibration tests the correction factors developed are not used for the rest of this study, instead the average of all 6 black stickers and all 6 gold stickers are used.

Corrected Black Sticker Matrix Heat Flux [W/m ²]								
Correction Factor		Position 1	Position 3	Position 6	Position 8	Position 9	Position 11	Sensor Average
0.990	Sensor 1	2646	2739	2762	2637	2552	2756	2682
1.003	Sensor 3	2580	2733	2828	2736	2643	2577	2683
1.010	Sensor 6	2575	2813	2833	2670	2521	2687	2683
1.044	Sensor 8	2771	2578	2792	2792	2610	2519	2677
0.977	Sensor 9	2677	2705	2704	2805	2612	2581	2681
0.976	Sensor 11	2591	2770	2775	2753	2496	2704	2682
	Position Average	2640	2723	2783	2732	2572	2637	

Corrected Gold Sticker Matrix Heat Flux [W/m ²]								
Correction Factor		Position 2	Position 4	Position 5	Position 7	Position 10	Position 12	Sensor Average
1.000	Sensor 2	730	747	688	721	739	746	729
0.972	Sensor 4	711	727	706	735	757	731	728
0.984	Sensor 5	736	758	694	701	727	756	729
1.007	Sensor 7	723	782	666	758	724	721	729
1.006	Sensor 10	743	781	689	715	739	707	729
1.031	Sensor 12	695	755	703	788	699	728	728
	Position Average	723	758	691	736	731	732	

Table 12 Correction coefficient matrix for assembly calibration testing. The initial heat flux matrices are multiplied by the correction coefficients to obtain these corrected heat flux values

Run #	Unit Power [kW]	Center Oven Temperature [F]	Right Wall Average [F]	Left Wall Average [F]	Bottom Wall Average [F]	Top Wall Average [F]	Back Wall Average [F]	Door Average [F]
1	1.93	345	342	336	499.2	364	353	196
2	1.81	336	343	336	490.7	364	353	202
3	1.80	354	346	337	504.4	366	356	199
4	1.77	357	350	346	497.1	371	360	212
5	1.76	363	352	349	503.1	372	361	210
6	1.86	365	353	348	508.1	372	360	212
Average	1.82	353	348	342	500	368	357	205
Range	0.17	29	10	12	17	8	8	16

Table 13 Unit power and temperature averages during assembly calibration testing

5.3 Oven Test Results

For each oven mode in this study three tests were run where thermal data of the unit and heat flux data of the sensor is collected and compared. For each run heat flux is determined for an individual sensor by using the voltage reading and the sensors rated sensitivity. Additional calculations are performed for each sensor to determine the energy storage rate of the top and bottom mass. With these components for each individual sensor a conduction heat transfer rate is determined as well as convection and radiation depending on the sensors sticker.

5.3.1 Traditional Bake Results

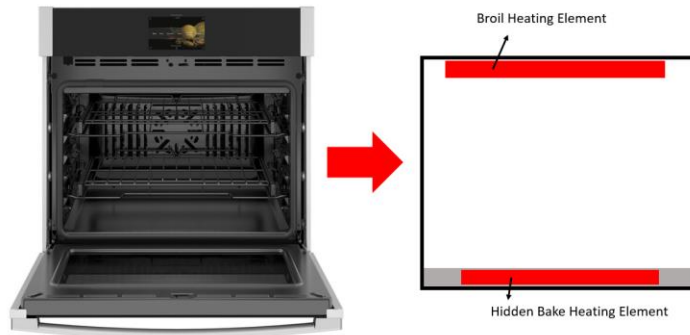


Figure 5-7 Electric wall oven heating elements used in traditional bake

The heating elements used in traditional bake during normal operations are shown in Figure 5-7. The heat flux over time plot for run one of traditional bake can be seen below in Figure 5-8. This shows the change of heat flux over time for a traditional bake run. In Figure 5-9 a summary of unit temperatures can be seen. It is worth noting that these averages represent an average for the

duration of the test that are also a product of a 5-sensor array on each surface as shown in Figure 5-2. For the thermocouple array on the door one thermocouple is taped onto the glass using aluminum tape as opposed to being welded onto the oven wall like other surface thermocouple.

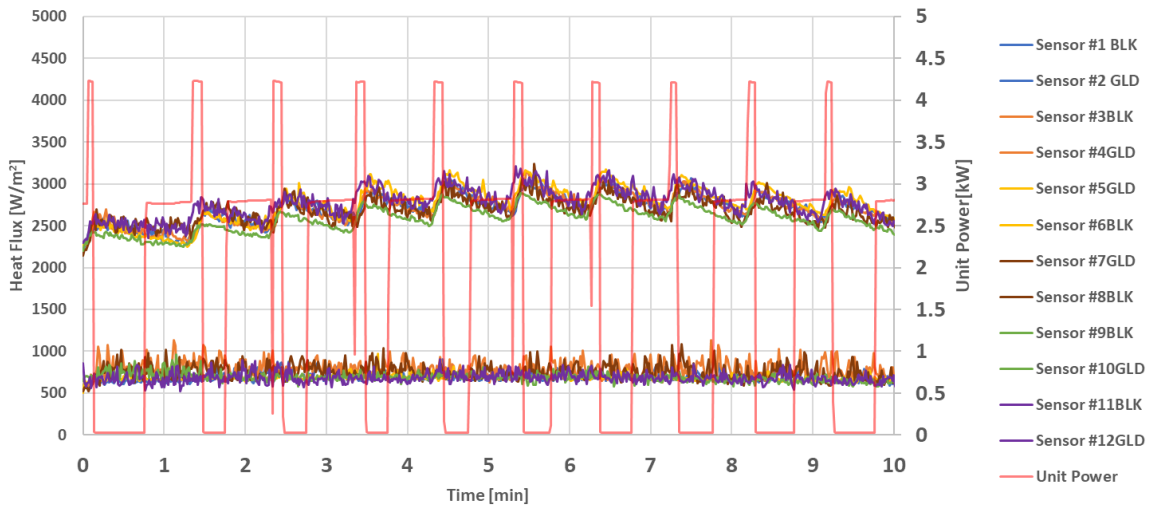


Figure 5-8 Heat flux measure for Traditional Bake, run 1 heat flux over time

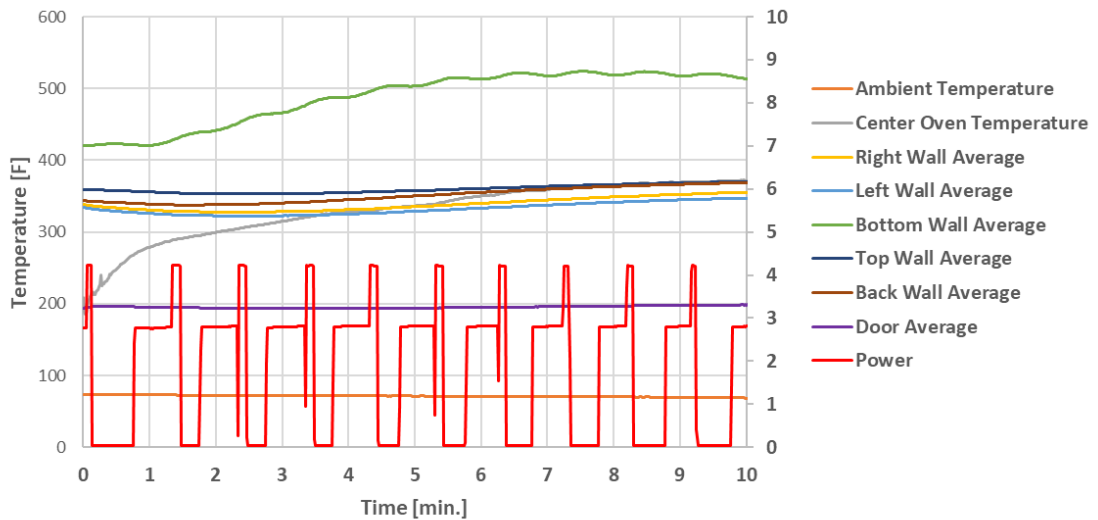


Figure 5-9 Interior oven temperatures measured for Traditional Bake, run 1

In the secondary axis the unit input power is plotted. Input power can be used to determine when heating elements are cycling on and off. For the traditional bake cycle the unit first turns on the hidden bake element for a variable duration then follows up with the broil and broil assist element then cycles off. This can be seen as the unit goes from no power consumption to 2.85 kilowatts to 4.3 kilowatts. For unit temperatures in this mode the surface temperatures remain stable while air temperatures decrease due to the door opening leading to more power demand initially. The exception for surface temperature stability of the unit is the bottom surface which is the main absorber of energy from the hidden bake element.

The black sensors, which represent the radiation and convection heat transfer values, increase each time the broil element is turned on. The response to the broil element cycling is not as prominent in the gold sticker. To compare sensors in the same run amongst each other the average reading of each sensor was taken for the ten-minute duration of the test. The averages can be seen in Figure 5-10. The supplier given uncertainty for each sensor is displayed as an error bar.

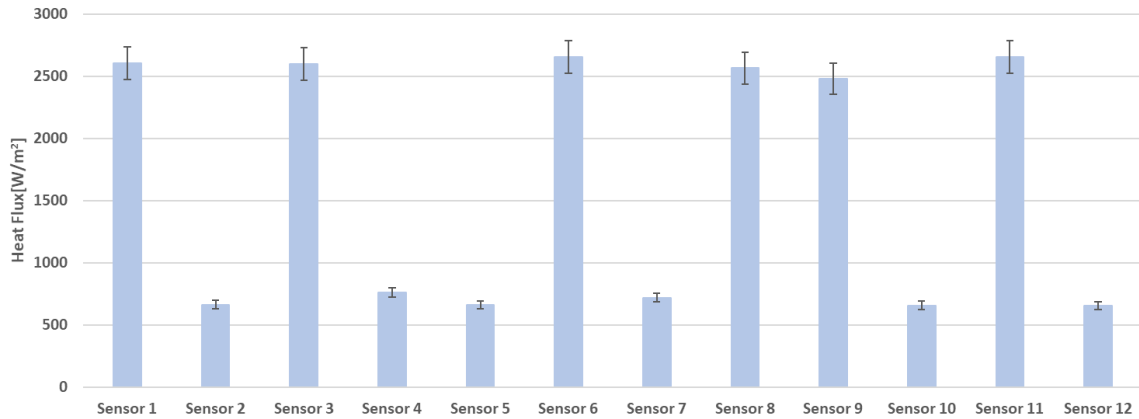


Figure 5-10 Average heat flux measured for a 10 minute test in Traditional Bake, run 1

Using data from Figure 5-10 the average for all black and gold stickered sensors was calculated to be 2700 and 715 W/m², respectively. On average the difference between the black sensor and the gold sensor is 1990 W/m². This value can be used to represent the average radiation heat flux in this run.

Traditional bake is designed to be a radiation dominated mode so the measured difference between black and gold stickered sensors is in agreement with the oven mode design.

Temperature of both top and bottom masses for each sensor was collected and can be seen in Figure 5-11 and Figure 5-12 respectively. The difference in slope and magnitude of each mass temperature profile is a result of different input energy to each mass or due to the slight variation in actual mass. This difference in input energy is assumed to be a result of spatial variation in heat flux in the oven and differences in sensor assembly. Once source of

variation is the thermal mass for each sensor. A summary of the mass of each aluminum and the plastic base can be seen in Appendix IV.

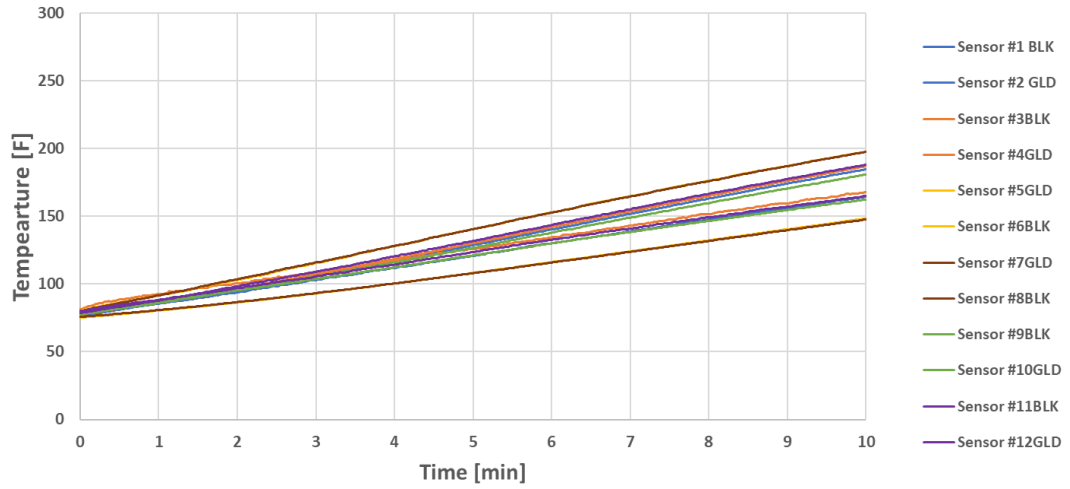


Figure 5-11 Temperature over time for the top mass for top mass in Traditional Bake, run 1

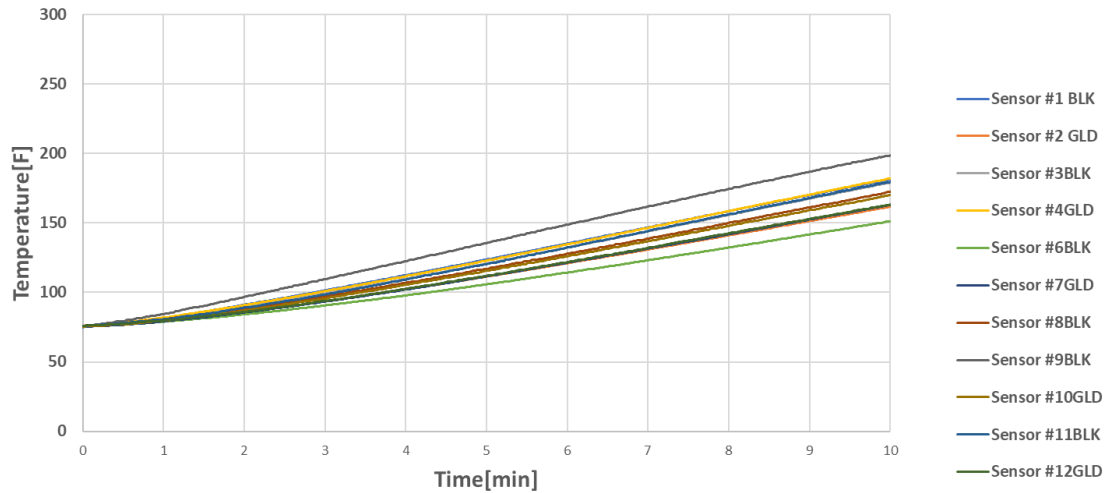


Figure 5-12 Temperature over time for bottom mass in Traditional Bake, run 1

To allow radiative heat flux to be isolated from convective heat flux a zonal approach is taken to separate sections of the heat flux sensor array. This zonal approach pairs a black and gold sensor assembly for each zone. Sensor 1 is positioned to the back left of the oven.

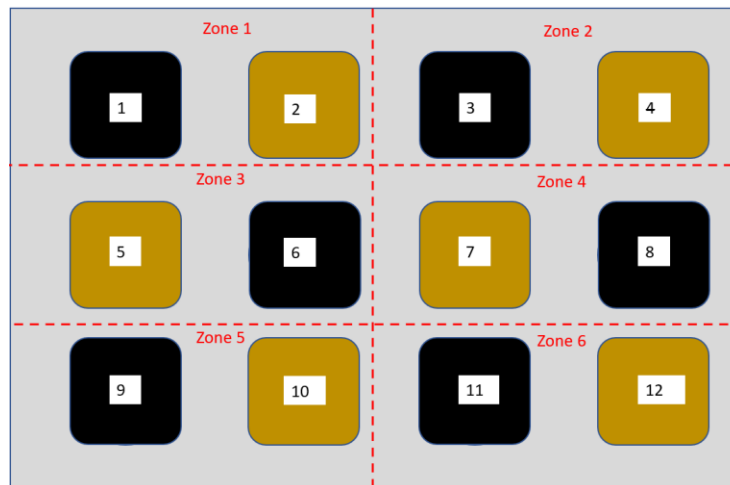


Figure 5-13 Diagram of sensor zone configuration

With this zonal approach, convection and radiation heat flux measurements are taken from the heat flux sensors in the zone. The conduction measurement is obtained from the average of both bottom aluminum masses in each zone. The result of this zonal approach can be seen in Figure 5-14. For the conduction element of heat flux the instantaneous power storage term from Equation 2 is divided by the area of the mass that contacts the cookie sheet. A

breakdown of the three modes of heat flux can be seen below in

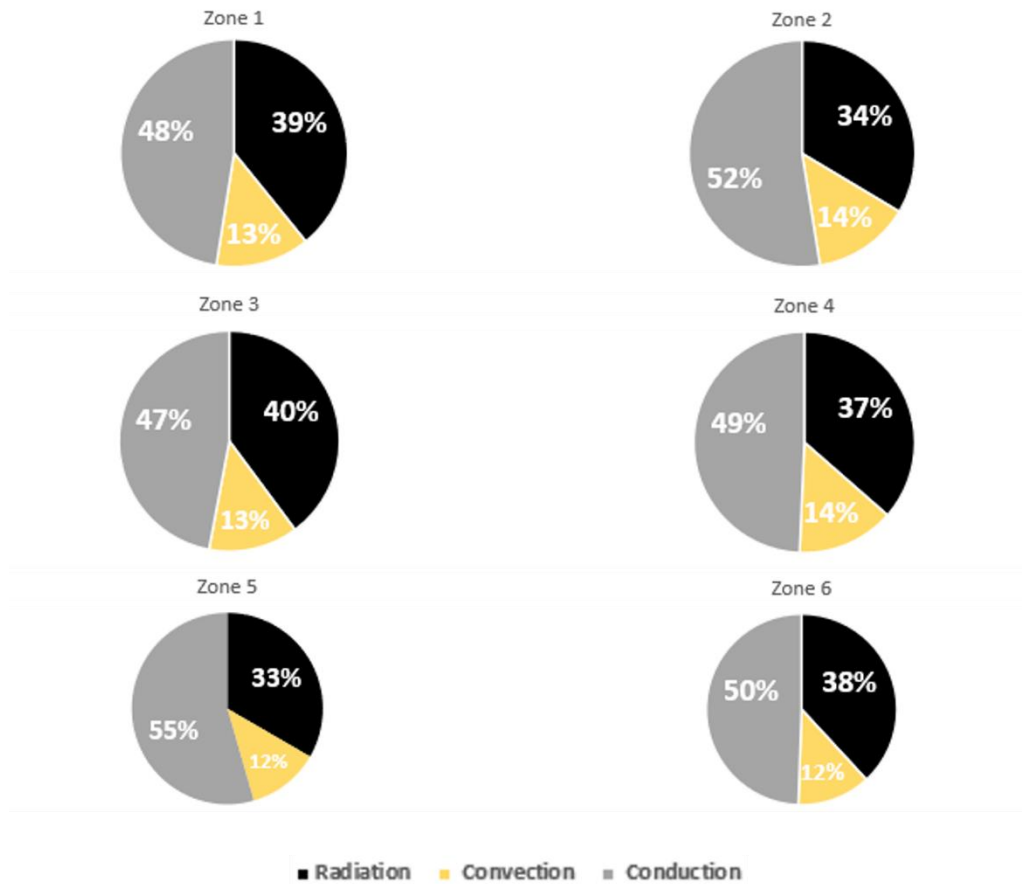


Figure 5-15. The conduction represents conduction between the aluminum cookie sheet and bottom mass where the aluminum cookie sheet serves as an absorber of energy with significant surface area.

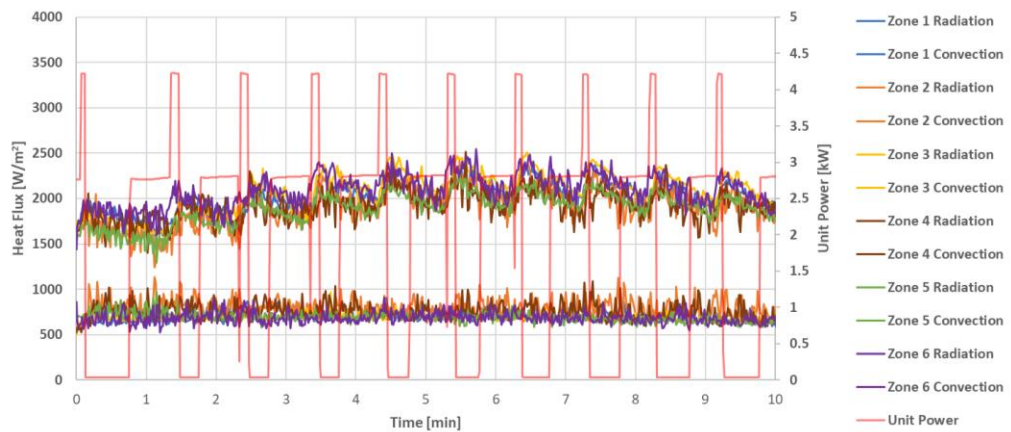


Figure 5-14 Zonal heat flux vs time for TB run 1

The top mass flux calculated for sensor 1 using the aluminum mass is plotted along with the heat flux sensor reading of sensor 1 in Figure 5-16. The difference between the two over time can be seen in this figure. Both heat flux sensor and top mass flux exhibit the same behavior throughout the cycle, but the top mass doesn't respond to the broil element as rapidly as the mounted heat flux sensor. The top mass flux reading is generally higher than the heat flux reading. This difference in heat flux magnitude is attributed to the heat leak from the insulation onto the aluminum mass. For the remainder of this study the heat flux sensor reading is analyzed as opposed to the top mass flux.

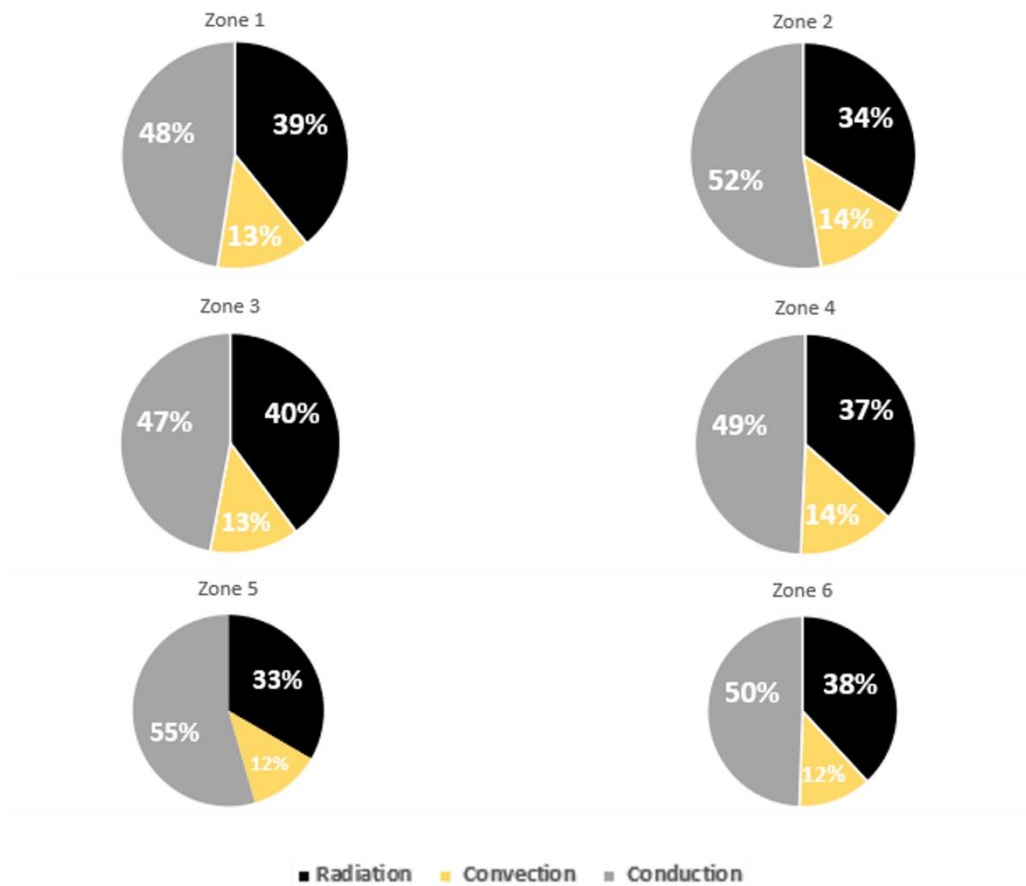


Figure 5-15 Fraction of each mode of heat transfer by zone for Traditional Bake, run 1

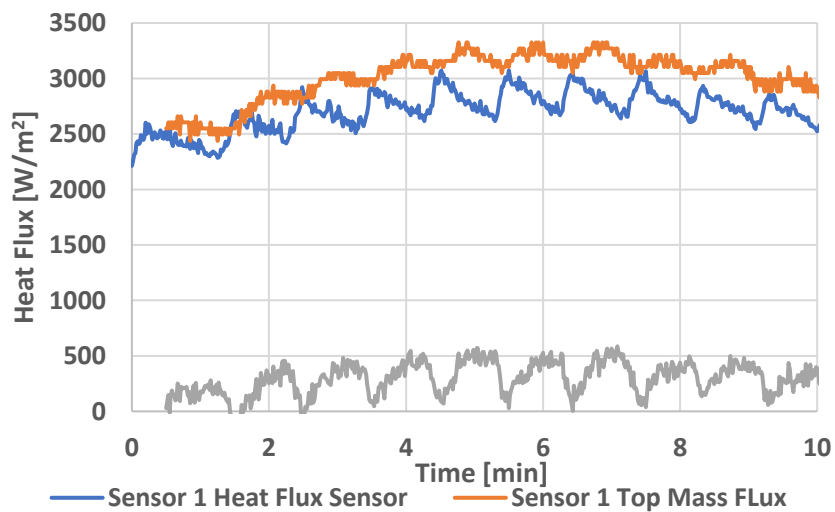


Figure 5-16 Heat flux sensor measurement versus top mass flux calculated using aluminum mass temperature

5.3.2 Convection Bake Multi-Rack Results

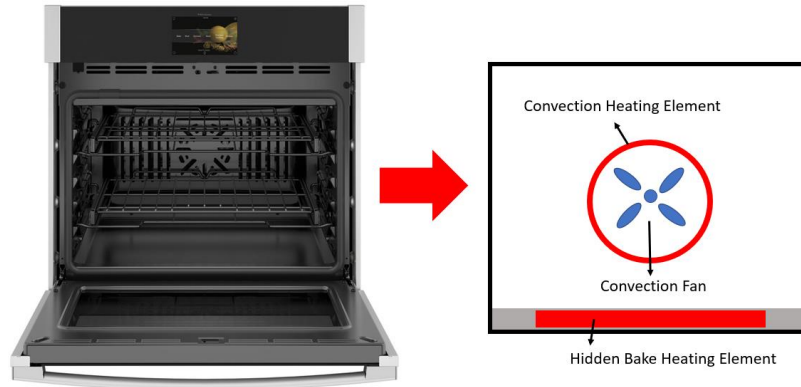


Figure 5-17 Heating elements and fans used in Convection Bake Multi

The heating elements and fan used in Convection Bake Multi (CBM) are shown in Figure 5-17. A plot for heat flux versus time in CBM is shown below in Figure 5-18. A plot of oven temperatures during this CBM run can be seen in Figure 5-19. The center oven temperature for CBM varies with the cycling of the convection fan and element. For CBM the convection rotates in a way that leads to predominantly horizontal flow across the heat flux sensor assembly.

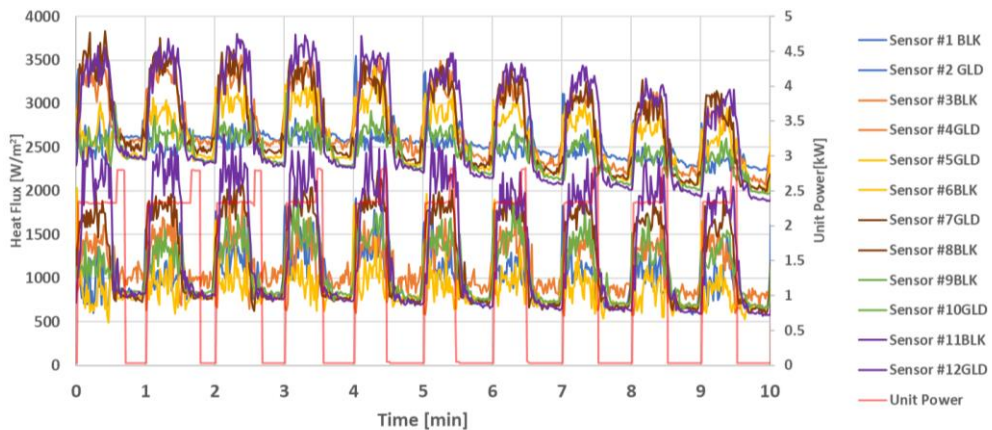


Figure 5-18 Heat flux measured for Convection Bake Multi, run 1

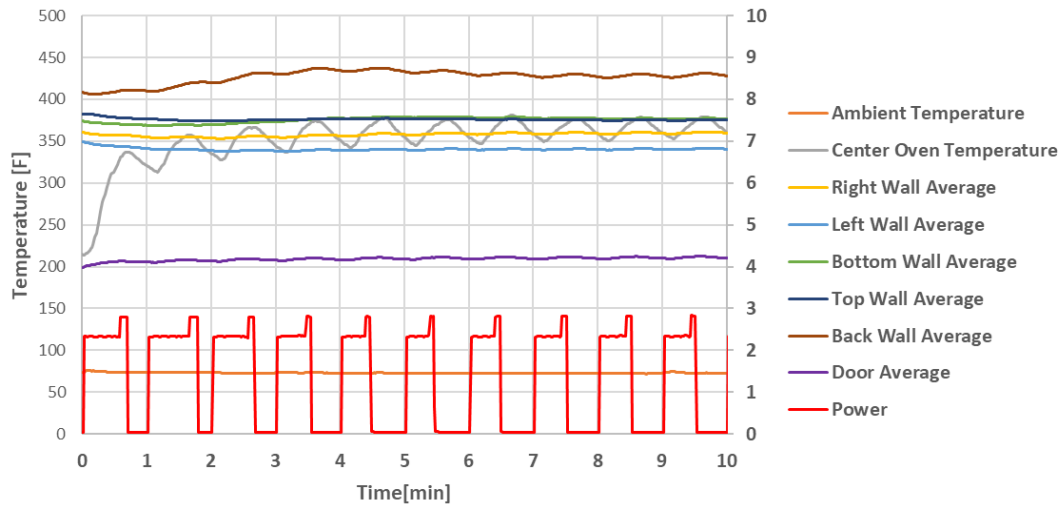


Figure 5-19 Interior oven temperatures measured for Convection Bake Multi, run 1

For CBM testing the heat flux sensors showed a high responsiveness in both black and gold stickered sensors. This is expected due to the design intent for CBM. The peaks of each cycle for high heat flux measurement corresponds with the cycling of the convection element and the convection fan. The average reading for the black sensors and the average reading for the gold sensors are 2500 W/m^2 and 1052 W/m^2 , respectively. Taking the zonal approach and subtracting the gold sensor from the black sticker yields a radiative heat flux of 1490 W/m^2 . Considering that CBM replaced the use of the broil element with the use of the convection fan and convection element it is in line with design intent for this mode. The zonal approach to breaking down convection and radiation is applied to the CBM results and shown in Figure 5-20. The behavior

for both radiation and convection are identical for CBM where they oscillate in unison with the convection fan and element.

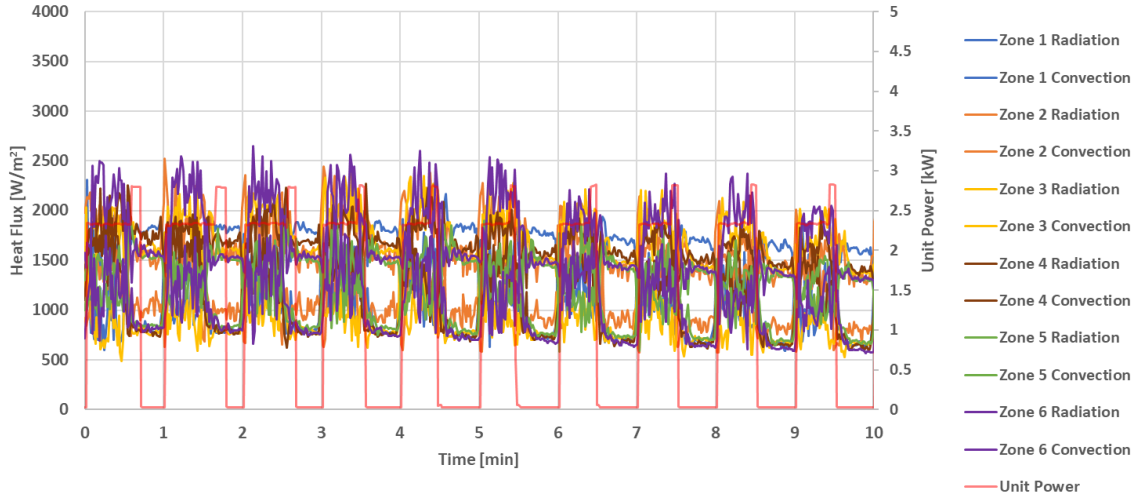


Figure 5-20 CBM Zonal heat flux over time

The average reading for each sensor during the duration of the test can be seen in Figure 5-21. The zonal break down using the average readings of each sensor can be seen in Figure 5-22 and the ratios can be seen in Figure 5-23. For CBM the dominant mode of heat transfer to each sensor is conduction.

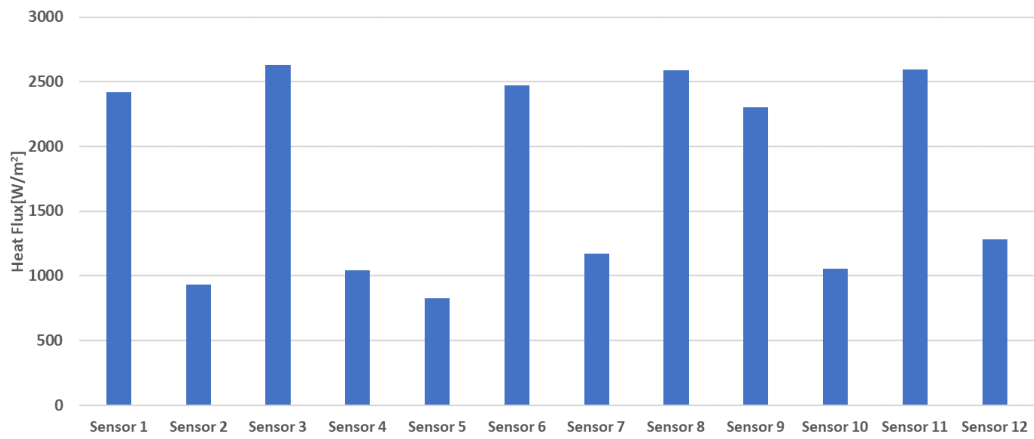


Figure 5-21 Average heat flux sensor reading Convection Bake Multi, run 1

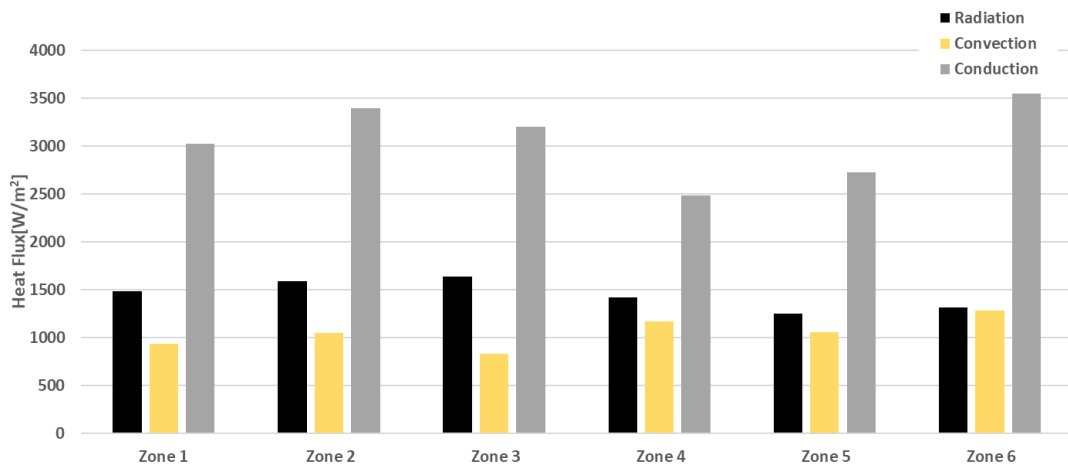


Figure 5-22 Heat flux for each mode of heat transfer for Convection Bake Multi, run 1

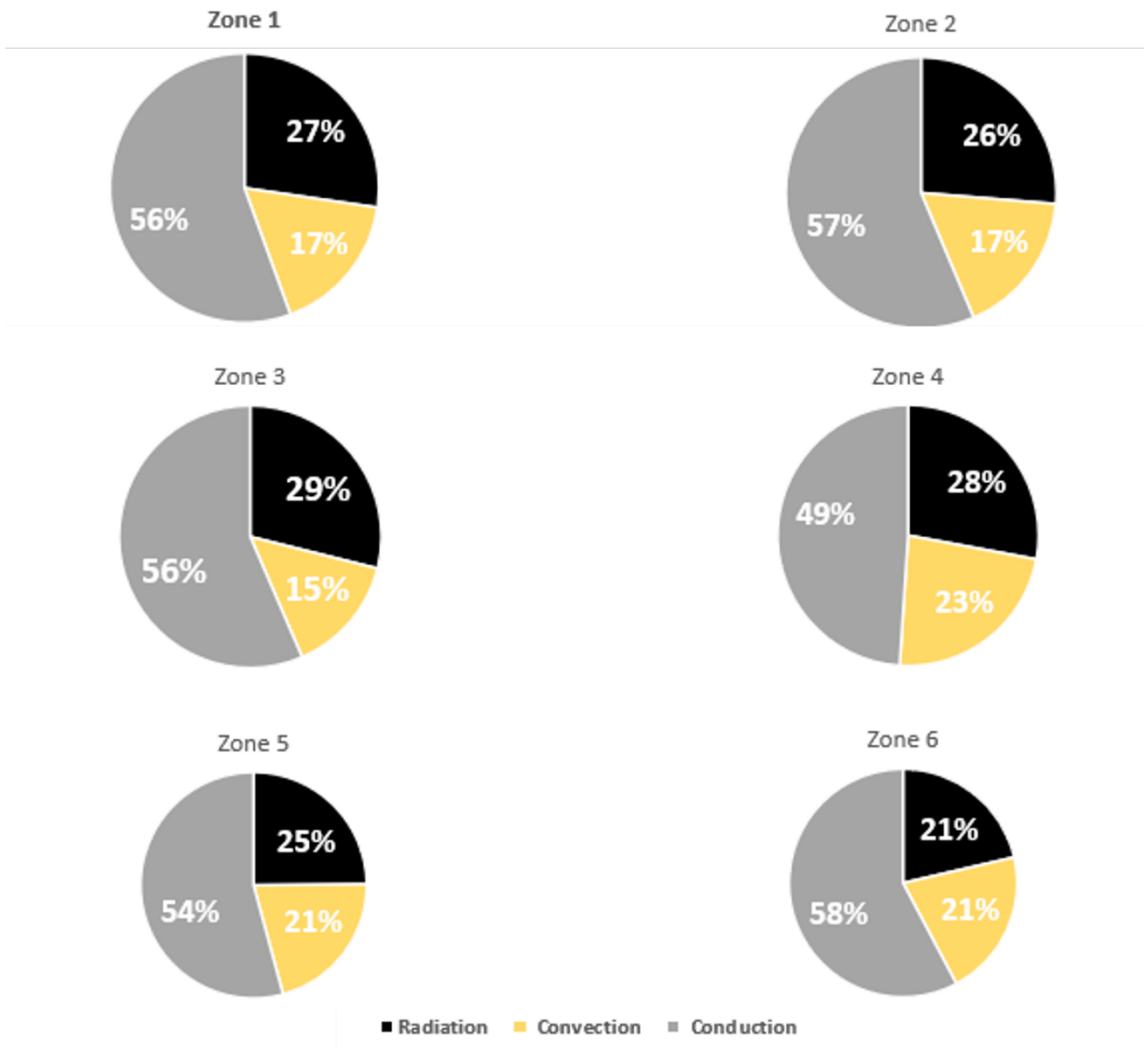


Figure 5-23 Fraction of each mode of heat transfer by zone for Convection Bake Multi, run 1

5.3.3 Air Fry Results

The heating elements and fan used in air fry mode are shown in Figure 5-24. The hidden bake element is not used, and the main heating elements are the broil and convection heating elements. Air fry mode has the highest broil compared to the other modes, and the broil element is the highest-powered element. The heating elements cycle less frequently during this mode and are on for extended periods of time. The cycle time and frequency for air fry mode isn't

as consistent as the other modes studied due to the difference in oven algorithm for this mode. In this mode the convection fan is on for 93% of the test time compared to 50% of the time in CBM. This increased convection fan on time makes up for the decreased heating element times by improving air circulation in the oven. A graph of heat flux versus time for air fry mode is shown in Figure 5-25.

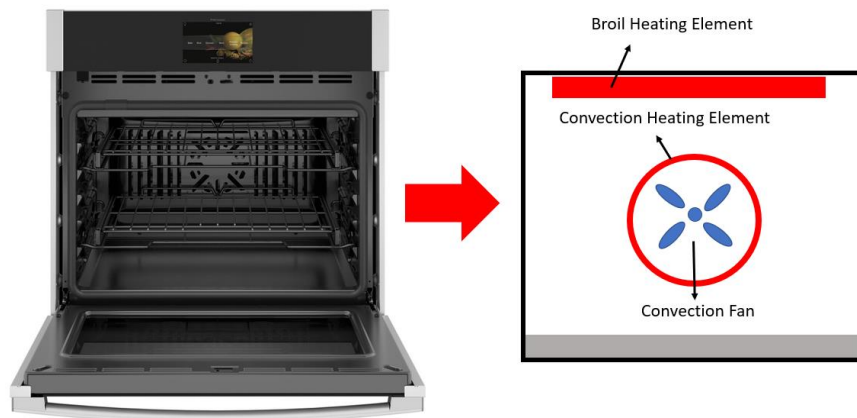


Figure 5-24 Air fry elements used

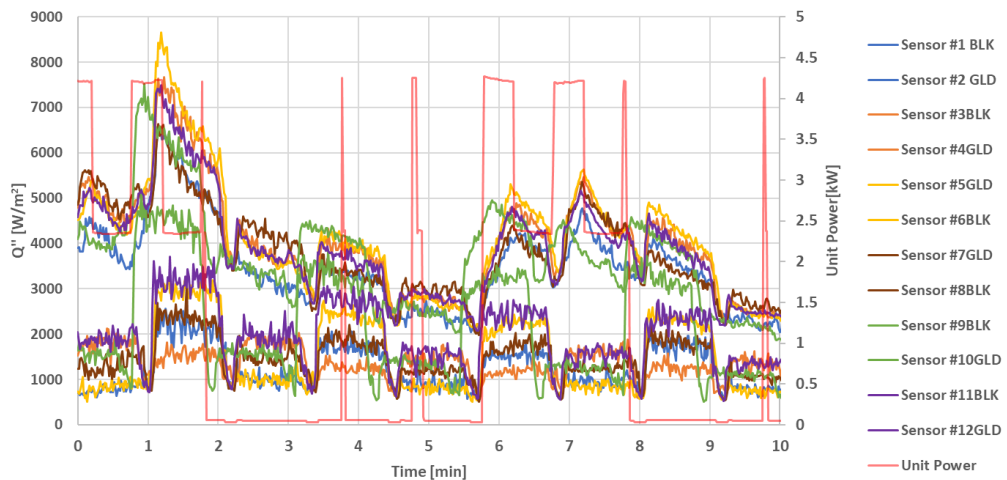


Figure 5-25AF run 1 heat flux vs time

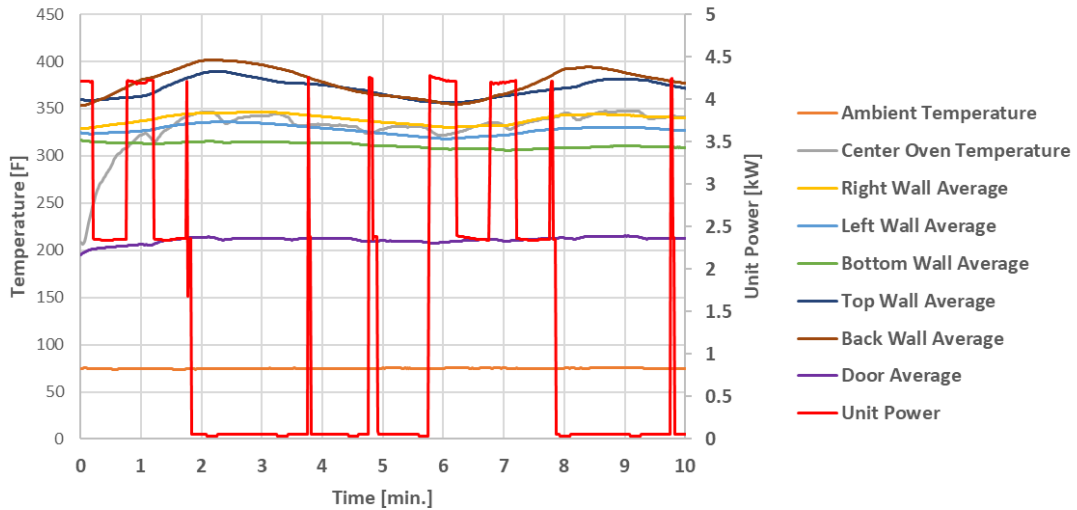


Figure 5-26 Air fry run 1 unit temperature and power over time

In air fry mode the magnitude of heat flux observed is far greater than the other modes. The convection fan operates in two different configurations for this mode. The convection fan is on near continuously cycling on for 60 seconds then cycling off for 10 and switching fan direction. The convection fan rotates clockwise which leads to a horizontal flow condition for the sensors and counterclockwise which leads to perpendicular flow condition for the sensors as shown in Figure 5-5. Initially the greatest magnitude of heat flux is collected for both black and gold sensor since at the start of the test both convection element and convection fan are on. As the test continues there is a drop in heat flux reading every time the convection element cycles off and an increase in heat flux every time it cycles on. An increase in heat flux is measured when the convection element and fan cycles on together at minute 6 and 7 of this test, although it isn't as high in magnitude as the start of test.

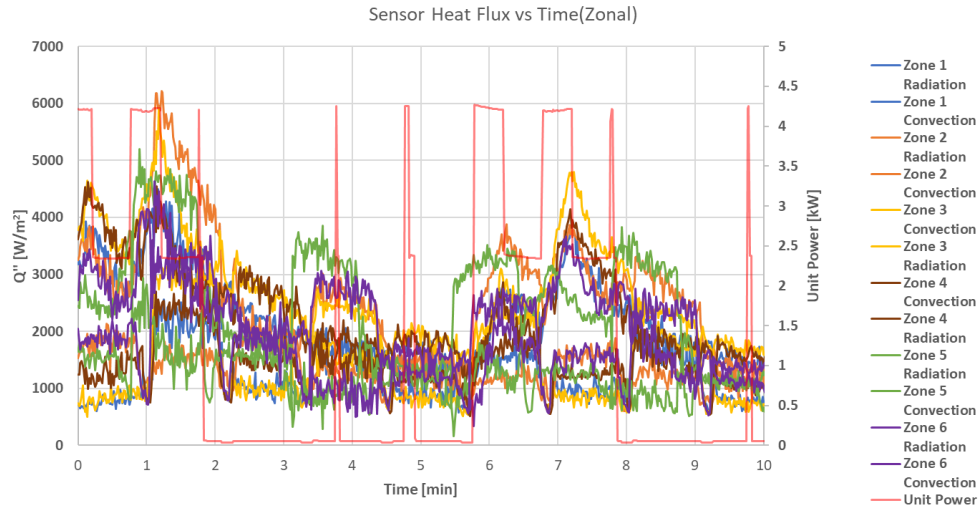


Figure 5-27 AF run 1 Zonal Approach

The average heat flux readings for the air fry run are shown in Figure 5-28. The zonal approach shown in Figure 5-13 is used to break down the components of heat transfer to determine the radiative and convective heat flux. For this run the average black and gold sticker reading is 3412 W/m^2 and 1463 W/m^2 . Using the difference between the average black stickered sensor and gold stickered sensor the radiative heat flux reading for this test is 1949 W/m^2 .

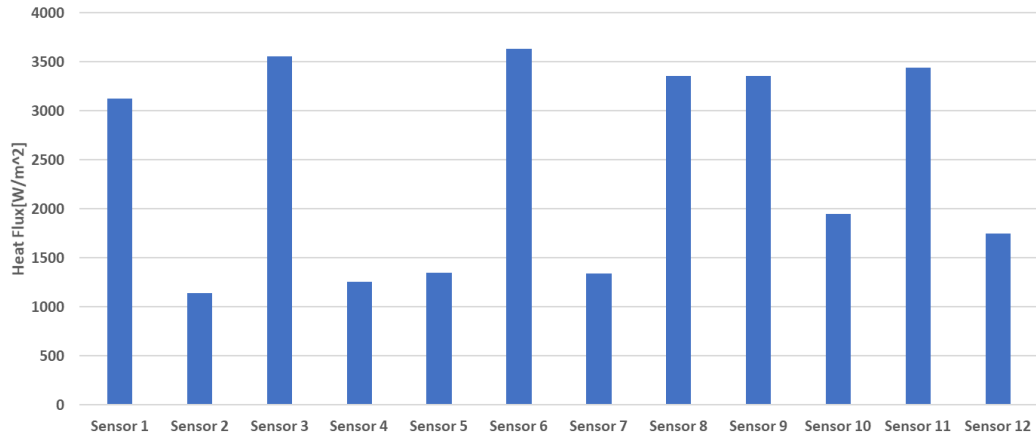


Figure 5-28 Air fry run 1 heat flux averages over 10-minute test

A break down for the different modes of heat transfer and the corresponding ratios can be seen for each zone in Figure 5-29 and Figure 5-30.

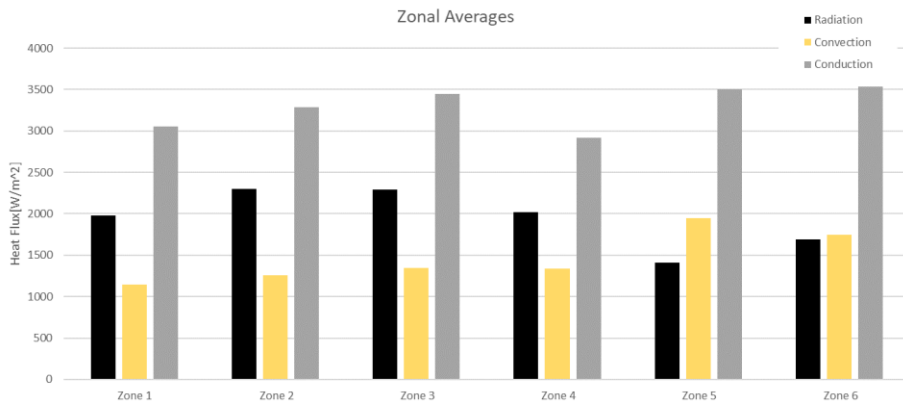


Figure 5-29 Air fry run 1 zonal heat flux breakdown

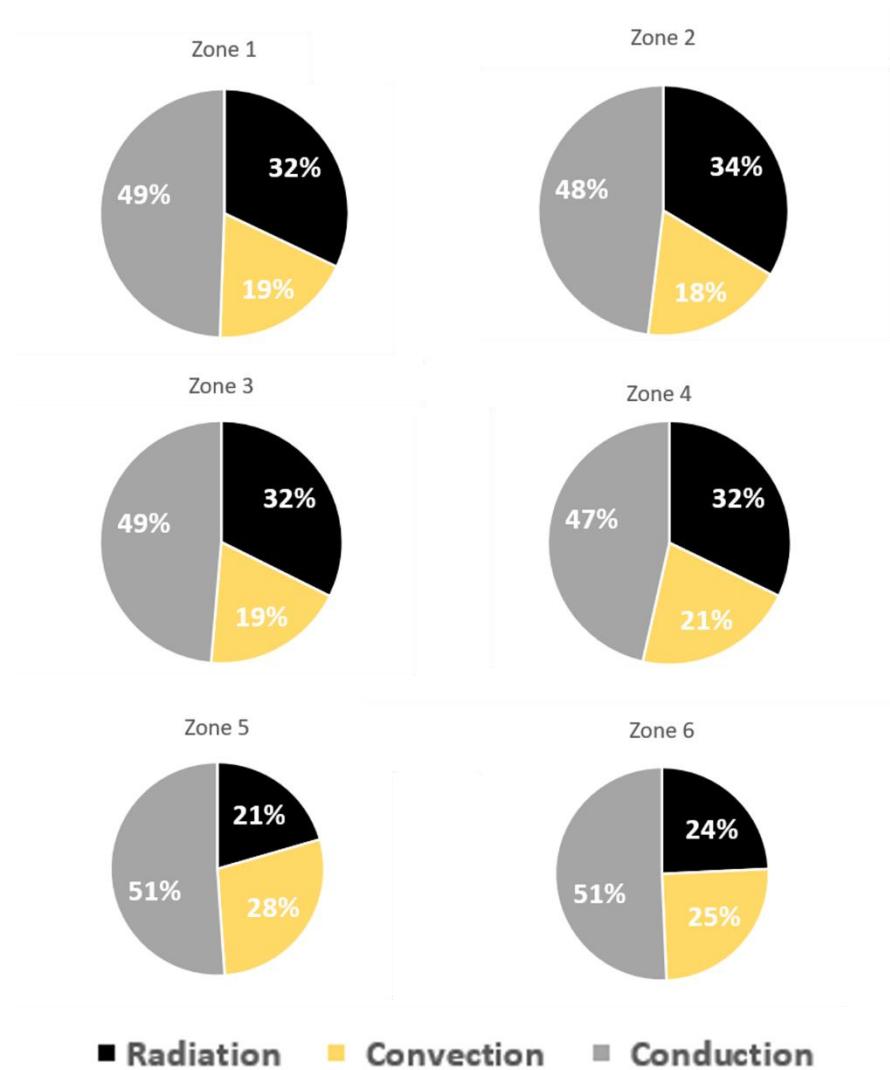


Figure 5-30 Air fry run 1 energy ratios

For air fry, conduction provided the highest heat transfer rate followed by radiation for many of the zones. Air fry is designed to be a convection dominated but using this sensor array considerable radiation is measured. The high levels of radiation can be explained by the extended use of the broil element in this mode.

5.4 Repeatability

5.4.1 Traditional Bake Repeatability

Following initial runs in each cooking mode, repeatability was investigated by running two additional tests in each mode. The exact same procedure was followed in every test but there are slight differences in thermal environment that can be seen in the unit summary in Table 14. These varying test conditions are a product of the dynamic response of the wall oven which considers the center oven temperature to determine when heating elements should be turned on. This variability in element cycling leads to different input energies. The difference between the maximum and minimum average power for the duration of the tests for traditional bake is 0.12 kW which equates to a difference of 70,577 Joules for the duration of the tests. The graphical summary for heat flux during traditional bake can be seen in Figure 5-31 accompanied by a tabular summary in Table 14.

For comparison the average of black and gold stickers is taken as a comparison basis across the three different runs. The average is considered to account for the spatial variation in heat flux measurement for each sensor by considering the average heat flux across the entire run. The coefficient of variation (COV) which represents the ratio of standard deviation to the mean is used to compare the variation between black and gold stickered sensors. For the black and gold stickered sensors there is a relatively low coefficient of variation with a maximum of 3.4% observed in sensor 12. This low coefficient of variation,

given similar thermal environments, demonstrate that the heat flux sensors in each position measure consistently.

For the conduction heat flux measured for each run there is an average range of 630 W/m² with a maximum coefficient of variation of 22%. This large range of conduction heat flux readings may be a result of varying contact resistances between sensor and aluminum cooking sheet. The only pressure that each sensor is subject to is that of its own weight which is consistent but different bottom mass surface finishes as well as different aluminum cooking sheet sections may lead to varying contact resistances. The contact pressure each sensor is able to apply can also be influenced by the wiring of the thermocouples and the tension differences due to the assembly set up.

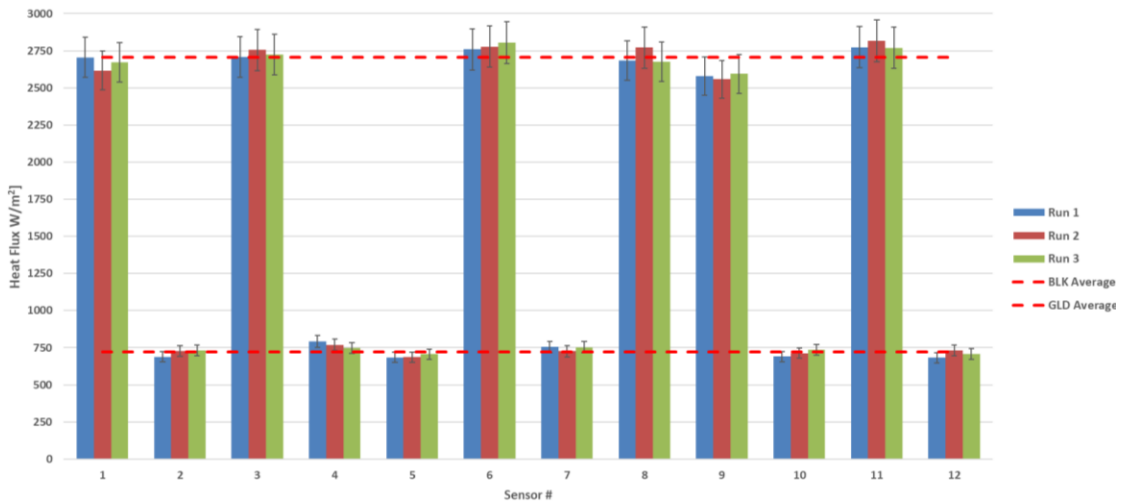


Figure 5-31 Comparison of average heat flux measured for three runs of Traditional Bake

Table 14 Traditional bake unit summary

Run #	Power [kW]	Center Oven Temperature [F]	Right Wall Average [F]	Left Wall Average [F]	Bottom Wall Average [F]	Top Wall Average [F]	Back Wall Average [F]	Door Average [F]
1	1.81	329	338	331	488	360	351	195
2	1.86	324	337	328	490	359	350	191
3	1.93	345	342	336	499	364	353	196

Table 15 Traditional Bake 3-run heat flux summary for heat flux sensor and bottom mass

		Run 1	Run 2	Run 3	Average	StDev	COV [%]
Sensor Heat Flux [W/m²]	Sensor 1	2706	2617	2672	2665	45	1.7%
	Sensor 2	688	729	730	716	24	3.4%
	Sensor 3	2708	2755	2724	2729	24	0.9%
	Sensor 4	793	770	747	770	23	3.0%
	Sensor 5	684	686	706	692	12	1.7%
	Sensor 6	2759	2778	2805	2781	23	0.8%
	Sensor 7	754	726	753	744	16	2.2%
	Sensor 8	2684	2770	2675	2710	53	1.9%
	Sensor 9	2579	2558	2594	2577	18	0.7%
	Sensor 10	690	713	734	712	22	3.1%
	Sensor 11	2773	2817	2770	2787	26	0.9%
	Sensor 12	682	730	707	706	24	3.4%

		Run 1	Run 2	Run 3	Average	StDev	COV [%]
Bottom Flux [W/m²]	Sensor 1	3044	2993	3009	3015	26	0.9%
	Sensor 2	2448	2501	2659	2536	110	4.3%
	Sensor 3	2971	3021	3104	3032	67	2.2%
	Sensor 4	3023	3082	3253	3119	119	3.8%
	Sensor 5	2744	2716	2978	2813	143	5.1%
	Sensor 6	2156	3327	3196	2893	642	22.2%
	Sensor 7	2501	2569	2712	2594	108	4.2%
	Sensor 8	2722	2929	3144	2932	211	7.2%
	Sensor 9	3458	3772	3202	3477	285	8.2%
	Sensor 10	2714	2791	2228	2577	305	11.8%
	Sensor 11	2939	3219	3340	3166	206	6.5%
	Sensor 12	2485	2536	2781	2601	158	6.1%

Table 16 Average heat flux for all gold or black sensors and for all three Traditional Bake runs

	Sensor Heat Flux (W/m ²)	Bottom Mass Heat Flux (W/m ²)
6 Sensor Black Average	2708	3086
6 Sensor Gold Average	723	2707

The results that will be used for comparison to different modes can be seen in Table 16. Reporting the 6-sensor average for black and gold sticker removes some of the biases that each sensor might have by incorporating it into the average measurement for each run. This data neglects the spatial effects across the cookie sheet and focuses on the average performance of the oven for that run. The conduction measured for black and gold sensors seemed to have distinct averages with similar ranges across that average. This is an indicator that the radiation received due to the different emissivity of sensors may play a role in the energy storage of the bottom mass.

5.4.2 Convection Bake Multi Repeatability

A similar three-run study was completed for CBM. The graphical summary for the 3-run study can be seen below in Figure 5-32. A summary of unit temperatures for the three runs and the heat flux averages can be seen in

Table 17 and

Table 19 respectively. For CBM the power as well as center oven temperature and surfaces temperatures are reasonably consistent. The maximum coefficient of variation observed in the study was 6.6% with sensor 12.

Sensor 12 had the highest coefficient of variation for both TB and CBM. Although higher than in traditional bake, convection bake multi has similar performance from run-to-run showing that in the same environment each sensor behaves similarly. The same trends for conduction flux observed in TB are observed in CBM.

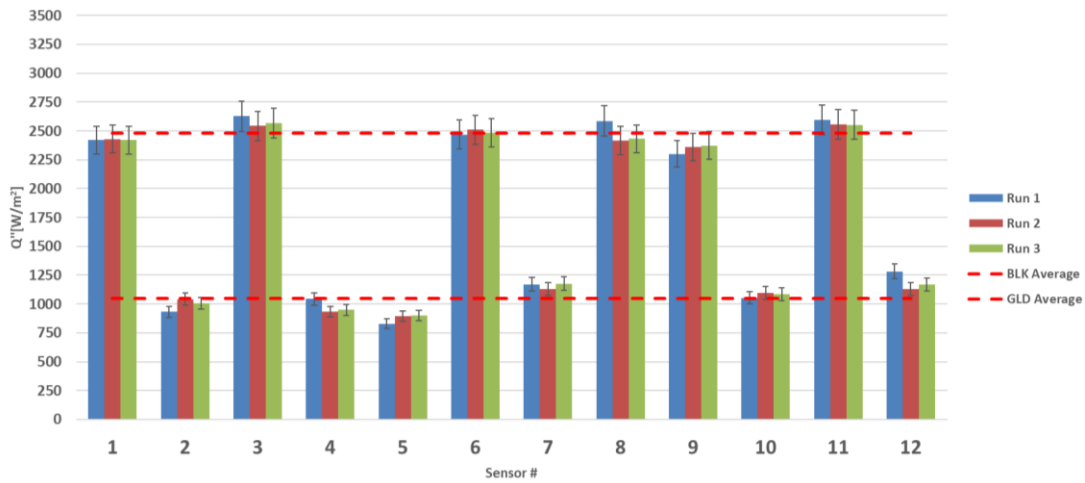


Figure 5-32 Convection bake multi 3 run averages

Table 17 Convection bake multi three run unit summary

Run #	Power [kW]	Center Oven Temperature [F]	Right Wall Average [F]	Left Wall Average [F]	Bottom Wall Average [F]	Top Wall Average [F]	Back Wall Average [F]	Door Average [F]
1	1.34	352	358	340	375	376	427	209
2	1.35	347	355	340	371	375	425	209
3	1.35	341	354	339	369	376	425	209

Table 18 Convection bake multi black and gold Sensor 3-run Average summary

	Sensor Heat Flux	Bottom Mass Heat Flux
6 Sensor black Average	2481	3235
6 Sensor gold Average	1046	2958

Table 19 Convection bake multi 3-run heat flux summary for heat flux sensor and bottom mass

		Run 1	Run 2	Run 3	Average	StDev	COV [%]
Sensor Heat Flux	Sensor 1	2420	2431	2420	2423	6	0.3%
	Sensor 2	933	1042	1004	993	55	5.6%
	Sensor 3	2629	2544	2568	2580	44	1.7%
	Sensor 4	1045	934	950	976	60	6.1%
	Sensor 5	830	894	900	875	39	4.4%
	Sensor 6	2470	2511	2482	2488	21	0.9%
	Sensor 7	1171	1130	1177	1160	25	2.2%
	Sensor 8	2587	2417	2431	2479	94	3.8%
	Sensor 9	2301	2362	2374	2345	39	1.7%
	Sensor 10	1052	1096	1085	1078	23	2.1%
	Sensor 11	2595	2555	2553	2568	24	0.9%
	Sensor 12	1282	1129	1169	1193	79	6.6%
		Run 1	Run 2	Run 3	Average	StDev	COV [%]
Bottom Flux	Sensor 1	3380	3344	3302	3342	39	1.2%
	Sensor 2	3025	2924	2878	2942	75	2.6%
	Sensor 3	3561	3453	3264	3426	150	4.4%
	Sensor 4	3231	3092	3123	3148	73	2.3%
	Sensor 5	3243	3009	3040	3098	127	4.1%
	Sensor 6	3167	2896	3020	3028	136	4.5%
	Sensor 7	2207	2440	2462	2369	141	6.0%
	Sensor 8	2758	3372	3018	3049	308	10.1%
	Sensor 9	3323	3116	3095	3178	126	4.0%
	Sensor 10	2121	3114	3119	2785	575	20.7%
	Sensor 11	3439	3408	3309	3385	68	2.0%
	Sensor 12	3658	3139	3413	3403	259	7.6%

5.4.3 Air Fry Repeatability

A three-run study was conducted in the AF mode. Compared to the other modes there was a bigger difference between the input energy for the three runs. Between run 1 and 3, there was an average power range of 0.42 kW equating to 252,000 joules (

Table 20). Despite that, the unit temperatures are consistent for the duration of the tests across the three tests. The graphical summary for the 3-run average and the tabular heat flux summary can be seen in Figure 5-33 and Table 22, respectively. For AF mode the sensor with the largest coefficient of variation is sensor 10 with a coefficient 6.1%. The bottom flux has a smaller coefficient of variation than the other modes in AF but still shows the behavior of black bottom masses measuring higher flux than gold bottom masses.

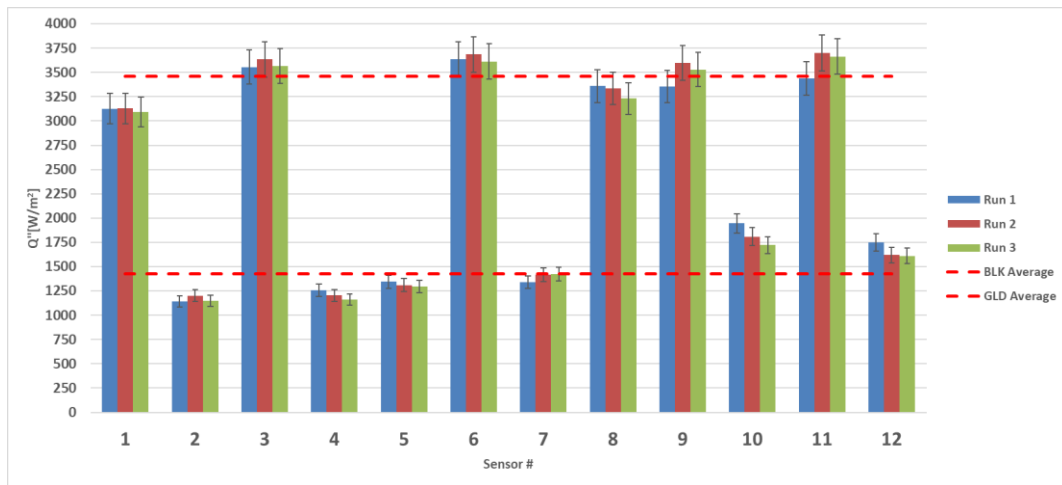


Figure 5-33 Average heat flux measured three runs of the Air Fry cooking mode

Table 20 Air fry three run unit summary

Run #	Power [kW]	Center Oven Temperature [F]	Right Wall Average [F]	Left Wall Average [F]	Bottom Wall Average [F]	Top Wall Average [F]	Back Wall Average [F]	Door Average [F]
1	1.34	330	339	327	311.1	371	378	211
2	1.57	339	341	332	314.5	373	380	211
3	1.76	338	338	325	309.2	369	375	205

Table 21 Air fry black and gold sensor 3-run average summary

	Sensor Heat Flux [W/m ²]	Bottom Mass Heat Flux [W/m ²]
6 Sensor black Average	3458	3445
6 Sensor gold Average	1428	3221

Table 22 Air fry 3-run heat flux summary for heat flux sensor and bottom mass

		Run 1	Run 2	Run 3	Average	StDev	COV [%]
Sensor Heat Flux	Sensor 1	3126	3129	3092	3116	21	0.7%
	Sensor 2	1144	1202	1149	1165	32	2.8%
	Sensor 3	3555	3633	3564	3584	43	1.2%
	Sensor 4	1256	1205	1158	1206	49	4.0%
	Sensor 5	1345	1310	1297	1317	25	1.9%
	Sensor 6	3636	3684	3612	3644	37	1.0%
	Sensor 7	1340	1414	1421	1392	45	3.2%
	Sensor 8	3359	3337	3231	3309	68	2.1%
	Sensor 9	3354	3597	3529	3493	125	3.6%
	Sensor 10	1945	1809	1723	1826	112	6.1%
	Sensor 11	3440	3698	3662	3600	140	3.9%
	Sensor 12	1749	1619	1610	1659	78	4.7%
		Run 1	Run 2	Run 3	Average	StDev	COV [%]
Bottom Flux	Sensor 1	3499	3628	3463	3530	87	2.5%
	Sensor 2	3056	3167	3082	3102	58	1.9%
	Sensor 3	3494	3632	3595	3574	71	2.0%
	Sensor 4	3084	3132	3085	3100	27	0.9%
	Sensor 5	3557	3521	3476	3518	41	1.2%
	Sensor 6	3335	3395	3324	3351	38	1.1%
	Sensor 7	2632	2729	2656	2672	51	1.9%
	Sensor 8	3199	3192	3260	3217	37	1.2%
	Sensor 9	3533	3593	3576	3567	31	0.9%
	Sensor 10	3479	3496	3376	3450	65	1.9%
	Sensor 11	3467	3383	3442	3431	43	1.2%
	Sensor 12	3602	3655	3197	3485	250	7.2%

The run-to-run variation observed by the heat flux sensors are relatively low with all individual sensors measuring with coefficients of variation of less than 10 percent. Within an individual run there is considerable variation from sensor to sensor. This variation is a result of real spatial differences in heat flux as well as some of the biases that is a product of the sensor at a component level or result from assembly level differences in each sensor.

5.5 Oven mode comparison

The average heat flux for radiation, convection, and conduction is shown in Figure 5-34 across the three cooking modes. The averages represent the average of all radiation readings (six black sensors minus all six gold sensors), convection readings (average of all six gold sensors), and conduction (average of all 12 sensors conduction calculations) for all three runs in each mode. In general, the ratios of heat flux observed for each mode matched design intent for each mode. Air fry isn't the most energy intensive mode amongst the three explored, but it is amongst the most aggressive. Air fry uses near continuous duty cycles for the convection fan and incorporates the convection element and broil element to ensure that there is continuous circulation of the hot air in the oven. It corresponded with the highest radiation, convection, and radiation when compared to the other modes. Convection bake multi is the least energy intensive mode amongst the three but has comparable heat flux performance to traditional bake. Convection bake multi has a higher convection reading but lower radiation reading than traditional bake. A summary of the average heat flux of all 3 modes is shown below in

Table 23. The range for the six black and six gold heat flux sensors can be seen in Table 24. For both black and gold heat flux sensors air fry had the biggest range across the three runs.

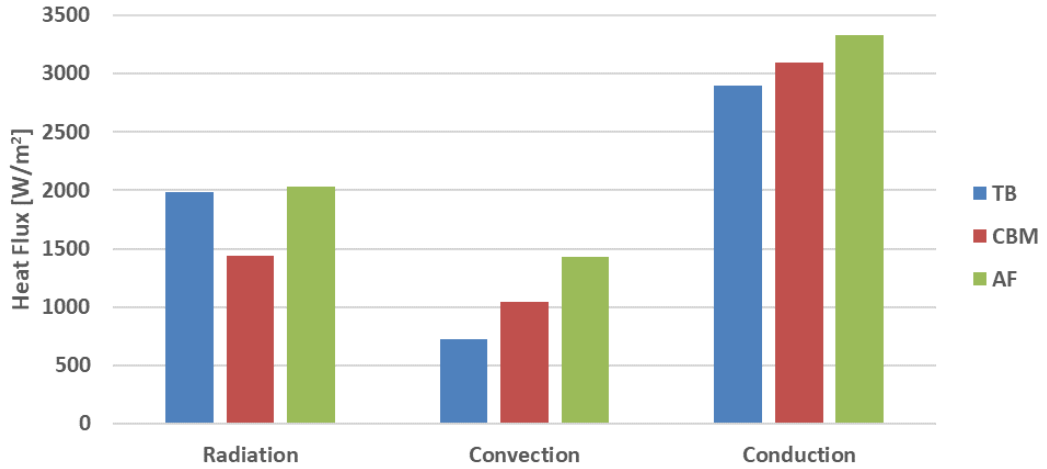


Figure 5-34 Radiation, convection, and conduction average for each cooking mode using the average of all sensors for each run across all three runs for each mode

Table 23 Traditional bake, convection bake multi, and air fry 3 run average summary

	Traditional Bake		Convection Bake Multi		Air Fry	
	Sensor Heat Flux [W/m²]	Bottom Mass Heat Flux [W/m²]	Sensor Heat Flux [W/m²]	Bottom Mass Heat Flux [W/m²]	Sensor Heat Flux [W/m²]	Bottom Mass Heat Flux [W/m²]
6 Sensor black Average	2708	3086	2481	3235	3458	3445
6 Sensor gold Average	723	2707	1046	2958	1428	3221

Table 24 Range of 6 black and 6 gold heat flux sensors across each run in the three different oven modes

	Traditional Bake		Convection Bake Multi		Air Fry	
	Black Sensor Range [W/m²]	Gold Sensor Range [W/m²]	Black Sensor Range [W/m²]	Gold Sensor Range [W/m²]	Black Sensor Range [W/m²]	Gold Sensor Range [W/m²]
Run 1	194	110	328	452	511	802
Run 2	260	83	193	237	569	607
Run 3	211	47	194	277	570	573

To compare the heat flux profiles of each oven mode an overlay of sensor 6 and sensors 7 for run 1 of each mode is shown in Figure 5-35. Each flux profile has a moving average that uses a period of 10 seconds to smoothe the high frequency responses of the sensor. Sensors 6 and 7 are selected since they are the central sensors of the 12-sensor array. These heat flux profiles demonstrate the difference in oven behavior and its impact in heat flux readings for each test.

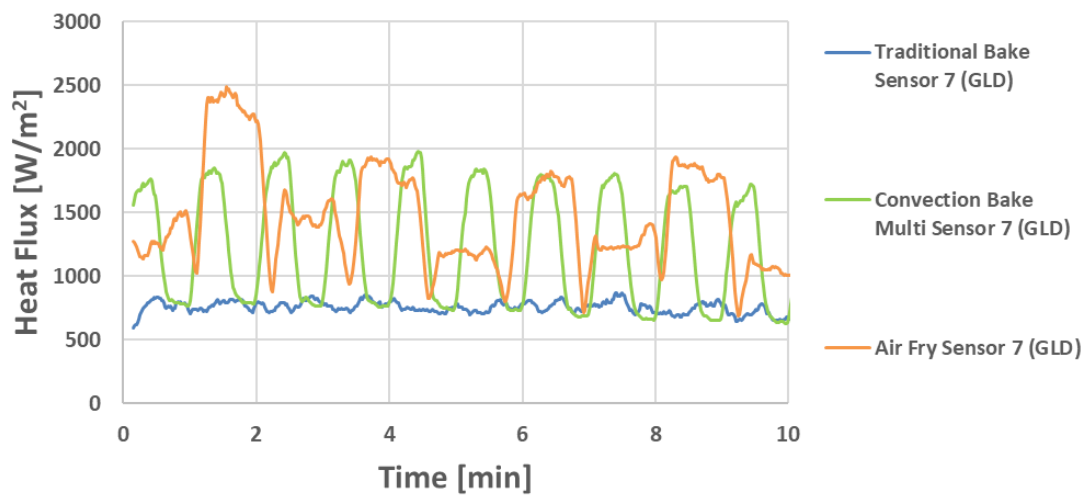
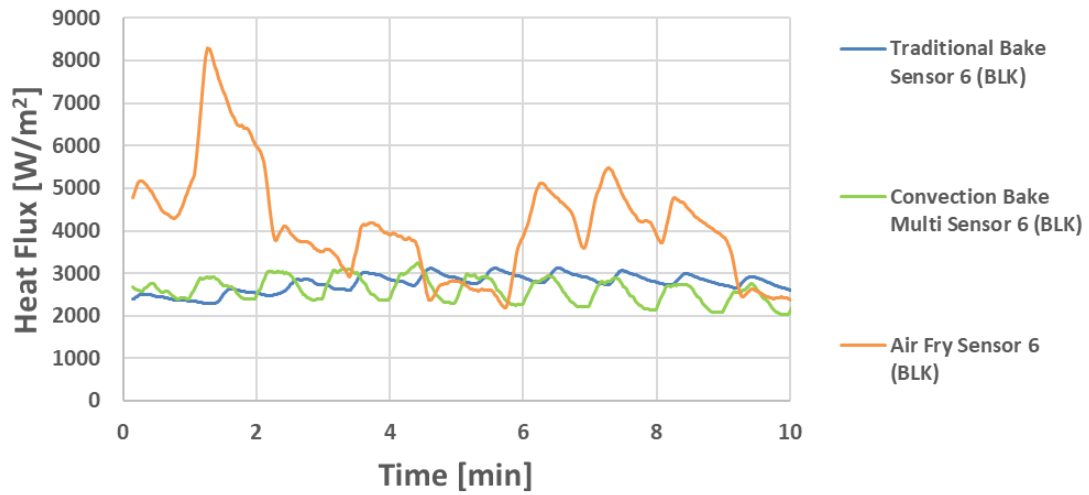


Figure 5-35 Ten second moving averages of heat flux profile for one run of the three oven modes using sensor 6 and 7.

An analysis to compare effectiveness of each mode at transferring energy into the sensor was performed. The oven operation energy uses the average power reading of the oven during operation and multiplies it by the duration of the test. This oven operation power is the sum of the heating element, convection

fan, and miscellaneous components such as controlling the oven display board. The energy storage of the sensors is derived from the total energy stored from the bottom and top mass of the sensor. This equation for run efficiency can be seen in (14) and a summary of the analysis can be seen in Table 25. This analysis neglects the energy storage term of the sensor insulation base, energy storage of the cookware used, energy loss due to initial door opening and is done on a pre-heated oven so neglects the energy it takes to get oven to temperature. From this analysis CBM and AF display similar run efficiencies with a difference of 0.9%. The energy analysis showed the effectiveness of improving energy transfer from unit to load by incorporating the convection fan to improve air circulation.

	Run 1	Run 2	Run 3	Average
TB	10.48%	10.60%	15.39%	12.16%
CBM	22.77%	22.62%	21.73%	22.37%
AF	25.17%	21.85%	19.83%	22.28%

Table 25 Comparison of run efficiency for the three cooking modes

$$Run\ Efficiency = \frac{E_{top\ mass} + E_{bottom\ mass}}{P_{oven\ average} * t} \quad (14)$$

6 DISCUSSION

6.1 Conclusions

The goal of this study was to design a heat flux sensor able to determine the convection, radiation, and conduction component of heat transfer in a residential oven. Eventually the heat flux measurements would be used to determine the role that the different modes of heat transfer play in cooking performance and used that to guide oven design.

The design criteria for this sensor included being capable of operating in an oven that is run in conditions upwards to 375°F, being able to determine spatial variations of heat flux in an oven, being able to break down the three modes of heat transfer, and finally being more cost effective than its predecessor, the RC01 heat flux sensor. The heat flux sensors succeed at three of the four design criteria. The sensors designed can operate in a 375°F oven for the duration needed to follow cooking test procedures. The sensors provide a method of breaking down the three modes of heat transfer with the use of high and low emissivity sensors and insulated masses. The sensors provide a cost reduction from \$10,982 to \$1120 when comparing the RC01 sensor that is equipped with a low and high emissivity sensor to a pair of low and high emissivity sensors.

The heat flux sensor designed in this project were capable of measuring the radiation, convection, and conduction components of heat transfer in an oven. When comparing the performance of the heat flux sensor array developed across different modes, the design intent of each mode was reflected in sensor output. The radiation dominated modes were shown to have high radiation readings and low convection readings. The convection dominated oven modes measured higher convection readings and displayed heat flux profiles that followed oven fan behavior. The conduction readings of heat flux sensor increased across the different cooking modes in this study. Increases in radiation and convection led to increases in conduction due to the cooking sheet being exposed to higher magnitudes of heat flux.

From the calibration testing performed it was determined that the heat flux sensors are effective at predicting changes in heat flux that correspond with classical heat transfer cases. The absolute heat flux measurements for each sensor seemed to be influenced by the construction of the heat flux sensor assemblies which leads to the need for assembly level corrections. When comparing an individual sensor to itself across various runs, there was minimal variation of less than 6% in similar thermal environments. When comparing sensors to each other in an individual run there was significantly more variation in heat flux readings. This variation is a product of real spatial variation in heat flux and difference in each sensor's bias. An attempt was made to correct for the bias of each sensor by running the heat flux sensor array in multiple configurations so that the spatial variation of heat flux in an oven can be measured by each sensor.

In this correction attempt there were difficulties in getting a true correction without having the oven unit vary from run to run which effected the correction factor obtained.

The sensors designed and evaluated in this study provided a robust and novel way to measure all three modes of heat transfer in an oven. Although designed for a residential oven placed on a cookware surface, it can potentially be used for evaluating various thermal environments that don't exceed operating conditions of sensor.

6.2 Future Work

A key takeaway for this study was that heat flux sensors can be used to determine changes in oven conditions when investigating different modes, but more work can be done to determine the sensitivity within these modes. For example, running a sensitivity analysis considering the modes investigated in this study at various oven temperature setpoints. This sensitivity analysis would provide input on sensors performance within a single oven mode.

One criterion that the heat flux sensors failed at was in determining the impacts of spatial variation within a single oven run. Distinct heat flux values were measured but it is uncertain whether this variation is due to the true difference in heat flux or due to sensor error. A strategy for correcting for sensor-to-sensor errors introduced by the heat flux sensor would provide a way to improve confidence in the difference across the sensor array in each test run. Another area where confidence can be improved in this heat flux sensor design

is in the bottom mass. Results measured during this study demonstrates the thermal interaction between top and bottom mass, and higher variation in bottom mass readings. A study to determine the impacts of contact resistance from sensor to sensor would help in determining the true variation in conduction from sensor to sensor. This contact resistance is a product of various factors such as the surface roughness of the aluminum mass, cookie sheet surface roughness and flatness, and the contact pressure.

The design of this sensor was guided by the need to measure heat flux in a residential oven to eventually determine the impacts that the different modes of heat transfer on cooking performance of different foods. Once confidence in the heat flux sensor designed is established, the sensors can be deployed to start preliminary food to heat energy correlation. The goal is to determine how heat flux measurements effect cooking metric such as browning, rising, texture, and many more. If the same sensor is used throughout the study, then consistent measurements can be made to guide the food study. If looking at differences of foods at different regions within study, more development is needed on sensor-to-sensor correction.

REFERENCES

- Abishek, S., Srinivasa Ramanujam, K. and Katte, S.S, "View Factors between Disk/Rectangle and Rectangle in Parallel and Perpendicular Planes," *J. Thermophysics*, vol. 21, no. 1, pp. 236-239.(1995)
- Afkar H, Kianifar A, Zamani H. "Investigation of the Effect of Variable Heat Flux on Energy Consumption and Bread Quality in the Flat Bread Baking Process by Experimental and Numerical Methods." *Energy Sources, Part a: Recovery, Utilization and Environmental Effects*, (2020)
- Bergman, Theodore L, Adrienne S. Lavine, Frank P. Incropera, David P. Dewitt. *Fundamentals of Heat and Mass Transfer*, J. Wiley & Sons, Hoboken, (2011)
- Boulet Micael, Bernard Marcos, Michel Dostie, Christine Moresoli "CFD Modeling of Heat Transfer and Flow Field in a Bakery Pilot Oven." *Journal of Food Engineering*, vol. 97, no. 3, pp. 393–402., doi:10.1016/j.jfoodeng.2009.10.034. (2010)
- Cernela Jérémie Bertrand, Heyd Bertrand Broyart. "Evaluation of Heating Performances and Associated Variability of Domestic Cooking Appliances (Oven-Baking and Pan-Frying)." *Applied Thermal Engineering*, vol. 62, no. 2, pp. 758–765., doi:10.1016/j.applthermaleng.2013.08.045. (2014)
- Fahloul D, Trystram G, Duquenoy A, Barbotteau I. "Modelling Heat and Mass Transfer in Band Oven Biscuit Baking." *Lebensmittel-Wissenschaft Und-Technologie*, vol. 27, no. 2, pp. 119–124. (1994)
- Khaled M, Garnier B, Harambat F, Peerhossaini H. "A New Method for Simultaneous Measurement of Convective and Radiative Heat Flux in Car Underhood Applications." *Measurement Science & Technology*, vol. 21, no. 2pp. 025903–025903. (2010)
- Liu Qingtong, Park Haejun, Shen Ruiqing, Lahiru Jayathunga-Mudiyanselage. "A New Method to Calculate Incident Radiant Heat Flux by Using Plate Thermometer." *Fire Technology*, vol. 57, no. 1, 2021, pp. 341-359. doi:10.1007/s10694-020-01006-9. (2022)

- Ozen, E, and R.K Singh. "Heat Transfer in Breaded and Non-Breaded Chicken Nuggets Baked in a Pilot-Scale Radiant Wall Oven." *Lwt - Food Science and Technology*, vol. 124 (2020)
- Pullins, Clayton A, and Tom E Diller. "In Situ High Temperature Heat Flux Sensor Calibration." *International Journal of Heat and Mass Transfer*, vol. 53, no. 17, pp. 3429–3438.(2010)
- Ramirez-Laboreo Edgar, Sagues Carlos, Llrente Sergio "Dynamic Heat and Mass Transfer Model of an Electric Oven for Energy Analysis." *Applied Thermal Engineering*, vol. 93, pp. 683–691.(2016)
- Saxena D.C., Rao P.Haridas, Rao K.S.M.S.Raghava. "Analysis of Modes of Heat Transfer in Tandoor Oven." 4 Sept. (1994)
- Sato, Hidemi, Tsuneio Matsukmara, Shoko Shubukawa. "Apparent Heat Transfer in a Forced Convection Oven and Properties of Baked Foods." *Journal of Food Science*, vol. 52, no. 1 (1987)
- Shoko Shibukawa, Kunikio Sugiyama, Toshimasa Yano. "Effects of Heat Transfer by Radiation and Convection on Browning of Cookies at Baking." *Journal of Food Science*, vol. 54, no. 3 , pp. 621–624.(1989)
- Singh, Rakesh K, and Bilal Kirmaci. "Heat Transfer Coefficients during Baking of Potato Strips in a Pilot Scale Radiant Wall Oven." *International Journal of Food Properties*, vol. 24, no. 1, pp. 1737–1743. (2021)
- Standing, Charles E. "Individual Heat Transfer Modes in Band Oven Biscuit Baking." *Journal of Food Science*, vol. 39, (1974)
- Van der Ham E W M, C M Beer, M J Ballico. "Measurement of the Nonlinearity of Heat-Flux Sensors Employing A." *International Journal of Thermophysics : Journal of Thermophysical Properties and Thermophysics and Its Applications*, vol. 39, no. 1, pp. 1–12., (2018)
- Zareifard MR, M Marcotte, M Dostie. "A Method for Balancing Heat Fluxes Validated for a Newly Designed Pilot Plant Oven." *Journal of Food Engineering*, vol. 76, no. 3, pp. 303–312., doi:10.1016/j.jfoodeng.2005.05.037.(2006)

APPENDICES

A. Appendix I Radiation Calibration Graphs

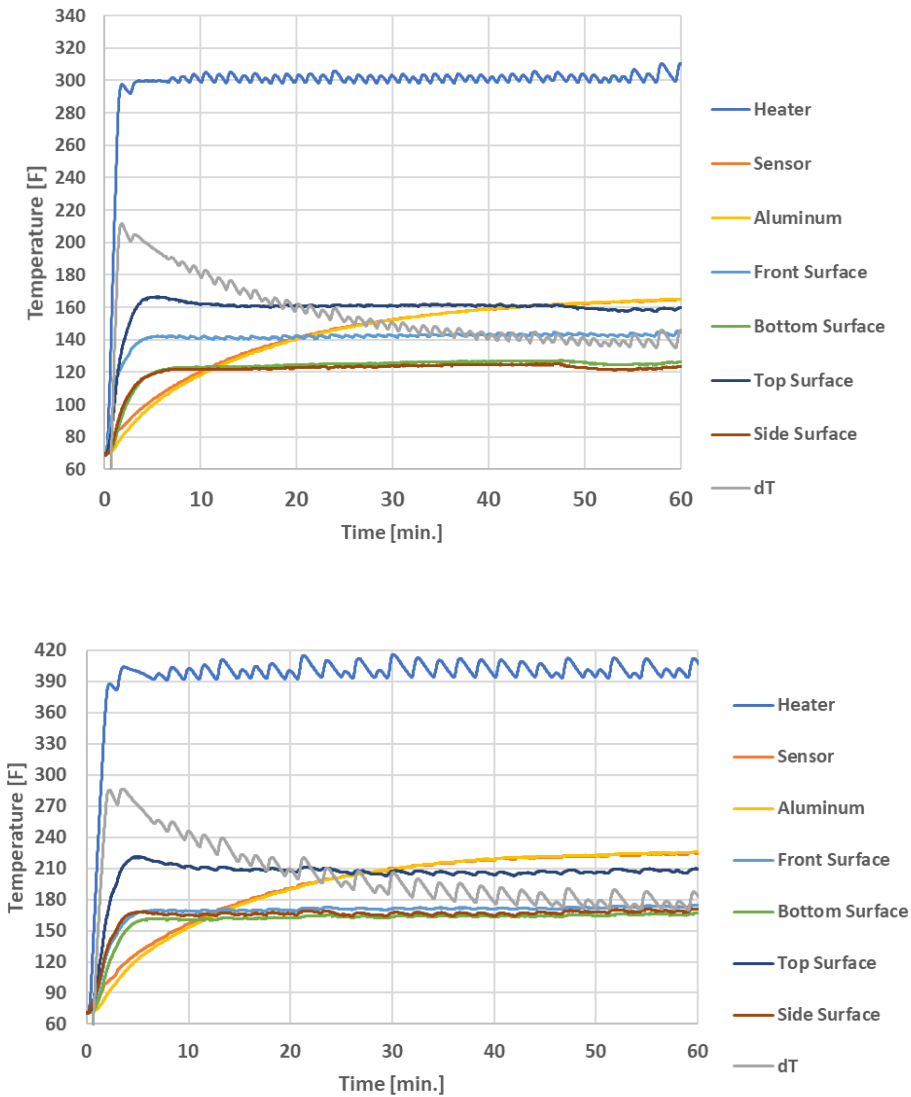


Figure 0-1 Sensor 2 radiation calibration thermal plots. Temperature data and heat flux data for 300°F test can be seen in top and 400°F test can be seen in bottom graph.

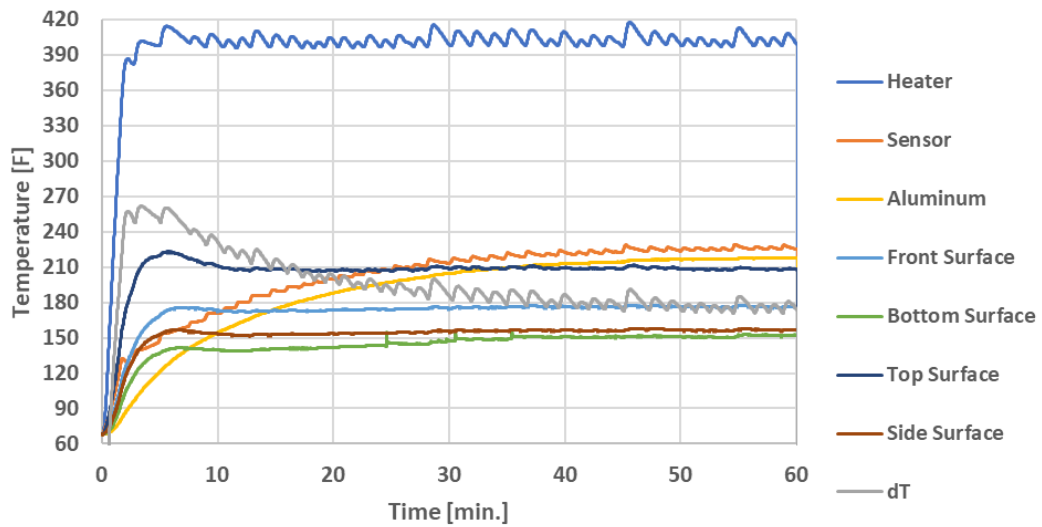
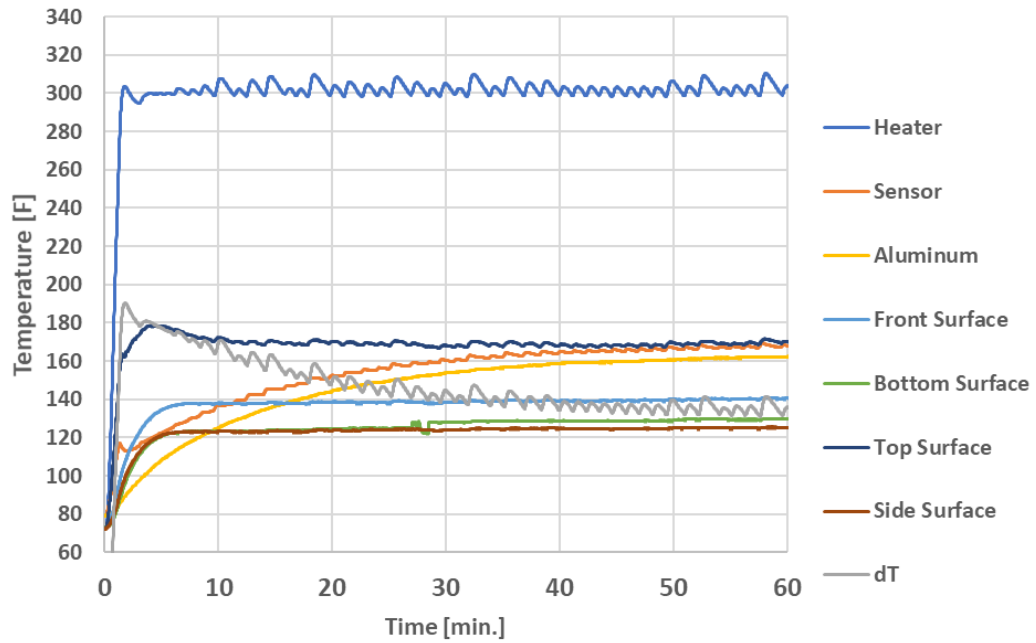


Figure 0-2 Sensor 3 radiation calibration thermal plots. Temperature data and heat flux data for 300°F test can be seen in top and 400°F test can be seen in bottom graph.

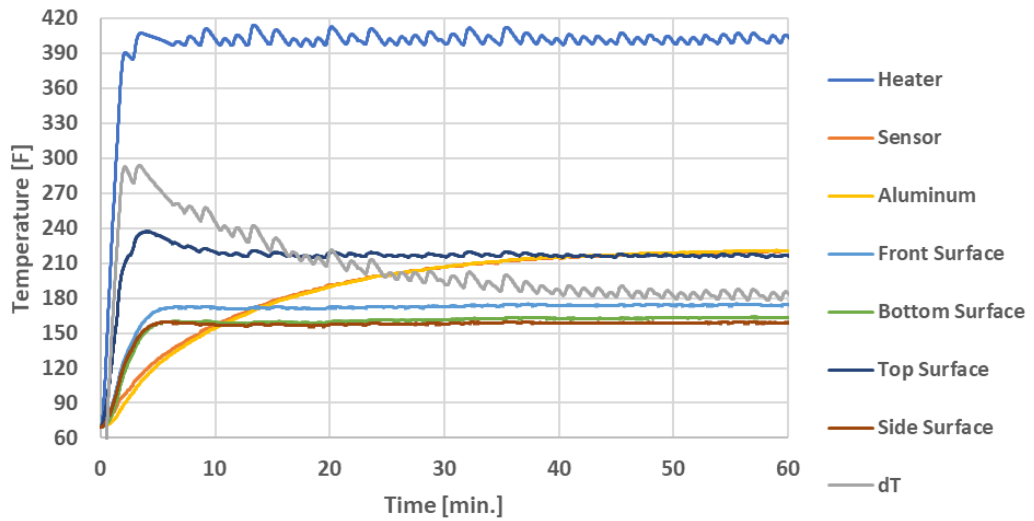
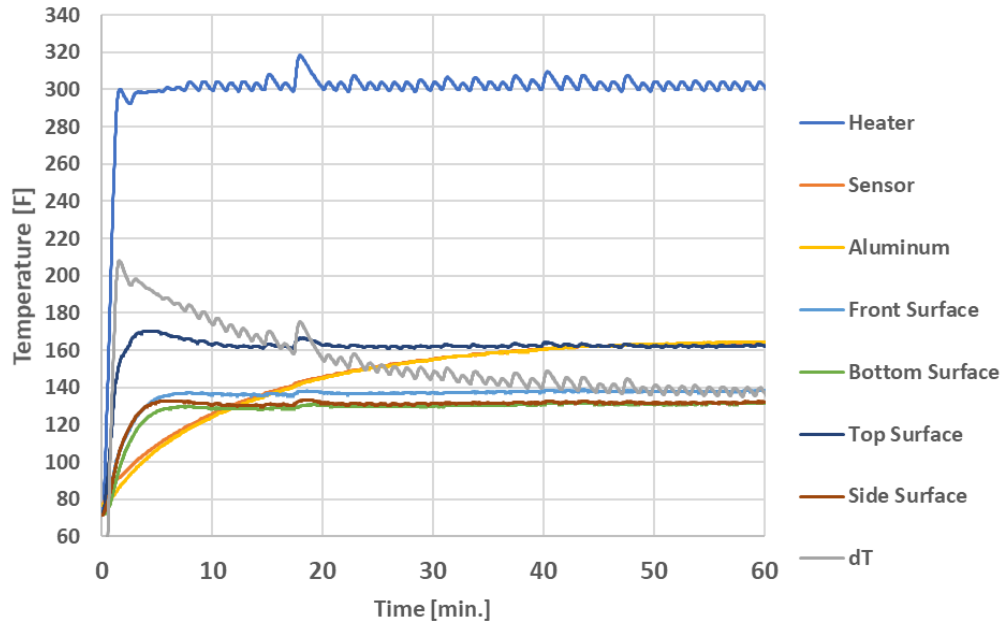


Figure 0-3 Sensor 4 radiation calibration thermal plots. Temperature data and heat flux data for 300°F test can be seen in top and 400°F test can be seen in bottom graph.

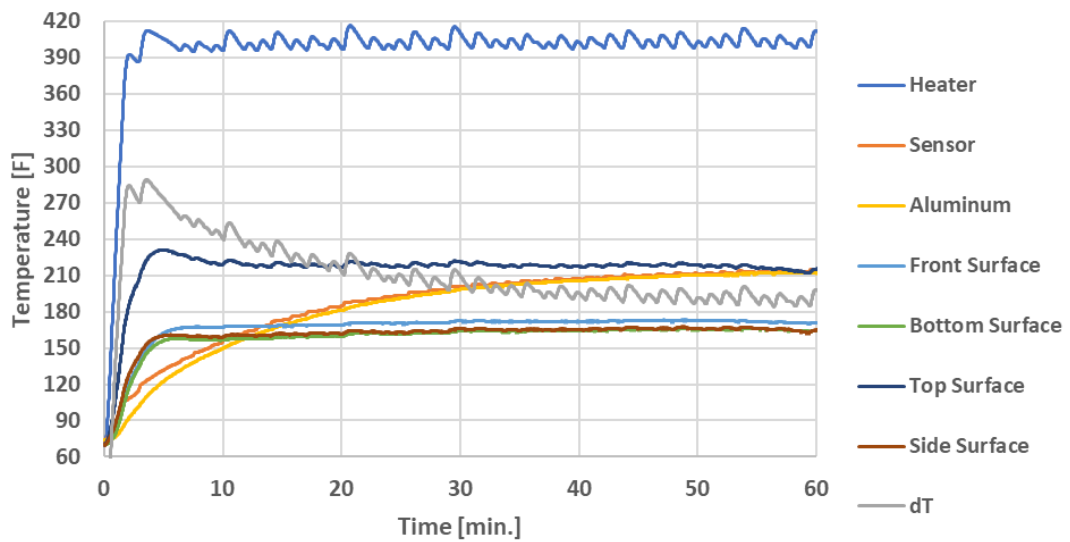
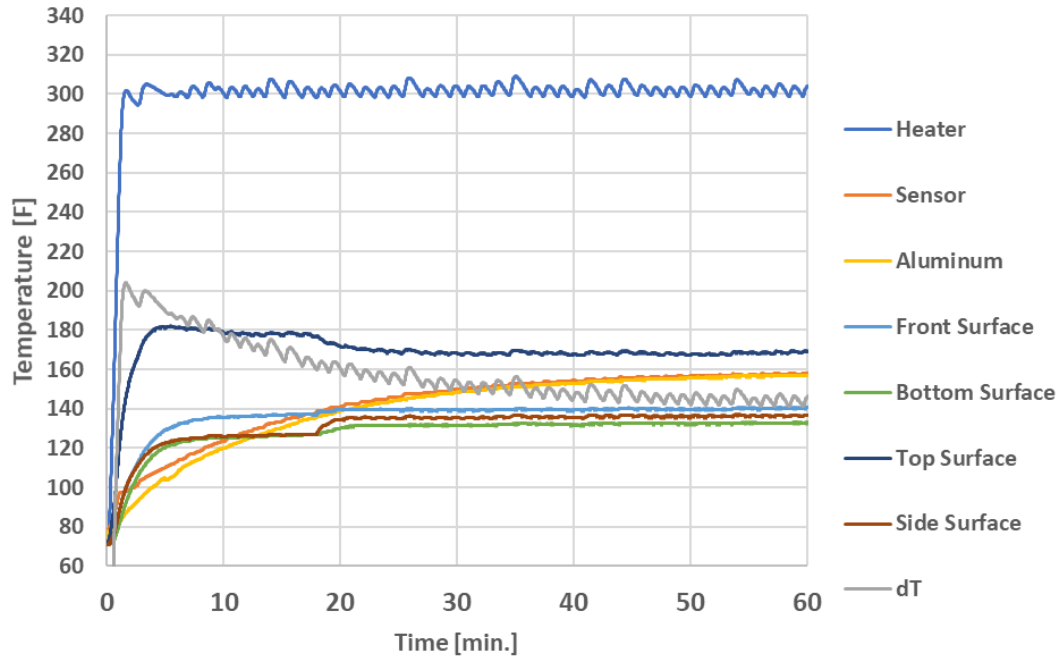


Figure 0-4 Sensor 5 radiation calibration thermal plots. Temperature data and heat flux data for 300°F test can be seen in top and 400°F test can be seen in bottom graph.

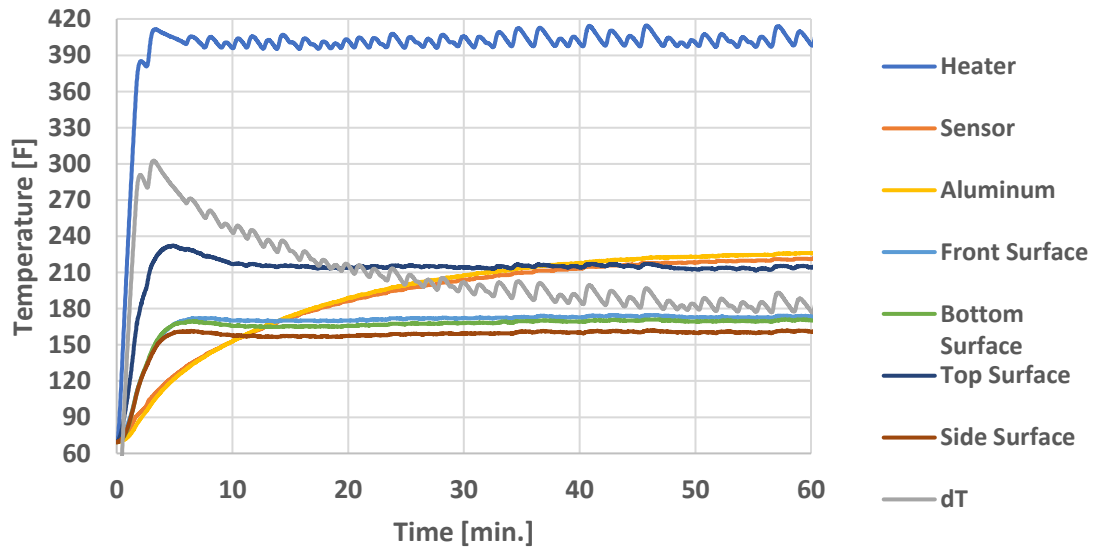
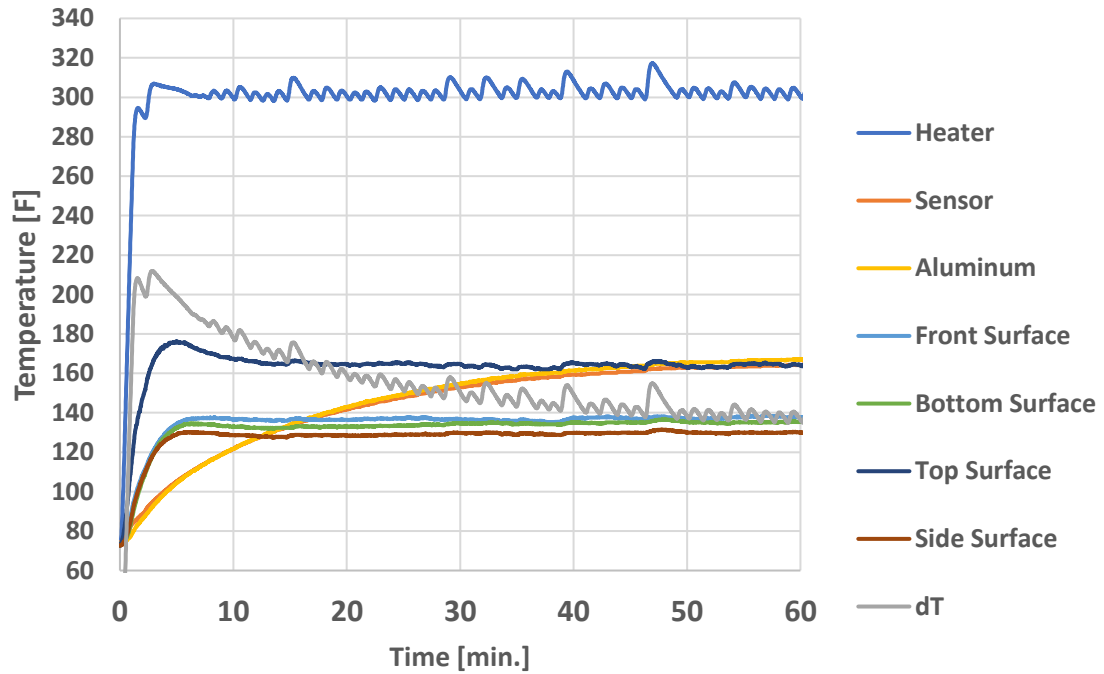


Figure 0-5 Sensor 6 radiation calibration thermal plots. Temperature data and heat flux data for 300°F test can be seen in top and 400°F test can be seen in bottom graph.

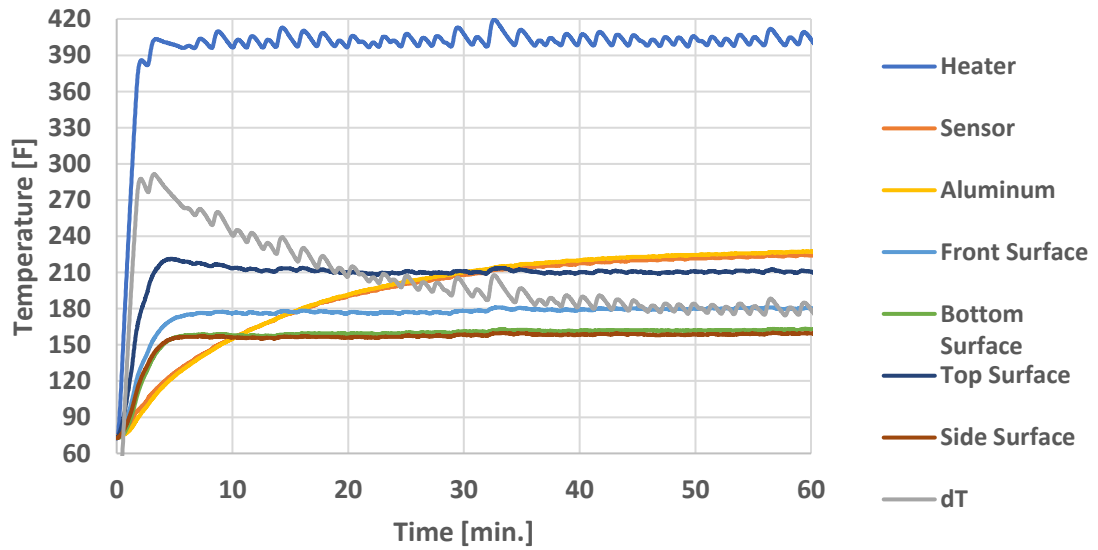
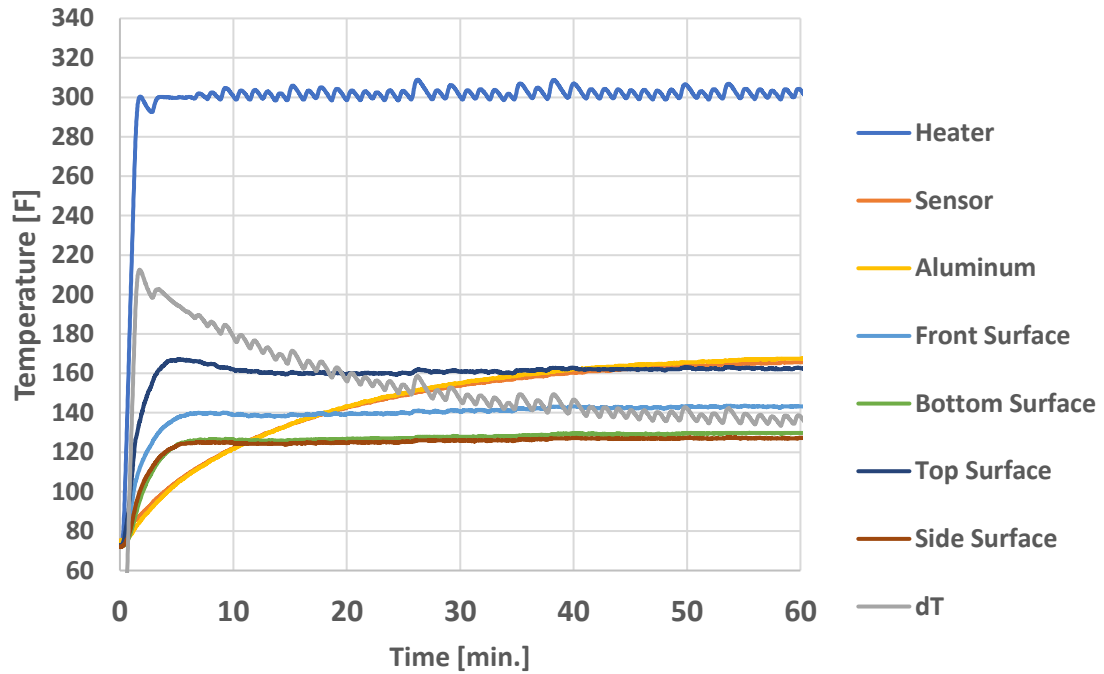


Figure 0-6 Sensor 7 radiation calibration thermal plots. Temperature data and heat flux data for 300°F test can be seen in top and 400°F test can be seen in bottom graph.

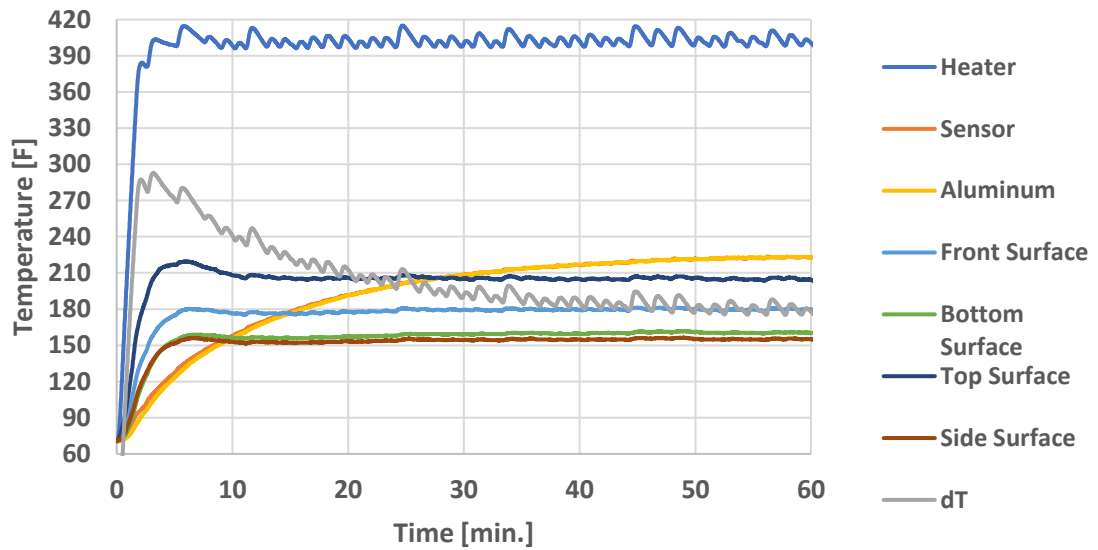
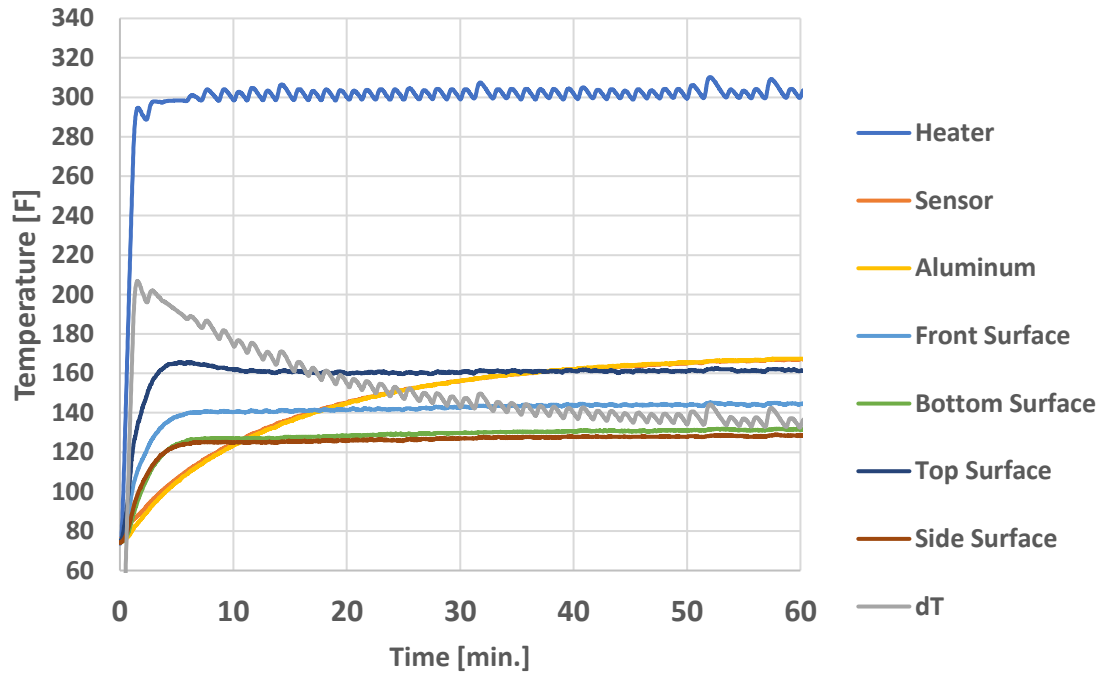


Figure 0-7 Sensor 8 radiation calibration thermal plots. Temperature data and heat flux data for 300°F test can be seen in top and 400°F test can be seen in bottom graph.

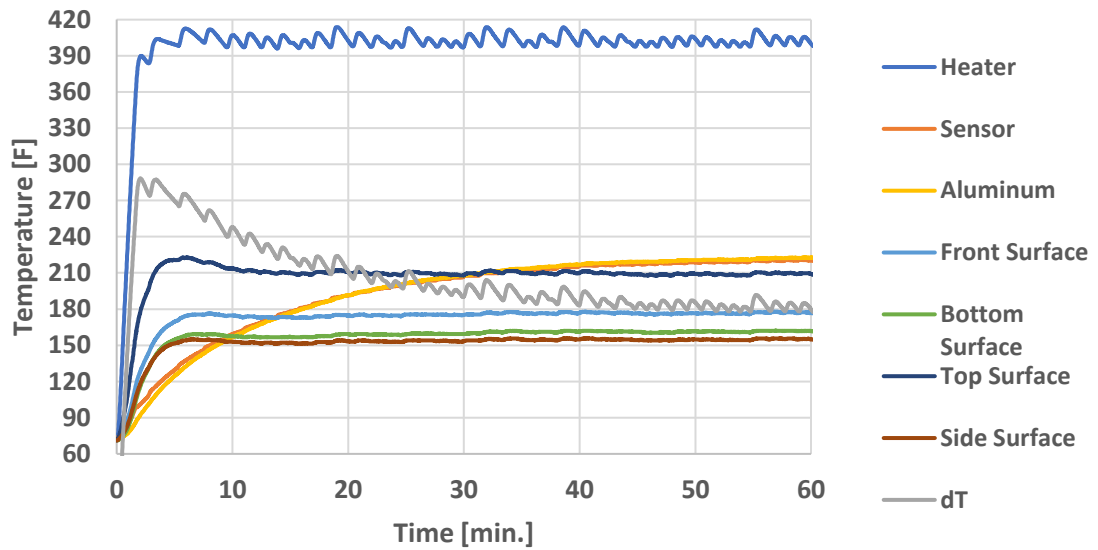
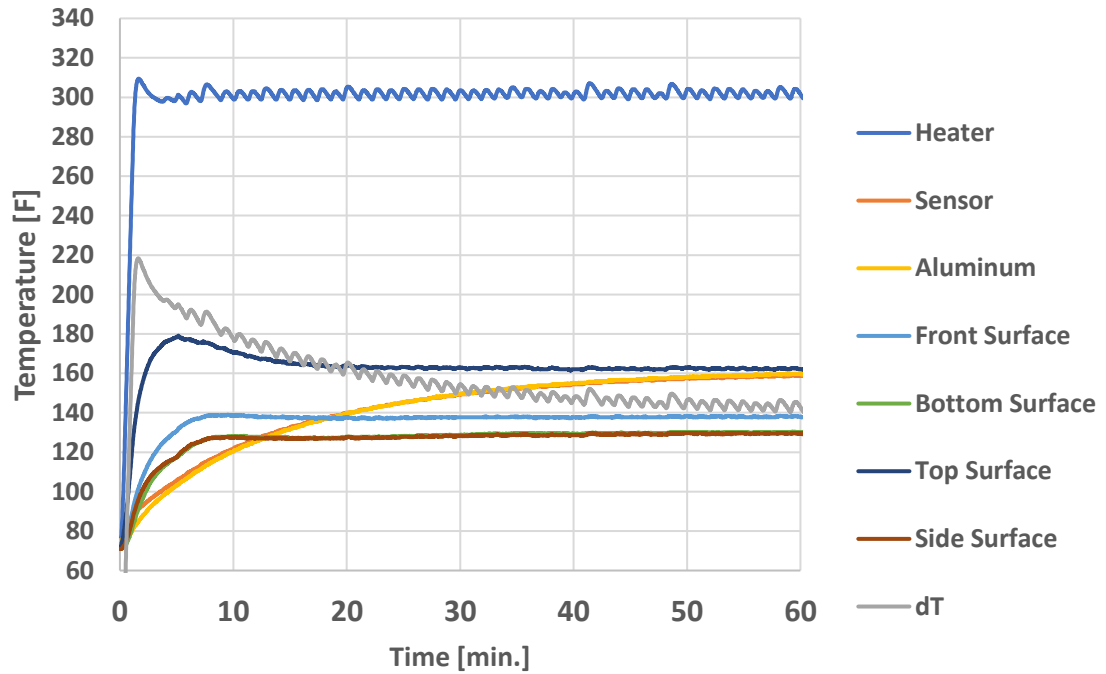


Figure 0-8 Sensor 9 radiation calibration thermal plots. Temperature data and heat flux data for 300°F test can be seen in top and 400°F test can be seen in bottom graph.

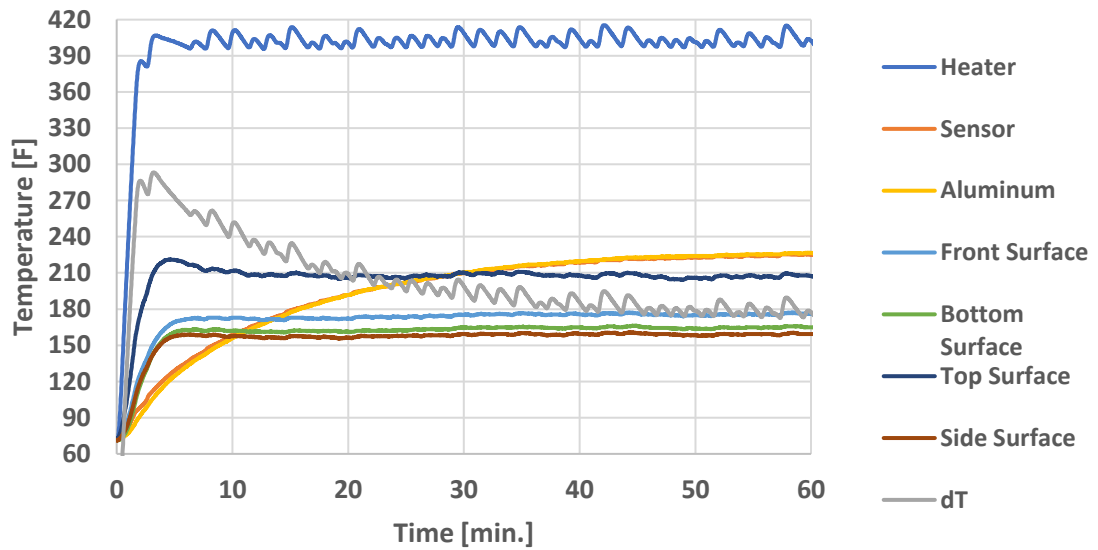
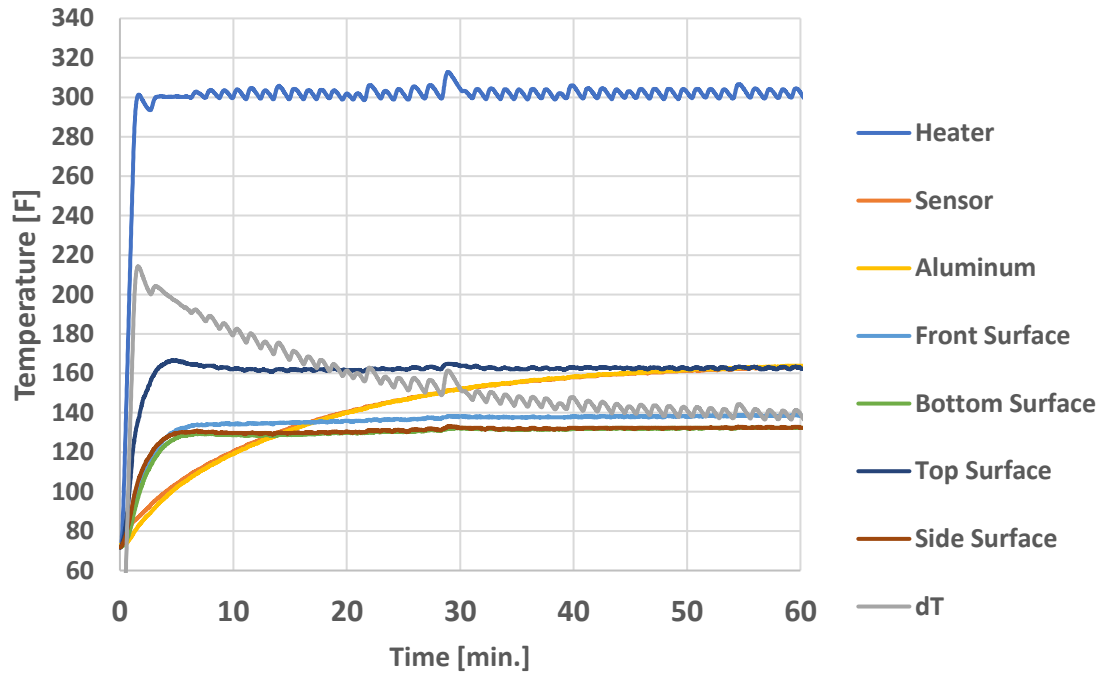


Figure 0-9 Sensor 10 radiation calibration thermal plots. Temperature data and heat flux data for 300°F test can be seen in top and 400°F test can be seen in bottom graph.

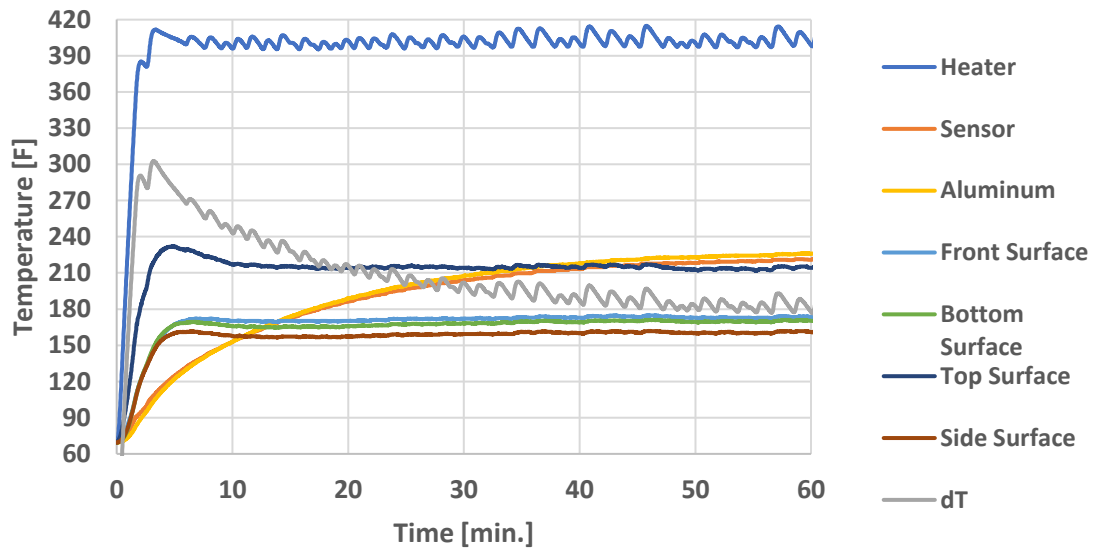
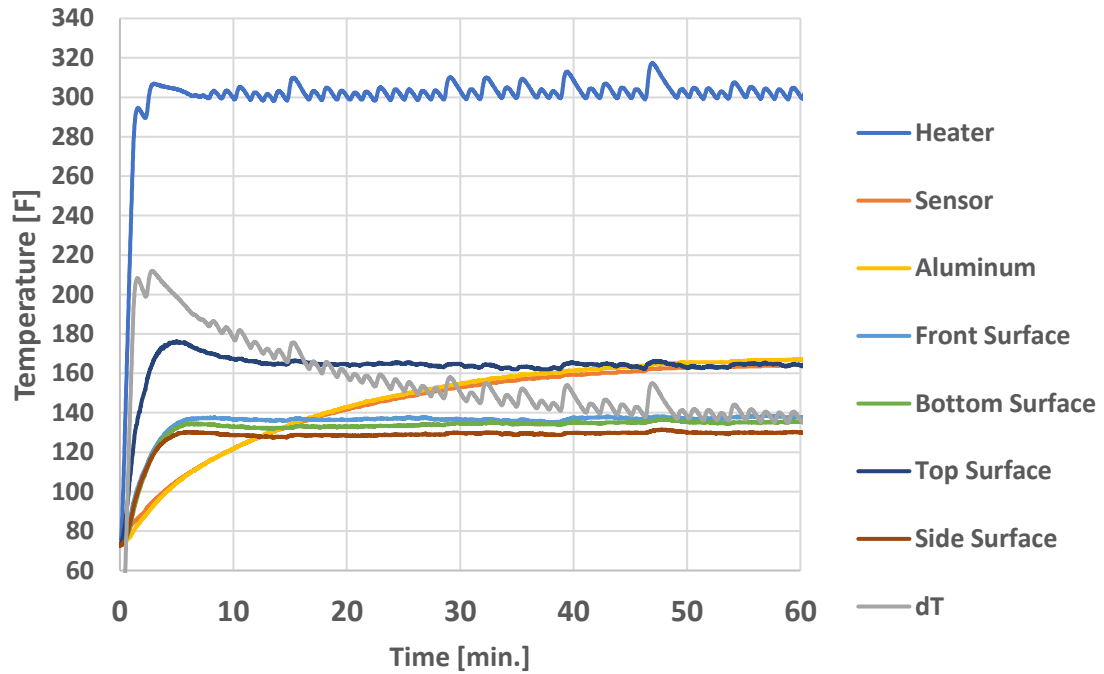


Figure 0-10 Sensor 11 radiation calibration thermal plots. Temperature data and heat flux data for 300°F test can be seen in top and 400°F test can be seen in bottom graph.

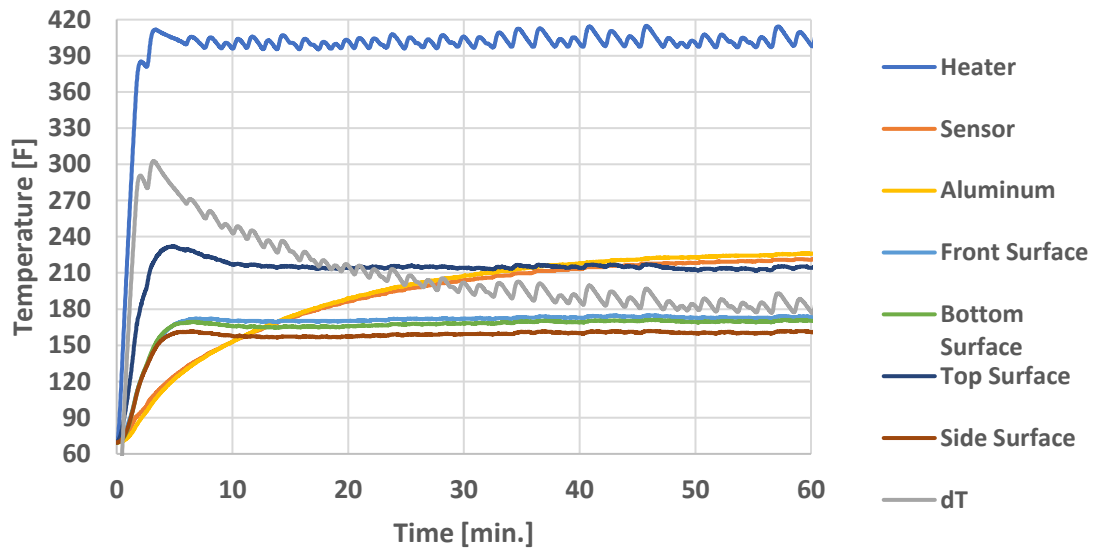
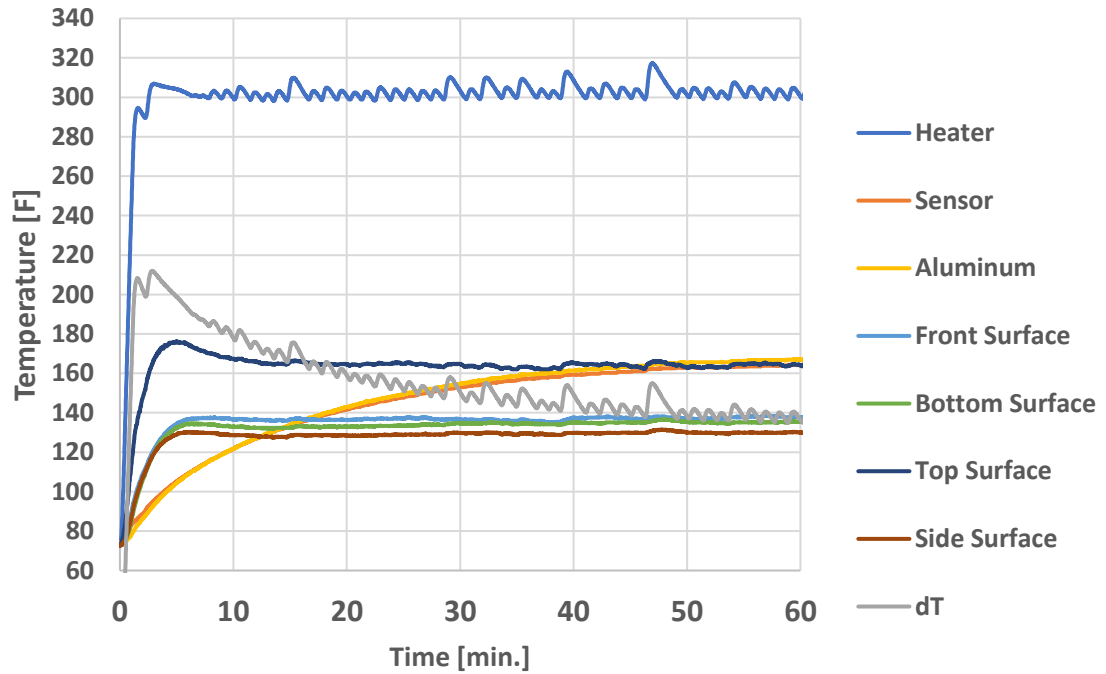
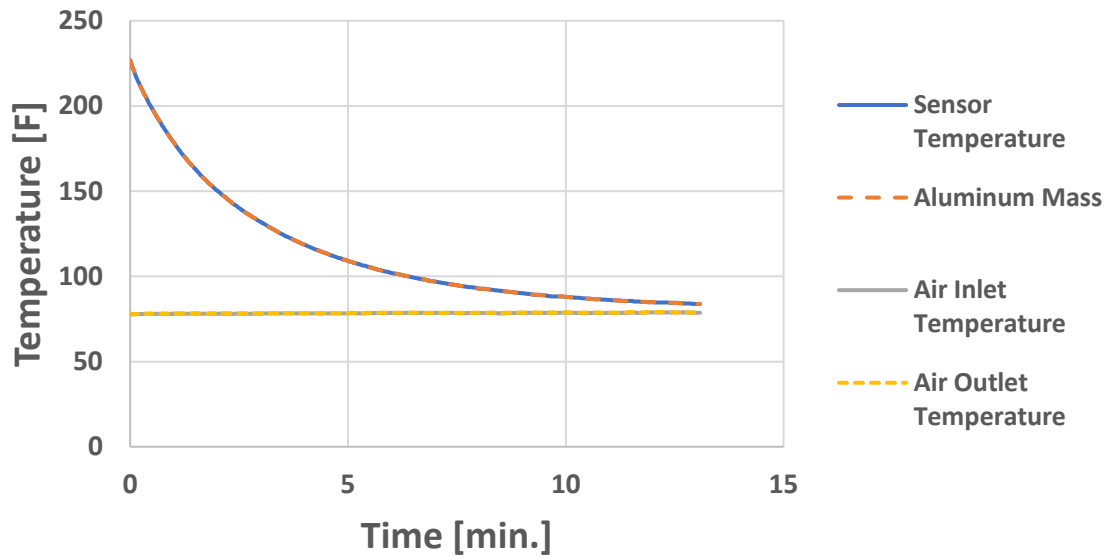
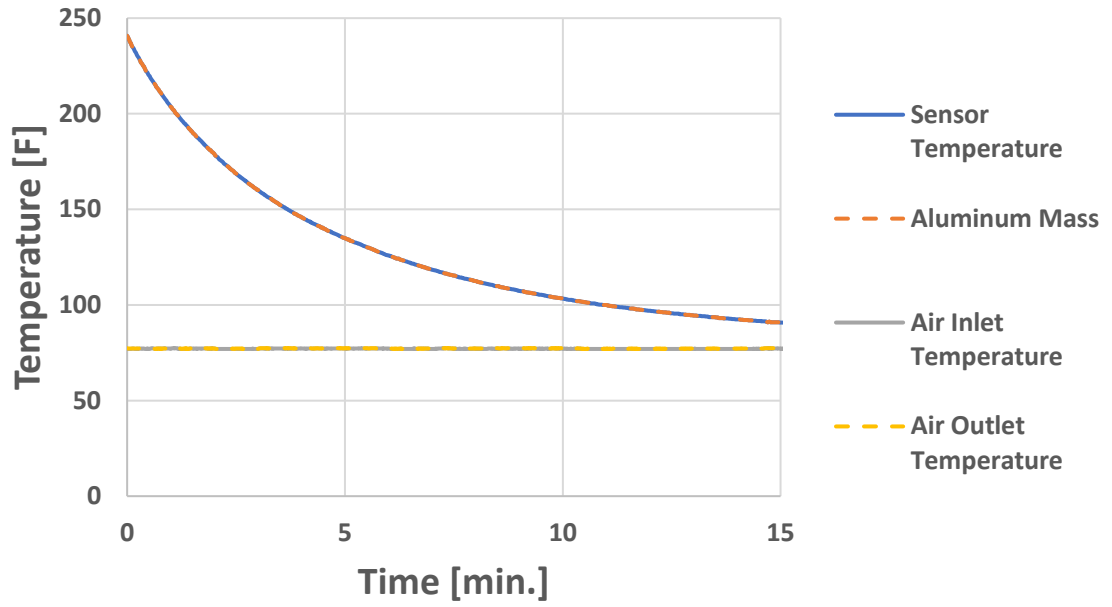


Figure 0-11 Sensor 12 radiation calibration thermal plots. Temperature data and heat flux data for 300°F test can be seen in top and 400°F test can be seen in bottom graph.

B. Appendix II Convection Calibration Graphs



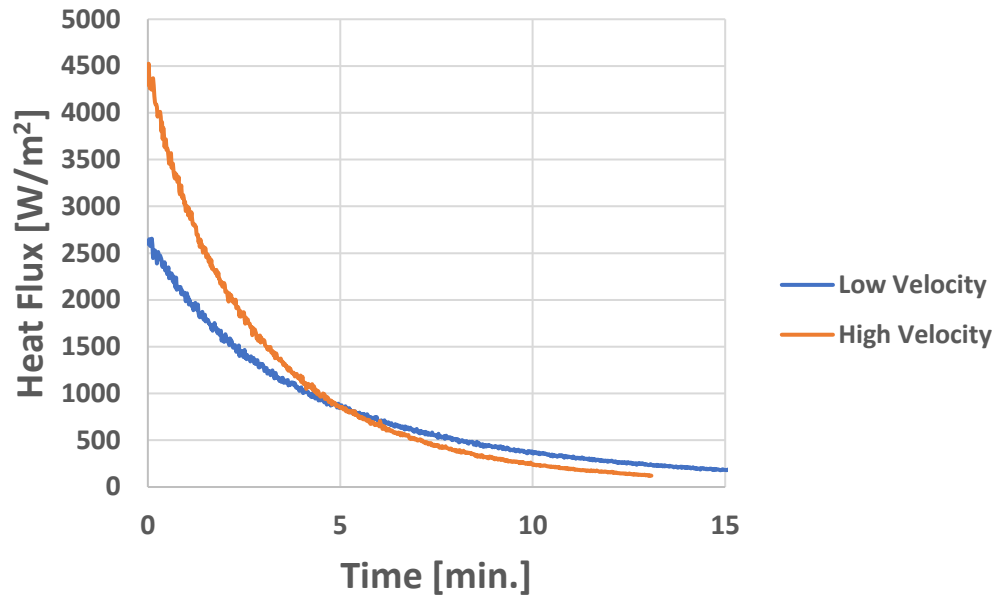
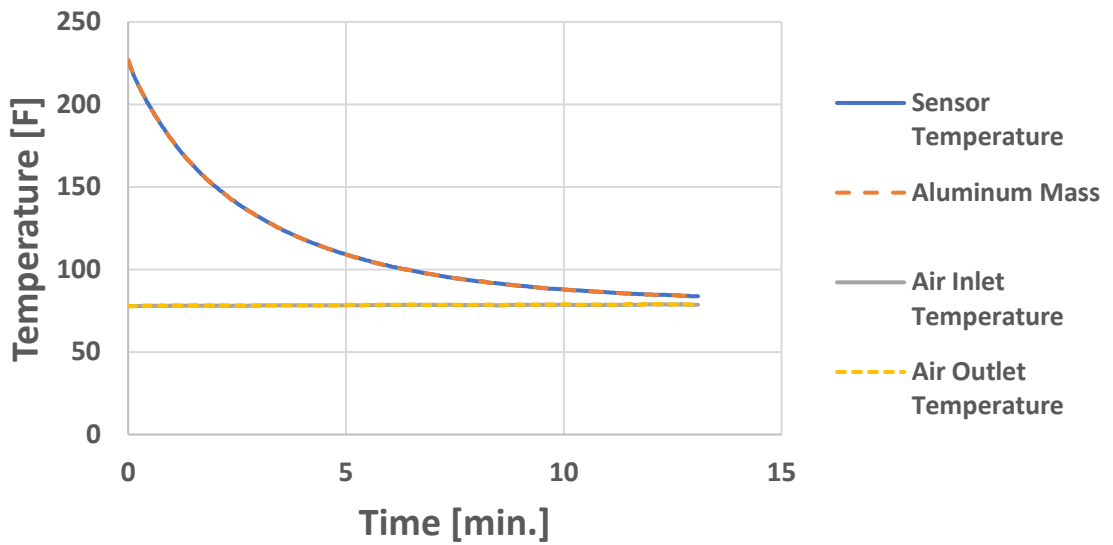
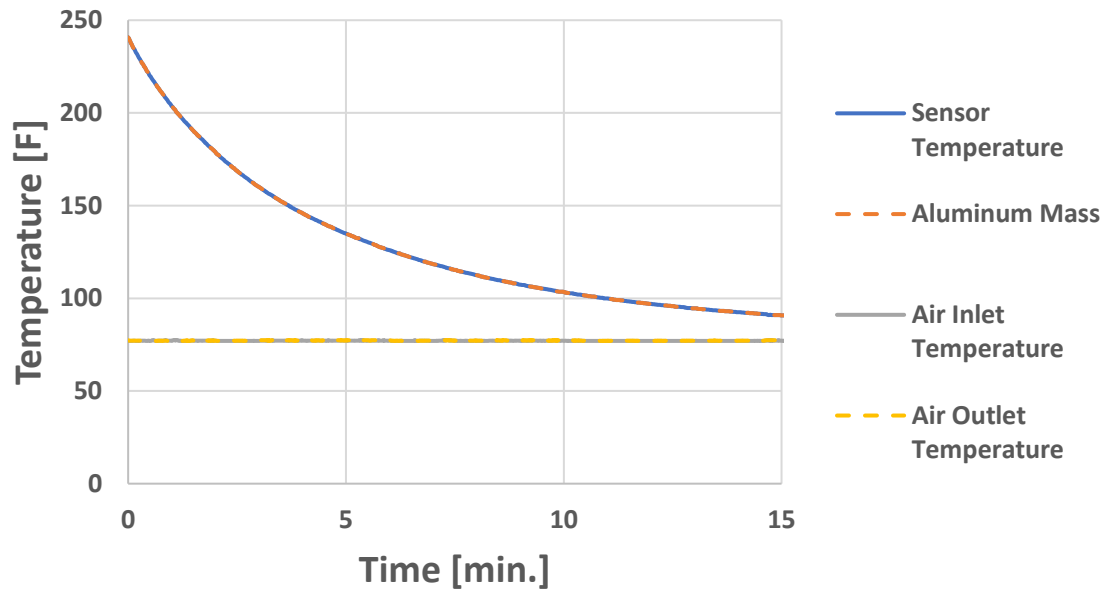


Figure 0-12 Sensor 2 convection calibration results. The first two graphs are temperature plots for the sensor, aluminum mass, and the air inlet and outlet temperature. The sensor temperature and aluminum temperature are measured to be the same. Inlet and outlet display no measurable changes in temperature. The bottom graph represents heat flux over time for low and high velocity tests.



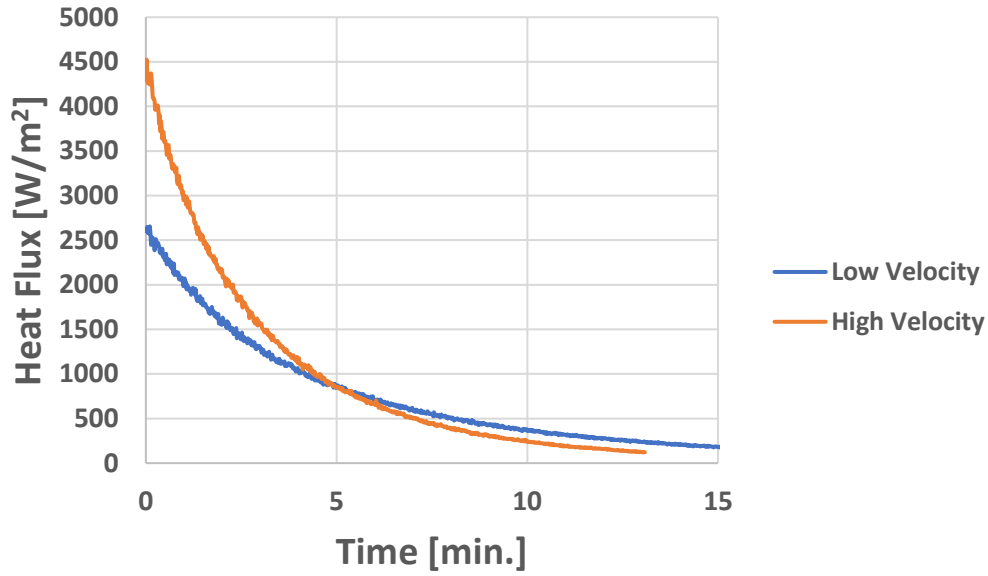
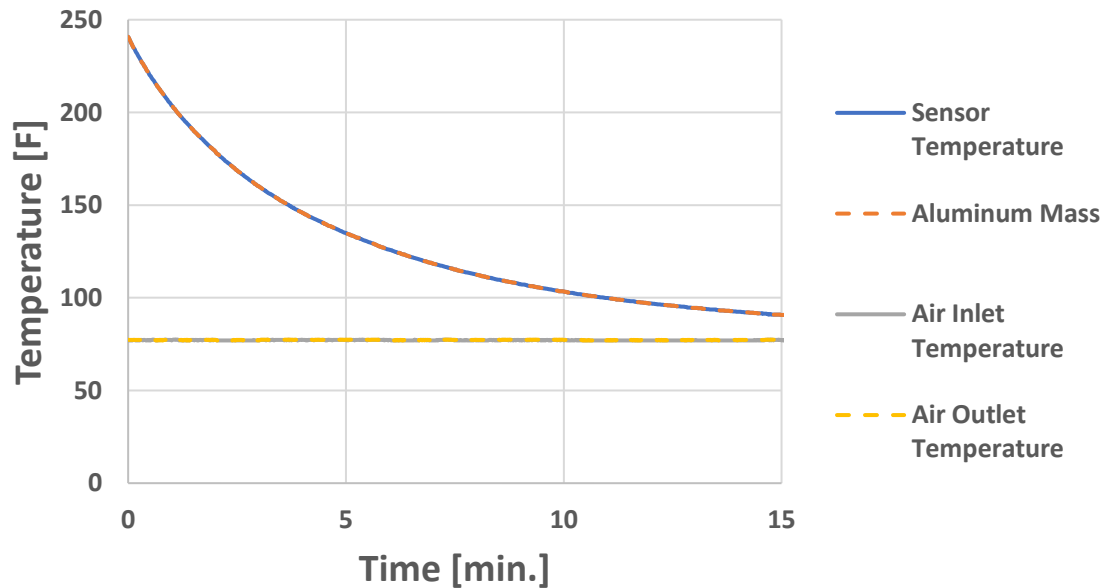


Figure 0-13 Sensor 3 convection calibration results. The first two graphs are temperature plots for the sensor, aluminum mass, and the air inlet and outlet temperature. The sensor temperature and aluminum temperature are measured to be the same. Inlet and outlet display no measurable changes in temperature. The bottom graph represents heat flux over time for low and high velocity tests.



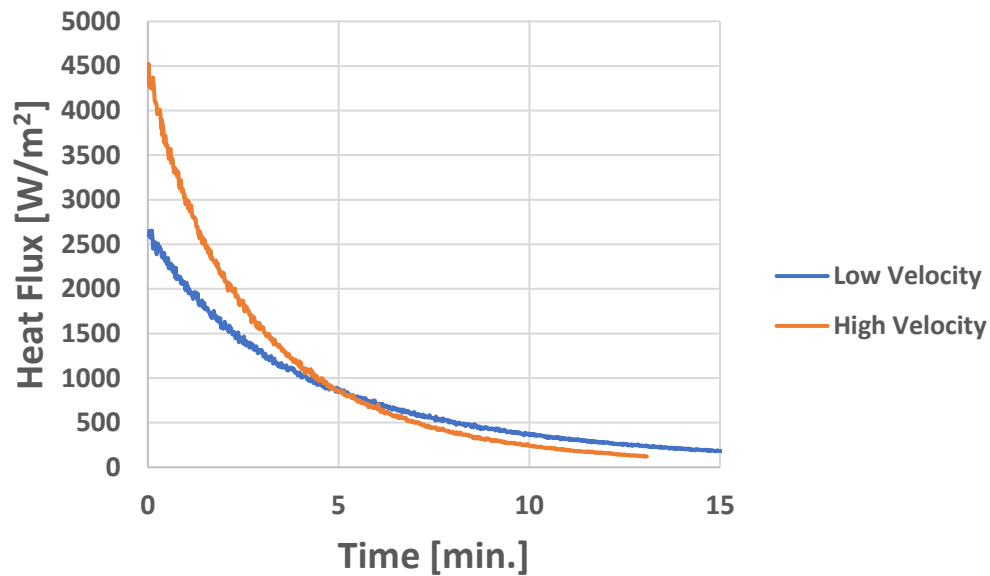
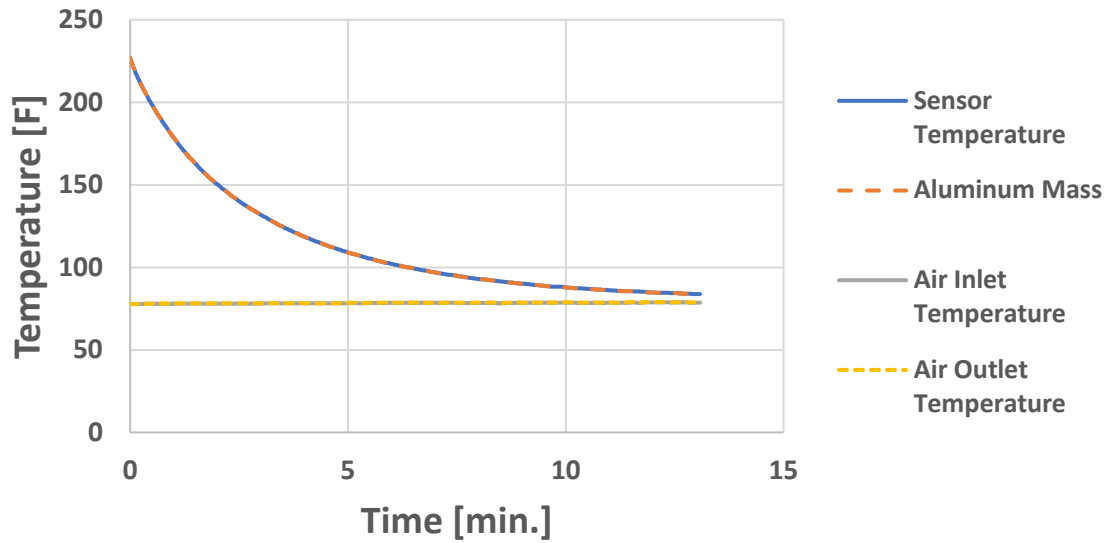
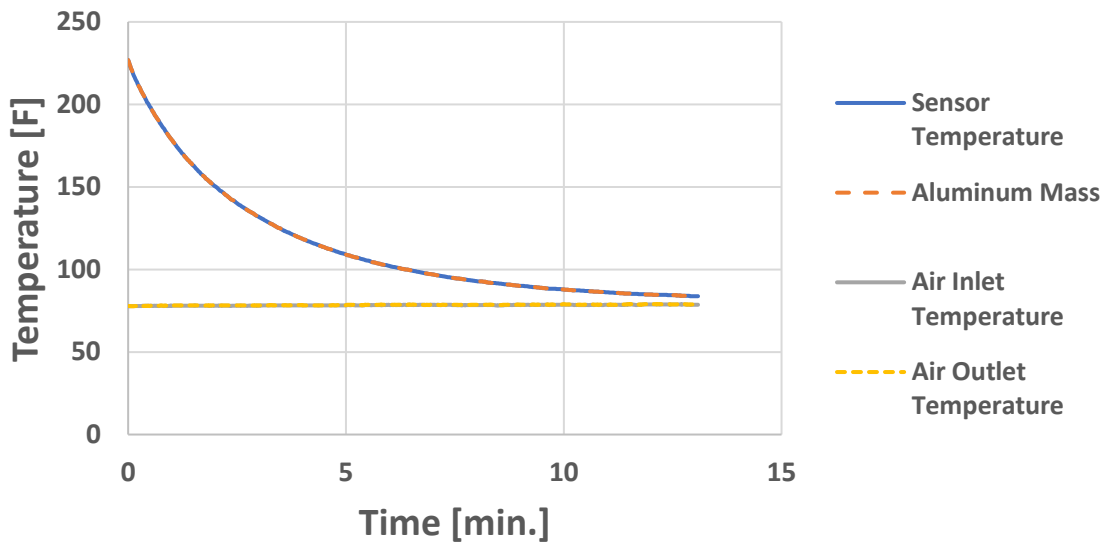
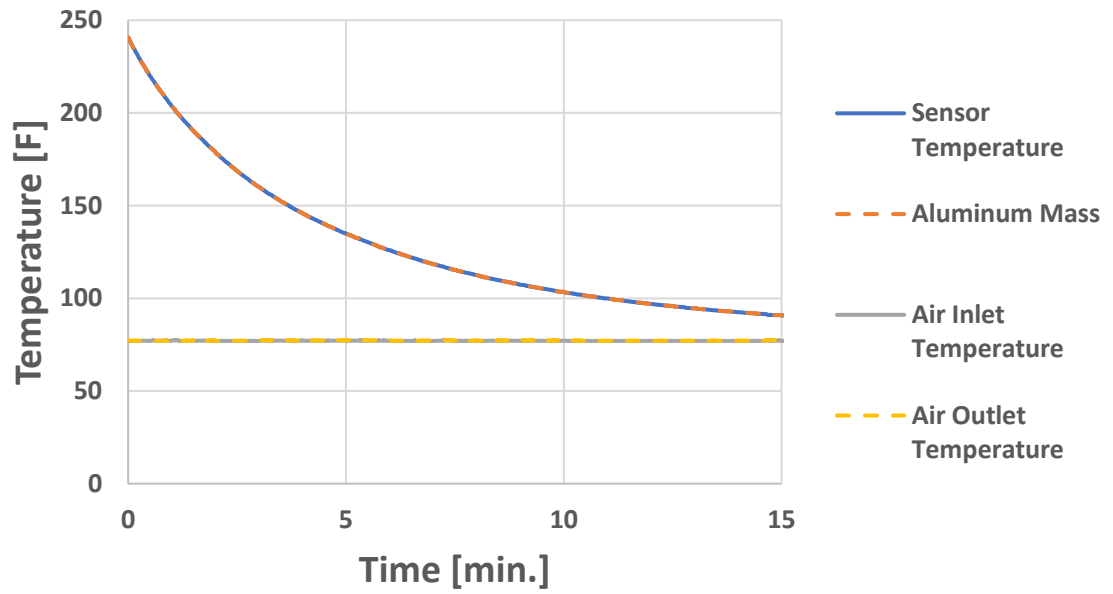


Figure 0-14 Sensor 4 convection calibration results. The first two graphs are temperature plots for the sensor, aluminum mass, and the air inlet and outlet temperature. The sensor temperature and aluminum temperature are measured to be the same. Inlet and outlet display no measurable changes in temperature. The bottom graph represents heat flux over time for low and high velocity tests.



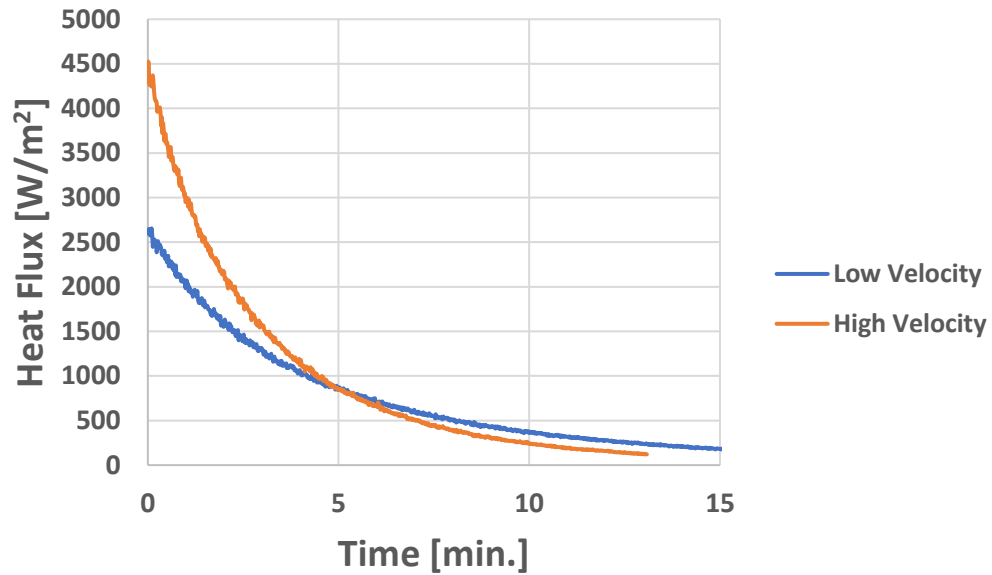
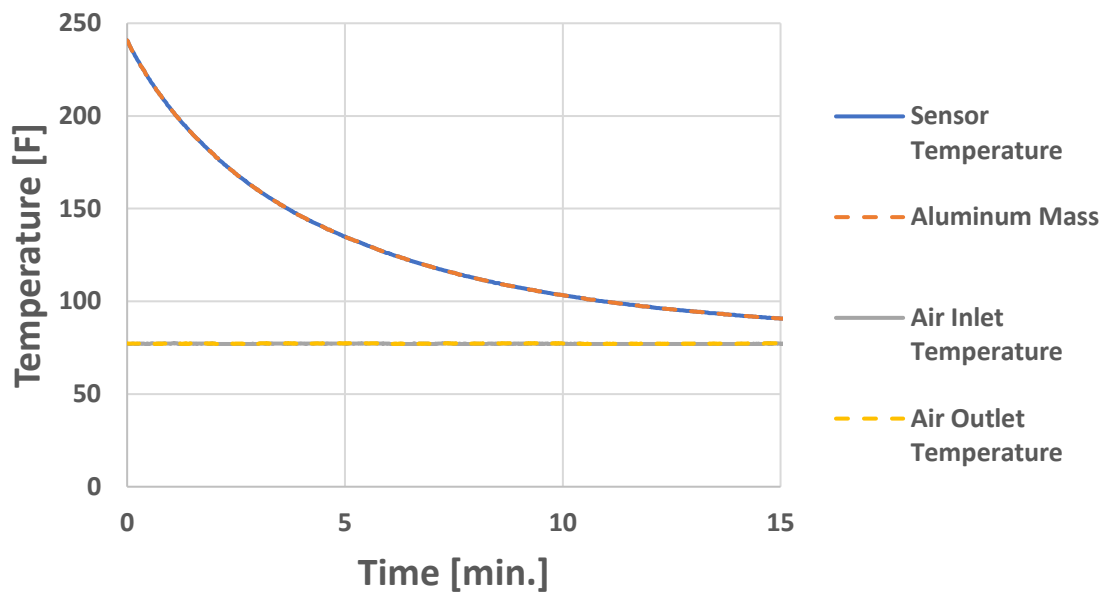


Figure 0-15 Sensor 5 convection calibration results. The first two graphs are temperature plots for the sensor, aluminum mass, and the air inlet and outlet temperature. The sensor temperature and aluminum temperature are measured to be the same. Inlet and outlet display no measurable changes in temperature. The bottom graph represents heat flux over time for low and high velocity tests.



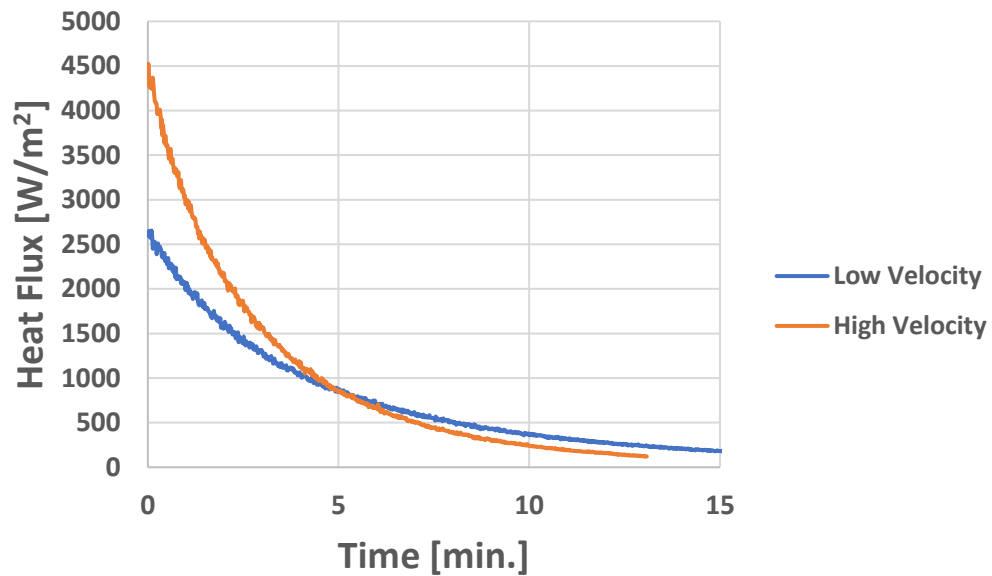
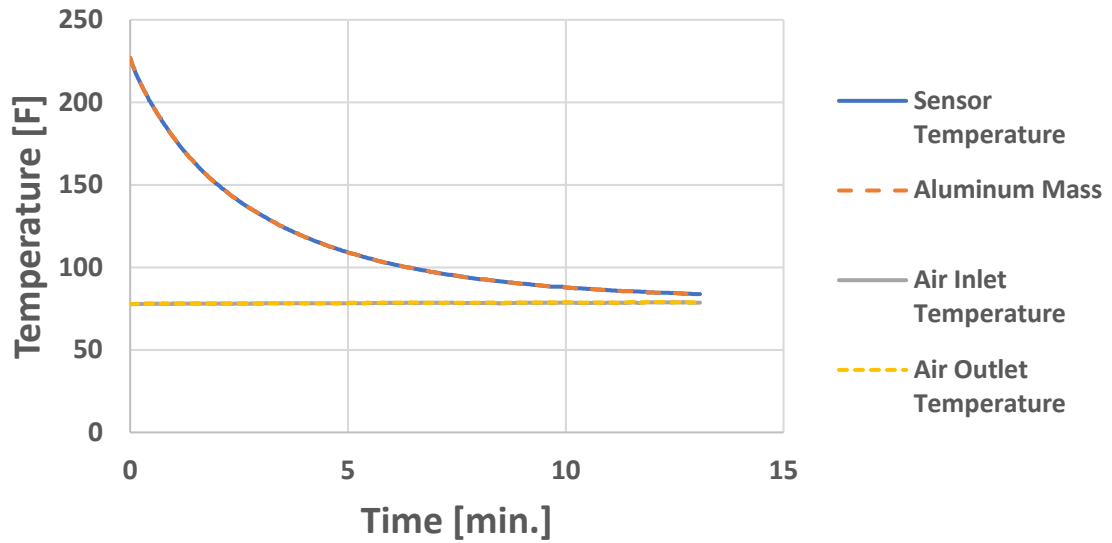
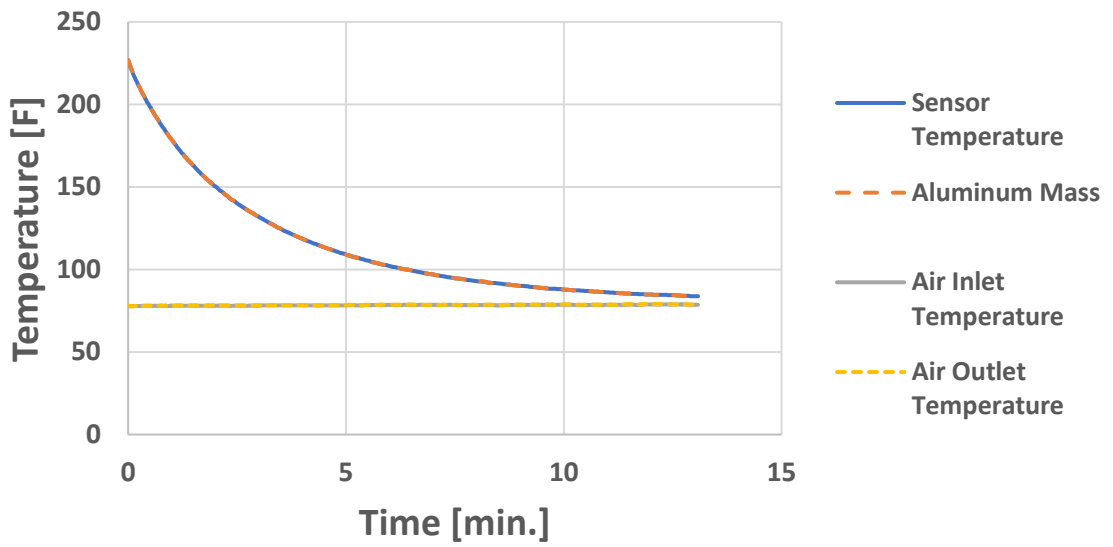
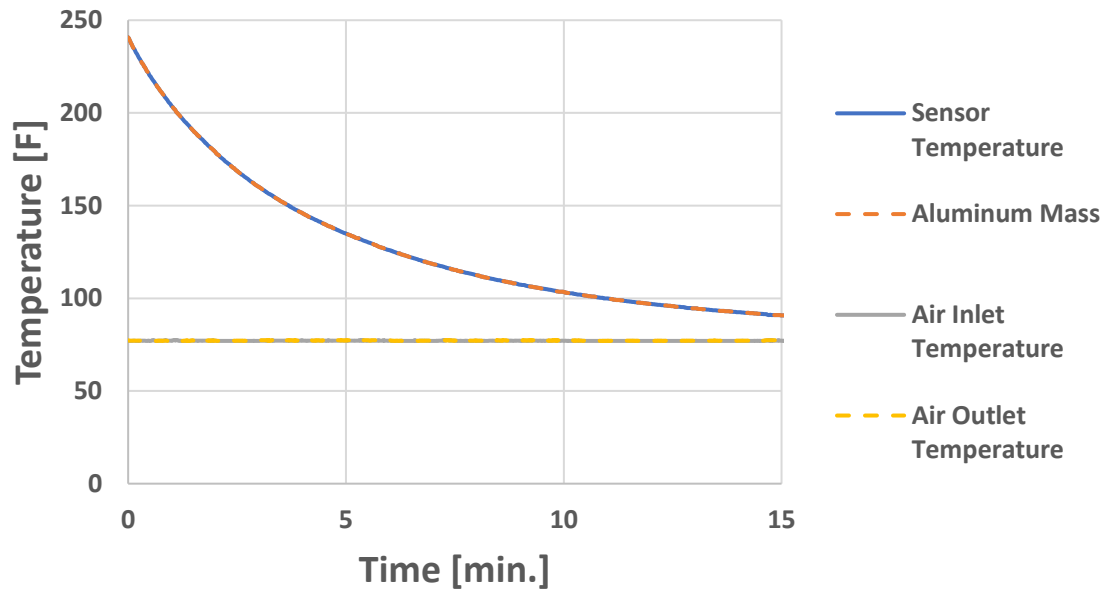


Figure 0-16 Sensor 6 convection calibration results. The first two graphs are temperature plots for the sensor, aluminum mass, and the air inlet and outlet temperature. The sensor temperature and aluminum temperature are measured to be the same. Inlet and outlet display no measurable changes in temperature. The bottom graph represents heat flux over time for low and high velocity tests.



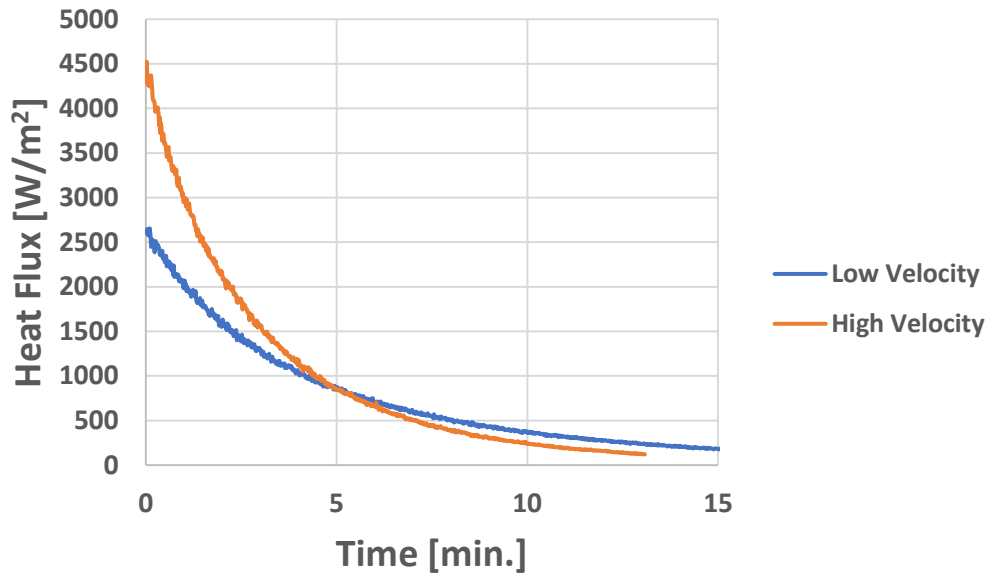
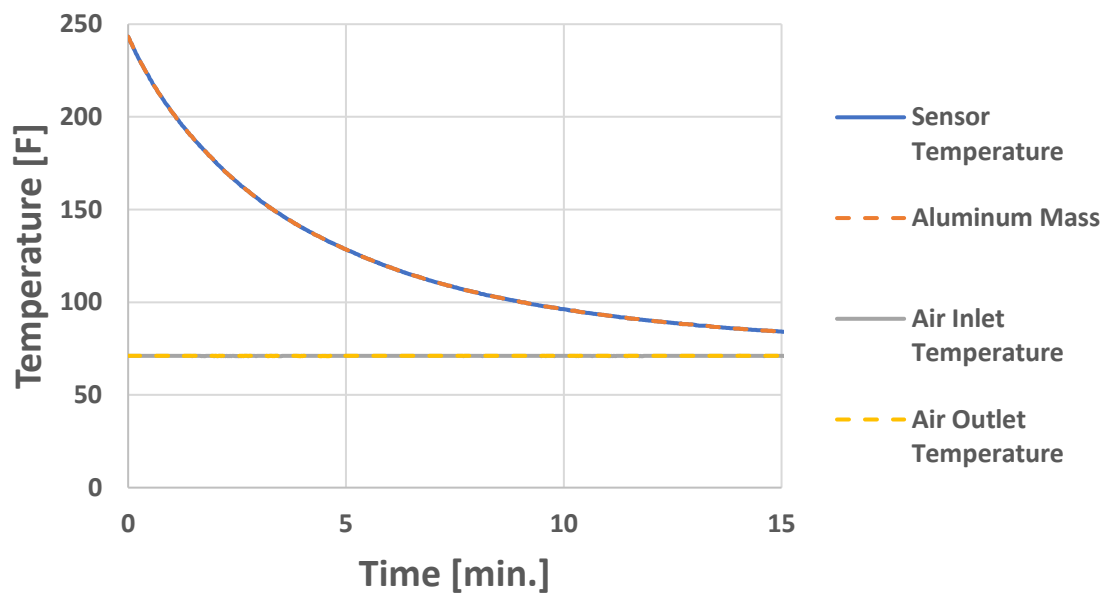


Figure 0-17 Sensor 7 convection calibration results. The first two graphs are temperature plots for the sensor, aluminum mass, and the air inlet and outlet temperature. The sensor temperature and aluminum temperature are measured to be the same. Inlet and outlet display no measurable changes in temperature. The bottom graph represents heat flux over time for low and high velocity tests



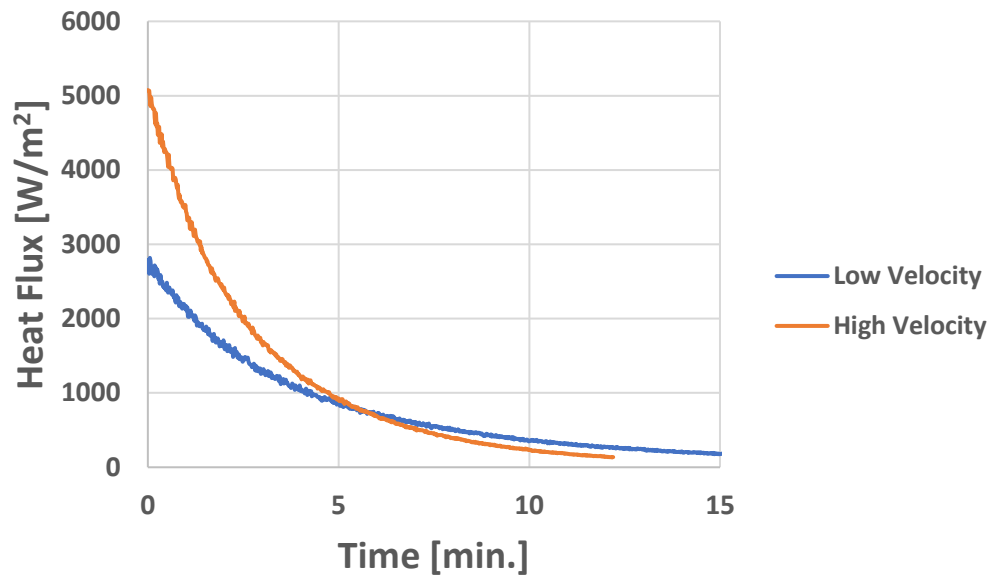
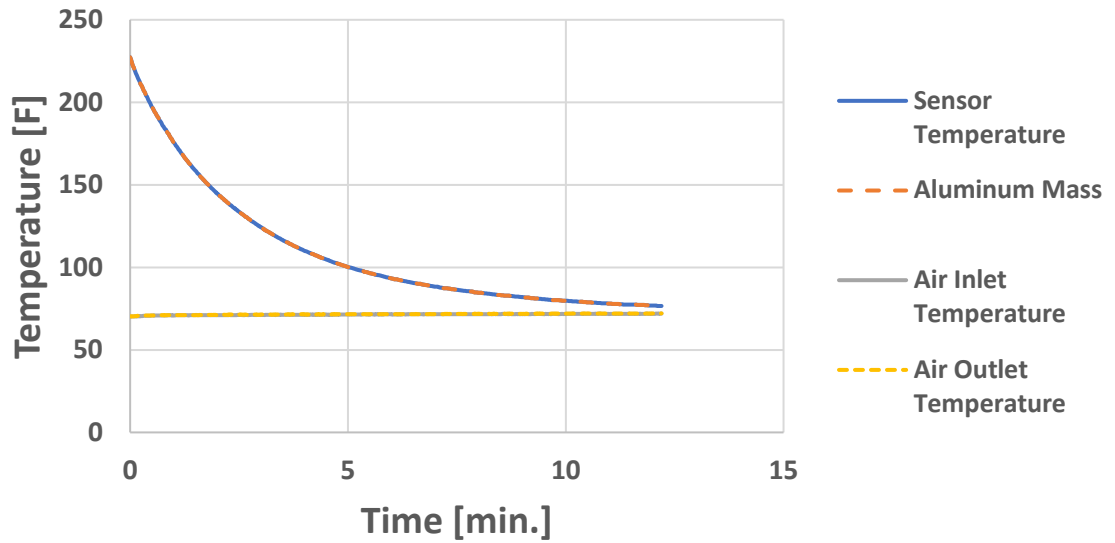
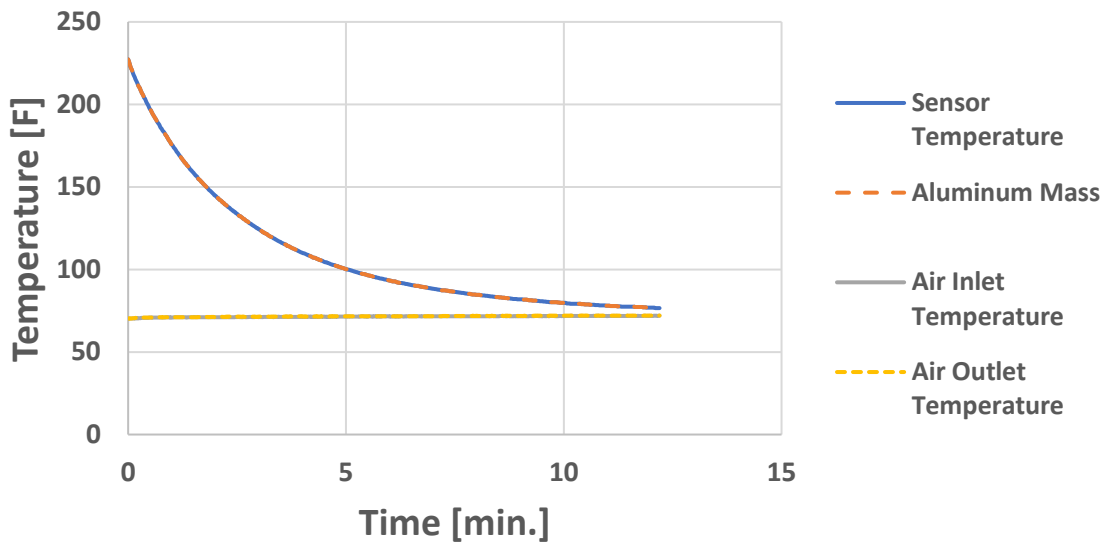
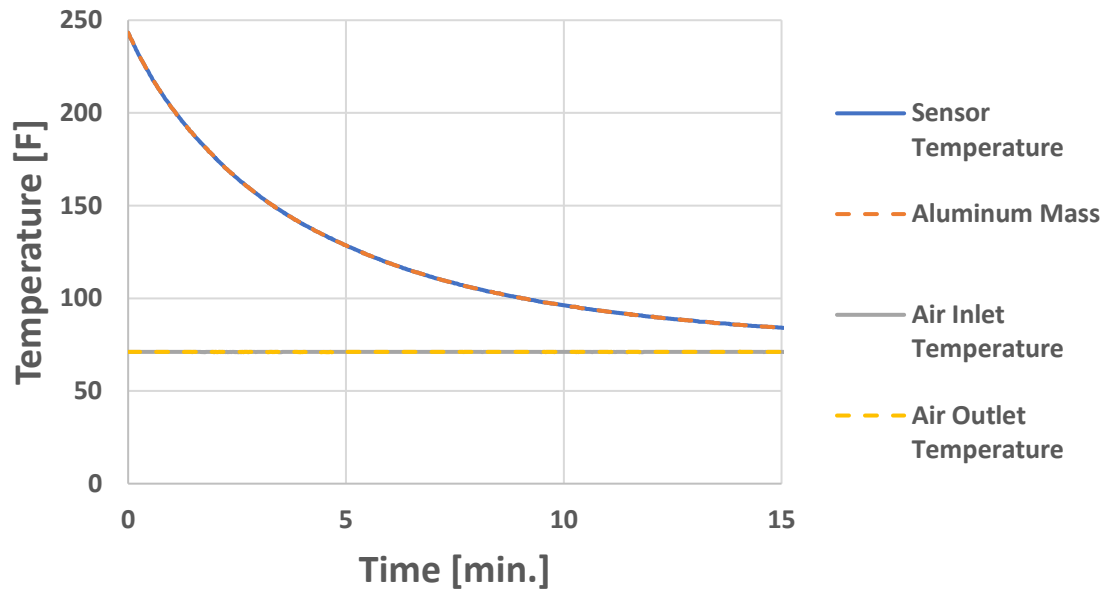


Figure 0-18 Sensor 8 convection calibration results. The first two graphs are temperature plots for the sensor, aluminum mass, and the air inlet and outlet temperature. The sensor temperature and aluminum temperature are measured to be the same. Inlet and outlet display no measurable changes in temperature. The bottom graph represents heat flux over time for low and high velocity tests.



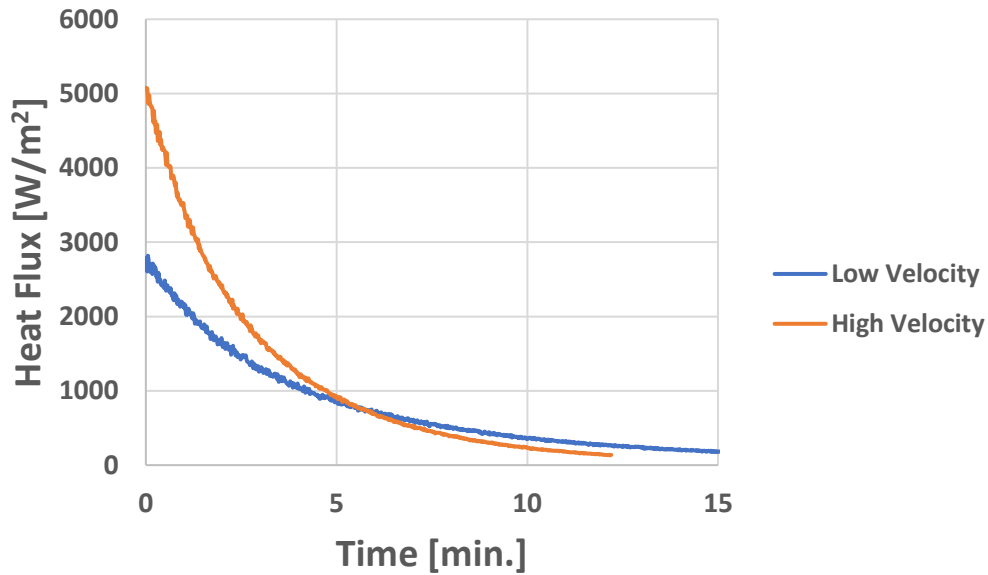
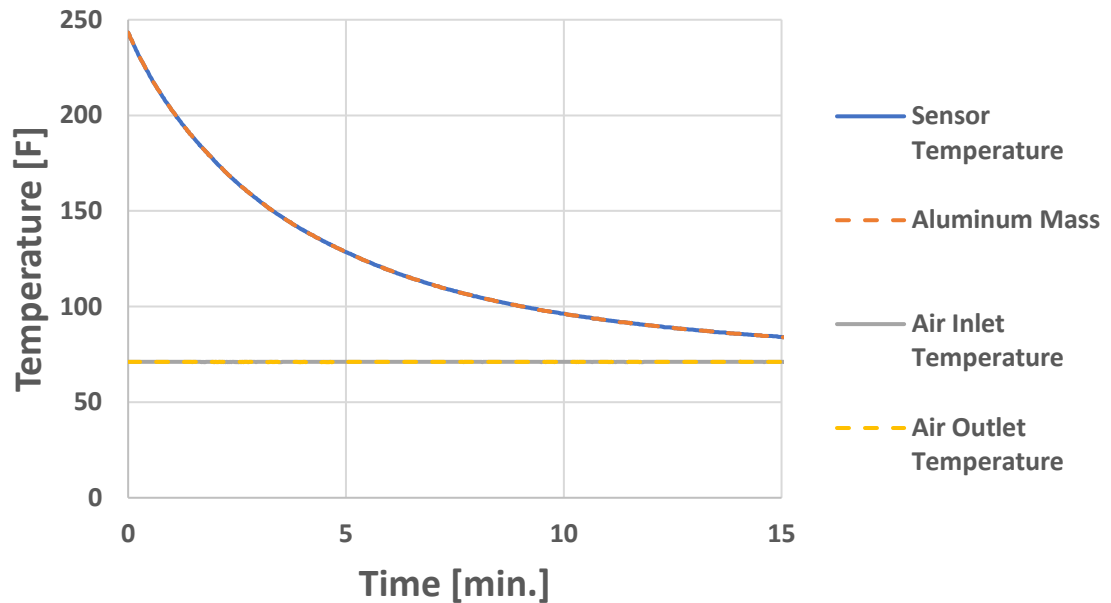


Figure 0-19 Sensor 9 convection calibration results. The first two graphs are temperature plots for the sensor, aluminum mass, and the air inlet and outlet temperature. The sensor temperature and aluminum temperature are measured to be the same. Inlet and outlet display no measurable changes in temperature. The bottom graph represents heat flux over time for low and high velocity tests.



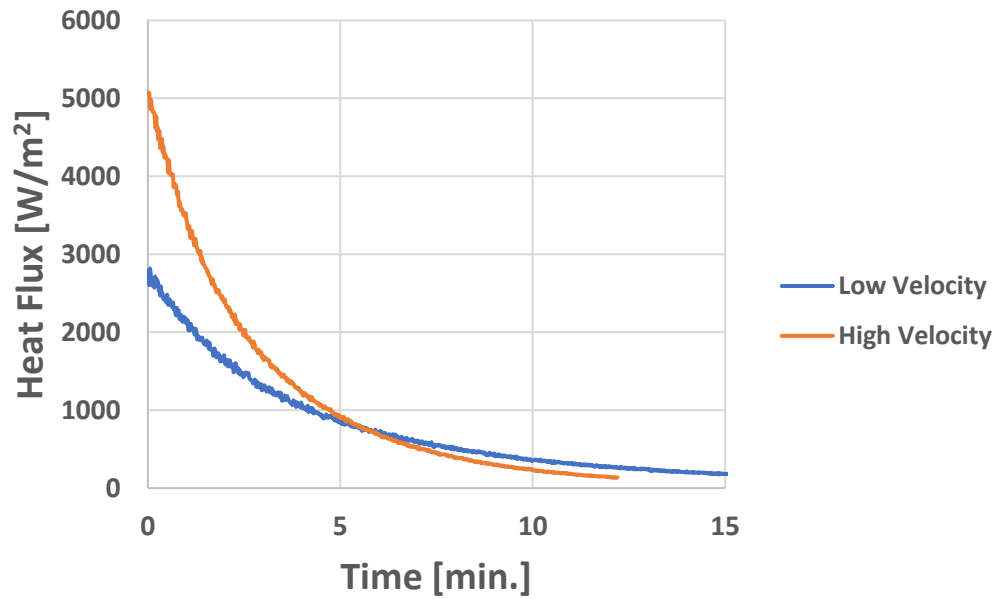
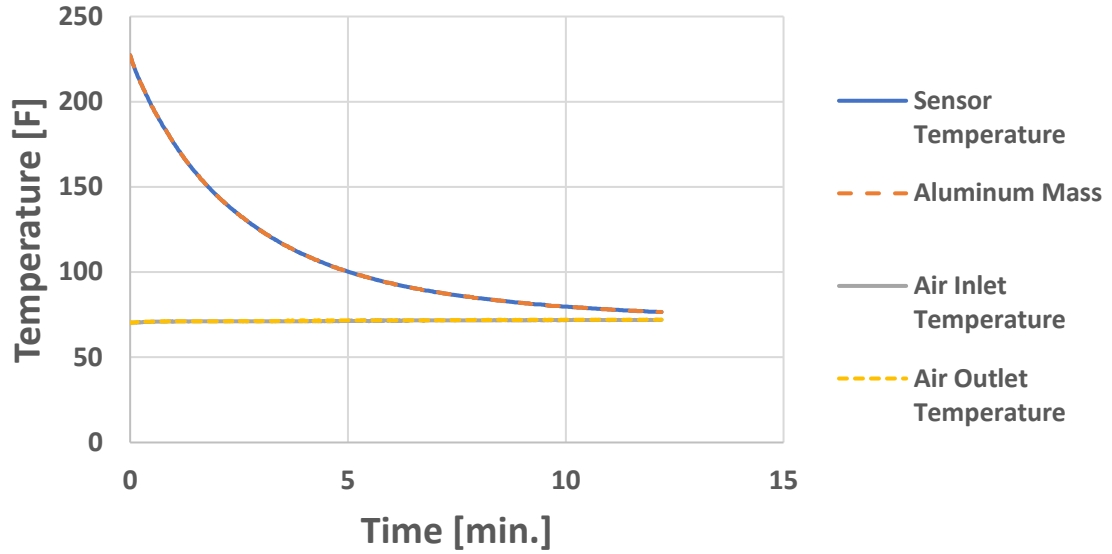
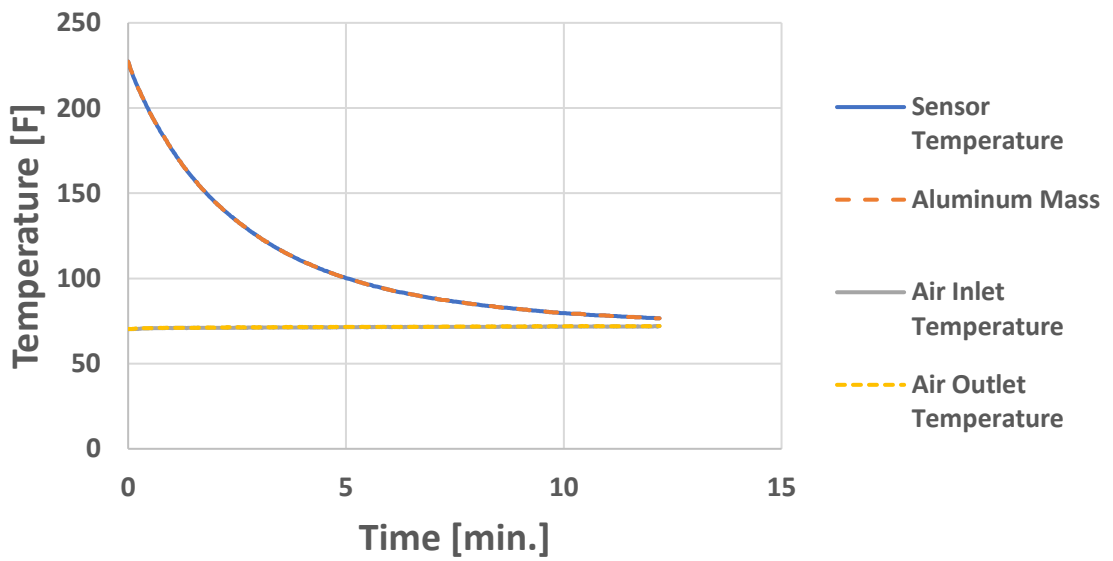
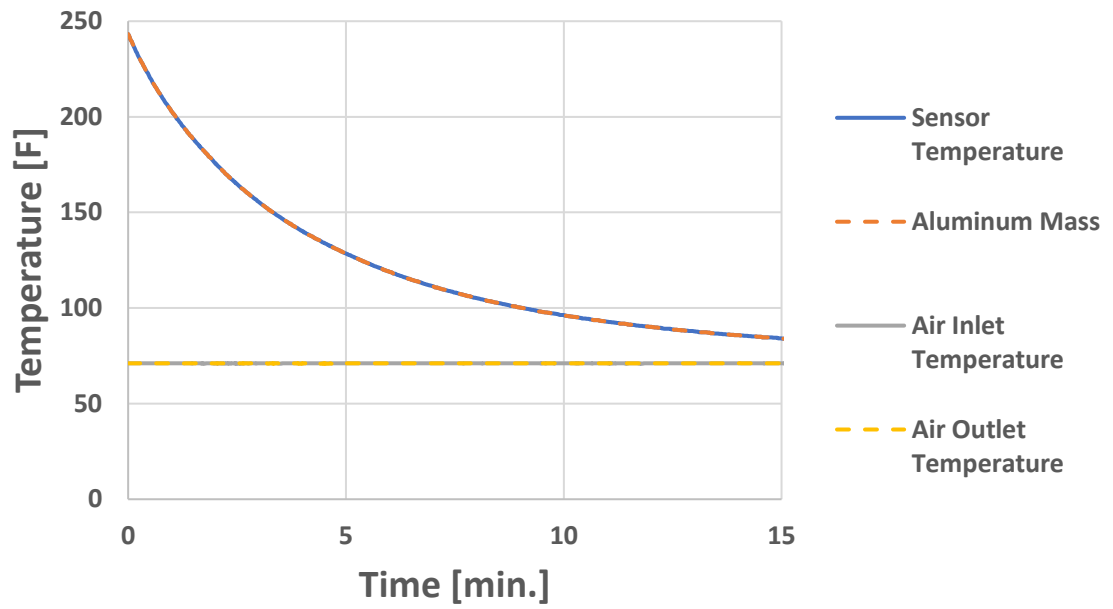


Figure 0-20 Sensor 10 convection calibration results. The first two graphs are temperature plots for the sensor, aluminum mass, and the air inlet and outlet temperature. The sensor temperature and aluminum temperature are measured to be the same. Inlet and outlet display no measurable changes in temperature. The bottom graph represents heat flux over time for low and high velocity tests.



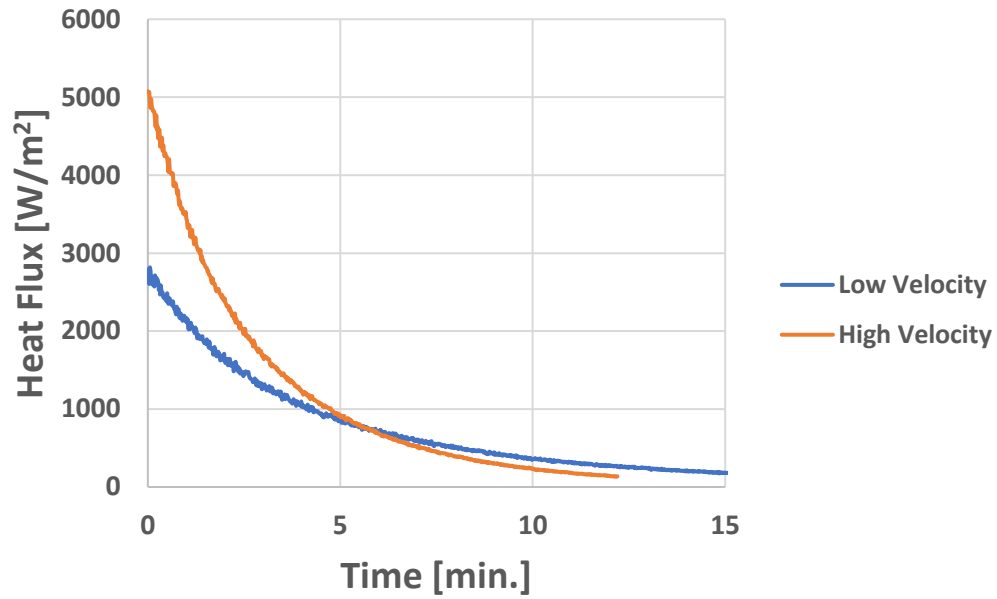


Figure 0-21 Sensor 11 convection calibration results. The first two graphs are temperature plots for the sensor, aluminum mass, and the air inlet and outlet temperature. The sensor temperature and aluminum temperature are measured to be the same. Inlet and outlet display no measurable changes in temperature. The bottom graph represents heat flux over time for low and high velocity tests.

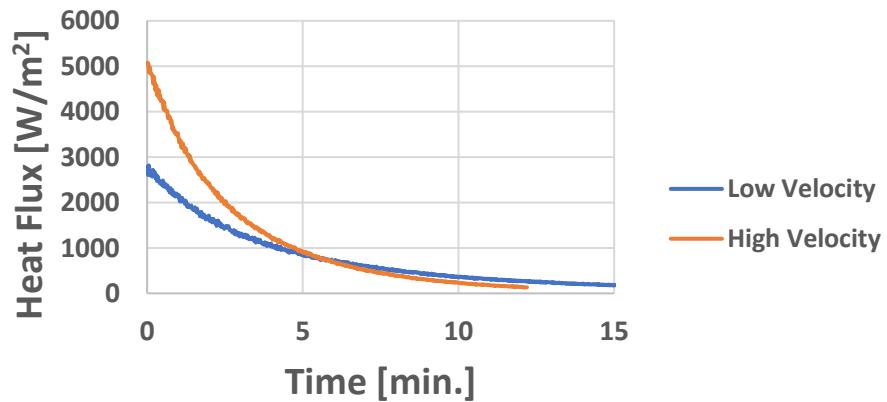
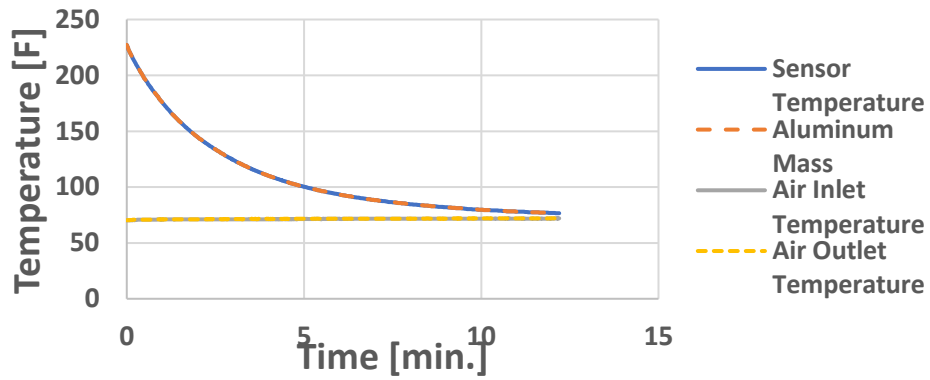
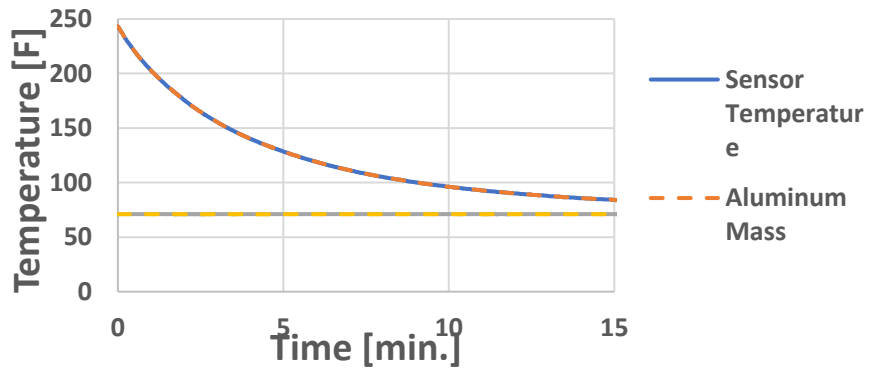


Figure 0-22 Sensor 12 convection calibration results. The first two graphs are temperature plots for the sensor, aluminum mass, and the air inlet and outlet temperature. The sensor temperature and aluminum temperature are measured to be the same. Inlet and outlet display no measurable changes in temperature. The bottom graph represents heat flux over time for low and high velocity tests.

C. Appendix III Oven Test Graphs

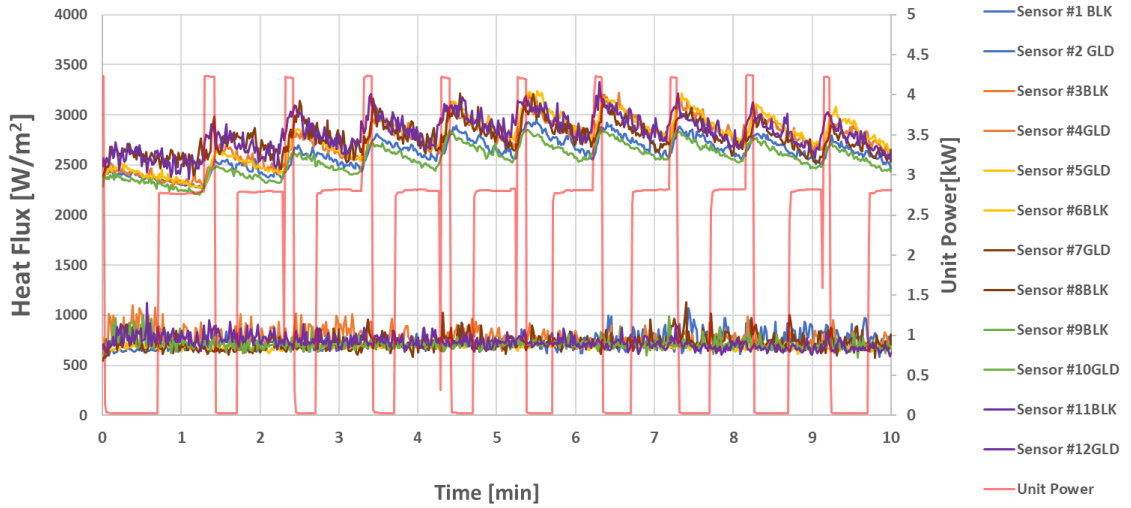


Figure 0-23 Heat flux measure for Traditional Bake, run 2 heat flux over time

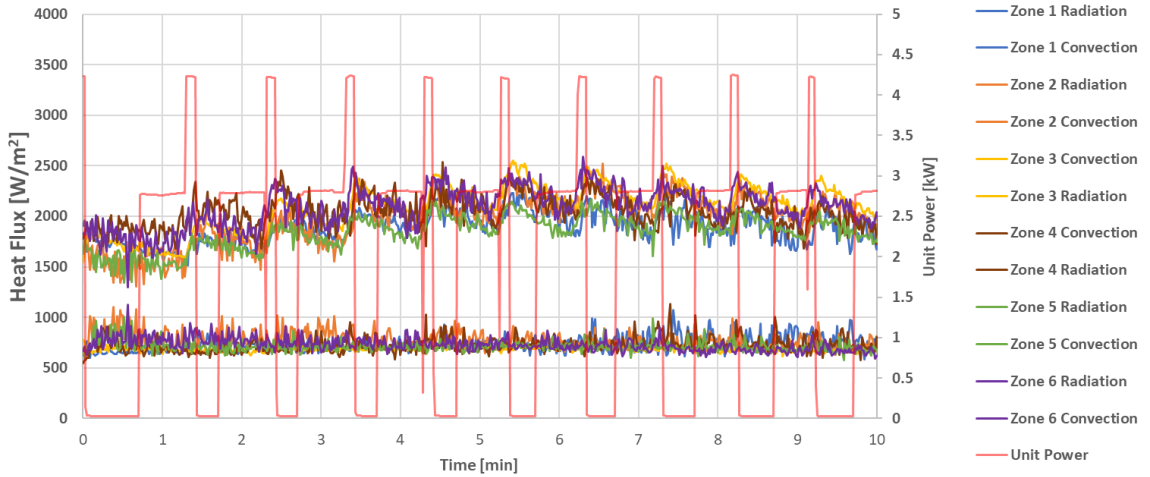


Figure 0-24 Zonal heat flux measure for Traditional Bake, run 2 heat flux over time

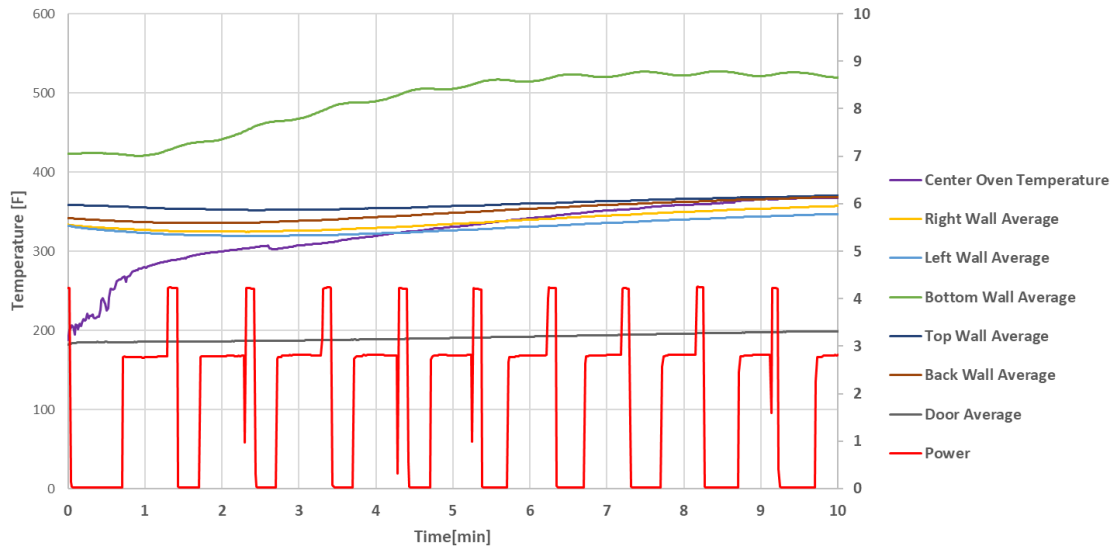


Figure 0-25 Heat flux measure for Traditional Bake, run 2 heat flux over time

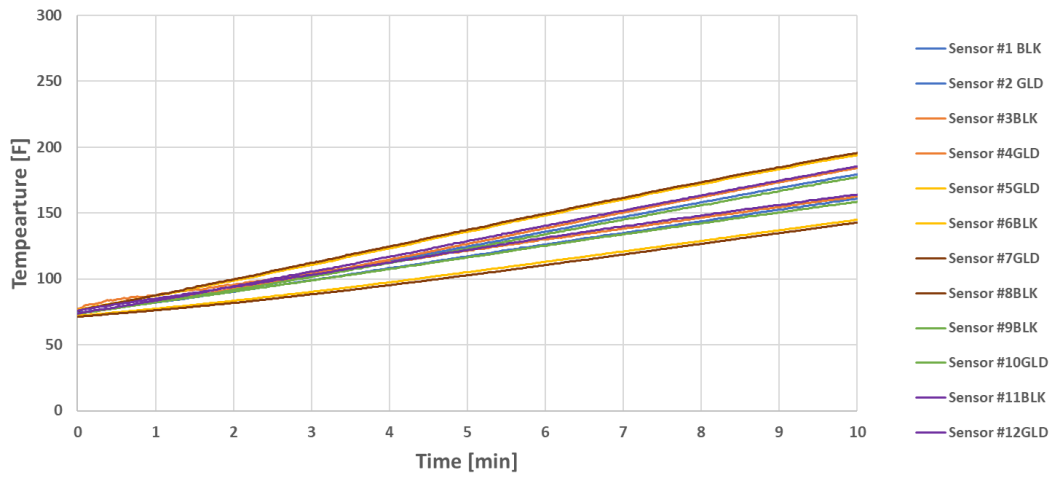


Figure 0-26 Temperature over time for the top mass for top mass in Traditional Bake, run 2

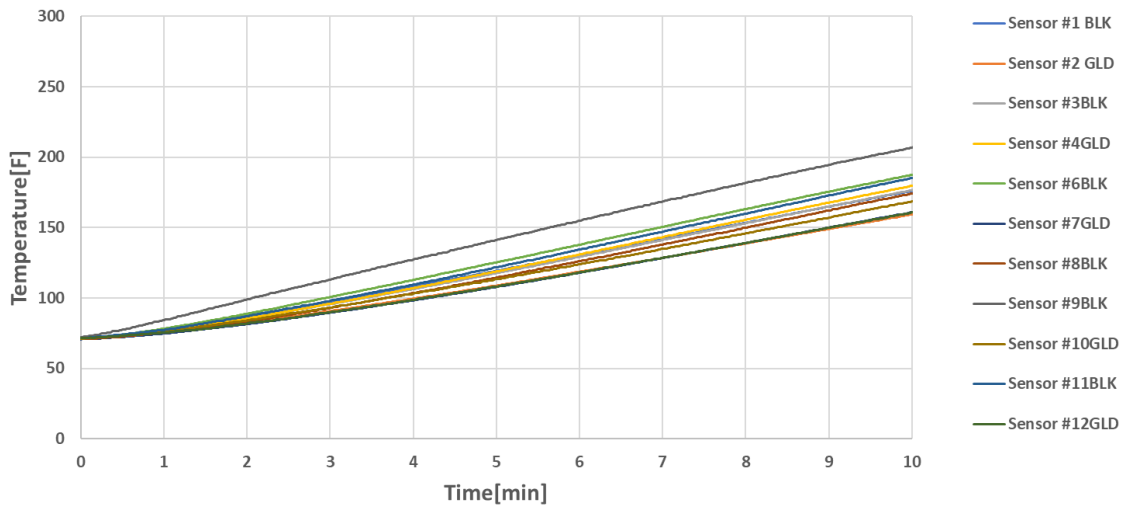


Figure 0-27 Temperature over time for the bottom mass for top mass in Traditional Bake, run 2

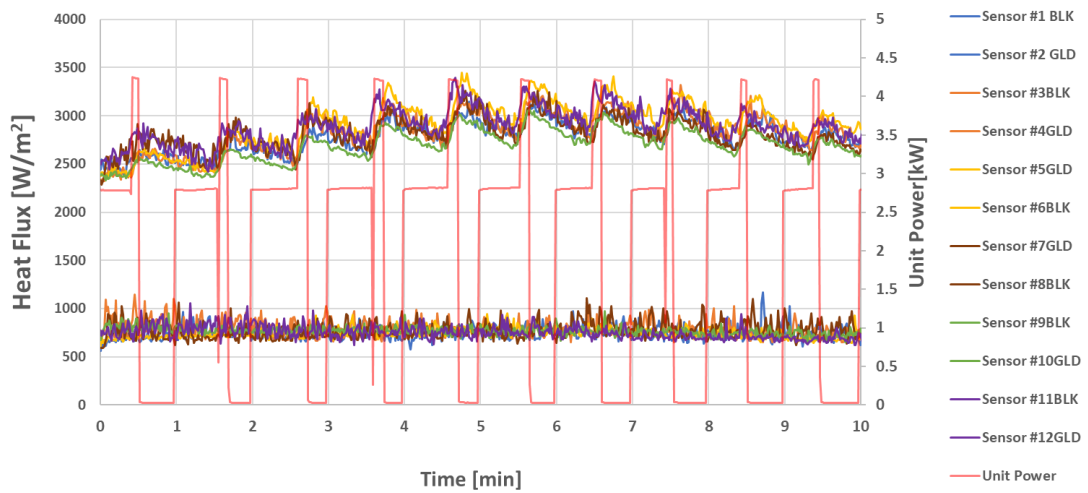


Figure 0-28 Heat flux measure for Traditional Bake, run 3 heat flux over time

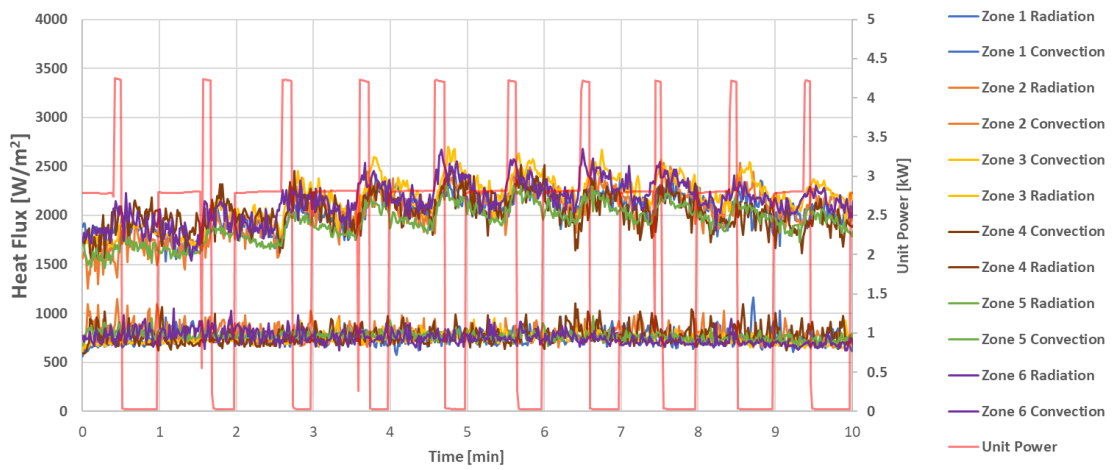


Figure 0-29 Zonal heat flux measure for Traditional Bake, run 3 heat flux over time

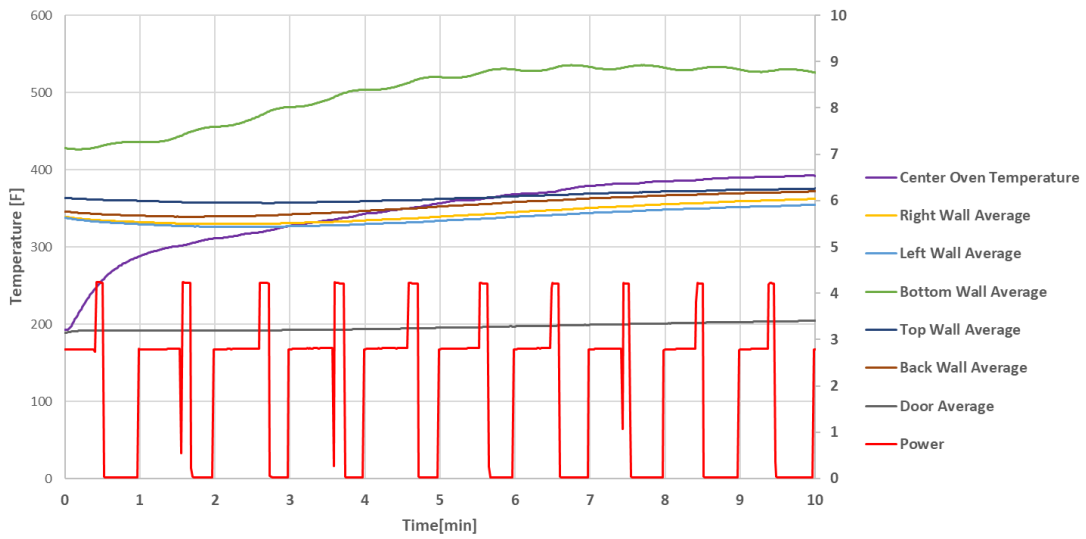


Figure 0-30 Interior oven temperatures measured for Traditional Bake, run 3

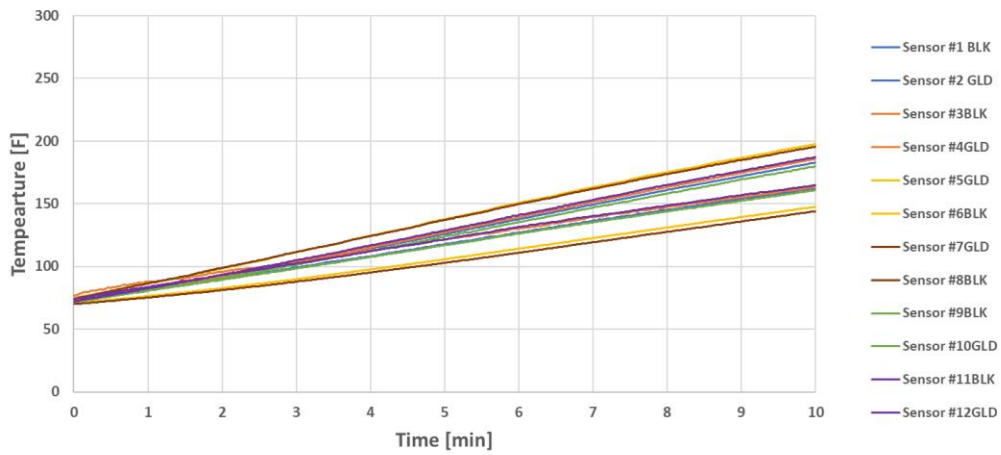


Figure 0-31 Temperature over time for the top mass for top mass in Traditional Bake, run 3

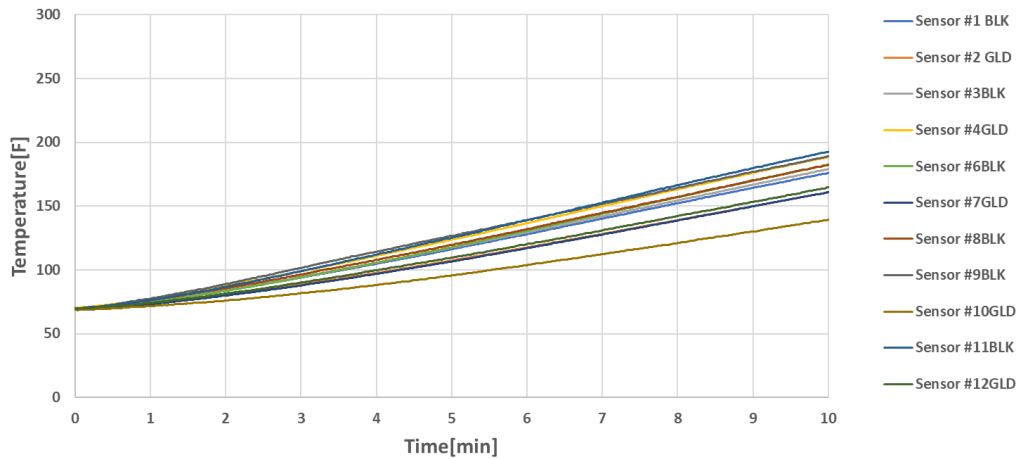


Figure 0-32 Temperature over time for the bottom mass for top mass in Traditional Bake, run 3

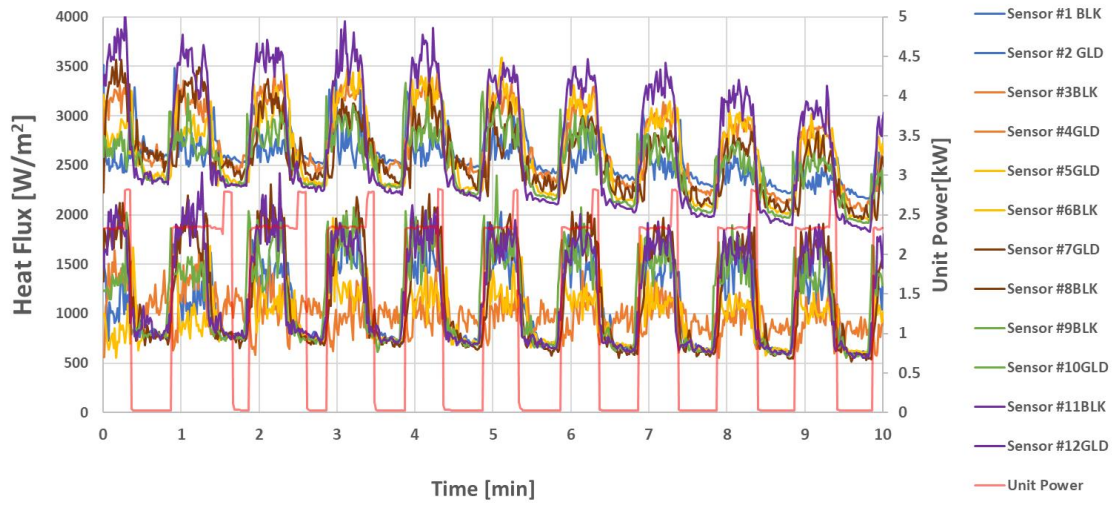


Figure 0-33 Heat flux measure for Convection Bake Multi, run 2 heat flux over time

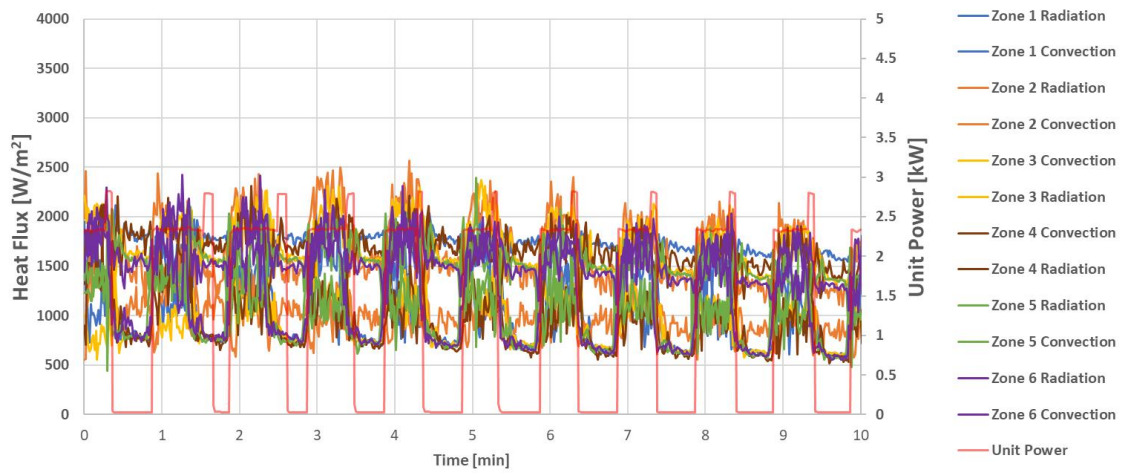


Figure 0-34 Heat flux measure for Convection Bake Multi, run 2 heat flux over time

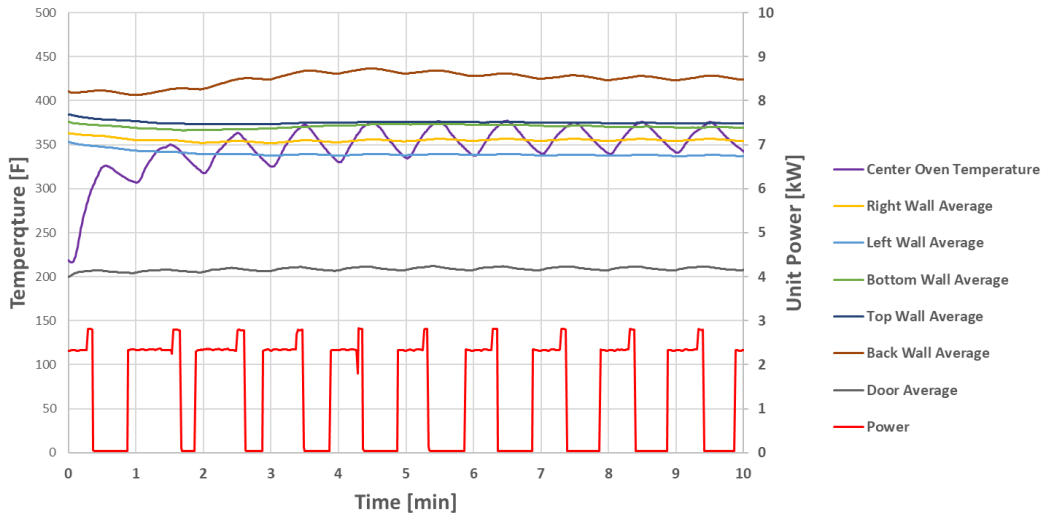


Figure 0-35 Heat flux measure for Convection Bake Multi, run 2 heat flux over time

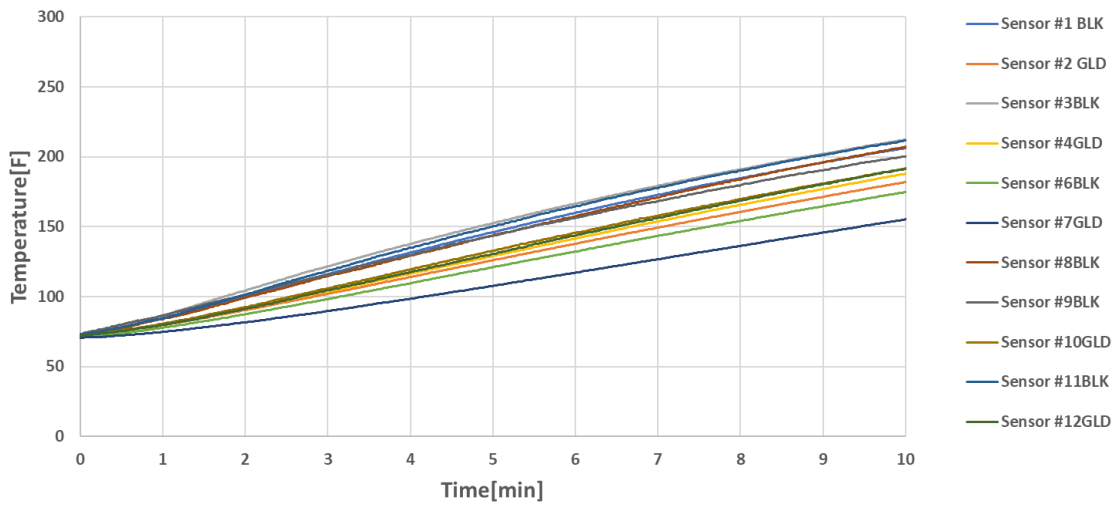


Figure 0-36 Temperature over time for the top mass for top mass in Convection Bake Multi, run 2

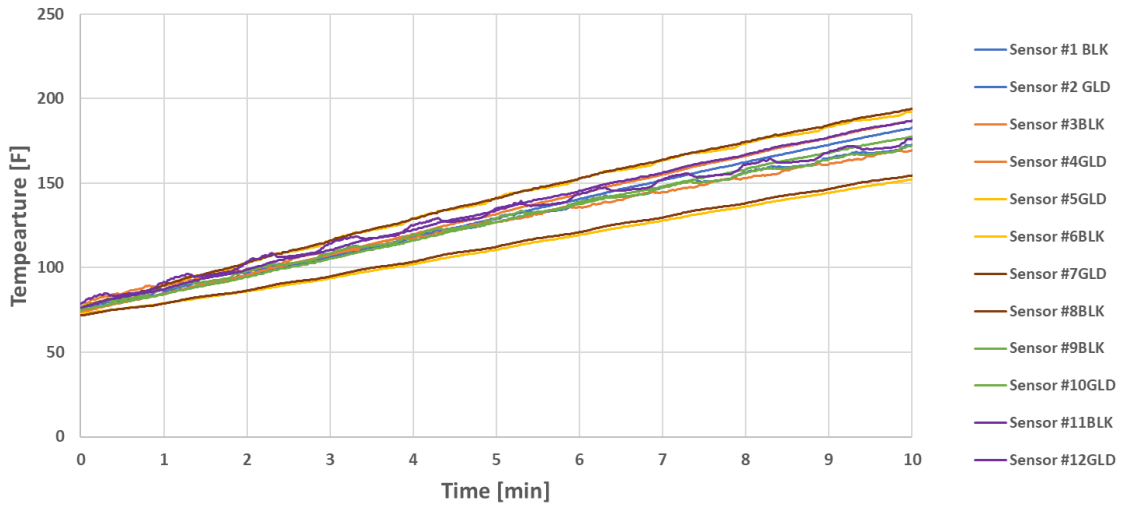


Figure 0-37 Temperature over time for the top mass for bottom mass in Convection Bake Multi, run 2

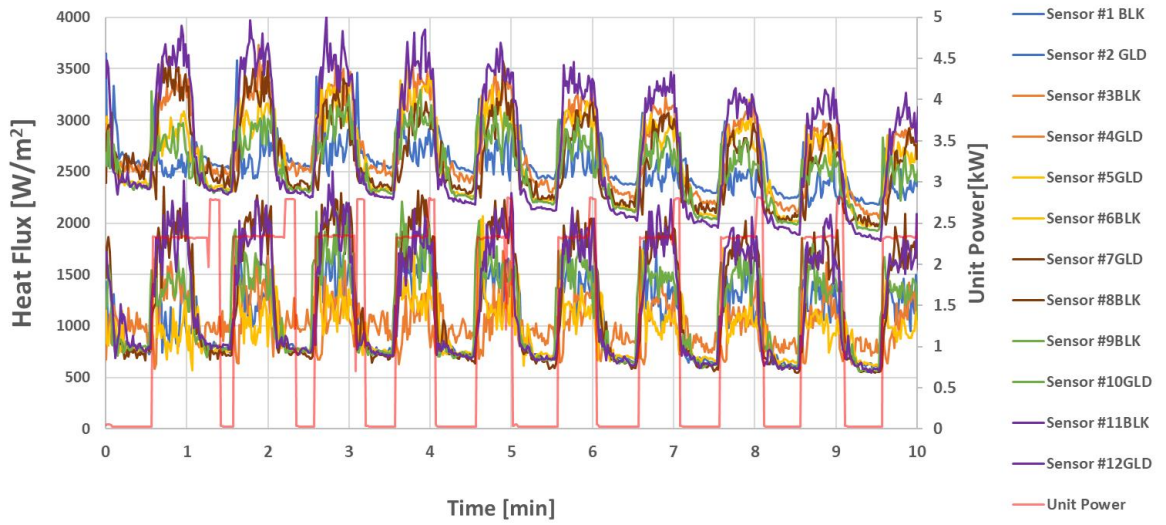


Figure 0-38 Heat flux measure for Convection Bake Multi, run 3 heat flux over time

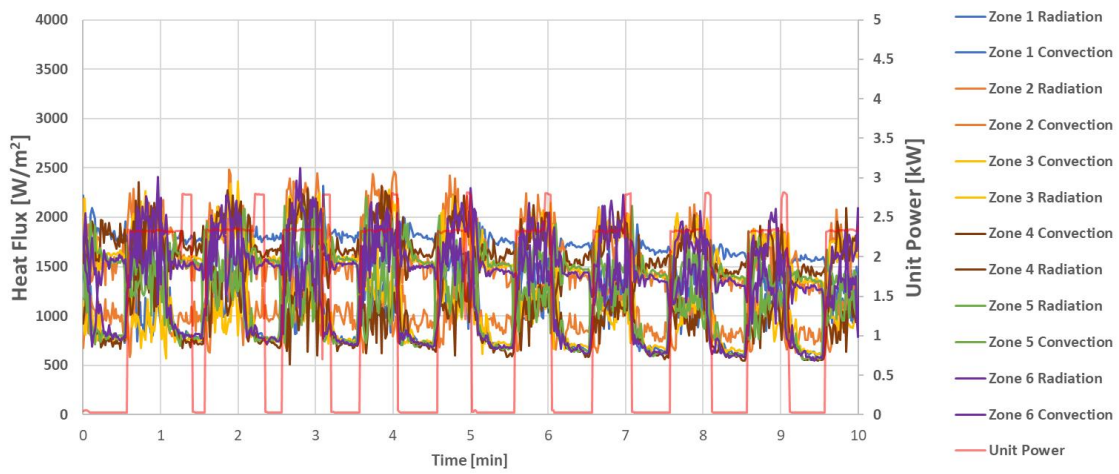


Figure 0-39 Zonal heat flux measure for Convection Bake Multi, run 3 heat flux over time

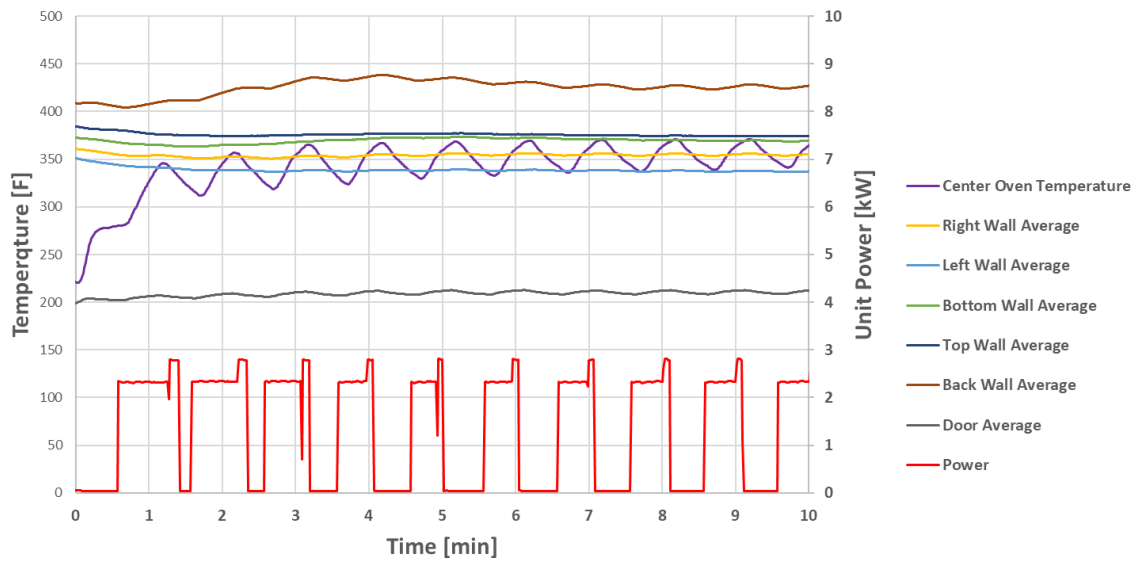


Figure 0-40 Heat flux measure for Convection Bake Multi, run 3 heat flux over time

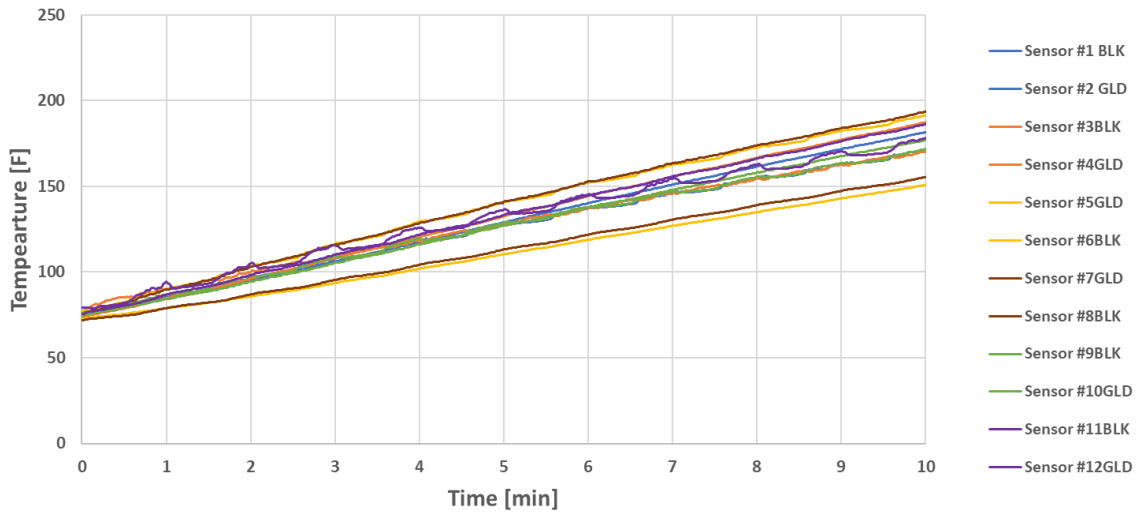


Figure 0-41 Temperature over time for the top mass for top mass in Convection Bake Multi, run 3

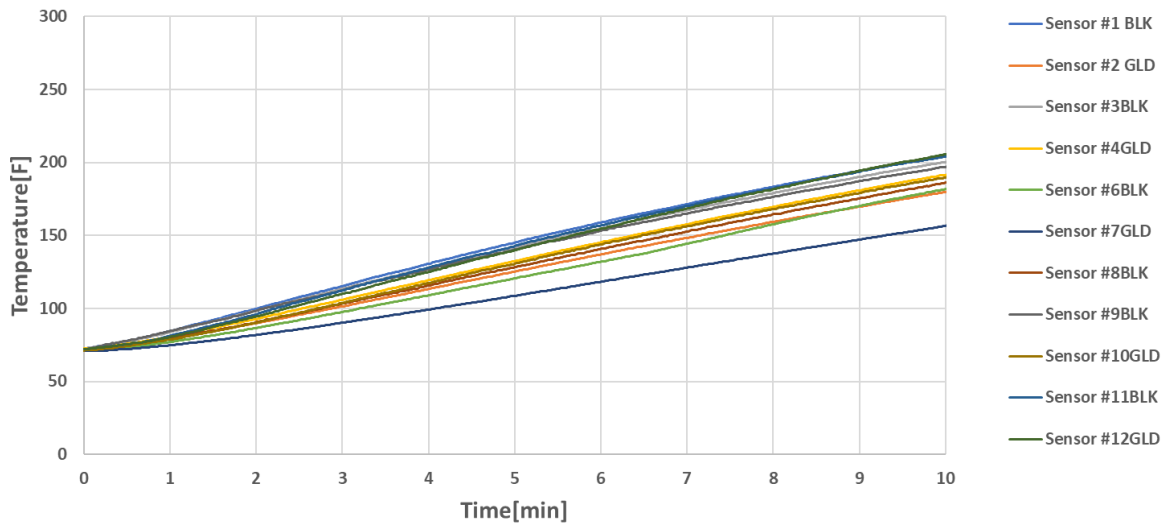


Figure 0-42 Temperature over time for the top mass for bottom mass in Convection Bake Multi, run 3

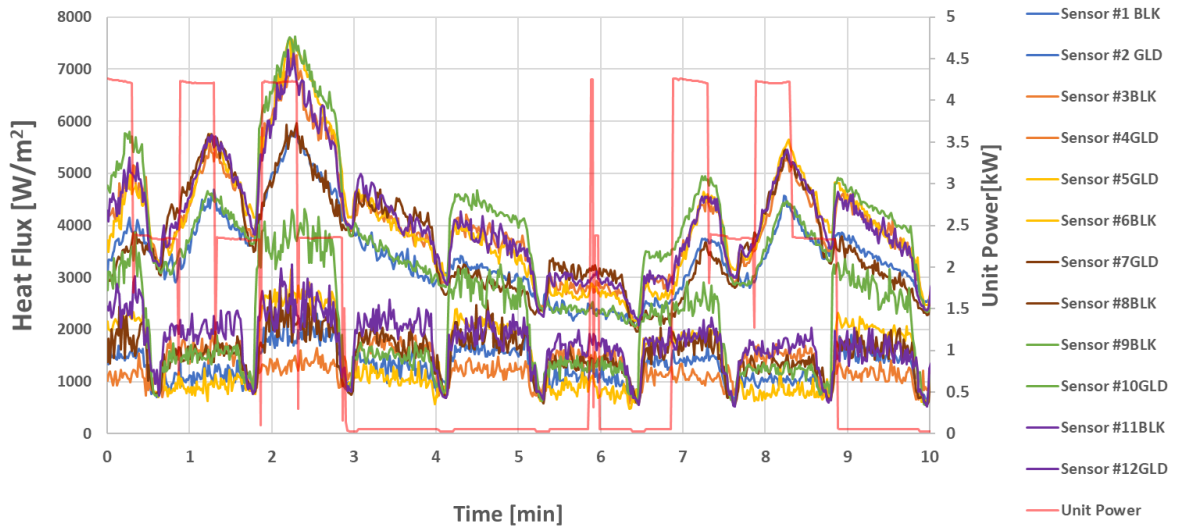


Figure 0-43 Heat flux measure for Air Fry, run 2 heat flux over time

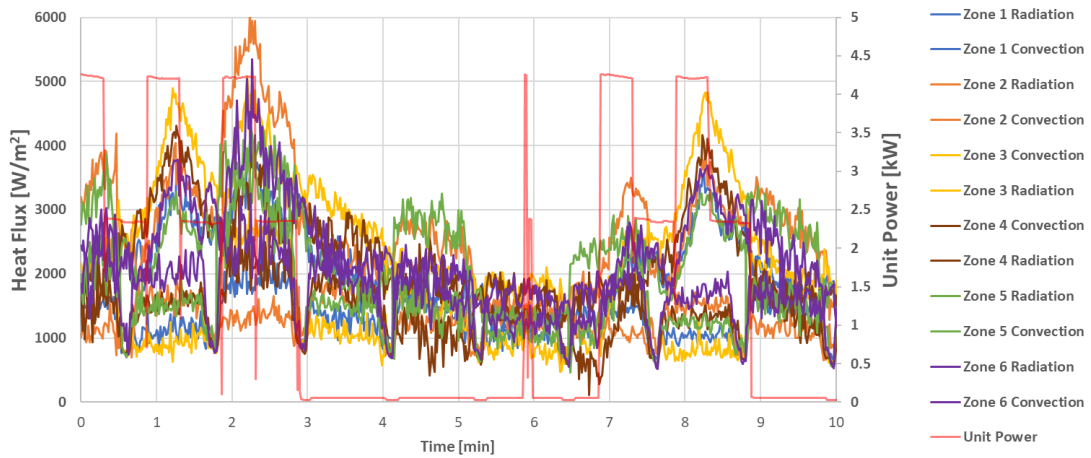


Figure 0-44 Zonal heat flux measure for Air Fry, run 2 heat flux over time

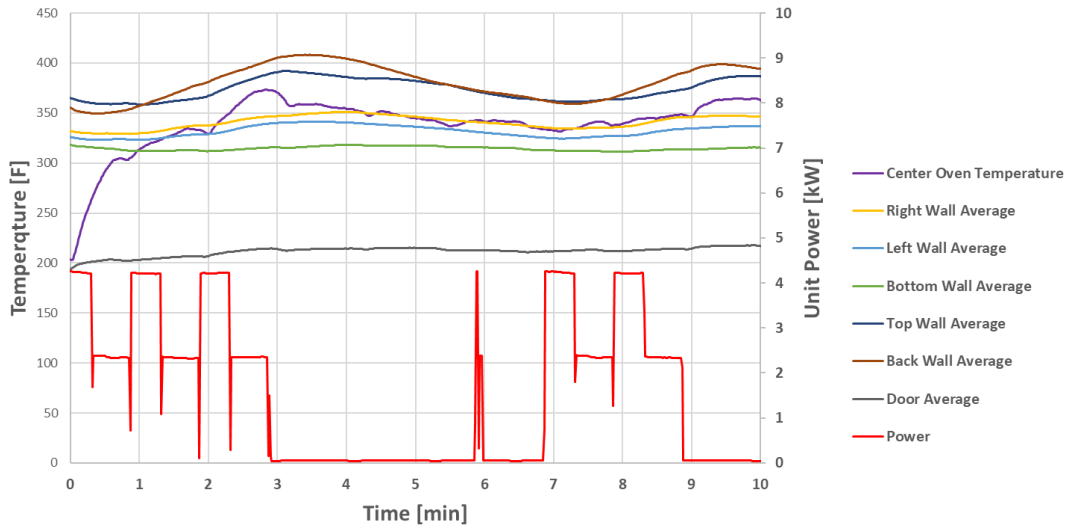


Figure 0-45 Heat flux measure for Air Fry, run 2 heat flux over time

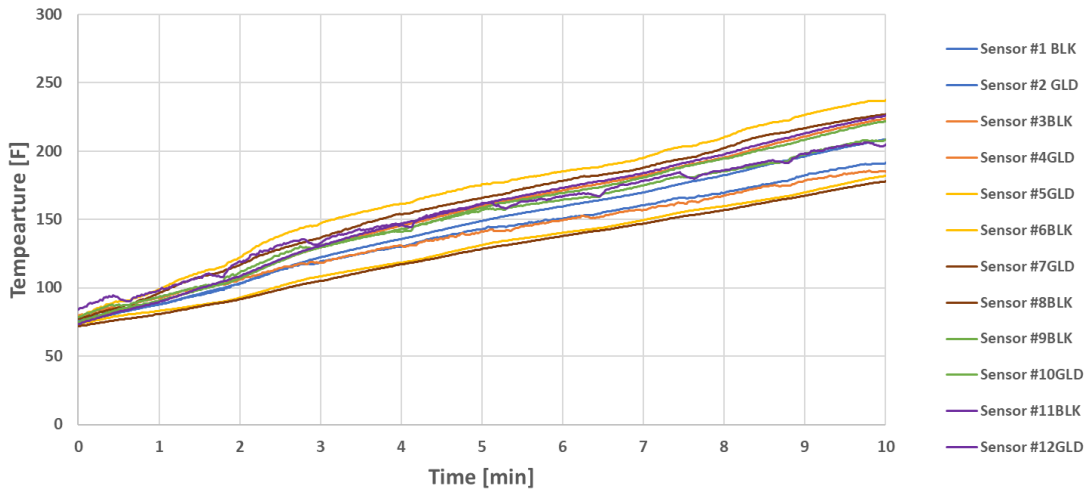


Figure 0-46 Temperature over time for the top mass for top mass in Air Fry, run 2

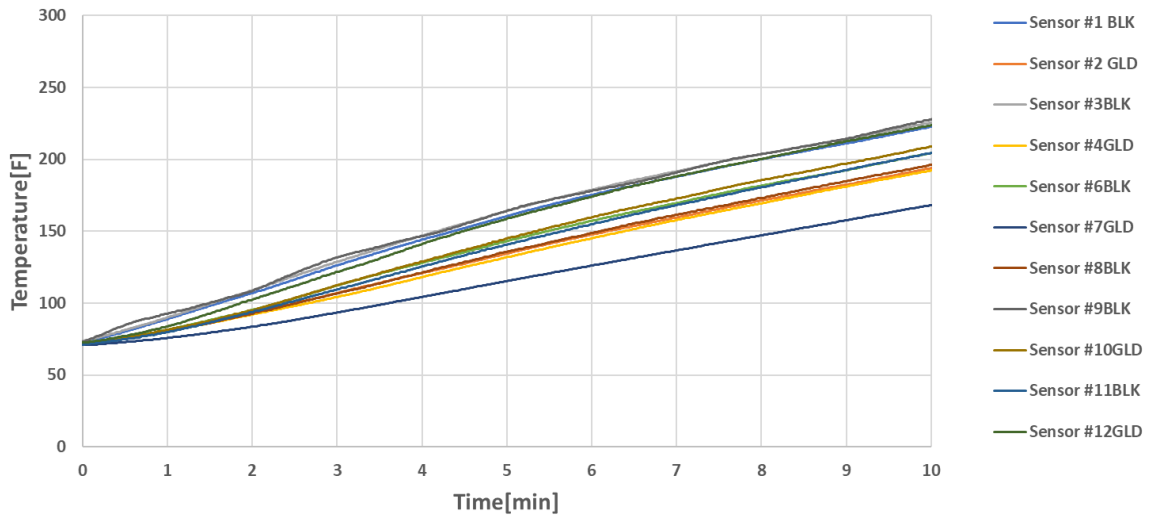


Figure 0-47 Temperature over time for the bottom mass for top mass in Air Fry, run 2

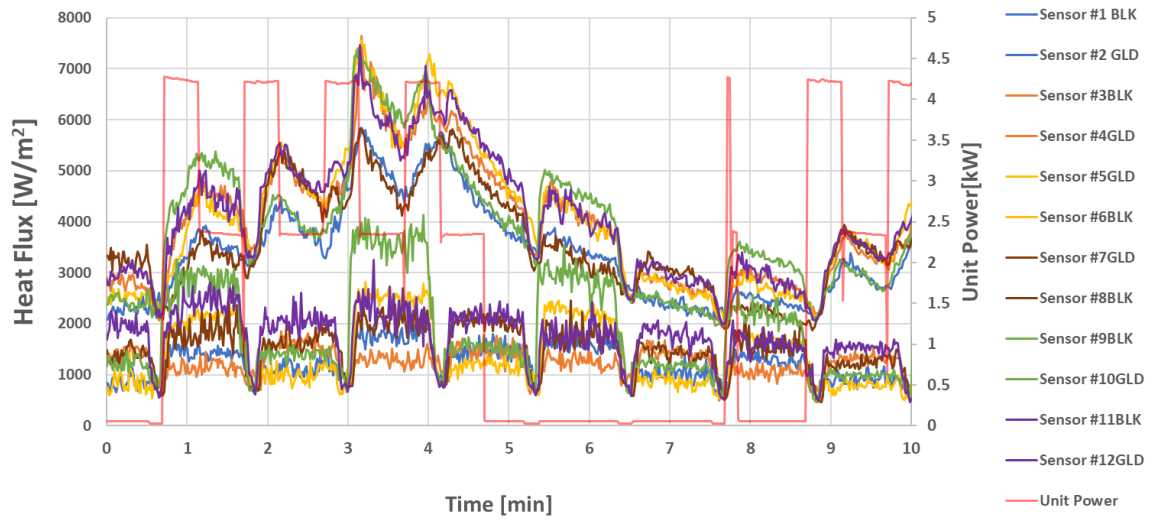


Figure 0-48 Heat flux measure for Air Fry, run 3 heat flux over time

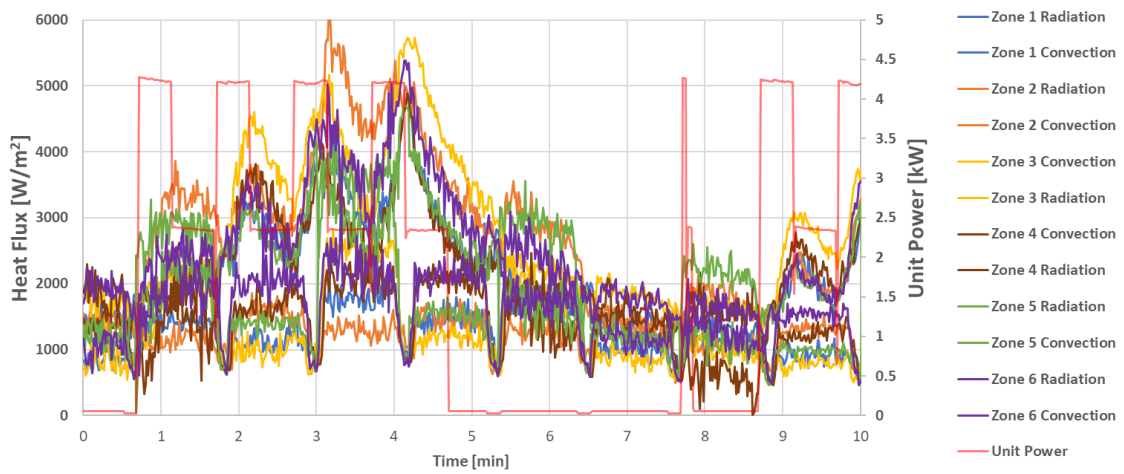


Figure 0-49 Zonal heat flux measure for Air Fry, run 3 heat flux over time

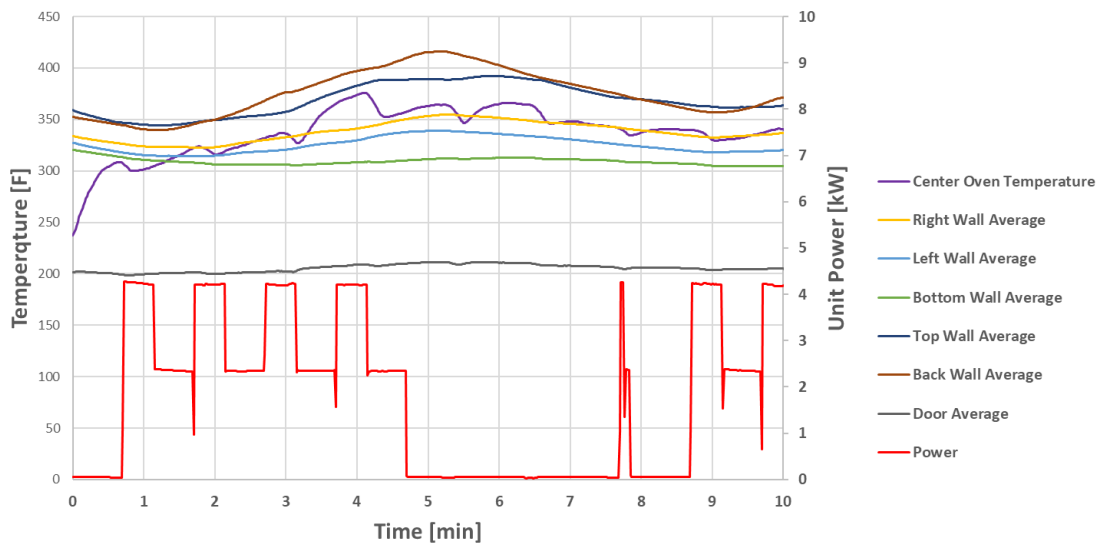


Figure 0-50 Heat flux measure for Air Fry, run 3 heat flux over time

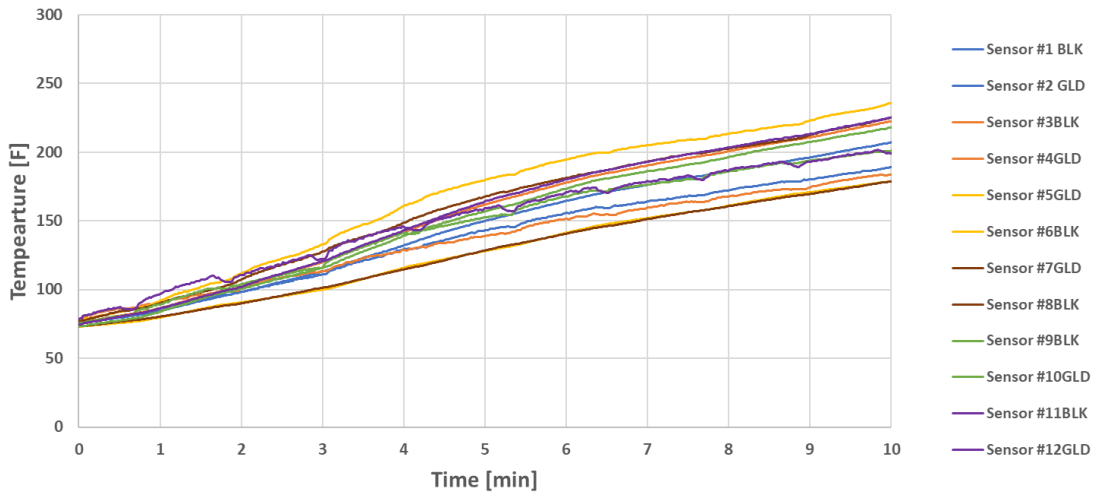


Figure 0-51 Temperature over time for the top mass for top mass in Air Fry, run 3

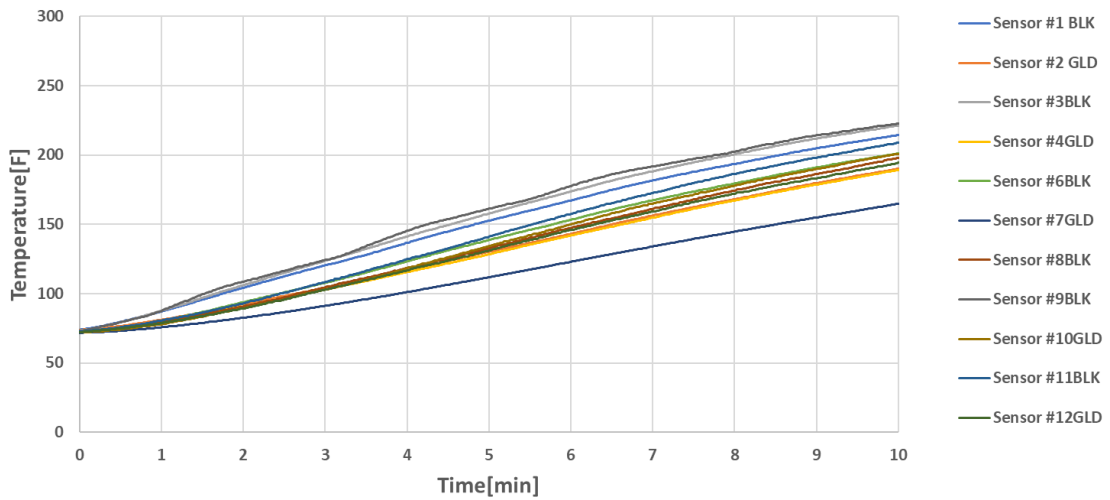


Figure 0-52 Temperature over time for the bottom mass for top mass in Air Fry, run 3

D. Appendix IV Sensor Material Specifications

Table 26 Top mass, bottom mass, and insulation base measurements for each heat flux sensor assembly

Sensor #	Sensor Serial #	Top Mass [g]	Bottom Mass [g]	Plastic Base [g]
1	2643	86.2	87.9	71.6
2	2635	87.0	87.0	71.2
3	2645	88.2	88.1	71.2
4	2636	87.0	87.3	71.4
5	2637	87.4	87.2	71.6
6	2641	87.0	87.8	71.4
7	2640	86.4	87.6	71.4
8	2644	87.0	87.0	71.4
9	2642	87.1	86.4	71.5
10	2639	87.7	88.2	71.6
11	2638	87.0	87.0	71.4
12	2597	87.0	87.5	71.4

FHF04 SPECIFICATIONS

Sensor type	foil heat flux sensor
Sensor type according to ASTM	heat flow sensor or heat flux transducer
Measurand	heat flux
Measurand in SI units	heat flux density in W/m^2
Measurement range	$(-10 \text{ to } +10) \times 10^3 \text{ W/m}^2$ at heat sink temperature $20 \text{ }^\circ\text{C}$ see appendix for detailed calculations
Sensitivity range	$9 - 13 \times 10^{-6} \text{ V/(W/m}^2)$
Sensitivity (nominal)	$11 \times 10^{-6} \text{ V/(W/m}^2)$
Directional sensitivity	heat flux from the back side to the front side (side with the dot) generates a positive voltage output signal
Increased sensitivity	multiple sensors may be put electrically in series. The resulting sensitivity is the sum of the sensitivities of the individual sensors
Expected voltage output	$(-100 \text{ to } +100) \times 10^{-3} \text{ V}$ turning the sensor over from one side to the other will lead to a reversal of the sensor voltage output
Measurement function / required programming	$\Phi = U/S$
Required readout	1 differential voltage channel or 1 single ended voltage channel, input resistance $> 10^6 \text{ } \Omega$
Optional readout	1 temperature channel
Rated load on wires	$\leq 1.6 \text{ kg}$
Rated bending radius	$\geq 7.5 \times 10^{-3} \text{ m}$
Rated temperature range, continuous use	$-70 \text{ to } +120 \text{ }^\circ\text{C}$
Rated temperature range, short intervals	$-160 \text{ to } +150 \text{ }^\circ\text{C}$ (contact Hukseflux when measuring at $-160 \text{ }^\circ\text{C}$)
Temperature dependence	$< 0.2 \text{ } \%/^\circ\text{C}$
Non-linearity	$< 5 \text{ } \%$ ($0 \text{ to } 10 \times 10^3 \text{ W/m}^2$)
Solar absorption coefficient	0.75 (indication only)
Thermal conductivity dependence	negligible, $< 3 \text{ } \%/(\text{W/m}\cdot\text{k})$ from $270 \text{ to } 0.3 \text{ W/m}\cdot\text{K}$
Sensor length and width	$(50 \times 50) \times 10^{-3} \text{ m}$
Sensing area	$9 \times 10^{-4} \text{ m}^2$
Sensing area length and width	$(30 \times 30) \times 10^{-3} \text{ m}$
Passive guard area	$16 \times 10^{-4} \text{ m}^2$
Guard width to thickness ratio	40
Sensor thickness	$0.4 \times 10^{-3} \text{ m}$
Sensor thermal resistance	$11 \times 10^{-4} \text{ K/(W/m}^2)$
Sensor thermal conductivity	$0.36 \text{ W/(m}\cdot\text{K)}$
Response time (95 %)	3 s
Sensor resistance range	160 to $240 \text{ } \Omega$
Required sensor power	zero (passive sensor)

Temperature sensor	type T thermocouple
Temperature sensor accuracy	$\pm 2\%$ (of temperature in °C), see appendix
Standard wire length	2 m
Wiring	3 x copper and 1 x constantan wire, AWG 24, stranded
Wire diameter	1×10^{-3} m
Marking	dot on foil indicating front side of the heat flux sensor; 1 x label on metal connection block, showing serial number and sensitivity
IP protection class	IP67
Rated operating relative humidity range	0 to 100 %
Use under water	FHF04 is not suitable for continuous use under water
Gross weight including 2 m wires	approx. 0.5 kg
Net weight including 2 m wires	approx. 0.5 kg
INSTALLATION AND USE	
Typical conditions of use	in experiments, in measurements in laboratory and industrial environments. Exposed to heat fluxes for periods of several minutes to several years. Connected to user-supplied data acquisition equipment. Regular inspection of the sensor. Continuous monitoring of sensor temperature. No special requirements for immunity, emission, chemical resistance.
Recommended number of sensors	2 per measurement location
Installation	see Chapter 5 on installation for recommendations
Bending	see Section 5.2 on installation on curved surfaces
Wire extension	see appendix on wire extension, or order sensors with longer wire
Sensor foil installation	see appendix on installation of FHF04 without wiring, without metal connection block
CALIBRATION	
Calibration traceability	to SI units
Product certificate	included (showing calibration result and traceability)
Calibration method	method HFPC, according to ASTM C1130 - 17
Calibration hierarchy	from SI through international standards and through an internal mathematical procedure
Calibration uncertainty	$< \pm 5\%$ ($k = 2$)
Recommended recalibration interval	2 years
Calibration reference conditions	20 °C, heat flux of 600 W/m ² , mounted on aluminium heat sink, thermal conductivity of the surrounding environment 0.0 W/(m·K)
Validity of calibration	based on experience the instrument sensitivity will not change during storage. During use the instrument "non-stability" specification is applicable. When used under conditions that differ from the calibration reference conditions, the FHF04 sensitivity to heat flux may be different than stated on its certificate. See the chapter on instrument principle for suggested solutions
Field calibration	is possible by comparison to a calibration reference sensor. Usually mounted side by side, alternative on top of the field sensor. Preferably reference and field sensor of the same model and brand. Typical duration of test > 24 h
MEASUREMENT ACCURACY	
Uncertainty of the measurement	statements about the overall measurement uncertainty can only be made on an individual basis.

Figure 0-53 HukseFlux heat flux sensor specifications

Sticker specifications

BLK

Measurand	convective and radiative heat flux
Spectral range (UV-VIS-NIR-FIR)	250 to $> 10000 \times 10^{-9}$ m
Absorption over range	> 95 %
Rated temperature range - continuous use	-40 to $+260$ °C*
Rated temperature range - short intervals	-40 to $+150$ °C*

GLD

Measurand	convective heat flux
Spectral range (NIR-FIR)	700 to $> 10000 \times 10^{-9}$ m
Reflection over range	> 95 %
Spectral range (VIS)	400 to 700×10^{-9} m
Reflection over range	> 80 %
Solar absorption	< 20 %
Rated temperature range - continuous use	-185 to $+260$ °C*
Rated temperature range - short intervals	-185 to $+150$ °C*

Figure 0-54 HukseFlux black and gold sticker specifications

CURRICULUM VITA

NAME: Kervins Petit-Bois
CONTACT INFORMATION: 1429 Delmar Ln, Louisville, KY 40216
Work: 502-452-3077
Cell: 786-541-6104
kpetitbois@gmail.com

DOB: January 2nd, 1996

EDUCATION & TRAINING M.S. Mechanical Engineering (exp. 08/2022)
University of Louisville
2019-2022

B.S. Mechanical Engineering
Florida International University
2014-2019

WORK/INTERNSHIP EXPERIENCE

General Electric Appliances Edison Engineer

July 2019 – July 2022

Participated in a rotational program at GE Appliances where 6 months to a year is spent working on various projects for various product lines.

During this 3-year program I led projects related to sealed system algorithms/design, thermal design, sensor development, and safety.

Engineering Mechanics Learning Assistant

January 2019-May 2019

Aid in the facilitation of learning for a Statics course with over 80 students.

My role is to help students understand concepts that they have difficulty understanding through lecture and traditional means.

General Electric Appliances Co-Op

January 2017 – August 2018

Applied knowledge of thermodynamics and heat transfer to perform analysis on a new model design to help test safety and validity.

Performed data validation on various studies using different statistical tools.

Led part design for various prototypes using Solidworks, Arduino, and C++ Programming. Also manufactured prototypes using waterjets and 3D printers.

STEM FYE Summer Bridge Program

June

2014 - August 2014

Worked along a team of 3 to build a robot and get it to navigate an obstacle course autonomously.

SKILLS

Technical: Intermediate Knowledge: C, C++, Python programming language;
Solidworks, Fusion 360, Creo Parametric; Minitab, Microsoft Office, Prototyping

Languages: English, Hatian-Creole